



THE UNIVERSITY
of ADELAIDE

Copper and Copper Alloy Electrocatalysts for the Conversion of Carbon Dioxide to Fuels

Anthony Joseph Vasileff

School of Chemical Engineering and Advanced Materials
Faculty of Engineering, Computer and Mathematical Sciences

A thesis submitted for the degree of Doctor of Philosophy
The University of Adelaide
April 2020

Contents

Abstract	v
Declaration.....	viii
Acknowledgements	x
1. Introduction	1
1.1 Project Significance.....	1
1.2 Research Objectives	2
1.3 Thesis Outline.....	3
1.4 References.....	4
2. Literature Review.....	5
Surface and Interface Engineering in Copper-Based Bi-Metallic Materials for Selective CO ₂ Electroreduction.....	5
2.1 Introduction.....	8
2.2 Fundamental Understanding of the CO ₂ RR.....	10
2.3 Improving Selectivity by Interfacial Engineering.....	13
2.4 Theoretical Prediction.....	28
2.5 General Trends	32
2.6 Conclusion and Outlook.....	35
2.7 Acknowledgement	37
2.8 References	38
3. Bronze Alloys with Tin Surface Sites for Selective Electrochemical Reduction of CO₂.....	44
3.1 Introduction.....	47
3.2 Results and Discussion.....	48
3.3 Conclusions	56
3.4 Acknowledgement	56
3.5 References	57
Supporting Information	59

4. Selectivity Control for Electrochemical CO₂ Reduction by Charge	
Redistribution on the Surface of Copper Alloys	69
4.1 Introduction	73
4.2 Results and Discussion	75
4.3 Conclusions	85
4.4 Acknowledgement	85
4.5 References	86
Supporting Information	88
5. Electrochemical Reduction of CO₂ to Ethane through Stabilization of an	
Ethoxy Intermediate	111
5.1 Introduction	114
5.2 Results and Discussion	115
5.3 Conclusions	124
5.4 Acknowledgement	124
5.5 References	125
Supporting Information	127
6. Improving Ethylene Selectivity of Copper-Based Electrocatalysts for CO₂	
Reduction by Gold Deposition	146
6.1 Introduction	148
6.2 Results and Discussion	150
6.3 Conclusion	156
6.4 Acknowledgment	156
6.5 References	157
Supporting Information	159
7. Conclusions and Outlook	168
Appendix A. Supplementary Literature Review	I
Carbon Solving Carbon's Problems: Recent Progress of Nanostructured Carbon-Based	
Catalysts for the Electrochemical Reduction of CO ₂	I
Appendix B. Publications and Presentations	XLVIII

Abstract

The electrochemical CO₂ reduction reaction (CO₂RR) can couple carbon sequestration with renewable energy to convert CO₂ into chemical feedstocks. For this process, copper is the only metal known to catalyze the CO₂RR to hydrocarbons with adequate efficiency but suffers from poor selectivity. Copper-based alloys and bi-metallic materials show improved CO₂ reduction selectivity compared to copper and the secondary element likely plays an important role. However, justification for the intrinsic effects of the secondary element on the catalytic mechanism and resultant selectivity is lacking. Therefore, the goal of this Thesis is to investigate how the selectivity of these copper-based systems are improved by the secondary elements. An understanding of their effects on the catalytic mechanism is gained through a combination of electrochemistry, *in-situ* spectroscopy, theoretical computations, and material characterization techniques.

In this Thesis, copper-tin alloys are studied and found to exhibit high selectivities towards CO and formate. As the tin concentration increases, a composition-dependent selectivity trend is observed, which is accompanied by a shift in intermediate binding preference of the first reaction intermediate. The binding configurations of this intermediate, either carbon-bound *COOH or oxygen-bound *OCHO, are identified using *in-situ* Raman spectroscopy. Theoretical computations also identify a gradual weakening of *COOH adsorption and strengthening of *OCHO adsorption with increasing tin concentration. This behavior is explained by the resultant charge redistribution which occurs from alloying. Consequently, local positive charge on the tin sites hinders nucleophilic attack of the carbon in the CO₂ molecule and preferences *OCHO adsorption in the first reaction step.

In-situ spectroscopy is further applied to study copper-based systems and their selectivities towards C2 products. Iodide-derived copper (ID-Cu) exhibits significantly greater ethane selectivity and more favorable kinetics compared to oxide-derived copper (OD-Cu). A key intermediate in the ethane mechanism is identified by *in-situ* X-ray adsorption and Raman spectroscopies and is likely better stabilized on ID-Cu due to its trace iodine species. It is also postulated that the ability of a catalyst to bind this intermediate determines the selectivity towards either ethane or ethanol in the C2 pathway. Using *in-situ* ATR-FTIR to study OD-Cu nanocubes, bridge-bonded *CO is found to be the dominant binding mode of CO at overpotentials relevant to C2 product generation. However, OD-Cu nanocubes with electrodeposited gold (OD-Cu-Au) achieve a higher selectivity for ethylene and maintain a higher population of linear-bonded *CO at these overpotentials. From these *in-situ* studies, it is demonstrated how the secondary element can affect the adsorption energetics of key reaction intermediates and improve the selectivity of copper-based electrocatalysts.

Declaration

I certify that this work contains no material which has been accepted for the award of any other degree or diploma in my name, in any university or other tertiary institution and, to the best of my knowledge and belief, contains no material previously published or written by another person, except where due reference has been made in the text. In addition, I certify that no part of this work will, in the future, be used in a submission in my name, for any other degree or diploma in any university or other tertiary institution without the prior approval of the University of Adelaide and where applicable, any partner institution responsible for the joint-award of this degree.

I acknowledge that copyright of published works contained within this thesis resides with the copyright holder(s) of those works.

I also give permission for the digital version of my thesis to be made available on the web, via the University's digital research repository, the Library Search and also through web search engines, unless permission has been granted by the University to restrict access for a period of time.

I acknowledge the support I have received for my research through the provision of an Australian Government Research Training Program Scholarship.

Signed:

✓ ✓

Date: 15/06/2020

Acknowledgements

Foremost, I would like to express my sincere appreciation towards my principal supervisor, Prof. Shizhang Qiao, and my co-supervisor, Dr. Yao Zheng. Without their ongoing support and encouragement to help me achieve to the best of my abilities, this Thesis would not be possible. I commend them on their enormous dedication to their students and their research.

Throughout my PhD, it has been a great pleasure working alongside the generous and hard-working people in Prof. Qiao's group. A special thanks goes to Chaochen Xu and Dr. Susan Wang for their huge support and involvement in developing the CO₂RR research group. I would also like to thank Dr. Yan Jiao, Dr. Yongqiang Zhao, Xin Liu, Dr. Ke Zhang, Xing Zhi, Dr. Eric Xie, Dr. Chao Ye, Huanyu Jin, Jieqiong Shan, and Laiquan Li for their involvement in my research and their friendship. While there are too many people to mention from Prof. Qiao's group, I have cherished my time working alongside all of them.

I would like to thank the many research and technical staff whose hard work was crucial to the completion of this Thesis. My deepest gratitude goes to Dr. Qiuhong Hu for her generous support with the analytical equipment, Jason Peak for his exceptional technical skills, Dr. Ashley Slattery for his TEM imaging, Prof. Haoming Chen and Dr. Yanping Zhu at the National Taiwan University for their collaboration on *in-situ* XAS studies, Philip Clements for his help throughout my PhD with NMR, Dr. Lei Ge at the University of Southern Queensland for all his help with XPS, Ken Neubauer for his help with SEM, and Dr. Sarah Gilbert for her ICP-MS work. I would also like to acknowledge The University of Adelaide and the Australian Research Council for their financial support.

To the staff in the School of Chemical Engineering, I would like to thank them all for their kindness and for making the School such an inviting and friendly place. Special thanks must be given to Prof. Sheng Dai for his help in securing my PhD scholarship, Prof. David Lewis for supporting my conference travel, and Michelle Fitton and Sue Earle for their help with everything office related. To my great friends made at the School, I thank you for the many laughs shared together and the help given throughout the tough times.

Finally, I am forever grateful to all my family and friends for their love and support throughout my life. I am certain this PhD would not be possible without them. To Rocca (soon Dr. Roccisano), thank you for all the lunchtime coffees and therapy sessions which truly kept me going over the past four years. To Mum, Dad, Paul, and Matthew, thank you for always supporting my goals in life and helping me to be the person I am today. And to Elena, who brings out the best in me (even when I'm hungry), thank you for your continual love and encouragement to always believe in myself.

Chapter 1

Introduction

1.1 Project Significance

A major hurdle to the proliferation of renewable energy is the development of effective energy conversion and storage technologies. This is largely due to the need to address issues involving intermittency and baseload power.¹ However, the relatively high cost and low energy densities of current energy conversion/storage devices greatly hinders their commercial integration into renewable energy systems. A long proposed method of energy conversion and storage is to use renewable energy sources to drive the conversion of CO₂ to useful molecules such as methane, ethylene, and carbon monoxide.² This process is known as the CO₂ reduction reaction (CO₂RR). Methods proposed in the literature for the CO₂RR are primarily: electrocatalytic reduction, photocatalytic reduction, chemical, and biochemical,³ and have all been extensively studied in recent years.⁴⁻⁶ Of all the processes studied, electrocatalytic reduction appears to be the most feasible. This is because it can be conducted in ambient conditions, has relatively high conversion efficiency, and can be driven directly by existing renewable energy systems.^{3, 7} An integrated CO₂RR system is attractive because it can (i) sequester carbon from the atmosphere, (ii) provide an energy storage solution with high energy density (i.e. in chemical bonds), and (iii) it can be used to produce industrial chemicals and fuels. However, in order to operate the CO₂RR at any meaningful reaction rate, effective catalysts are required to drive the conversion process without the cost of huge overpotential.³ Therefore, fundamental to the success of this technology is the development of effective and selective CO₂RR catalysts.

1.2 Research Objectives

The main goal of this Thesis is to use copper as a catalyst platform for the CO₂RR and to investigate how its selectivity can be improved through alloying and introducing secondary elements. To achieve this, a combination of electrochemistry, *in-situ* spectroscopy, theoretical computations, and material characterization techniques will be used. The specific objectives of this Thesis are to:

- Provide a framework to predict the selectivity of copper alloy and bi-metallic catalysts based on their composition.
- Synthesize a range of copper alloy catalysts to characterize their electrochemical performance and determine their kinetic parameters and selectivity towards CO₂RR products.
- Study the copper alloy system using *in-situ* Raman spectroscopy in order to determine the key reaction intermediates present during reaction. From this, use computation to provide fundamental reasoning which explains the inherent selectivity trends.
- Investigate copper-based systems using *in-situ* X-ray adsorption spectroscopy and *in-situ* Raman spectroscopy to address persistent inconsistencies related to the ethane mechanism.
- Explore the properties of copper-based catalysts which govern selectivity for C₂ products and provide a rational strategy to engineer copper-based catalysts to exploit these.
- Utilize *in-situ* ATR-FTIR spectroscopy to detect the key reaction intermediates on copper bi-metallic catalysts and determine how the secondary metal steers the reaction pathway to ethylene.

1.3 Thesis Outline

This Thesis presents the outcomes of my PhD research and is presented as a sequence of journal publications. The Chapters in this Thesis are presented as follows:

- **Chapter 1** provides background to the Thesis and outlines the project scope and key contributions to the field.
- **Chapter 2** presents a review of recent literature covering the development of copper alloy and bi-metallic materials for use as CO₂RR electrocatalysts and explores the fundamental role of the secondary metal.
- **Chapter 3** characterizes the electrochemical performance of Cu-Sn alloys and determines their reaction kinetics. From this, a preliminary hypothesis is made regarding the key reaction parameters governing selectivity.
- **Chapter 4** explores the Cu-Sn system further by combining *in-situ* spectroscopy and computations to provide a fundamental basis for the composition-dependent selectivity trend observed.
- **Chapter 5** studies the key properties of copper-based materials which influence their selectivity to C₂ products. New insights into the C₂ pathway are gained from *in-situ* spectroscopic results.
- **Chapter 6** utilizes *in-situ* spectroscopy to examine the key reaction intermediates on copper-based bi-metallic materials and how introducing a secondary metal can improve ethylene selectivity.
- **Chapter 7** presents the key findings and conclusions and provides some recommendations for future work on the design and study of copper-based electrocatalysts. Recommendation and justification for the study of other catalyst systems, namely carbon-based materials, is also provided along with a review of recent literature reporting these materials (Appendix A).

1.4 References

1. B. Endrődi, G. Bencsik, F. Darvas, R. Jones, K. Rajeshwar, C. Janáky, *Prog. Energy Combust. Sci.* 2017, *62*, 133.
2. Y. Hori, in *Handbook of Fuel Cells*, John Wiley & Sons, Ltd, 2003.
3. E. V. Kondratenko, G. Mul, J. Baltrusaitis, G. O. Larrazabal, J. Perez-Ramirez, *Energy Environ. Sci.* 2013, *6*, 3112.
4. J. Low, J. Yu, W. Ho, *J. Phys. Chem. Lett.* 2015, *6*, 4244.
5. A. M. Appel, J. E. Bercaw, A. B. Bocarsly, H. Dobbek, D. L. DuBois, M. Dupuis, J. G. Ferry, E. Fujita, R. Hille, P. J. A. Kenis, C. A. Kerfeld, R. H. Morris, C. H. F. Peden, A. R. Portis, S. W. Ragsdale, T. B. Rauchfuss, J. N. H. Reek, L. C. Seefeldt, R. K. Thauer, G. L. Waldrop, *Chem. Rev.* 2013, *113*, 6621.
6. S. G. Jadhav, P. D. Vaidya, B. M. Bhanage, J. B. Joshi, *Chem. Eng. Res. Des.* 2014, *92*, 2557.
7. J. Qiao, Y. Liu, F. Hong, J. Zhang, *Chem. Soc. Rev.* 2014, *43*, 631.

Chapter 2

Literature Review

Surface and Interface Engineering in Copper-Based Bi-Metallic Materials for Selective CO₂ Electroreduction

This Chapter includes work published in the journal article *Chem*, 2018, 4, 1809. It presents a review of recent literature covering the development of copper alloy and bi-metallic materials for use as CO₂RR electrocatalysts. This topic is relevant because, as discussed, copper bi-metallic materials have exhibited improvements in CO₂RR selectivity compared to copper and it is likely that the secondary metal plays a key role. This Chapter explores the fundamental role of the secondary metal in copper bi-metallic materials with a focus on how their oxygen and hydrogen affinities affect selectivity in the bi-metallic material. Here, four metal groups categorized by oxygen affinity and hydrogen affinity are identified to determine their CO₂RR selectivity trends. By considering experimental and computational studies, the effects of extrinsic chemical composition and physical structure are linked to intrinsic intermediate adsorption and reaction pathway selection. Following this, some general trends are summarized and design strategies for future electrocatalysts are proposed.

Statement of Authorship

Title of Paper	Surface and Interface Engineering in Copper-Based Bi-Metallic Materials for Selective CO ₂ Electroreduction
Publication Status	<input checked="" type="checkbox"/> Published <input type="checkbox"/> Accepted for Publication <input type="checkbox"/> Submitted for Publication <input type="checkbox"/> Unpublished and Unsubmitted work written in manuscript style
Publication Details	A. Vasileff, C.C. Xu, Y. Jiao, Y. Zheng, S.Z. Qiao, Surface and interface Engineering in Copper-based Bi-metallic Materials for Selective CO ₂ Electroreduction, Chem, 2018, 4, 1809-1832

Principal Author


Name of Principal Author (Candidate)	Anthony Vasileff		
Contribution to the Paper	Devised the idea of the paper with supervisors, gathered the bulk of the information and wrote the bulk of the paper		
Overall percentage (%)	70		
Certification:	This paper reports on original research I conducted during the period of my Higher Degree by Research candidature and is not subject to any obligations or contractual agreements with a third party that would constrain its inclusion in this thesis. I am the primary author of this paper.		
Signature		Date	05/02/2020

Co-Author Contributions

By signing the Statement of Authorship, each author certifies that:

- the candidate's stated contribution to the publication is accurate (as detailed above);
- permission is granted for the candidate to include the publication in the thesis; and
- the sum of all co-author contributions is equal to 100% less the candidate's stated contribution.

Name of Co-Author	Chaochen Xu		
Contribution to the Paper	10% Gathered information and helped to write some sections of the paper		
Signature		Date	05/02/2020

Name of Co-Author	Yan Jiao		
Contribution to the Paper	4% Provided specialist guidance and helped to write certain sections of the paper related to her field.		
Signature		Date	05/02/2020

Name of Co-Author	Yao Zheng		
Contribution to the Paper	8% Provided guidance and supervision from conception through to submission and helped to revise the paper.		
Signature		Date	05/02/2020

Name of Co-Author	Shizhang Qiao		
Contribution to the Paper	8% Provided guidance and supervision from conception through to submission and helped to revise the paper.		
Signature		Date	05/02/2020

2.1 Introduction

The world currently relies on fossil fuels for energy production and its chemical industries. However, the burning of fossil fuels releases significant carbon dioxide (CO_2) emissions into the atmosphere, which is considered the primary driver for anthropogenic climate change. CO_2 is a highly stable molecule and is generally inert in most conditions. However, under appropriate cathodic reduction potentials and the assistance of protons in solution, CO_2 can be electrochemically activated and reduced *via* the CO_2 reduction reaction (CO_2RR) to reduced products. The CO_2RR is an elegant route to sustainable fuel and chemicals production when coupled with carbon capture storage technology and renewable energy sources like solar radiation. However, this process is kinetically sluggish due to the multiple electron transfer steps and high energy barriers involved. Therefore, efficient electrocatalysts are required to reduce the reaction overpotential and facilitate the kinetics to accomplish commercially significant rates. To date, a wide range of electrocatalysts for the CO_2RR have been reported, with reduction products being highly catalyst specific.¹⁻⁶ Copper (Cu) is a unique metal because it is the only metal that can form deep reduction products (*i.e.* hydrocarbons and alcohols) with acceptable activity and efficiency during the CO_2RR .⁷ However, the selectivity of Cu towards a certain product is typically poor, generating many reduction products concurrently which range from two electron (2e^-) transfer products (*e.g.* CO and HCOOH) to eight electron (8e^-) transfer products (*e.g.* CH_4) and above.⁸⁻¹⁰ On the microscopic level, the origin of copper’s poor selectivity is its moderate binding energy of most reaction intermediates.^{6, 11-12} Additionally, considering the Sabatier principle, improving the selectivity of copper is not a simple task given that the adsorption energies of different intermediates scale with one another.¹¹ Thus, it is extremely difficult to optimize the binding of a specific intermediate without affecting another.

For various heterogeneous catalytic processes, it has been found that the relative metal O-affinity and H-affinity play important roles in a catalyst’s activity and selectivity by influencing the binding strength of specific reaction intermediates on their surface.¹³⁻¹⁴ Towards the electrocatalytic CO_2RR , for higher O-affinity but lower H-

affinity metals compared to Cu (like In, Sn, Hg, and Pb), the $^*\text{COOH}$ intermediate formed after the first reaction step is weakly bound. Therefore, the primary CO_2 reduction product on these surfaces is HCOOH . Evidence even suggests that the reaction may proceed through an O-bound $^*\text{OCHO}$ intermediate on these metals.¹⁵ However, metals with both lower O-affinity and H-affinity compared to Cu (like Zn, Ag, and Au) can bind $^*\text{COOH}$ stronger relative to $^*\text{CO}$. Therefore, CO is desorbed as the main product with the formation of $^*\text{COOH}$ as the potential determining step (PDS).¹⁶ Other metals with both higher O-affinity and H-affinity compared to Cu (including Co, Ni, Fe, Ir, and Pt) tend to favor the competitive hydrogen evolution reaction (HER), although small amounts of hydrocarbons and alcohols have also been detected on these metal surfaces.^{14, 17-20}

The grouping of CO_2RR products based on a catalyst’s O-affinity and H-affinity leads to the idea that by alloying with specific O-binding or H-binding sites, Cu-based alloys can be engineered to have one or two active sites with tuned binding energies for key reaction intermediates. As a precedent, introducing a secondary metal to tune the activity of Pt is well documented, particularly for the oxygen reduction reaction (ORR) in fuel cells.²¹⁻²³ For the ORR, many Pt alloys show significantly improved activity and stability compared to pure Pt.²⁴⁻²⁵ Although many factors (strain, ligand effect, etc.) can contribute to altering the electronic structure (i.e. d-band center) of a material, it is likely that they all function to weaken the adsorption of O-bound species on the surface. Accordingly, targeting the key reaction intermediates in this way may also be useful for CO_2RR pathway selection. To be specific, metals with high O-affinity are favorable for C-O bond cleavage, while metals with high H-affinity favor proton transfer and provide protons or hydroxyl groups for hydrogenation.¹⁹ However, considering that the HER is generally highly competitive on metal surfaces, it is necessary to understand how these secondary metal sites affect Cu to be able to predict activity and selectivity. Further, the electronic structure and morphology are almost always different in the bi-metallic material compared to copper. This inevitably modifies intermediate binding and is therefore another necessary consideration when evaluating Cu bi-metallic catalysts.

In this Review, we first briefly provide some background to the CO₂RR process and the fundamental principles which govern the selectivity of copper catalysts. Then we introduce the concept of interfacial engineering of copper-based catalysts and review current examples of Cu bi-metallic electrocatalysts. Each example is categorized into sections based on the O-affinity and H-affinity of the secondary metal and we highlight the effects from the introduced O-binding and H-binding sites on the selectivity of the Cu bi-metallic system. The effects of the secondary metal on the chemical composition, electronic structure, geometry, morphology, and electrocatalytic activity of these bi-metallic catalysts are then linked to their intermediate binding energetics. This is done with the aim to interpret any trends in CO₂RR selectivity which may result from modification of the Cu interface with another metal. To further this, we discuss some key examples which combine experimental and computational studies in this field. Finally, we propose some general trends based on these metal groups with strategies for future design of Cu bi-metallic electrocatalysts.

2.2 Fundamental Understanding of the CO₂RR

2.2.1 CO₂RR Reaction Mechanism on Cu

Cu has been widely studied as an electrocatalyst for the CO₂RR due to its ability to produce hydrocarbons/alcohols at modest overpotentials.^{8, 17, 26-28} Electrocatalytic CO₂RR on Cu proceeds *via* multiple electron-proton coupled transfer steps to adsorbed intermediates through multiple pathways. Therefore, it is very non-selective and produces a range of products concurrently. Pioneering work by Hori and co-workers found that on Cu electrodes, generally, 2e⁻ products (H₂, CO, HCOOH) are formed at lower overpotentials while higher e⁻ products (CH₄: 8e⁻ and C₂H₄: 6e⁻) are formed at higher overpotentials (Figure 2.1a).^{17, 27, 29-30} However, the specific mechanism of the CO₂RR on Cu is surface and condition sensitive,³¹⁻³² and a comprehensive understanding is still lacking. As shown in Figure 2.1b, the most widely accepted reaction pathway to CH₄ proceeds *via* the hydrogenation of adsorbed *CO to the *CHO intermediate, which is identified as the PDS.³³⁻³⁴ Further hydrogenation to *CH₂O and

$\text{*CH}_3\text{O}$ then leads to CH_4 production with the remaining reaction steps being exergonic. Additionally, the hydrogenation of the methyl end of $\text{*CH}_3\text{O}$ is more readily achieved with solvated protons to produce CH_4 , compared to hydrogen addition at the oxygen end *via* co-adsorbed *H to produce CH_3OH . Besides the thermodynamic analysis, the role of kinetics for the reactions on Cu surfaces has also been considered.³⁵ It was found that CH_4 production through the CHO* intermediate faced a 1.21 eV kinetic barrier at a potential of -1.15 V *vs.* RHE, whereas CH_3OH only needed to overcome 0.15 eV at this potential. Therefore, in order to explain why CH_4 is predominantly produced experimentally, it was proposed that *CO reduction to the *COH intermediate is favoured over CHO* (Figure 2.1c).³⁶ This *COH intermediate then undergoes further reduction to *C and is then hydrogenated by co-adsorbed *H , as has been proposed previously.¹⁰ This pathway also explains the experimentally observed production of CH_4 and C_2H_4 concurrently, due to the identification of a common intermediate (*CH_2). After considering the kinetic aspects, some other studies support the route through the *CHO intermediate to *CH_2 *via* *CHOH , mainly due to the sluggish kinetics involved in the hydrogenation of $\text{*CH}_3\text{O}$ at the methyl end and other experimental observations.^{28, 37}

2.2.2 Scaling Relationships

An inherent challenge of the CO_2RR is that the binding of intermediates follows conventional scaling relationships due to the formation of similar surface-adsorbate bonds amongst different intermediates (*e.g.* *COOH , *CO , *COH all involve C-bound intermediates). Given this, the adsorption energy of a certain intermediate cannot be optimally tuned without affecting another.^{11, 38-39} For example, Figure 2.1d shows the calculated scaling relationships between various C-bound intermediates in the reaction pathway to CH_4 . As previously discussed, the hydrogenation of *CO to *CHO is considered the PDS of this process due to having the highest free energy change (0.74 eV); the magnitude of this energy change predominantly originates from the weak binding of *CHO relative to *CO binding.³⁹ In order to reduce this, the surface would have to bind *CHO stronger relative to *CO . However, this is difficult to realize due

to the constraint imposed by conventional scaling relationships.¹¹ Experimentally, the large overpotentials and poor turnover frequencies (TOFs) for CO₂ reduction to CO on Au and Ag electrodes can also be attributed to the similar weak adsorption of *COOH due to the linear scaling between *COOH and *CO.⁴⁰

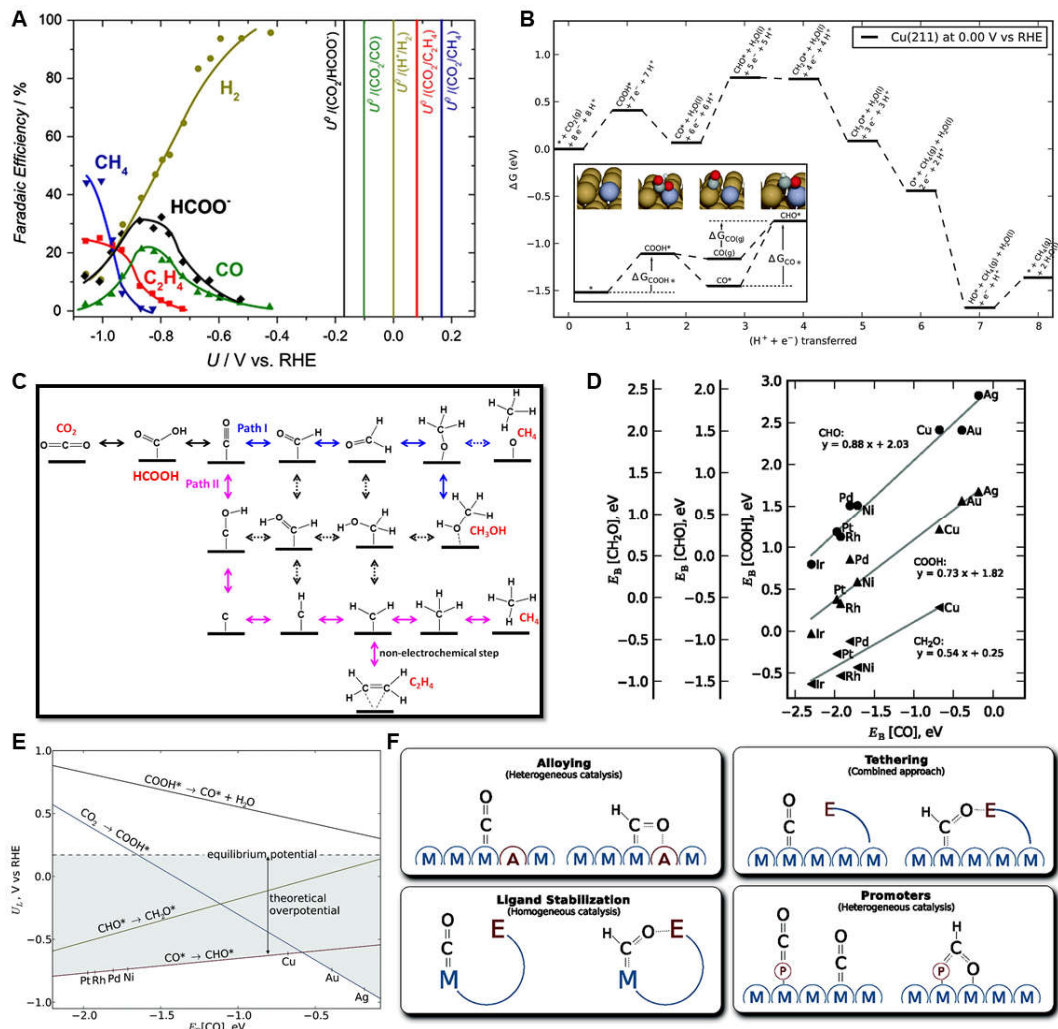


Figure 2.1 Fundamental understanding of the CO₂RR on Cu surfaces. a) Product distribution expressed as FE as a function of potential on a polycrystalline Cu electrode. The vertical lines represent the reversible potentials for various products [a) adapted with permission from Jovanov et al.³⁰]. b) Proposed reaction pathways for the reduction of CO₂ to CH₄ on Cu(211) surface through the *CHO intermediate [b) adapted with permission from Hansen et al.³³]. c) The reaction pathway (path II) of the CO₂RR through the *COH intermediate to CH₄, CH₃OH, and C₂H₄. Path I reflects the reaction presented in panel b) [c) adapted with permission from Nie et al.³⁶]. d) Scaling relationships for C-bound intermediates relevant to the CO₂RR pathway on a range of metal surfaces. e) Limiting potentials (U_L) for elementary proton-transfer steps in the mechanism of panel b). f) Suggested decoupling strategies to break the scaling relationships [d) to f) adapted with permission from Peterson et al.¹¹].

Regarding Cu, the fundamental reason for its ability to produce products other than CO at reasonable overpotentials is that it binds *CO neither too weakly nor too strongly (Figure 2.1b). Therefore, *CO formed on the surface does not desorb immediately (adsorption not too weak) and does not poison the surface (adsorption not too strong). Furthermore, from Figure 2.1e, it can also be seen that out of all transition metals, Cu has relatively moderate binding of most C-bound intermediate species.¹¹ As a result, Cu is at the top of the “volcano” plot for the calculated limiting potentials of the two reaction steps which present the largest free energy barriers (*i.e.* proton-electron coupled steps: CO₂ to *COOH and *CO to *CHO).^{11, 37} However, having moderate-level binding of the various surface adsorbates in the pathway also leads to poor selectivity for a particular final product. Therefore, by breaking the above scaling relationships, it is possible to optimize the adsorption energy of a particular intermediate(s) not only for a reduction in overpotential, but also for enhanced selectivity. Some useful strategies that focus on tuning the intrinsic electronic parameters underlying the scaling relationships, such as alloying with strong O-binding metals, ligand stabilization, tethering, and addition of promoters, *etc.*, have been proposed (Figure 2.1f).¹¹ Ultimately, the aim of these strategies is to strengthen the binding energy of *CHO (*i.e.* more negative) relative to that of *CO for improved selectivity to deep reduction products.

2.3 Improving Selectivity by Interfacial Engineering

2.3.1 Classification

Various strategies have been employed to enhance the activity of Cu catalysts, and these mainly involve exploiting nanostructuring techniques and morphological control.^{9, 41-44} However, these approaches generally reduce the overall overpotential for the CO₂RR, improving its selectivity over the HER, while a distinct reduction pathway is not always achieved.⁹ In regards to metal catalysts, by coupling two (or more) metal species in alloy or bi-metallic materials, the catalyst interface can be engineered to contain multiple sites which contribute to binding of key intermediates in the pathway.^{39,}

⁴⁵ As a result, design of catalysts based on this principle could lead to conventional scaling relationships being broken in order to tune the selectivity for the reduction of CO₂. Cu is a logical model since it is the only metal catalyst that can promote the CO₂RR toward various hydrocarbon products at non-negligible Faradaic Efficiency (FE).⁴⁶ Recently, it has been suggested that alloying Cu, as a form of interfacial engineering, can tune the adjacent chemical environment around the Cu atoms. Therefore, this makes it possible to tune the binding strength of targeted intermediates on the catalyst surface and enhance the reaction kinetics and selectivity of the alloys/bi-metal.

In general, the changes to intermediate binding energy, and consequently the reaction pathway, highly depend on the nature of the secondary metal. Herein, we classify the introduced metals based on two factors: hydrogen affinity (H-affinity) and oxygen affinity (O-affinity); high H-affinity describes a metal which binds hydrogen stronger compared to Cu, while high O-affinity describes a metal which binds oxygen stronger compared to Cu. The choice of these two descriptors is based on the following considerations. Given that the hydrogenation of *CO is the PDS for deep reduction of CO₂, a secondary site with strong H-affinity or O-affinity can facilitate the adsorption of *CHO species with alternative configurations (Figure 2.2a). As a result, the inherent scaling relationship of *CO and *CHO/*COH may be broken. Additionally, the adsorption strength of O-bound reaction intermediates (*e.g.* *CH₂O and *CH₃O), which appear in the latter half of the CO₂RR pathway, directly relates to the selectivity of hydrocarbon/alcohol products.⁴⁷ For determining H-affinity and O-affinity, a scatter plot presented in Figure 2.2b provides the trend of H adsorption energy (ΔE_H) against O adsorption energy (ΔE_O) for various metal surfaces. These trends have been extensively used as activity descriptors for the HER and ORR, respectively.⁴⁸⁻⁴⁹ It can clearly be seen that the metals located to the top-left (*e.g.* Ag, Au) have weaker ΔE_H and ΔE_O than Cu. These metals therefore have to overcome a higher energy to bind hydrogen or oxygen. While the metals to the bottom-right of Cu (*e.g.* Ir, Rh, *etc.*) show stronger H-affinity and O-affinity. The metals located to the top-right of Cu (*e.g.* Pt, Pd) show stronger H-affinity but weaker O-affinity. Importantly, these trends can

be presented in other forms of H- and O-binding strength. A similar scatter plot shown in Figure 2.2c provides the trend of the hydrogen-metal bond strength against the enthalpy of bond dissociation of metal oxides (MO) as an alternate form. Specifically, for determining H-affinity, the strength of the metal-hydrogen (M-H) bond was experimentally measured on various metal surfaces; a greater M-H bond strength favors hydrogen binding.⁵⁰ Similarly, a quantitative scale of O-affinity has been calculated by applying the enthalpy of bond dissociation for M-O as a descriptor, denoted as $D_O(M)$; metals with $D_O(M)$ values greater than $D_O(Cu)$ signify greater metal-oxygen bond strength (stronger O-affinity), and *vice versa*.⁵¹ As a result, four metal groups are identified depending on their H-affinity and O-affinity relative to Cu (Figure 2.2d). Based on this classification, our goal here is to comprehensively review recent Cu-based alloy (Cu-M) electrocatalysts for the CO₂RR and to evaluate any apparent selectivity trends that may be useful in the rational design of future electrocatalysts.

It should be noted that others have also found that the adsorption energetics of specific reaction intermediates can be applied to classify a wide range of single metals for the CO₂RR. For example, the binding energies of *COOH and *H were calculated as the descriptors to explain the trend of 2e⁻ CO and HCOOH generation for the CO₂RR, while binding energies of *CO and *H were applied as the descriptors to predict activity towards deep reduction products.⁶ Specifically, as shown in Figure 2.2e, the metals can be separated into three groups when considering only ΔE_H as the descriptor: metals with stronger hydrogen affinity compared to Cu (*i.e.* within the hydrogen underpotential deposition, H_{upd} , zone) mainly form H₂; metals with moderate H adsorption energy at the CO₂ reduction potential mainly form CO, and metals with weaker H adsorption at the CO₂ reduction potential form HCOOH.⁶ Additionally, binding energies of *CO and *H separate Cu from all other metals, as shown in Figure 2.2f. In this plot, Cu is the only metal in the bottom-right zone, possessing relatively weaker *H binding and stronger *CO binding along with the ability to reduce CO₂ to hydrocarbon products or partly reduced alcohol products. It was also found that the C-bound (*CH₂OH) and the O-bound (*CH₃O) intermediates can distinguish hydrocarbon or alcohol formation (Figure 2.2g).

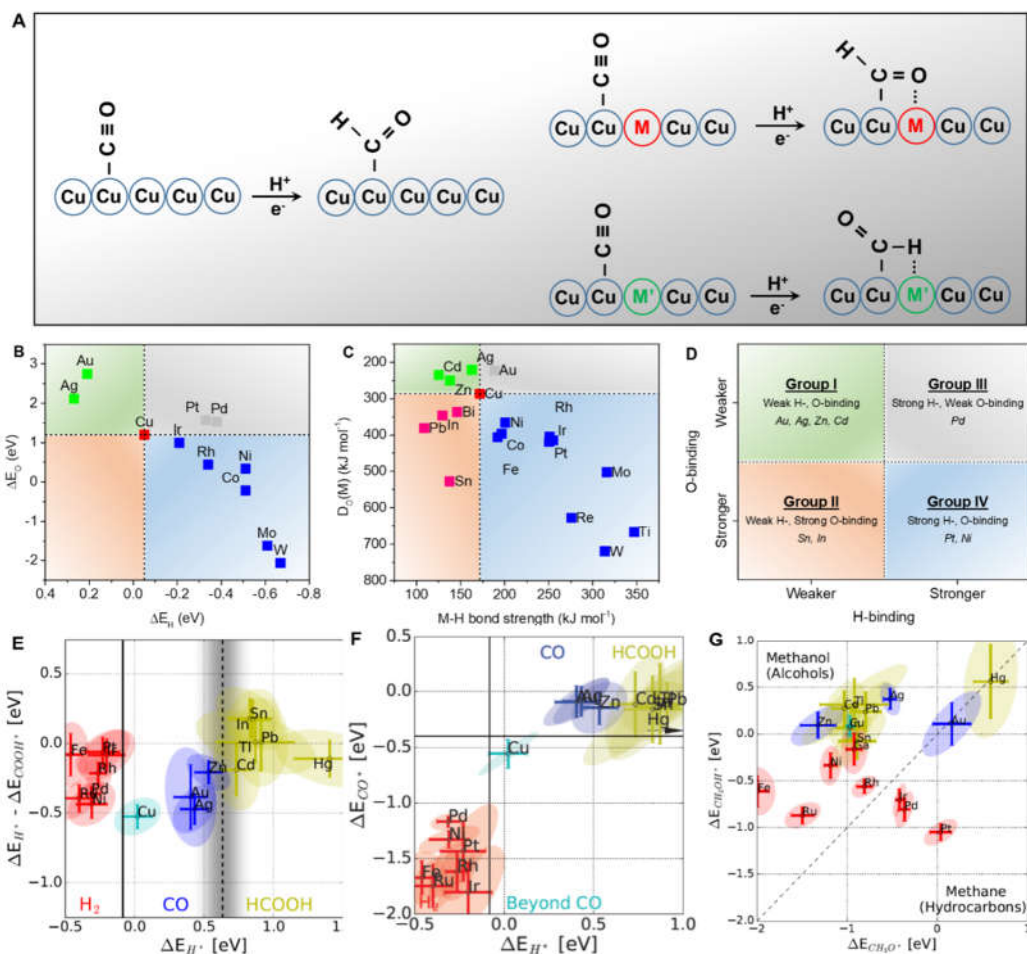


Figure 2.2 Grouping of various metals in relation to copper based on various descriptors. a) Schematic illustration of $^*\text{CHO}$ adsorption on pure Cu and Cu-M alloy surfaces. M indicates a site with strong O-affinity and M' indicates a site with strong H-affinity. b) The oxygen adsorption energy plotted as a function of the hydrogen adsorption energy over different metals [Data of ΔE_{O} and ΔE_{H} is read from ref.⁴⁸]. c) The intermediate metal-hydrogen bond strength plotted as a function of the bond dissociation enthalpy of MO. [M-H bond strength data is read from ref.⁵⁰; $D_{\text{O}}(\text{M})$ data is read from ref.⁵¹]. d) Grouping of various metals in relation to copper alloys based on O-affinity and H-affinity from previous studies. e) The experimental product classification of H_2 , CO, and HCOOH by the ΔE_{H}^* descriptor. f) The binding energies of the intermediates ΔE_{CO}^* and ΔE_{H}^* categorizing metal catalysts into three distinct groups. g) The DFT energy relation between $\Delta E_{\text{CH}_2\text{OH}}^*$ and $\Delta E_{\text{CH}_3\text{O}}^*$ descriptors as a measure of CH_3OH or CH_4 production from carbon-oxygen compounds [e) to g) adapted with permission from Bagger et al.⁶].

Therefore, four intermediates: ΔE_{H^*} , ΔE_{CO^*} , ΔE_{COOH^*} , and $\Delta E_{\text{CH}_3\text{O}^*}$ can be used to explain product groups and selectivity distributions for the CO_2RR on most pure metal surfaces. To predict the products selectivity of Cu-based bi-metallic materials, herein we use metal categories based on the O- and H-affinities of the secondary metal.

2.3.2 Group 1: Weak H-, Weak O-Binding

Gold (Au)

Au is a d-block metal with both weak hydrogen and oxygen adsorption and has been the most common Group 1 metal alloyed with Cu for the CO_2RR . Experimentally, it was shown that increased Au content favors CO production, while the pathway to CH_4 is suppressed.⁵² Mechanistically, the desorption of CO on Cu sites was promoted due to the lower activation energy for CO desorption caused by Au alloying. In another example, it was found that both the composition and nanostructure of Cu-Au nanoparticles affected the catalytic performance, with CH_3OH and $\text{C}_2\text{H}_5\text{OH}$ being selectively produced.⁵³ The optimal $\text{Cu}_{63.9}\text{Au}_{36.1}$ composition exhibited a FE of 28 % for alcohols (including 15.9 % for CH_3OH), which is 19 times higher than that of pure Cu. This study claimed that $^*\text{CO}$ is a significant intermediate for CO_2 reduction towards hydrocarbons and alcohols, whereby binding of $^*\text{CO}$ was likely optimized in this Cu-Au system. As a comprehensive investigation into the effect of the Cu-Au stoichiometric ratio in bi-metallic catalysts,⁴⁶ electrochemical results showed that alloys with increased Cu content obtained various reduction products, while increased Au content simultaneously improved CO formation and suppressed other pathways. It was indicated that Cu-Au alloys favored CO production due to synergistic electronic and the geometric effects. Specifically, density functional theory (DFT) calculations demonstrated that the d-band center shifts downwards from pure Cu to pure Au (Figure 2.3a). As a result, the binding strength for $^*\text{COOH}$ and $^*\text{CO}$ should decrease as the Au content increases, and the formation of CO in Cu-Au systems should exhibit a monotonic tendency (Figure 2.3b). However, $^*\text{COOH}$ binding was found to be relatively unaffected due to an observed geometric effect that stabilized $^*\text{COOH}$ intermediates. This explains their experimental observations whereby the highest FE

toward CO was obtained on Au₃Cu alloy (Figure 2.3c), and provides a better understanding of the effects of electronic structure and geometric modification in bi-metallic materials. Additionally, it was found that increasing the degree of atomic ordering in Cu-Au alloys can tune the selectivity of CO₂ reduction toward CO with a high FE of ~80 %, due to the stabilization *COOH intermediates on compressively strained Au sites.⁵⁴

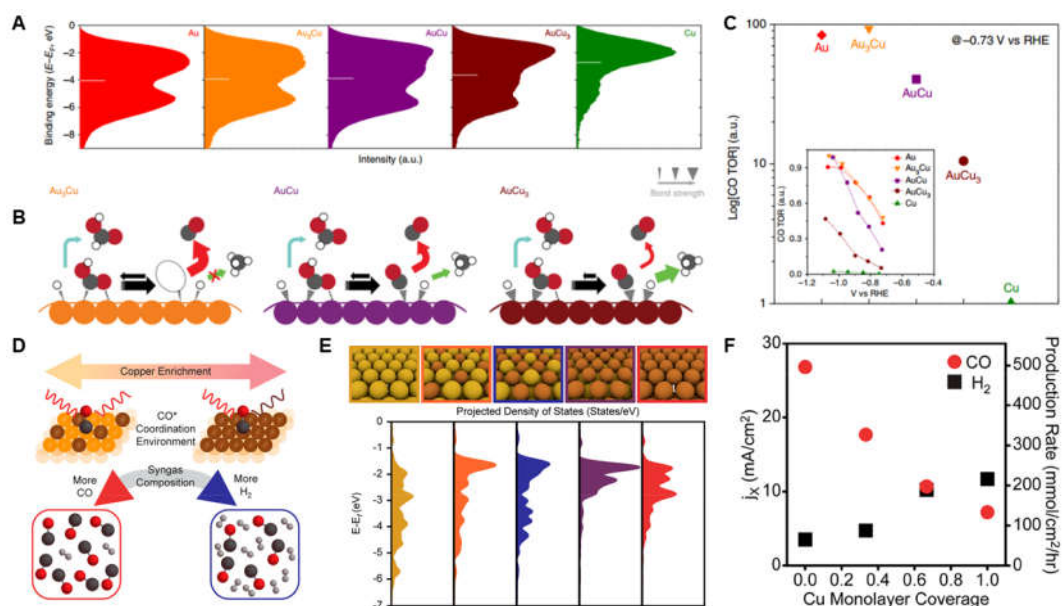


Figure 2.3 Characterization and performance of Cu-Au catalysts for the CO₂RR. a) Surface valence band photoemission spectra of Au-Cu bi-metallic nanoparticles. The white bar shows its d-band centre. b) Proposed mechanism for the CO₂RR on the surface of Au-Cu bi-metallic nanoparticles. Grey, red, and white atoms represent C, O, and H, respectively. c) CO generation rate on various alloy electrocatalysts at a certain overpotential. Inset shows relative CO generation rate as a function of the applied potential [a) to c) adapted with permission from Kim et al.⁴⁶]. d) Scheme depicting the relationship between the Cu-enriched Au surface, *in-situ* characterization of CO* coordination, and syngas composition. e) Calculated d-band electronic states for increasingly Cu-enriched Au surfaces. f) Partial current densities (left axis) and production rates (right axis) for CO and H₂ as a function of Cu monolayer deposition on Au [d) to f) adapted with permission from Ross et al.⁵⁵].

Underpotential deposition (UPD) was used to construct another type of Cu-Au alloy by depositing a single layer of Cu with different coverages (1/3, 2/3, and 1).⁵⁵ It was found that less Cu coverage increases CO production, while increased Cu coverage promotes H₂ evolution. Employing *in-situ* Raman microscopy, the vibration of the C-

O bond (ν_{C-O}) in *CO species was used as a descriptor to understand the effects of the Cu/Au ratio on the *CO adsorption strength. It was found that with greater Cu coverage, ν_{C-O} experiences a red-shift, which is associated with bond lengthening due to greater interaction with the metal (Figure 2.3d). DFT calculations showed the projected density of states (DOS) moved further away from the Fermi level on increasingly Au-dominant surfaces, favoring CO production (Figure 2.3e). On the other hand, Cu enrichment provided a greater improvement to *H adsorption relative to *CO . Therefore, the degree of Cu enrichment can affect the relative activity of the HER to the CO₂RR, which can realize controllable syngas production (Figure 2.3f). Similarly, in an Au-Cu core-shell (Au@Cu) system, experimental results indicated that 7-8 layers of Cu resulted in a better selectivity for C₂H₄, while CH₄ production slightly increases for 14 or more Cu layers.⁵⁶ This was explained by the calculated DFT results showing that *COH intermediates are favored over *CHO on terraces, however, *CHO is slightly favored as *CO coverage increases.⁵⁷ Therefore, both structural and electronic effects that change the binding of *CO have a significant impact on selectivity and products distribution on the Au@Cu catalysts. In another study, Cu-Au core-shell nanostructures (Cu@Au) also exhibited enhanced current density over polycrystalline Cu and achieved a greater FE towards CO.⁵⁸

Silver (Ag)

Ag is another Group 1 metal that has been coupled with Cu for CO₂ reduction. In the Ag-Cu core-shell nanoparticle (Ag@Cu) system, samples with low Cu coverage showed high conversion of CO₂ toward CO, while Cu-dominant nanoparticles had greater selectivity for hydrocarbons.⁵⁹ As with the Au@Cu material, both electronic effect and geometric effects were important factors involved in the catalytic activity of the Ag@Cu system. Specifically, for the electronic effect, the binding energy of *CO on Ag active sites was weaker than that on Cu. Therefore, desorption of CO was facilitated when the coverage of Cu was low. For the geometric effect, the binding strength of intermediates can be tuned by changing the local atomic arrangement at the active sites. Additionally, in the electrodeposited Cu-Ag alloys, it was found that Cu segregation caused Cu enrichment on the catalyst surface.⁶⁰ As a result, the Ag₅₇Cu₄₃

alloy achieved 2.2 times higher mass-normalized activity than the Ag₁₀₀ catalyst. In another study, electrodeposited nanocoral Cu-Ag bi-metallic catalysts exhibited only 30% FE towards hydrogen and around 70 % for total C₁-C₃ products by a solar driven electrochemical cell.⁶¹ In this system, it appears that Cu contributed the dominant binding effect, as overall product selectivity was poor. However, the Cu-Ag electrode was more active towards producing alcohols and oxygenates compared to pure Cu. Cu-Ag bi-metallic catalysts have also been prepared by melting mixtures of Cu and Ag powders with specific atomic ratios.⁶² When the Cu content was low, it was found that the Cu was dissolved in the Ag phase and segregated on the surface during the CO₂RR. These Ag-dominant catalysts produced CO as the major product on the surface although the Cu sites formed the reactive sites. On the other hand, the Cu-dominant catalysts suppressed the HER by about 75 % without effecting the ability to produce deep reduction products from CO. On the atomic level, it is believed that compressive strain on Cu introduced by neighboring Ag causes a shift in the valence band DOS therefore causing weaker binding of *H and *O relative to *CO.

Zinc (Zn)

Cu-Zn bi-metallic catalysts were also found to be selective towards CO₂ reduction to alcohols, in which Cu₄Zn achieved the highest FE of 29.1%.⁶³ The authors indicated that CO₂ is reduced to *CO on either Cu or Zn active sites in the first step, and is further reduced to *CHO or *CH_x (x = 1–3) on the Cu sites. However, due to the weak adsorption of *CO on Zn sites, desorbed CO may diffuse and spillover on the Cu sites, whereby the *CO can insert between Cu sites and *CH₂ intermediates to form *COCH₂, which is then reduced further to produce C₂H₅OH.

Cadmium (Cd)

Hori investigated *in-situ* Cd electrodeposited Cu electrodes under different Cd coverages.⁶⁴ At a constant current density, Cd electrodeposition occurred along with the HER and CO₂RR. Therefore, as Cd deposition increased with time, a trend in product selectivity could be observed. The results showed that the FE towards CO increases with increasing Cd coverage, while the FE towards other gas products decreases significantly. However, the FE towards CO reaches a maximum, and with further increase to Cd coverage, production of HCOOH is favored.

2.3.3 Group 2: Weak H-, Strong O-Binding

Tin (Sn)

Sn is identified as a Group 2 metal with higher O-affinity and weaker H-affinity relative to Cu.⁵¹ Due to its weak H adsorption, Sn metal is relatively inactive towards the HER and Sn electrodes have been found to mainly produce HCOO⁻.^{7, 65} This suggests that on Sn, the CO₂RR overwhelmingly proceeds *via* the *COOH intermediate, or as has been suggested, through the bidentate *OCHO intermediate.¹⁵ In the Cu-Sn bi-metallic system, theoretically, *CO intermediates are unaffected by O-binding sites (*e.g.* Sn) as they tend to bind in end-on configurations, where the O atom contributes little to the chemisorption. However, O atoms contribute more in the *COOH intermediate to overall adsorbate stabilization and its binding energy is likely increased when O-binding sites are present.³⁹ Further, O-binding sites likely play an even greater role if the CO₂RR proceeds via the *OCHO intermediate, as the two oxygens bond to the surface in a bidentate configuration.¹⁵ Cu-Sn bi-metallic materials for selective CO₂ reduction have only been demonstrated experimentally in a few cases and seems that Sn limits the usual CO₂RR pathway on Cu to 2e⁻ reduction products.⁶⁶ For example, it was found that while maintaining a similar onset potential to a Cu sheet electrode, a Cu-Sn material was significantly more selective to CO production with a FE of 90 % at -0.6 V *vs.* RHE (Figure 2.4a).⁶⁷ In comparison, the Cu sheet achieved a wide range of products (CO, HCOOH, and H₂) under the same conditions (Figure 2.4b). A noted consequence of coupling Sn with Cu was that the bi-metallic material exhibited approximately a third less catalytic current density compared to the Cu sheet electrode (Figure 2.4c). However, when considering the improved selectivity for the CO₂RR over the HER on the Cu-Sn material, this difference becomes less significant.

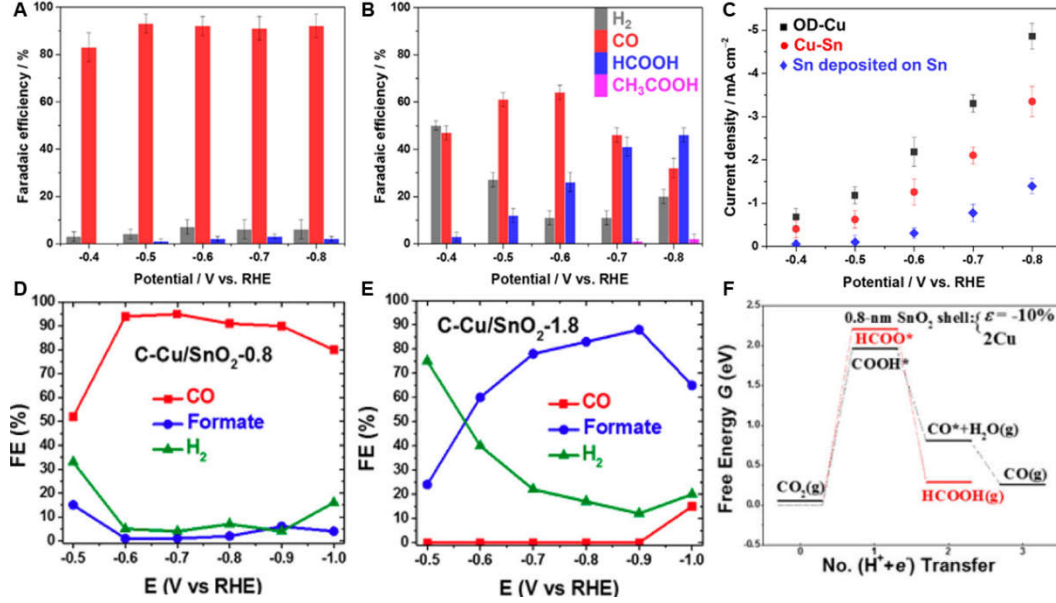


Figure 2.4 Characterization and performance of Cu-Sn catalysts for CO₂RR. FE analysis of a) Cu-Sn and b) Cu catalyst at different applied potentials. c) Overall current density of different electrocatalysts [a) to c) adapted with permission from Sarfraz et al.⁶⁷]. d) and e) Potential dependent FE's on different electrodes. f) Free energy diagrams of two reaction pathways on a 0.8 nm-SnO₂ shell with two Cu atoms on the surface and 10 % uniaxial compression. The red and black lines represent the path of HCOOH and CO generation, respectively [d) to f) adapted with permission from Li et al.⁶⁸].

Core-shell Cu-SnO₂ nanoparticles achieved a maximum FE of 93 % towards CO at -0.7 V *vs.* RHE for samples with a 0.8 nm thick SnO₂ shell (Figure 2.4d).⁶⁸ In this study, the thickness of the Sn shell was found to have a marked effect on product selectivity. When the shell thickness was increased to 1.8 nm, negligible CO was produced within this range, and instead, HCOOH was produced in preference along with increased HER at more positive potentials (Figure 2.4e). This sample exhibited a similar trend to Sn foil, indicating that for increased shell thickness the Sn characteristics dominated the electrocatalytic pathway. DFT calculations found that the 0.8 nm thick SnO₂ shell could induce a large compressive strain on the surface (~10 %), and Cu atoms simultaneously diffuse out on the SnO₂ shell. As a result, differing from the 1.8 nm thick SnO₂ shell model on which HCOOH production is energetically more favorable, the overpotential for CO production is less negative than that for HCOOH production on the model where both compression and Cu doping are present

(Figure 2.4f). Other studies also report the effect of the deposited Sn thickness in Cu-Sn systems, in which the thicker Sn layers favor HCOOH production while thinner layers favor CO production.^{66, 69} A mechanistic study on SnO₂ coated CuO nanoparticles found that the binding strength of *H and *CO is significantly lower than that of unmodified CuO nanoparticles.⁶⁹ As a result, firstly, CO will be more easily desorbed from the surface upon formation, and subsequent hydrogenation will be more difficult due to the dilution of adsorbed *H intermediates. Secondly, the weak *H adsorption will limit the HER and increase the selectivity for the CO₂RR. Given CO is the main product formed on Cu-Sn materials, this view gives a good overall explanation of the underlying mechanism.

Indium (In)

Similar with Sn, when In was alloyed with Cu, the resultant Cu-In electrocatalysts were reported to be highly selective and stable towards CO at low overpotential, reaching FEs of around 90 % for CO formation.^{45, 70} It was found that the presence of In increases the energy barrier to H adsorption but stabilizes the *COOH intermediate by 0.1 eV.⁷⁰ As with Sn, binding of *CO was relatively unchanged and the relative increase in stability of *COOH is likely responsible for the observed activity for CO production.

2.3.4 Group 3: Strong H-, Weak O-Binding

Palladium (Pd)

Pd is identified as a Group 3 metal and has been used extensively in the field of gas phase heterogeneous catalysis.⁷¹⁻⁷² Pd has little to no barrier towards H₂ adsorption and readily forms the metal hydride (PdH_x),⁷³⁻⁷⁴ which makes it a good candidate for catalyzing hydrogenation reactions. As dispersing Pd atoms on Cu surfaces has been shown to significantly reduce the barrier to hydrogen adsorption, Pd-Cu alloy nanoparticles were employed as heterogeneous catalysts in the hydrogenation of CO₂.⁷⁵⁻⁷⁶ It was proposed that the stronger binding of *H possibly facilitates this process and affects selectivity toward *COH/*CHO in the CO₂RR.³⁶ However, pure Pd mainly produces CO during the CO₂RR and only produces small amounts of CH₄, likely because hydride formation inhibits *CO binding.¹¹ For the Cu-Pd system, alloy

composition and intermetallic arrangement were found to have significant effects on activity and selectivity. For example, it was found that Cu-Pd nanoparticles with regular intermetallic arrangements exhibited selective CO₂RR towards CO.⁷⁷⁻⁷⁸ DFT calculations showed that on an ordered Pd-terminated Pd-Cu (111) surface, binding of *COOH was stronger compared to Pd (111), while *CO adsorption was significantly weakened. Interestingly, Pd is the active site in this system and the observed effects are the result of neighboring Cu atoms with higher O-affinity. Another study explains that the electronic effect of charge transfer from Pd to Cu causes the weaker adsorption of *CO in the Cu-Pd system.⁷⁹

According to d-band theory, a negative shift in the DOS away from the Fermi level normally results in weaker binding of adsorbates on a catalyst surfaces.⁸⁰ However, this does not encompass an example of phase separated Cu-Pd nanoparticles.⁸¹ Therefore, a comprehensive view of intermediates binding is required for catalyst design strategies beyond the d-band center theory. Expanding upon the above example, Cu-Pd bimetallic nanoparticles with various atomic mixing patterns (ordered, disordered, and phase separated) exhibited very different selectivities toward C1 and C2 products (Figure 2.5a-c).⁸¹ Specifically, for ordered Cu-Pd nanoparticles, the FE toward C1 products (primarily CO) reached approximately 80 %. However, for nanoparticles with distinct Cu and Pd phases (phase separated), C2 products (primarily C₂H₄) were selectively produced at an FE of >60 %. The underlying reason for this may be that in the phase separated system, the binding of *CO is less affected when the two sites are segregated. While Cu may facilitate C-C coupling, co-adsorbed H on Pd sites may facilitate further reduction and hydrogenation of *CO.⁷⁵ More importantly, as mentioned above, phase separated Cu-Pd had the lowest lying d-band center (shown in Figure 2.5d), while Cu nanoparticles had the highest. This would suggest that the former has the weakest binding, while latter has the strongest binding of *CO. However, given the experimental results showing that the phase separated Cu-Pd and Cu nanoparticles have similar catalytic selectivity and activity, geometric/structural effects probably played a more important role rather than electronic effects in determining catalytic performance among the various Cu-Pd samples.

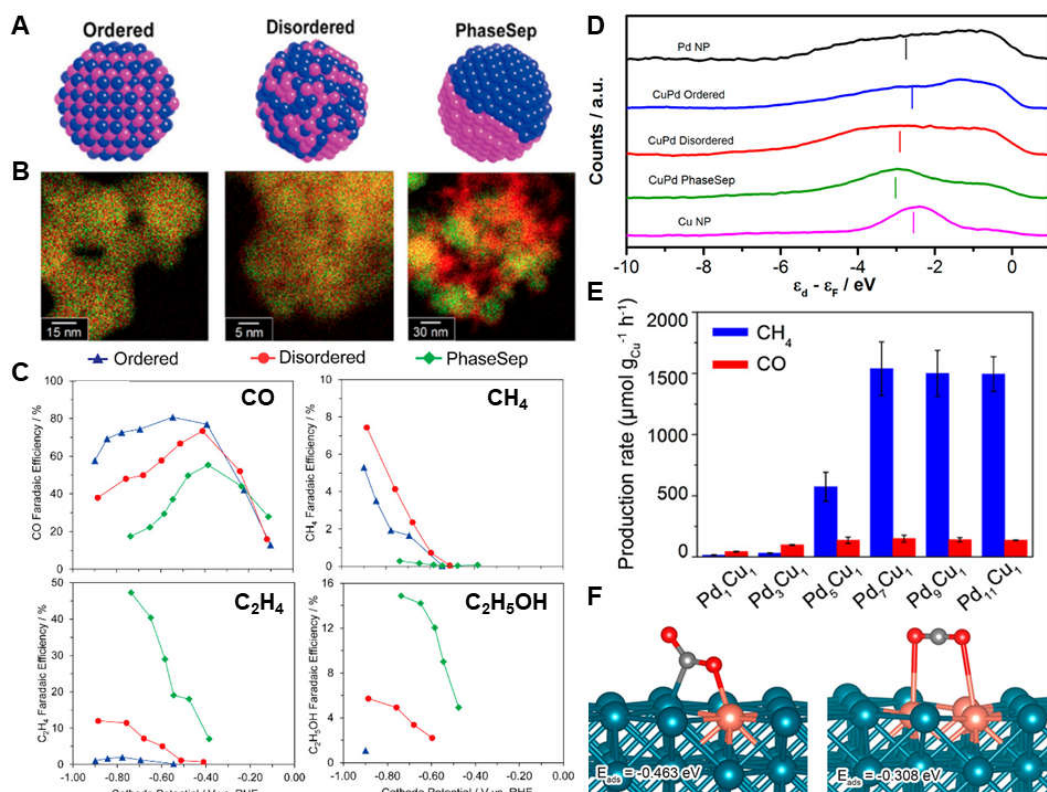


Figure 2.5 Characterization and performance of Cu-Pd catalysts for the CO₂RR. a) Cu-Pd nanoalloys with different atomic mixing patterns. b) Combined elemental maps of Cu (red) and Pd (green). c) FEs for CO, CH₄, C₂H₄, and C₂H₅OH for bi-metallic Cu-Pd catalysts with different mixing patterns: ordered (blue), disordered (red), and phase-separated (green). d) Background corrected surface valence band photoemission spectra of Cu-Pd nanoalloys relative to the Fermi level. The vertical line indicates the d-band center of each sample relative to the Fermi level [a) to d) adapted with permission from Ma et al.⁸¹]. e) Average production rates of CH₄ and CO normalized by the amount of Cu atoms in the Cu-Pd catalysts. f) Most favorable configurations and adsorption energies of CO₂ at an isolated Cu atom (Cu-Pd pair shown in the left panel), and two neighboring Cu atoms (Cu-Cu pair shown in the right panel) [e) and f) adapted with permission from Long et al.⁸²].

Cu-Pd nanoparticles have also been applied as photocatalysts for selective CO₂ reduction to CH₄.⁸² Nanoparticles with relatively low Cu concentration (Cu:Pd of 1:7), achieved a selectivity towards CH₄ of 96 % and effectively suppressed the HER (Figure 2.5e). The low concentration of Cu in this material was an important factor as it increased the number of isolated Cu atoms in the Pd lattice and hence the number of neighboring Cu-Pd sites. On this configuration, as shown in Figure 2.5f, the CO₂ adsorption energy was maximized at -0.46 eV, which is significantly stronger than on

sites with adjacent Cu-Cu atoms (-0.31 eV).⁸² Additionally, the Pd atoms had a significant electronic effect on the isolated Cu, causing an increase in their d-band centers and hence catalytic activity of the Cu active sites toward multi-electron pathways.

2.3.5 Group 4: Strong H-, Strong O-Binding

Platinum (Pt)

Few examples of Group 4 metals being coupled with Cu for CO₂RR electrocatalysts exist in the literature. This is likely due to their high activity for the competing HER and poisoning by CO. In one study, Cu UPD layers on Pt (111) and Pt (211) surfaces were fabricated to study the strain effect on Cu active sites for the CO₂RR.⁸³ In this study, hydrogen was the major product obtained on Cu/Pt(111) and Cu/Pt(211) samples, as shown in Figure 2.6a. However, it should be noted that the presence of *CO alters HER activity on the Cu/Pt interface. Specifically, Pt containing systems are not likely to be stable and result in Pt segregation due to the strong interaction between Pt and CO. This phenomenon would in turn promote the HER over the CO₂RR. Further, none of the Cu-Pt catalysts could promote CH₄ production as effectively as polycrystalline Cu (Figure 2.6b). Therefore, this work suggested that the second metal in a Cu bi-metallic catalyst should have a lower affinity for *CO. Another study demonstrated that Cu-Pt nanocrystals with controlled Cu:Pt atomic ratios performed with high FE for CH₄ (over 20 %; Figure 2.6c).⁸⁴ When the Pt content was high, the HER was dominant. With increased Cu content, more adsorbed *CO was generated, thereby improving the production of CH₄. However, further increasing the Cu content subsequently led to a higher density of adsorbed *CO, and thus, lower density of adsorbed *H (Figure 2.6d). Consequently, the overall performance of the alloy was limited as less co-adsorbed H was available to partake in the reaction. Based on experimental results, investigation into the possible mechanism showed that increasing the Cu content increased the surface coverage of *CO on active sites, and Pt facilitated their protonation to *CHO (Figure 2.6e). However, when insufficient Pt sites are present, *H generation is suppressed and hinders further reduction of *CO.

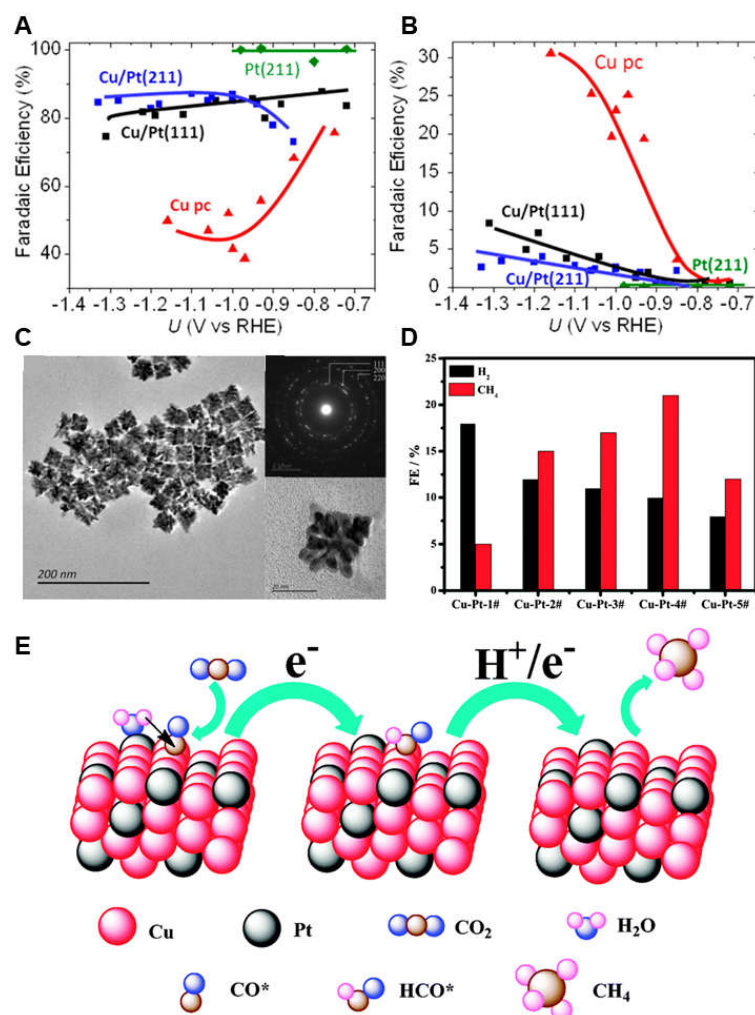


Figure 2.6 Characterization and performance of Cu-Pt catalysts for CO_2RR . FEs toward a) H_2 and b) CH_4 as a function of potential on different surfaces [a) and b) adapted with permission from Varela et al.⁸³]. c) Low magnification TEM image of the overall morphology of Cu-Pt. d) The FEs of H_2 and CH_4 on different Cu-Pt materials at -1.6 V. e) A proposed mechanism illustrating the steps of CO_2 electroreduction and CH_4 formation occurring at the Cu-Pt (3:1) catalyst [c) to e) are adapted with permission from Guo et al.⁸⁴].

2.4 Theoretical Prediction

2.4.1 Pathway to CO Production

In recent years, significant advances in computational modelling has made the screening of potential catalysts for various electrochemical processes much easier, including for the CO₂RR.^{14, 85} Activity trends for a range of metal catalysts and their alloys have also been formulated using activity descriptors, presenting useful predictors for rational catalyst design.^{12, 33} These trends generally include descriptors based on the PDS of a reaction, *e.g.* binding strength of the *CO intermediate has obvious influence on the rate of CO production. For precious metals like Pt, although activation and conversion of CO₂ to CO occurs readily, *CO binding is so strong that desorption is the limiting factor and poisons the surface.¹² In contrast, for Au and Ag, which have very weak binding of *CO, experimental studies have shown that they are some of the most selective metals for CO₂ reduction to CO.^{7, 11, 40, 86} Furthermore, alloying Au with Cu (Cu having higher O-affinity than Au) has shown to be beneficial for the binding strength of the *COOH intermediate, and hence, the activity for CO production can be further increased. For example, compared to Au (111) surfaces, it was found that the free energy change (ΔG) for *COOH formation (ΔG^{*COOH}) decreases on the alloy configurations (Figure 2.7a).⁸⁷ By constructing the Au nanostructures isolated on the Cu surface (Au-*i*@Cu), the ΔG^{*COOH} could be further reduced. In such configurations, the nanostructures increase the number of local under-coordinated sites, which have been shown to increase the binding of intermediates.^{86, 88} Additionally, corner Au sites adjacent to the Cu surface provide a bifunctional effect for the stabilization of the *COOH intermediate, whereby the high O-affinity Cu atoms can stabilize the O-end of *COOH (Figure 2.7b). A similar result was determined on A₃B alloy systems where A = Cu, Au, Ag, and B = p-group metals.³³ Firstly, it was found that scaling relationships between *COOH, *CO, and *CHO intermediates on the pure metals limit their activity for reduction of CO₂ to *CO and the reduction of *CO to *CHO and onwards. Alloying may preferentially increase the interaction of active sites with *COOH or *CHO

resulting in preferential stabilization of these intermediates over $\ast\text{CO}$ (Figure 2.7c). In this case, the C-end of $\ast\text{COOH}$ tends to bind to the A site, while the O-end has significant interaction with the B site. As a result, the inherent scaling relationship may be broken. Therefore, an important design principle for alloy materials is the coupling of different metal sites that interact with C-bound and O-bound species differently.

2.4.2 Pathways Beyond CO

It is known that the hydrogenation of $\ast\text{CO}$ to $\ast\text{CHO}$ is generally the PDS in the CO_2RR pathway beyond CO. Therefore, destabilization of the $\ast\text{CO}$ intermediate was found to be crucial in reducing the overpotential for the subsequent protonation steps.³²⁻³³ When O-binding sites are created through alloying, $\ast\text{CO}$ may be forced to bind in an unfavorable configuration, and therefore, $\ast\text{CHO}$ will be preferentially stabilized. For example, in the Cu-Ni system, C-bound species were generally found to be better stabilized on Ni (211) facets while binding of O-bound intermediates was not changed significantly compared to Cu (211).⁸⁹ Therefore, the Cu_3Ni alloy reflected the difference in intermediate binding between the two parent metals. In a follow up study, the ligand and strain effect on alloys of Cu with Ni and Rh were investigated.⁹⁰ In these systems, a significant reduction in overpotential was achieved on a Cu monolayer deposited on an expanded Ni (211) surface, due to the effect of expansive strain on the binding of $\ast\text{CO}$ *vs.* $\ast\text{CHO}$. For Rh overlayers on Cu, the Cu was found to experience a tensile strain which also led to a reduction in $\ast\text{CO}$ binding and, consequently, a reduction in the overpotential to CH_4 formation was achieved. In a comprehensive study, CO_2 reduction to CH_4 and CH_3OH on a range of Cu_3M (where $\text{M} = \text{Au}, \text{Ag}, \text{Pd}, \text{Pt}, \text{Ni}, \text{Co}, \text{Rh}, \text{and Ir}$) alloy surfaces was predicted using DFT modelling.⁹¹ Generally, on these alloys, CH_4 generation was found to be more favorable compared to pure Cu, except for Cu_3Pd and Cu_3Pt which favored a pathway to CH_3OH . Additionally, the protonation of CO^\ast to HCO^\ast or COH^\ast was the PDS on most surfaces. Of note here, binding of $\ast\text{CO}$, $\ast\text{O}$ and $\ast\text{H}$ species was analyzed in detail to reveal the inherent trend of the various surfaces. It was found that $\ast\text{CO}$ and $\ast\text{O}$ binding on the alloy surfaces exhibits a similar general trend to the pure secondary metal surfaces. For example,

alloying Cu with metals which have weaker O* adsorption than Cu, (Ag, Au, Pd, and Pt) remain to have relatively weaker O* adsorption and *vice versa* for the metals with stronger *O adsorption (Ni, Co, Rh, and Ir; Figure 2.7d). This principle is important for the design of Cu-based bi-metallic catalysts from both fundamental and functional perspectives. As shown in Figure 2.7e, the overpotentials on Cu₃Co, Cu₃Rh, and Cu₃Ir surfaces are lower than that on pure Cu, while those on Cu₃Ag, Cu₃Pd, and Cu₃Pt surfaces are similar to Cu with the same PDS. Additionally, all Cu₃M alloys increased the binding strength of both *CO and *H, except for Au and Ag. Interestingly, these calculations reveal that the activity on Cu-based alloy catalysts does not show a volcano type relation as was previously found on pure metal catalysts.

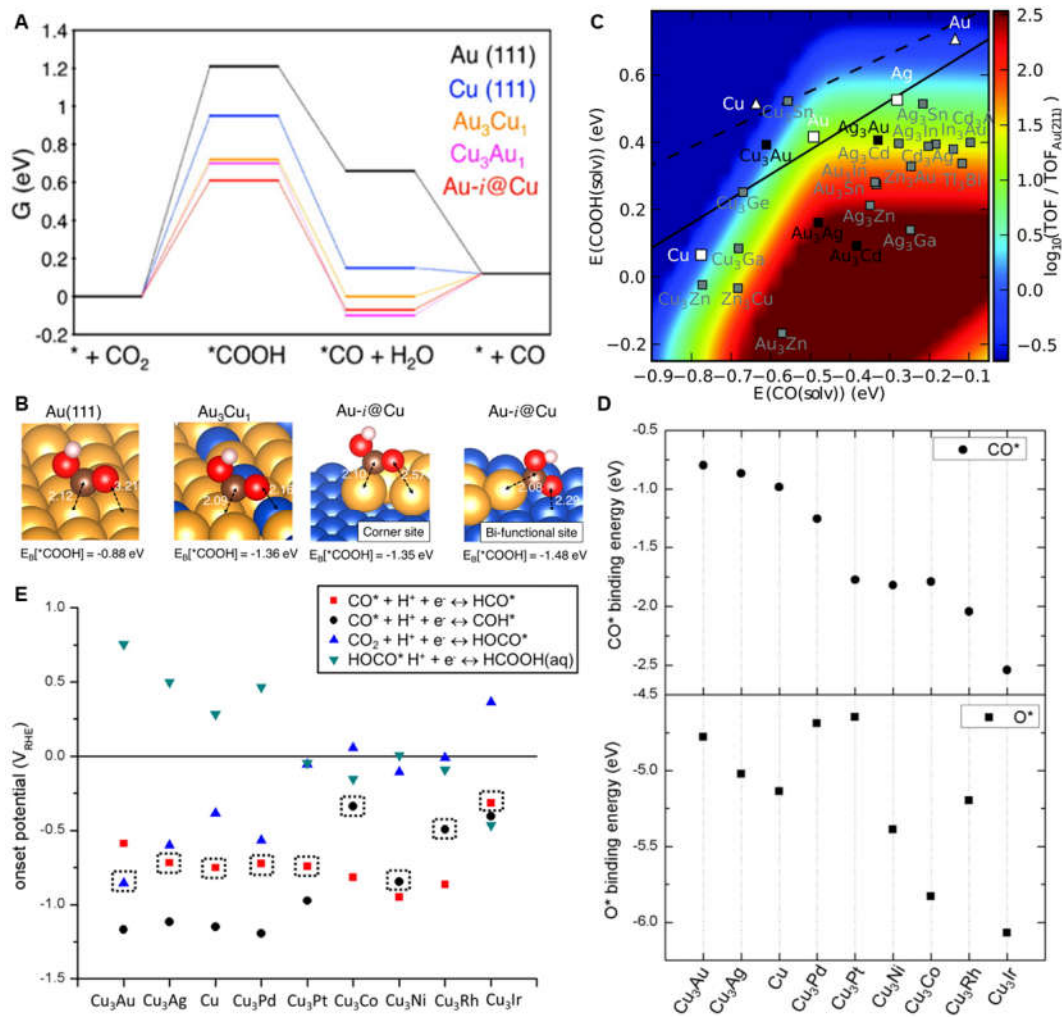


Figure 2.7 Computational studies of various Cu-based alloy catalysts for CO_2RR . a) Free energy diagrams for CO generation on various Cu-Au surfaces. b) Binding configurations of $^*\text{COOH}$ on Au(111), Au_3Cu_1 (111), and a corner and bifunctional site of Au-i@Cu . Yellow, blue, black, red, and white atoms indicate Au, Cu, C, O, and H, respectively [a) and b) adapted with permission from Back et al. ⁸⁷]. c) Breaking the scaling relationship between $^*\text{COOH}$ and $^*\text{CO}$ on various alloy surfaces. Colour bar indicates CO production on (211) steps normalized to the rate on Au(211). Alloys unstable against corrosion at 0 V vs. RHE and pH 7 are shown in grey [c) adapted with permission from Hansen et al. ³³]. d) $^*\text{CO}$ and $^*\text{O}$ binding energies on a range of Cu_3M alloy surfaces. e) Onset potentials of the CO_2 , $^*\text{COOH}$, and $^*\text{CO}$ protonation steps on a range of Cu_3M alloy surfaces. The dotted squares indicate the calculated limiting potential step [d) and e) adapted with permission from Hirunsit et al. ⁹¹].

2.5 General Trends

Based on the above examples, it has been shown that by coupling different metals together, the catalyst surface or interface can be engineered to contain multiple sites which contribute to the binding of key reaction intermediates. We posit that the O-affinity and H-affinity of these secondary sites are significant in this regard, and rational design strategies can be developed by understanding how they affect intermediate binding during the CO₂RR. Despite the effects of the secondary metal sites, different experimental conditions may also affect CO₂RR activity and selectivity, and these considerations have been investigated in recent studies.⁹²⁻⁹⁴ Therefore, a summary of the Cu-based bi-metallic catalysts presented in this article along with their reaction conditions are presented in Table 2.1 for comparison. In our analysis, we find that when Group 1 metals (M₁) are the dominant metal in Cu-M₁ systems, CO is the major product formed with a general improvement in FE compared to the parent metals.^{46, 54, 59, 62} This is likely due to the higher O-affinity of Cu increasing *COOH stabilization, while the weak *CO binding ability of M₁ metals assists in CO product desorption. Further, the weak H binding also suppresses the HER which increases the selectivity towards the CO₂RR overall. For Group 2 metals (M₂), the apparent trend is that the selectivity towards 2e⁻ products is favored in Cu-M₂ systems; pathways beyond CO are also likely suppressed due to weak H binding. When M₂ provides the dominant contribution to the active sites, it is found that HCOOH is the major reduction product.^{66, 68-69} Due to an increased number of available O-binding sites, *OCHO may be better stabilized and a pathway to HCOOH through this intermediate may be favored in these systems.¹⁵ However, when M₂ provides a moderate contribution in these systems, CO is generally produced at very high FE.^{45, 67-68, 70} By introducing these O-binding sites next to Cu active sites, it is likely that *COOH is better stabilized relative to *CO, reducing the barrier to CO formation. Limited studies exist on coupling Group 3 metals (M₃; Pd specifically) with Cu, in which the intermetallic arrangement of these materials had a significant impact on the product selectivity. When the metallic arrangement was more regular, CO was the major product produced with high FE.^{77,81}

As with Cu-M₁ systems, it is possible that the higher O-affinity of the Cu sites increases *COOH stabilization and reduces the barrier to CO formation. For phase separated Cu-Pd nanoparticles, C₂ products were selectively produced because the neighboring Cu sites may facilitate C-C coupling while spillover of H from Pd sites may facilitate hydrogenation.⁷⁵ Fewer examples of Group 4 metals (M₄) being coupled with Cu exist in the literature. Although M₄ metals with high CO affinity should likely be avoided, it is interesting that these materials can produce hydrocarbons at relatively high FE.

Table 2.1 Summary of Recent Reports on Cu-M Alloy and Bi-metallic Materials

		Catalyst	Electrolyte	Applied Potential	Highlighted Products FE [%]	Ref.
Group 1	Au	Cu@Au	0.5 M KHCO ₃	-0.65 V vs. RHE	CO (~30%)	58
		Au ₅₀ Cu ₅₀	PBS	-1.9 V vs. Ag/AgCl	Carbon-containing products (20±5%)	52
		Cu _{63.9} Au _{36.1} /NCF	0.5 M KHCO ₃	-1.1 V vs. SCE	CH ₃ OH (15.9%), C ₂ H ₅ OH (12%)	53
		Au ₃ Cu	0.1 M KHCO ₃	-0.73 V vs. RHE	CO (~65%), HCOO ⁻ (~3%)	46
		o-AuCu	0.1 M KHCO ₃	-0.77 V vs. RHE	CO (~80%)	54
		Au@Cu1 Au@Cu3	PBS	-0.6 V vs. RHE	C ₂ H ₄ (distribution ~20%) CH ₄ (distribution ~20%)	56
		1/3 Cu UPD Au	0.1 M KHCO ₃	-0.55 V vs. RHE	CO (~75%)	55
		Au ₃ Cu alloy nanocrystals	0.1 M PBS	-1.6 V vs. Ag/AgCl	CH ₄ (~35%), CO (~25%), HCOO ⁻ (~8%)	96
	Ag	Ag@Cu-7 Ag@Cu-20	0.1 M KHCO ₃	-1.06 V vs. RHE	CO (82%) C ₂ H ₄ (28.6%)	59
		Ag ₅₇ Cu ₄₃	0.5 M KHCO ₃	-1.5 V vs. SCE	CO (~40%)	60
		CuAg surface alloys	0.05 M Cs ₂ CO ₃		CO dominant (low at% Cu) H ₂ and C ₂ H ₄ dominant (high at% Cu)	62
		Nanocoral Cu-Ag	0.2 M CsHCO ₃	-1.0 V vs. RHE	C ₂ H ₄ (20%), H ₂ (30-35%)	61
	Zn	Oxide-derived Cu ₄ Zn	0.1 M KHCO ₃	-1.05 V vs. RHE	C ₂ H ₅ OH (29.1%), C ₂ H ₄ (~10%)	63
	Cd	Cu modified with Cd	0.1 M KHCO ₃	~-1.66 V vs. SHE ~-1.62 V vs. SHE	CO (~60%) CH ₄ (~40%)	64
Group 2	Sn	Cu@SnO ₂ -0.8 Cu@SnO ₂ -1.8	0.5 M KHCO ₃	-0.7 V vs. RHE -0.9 V vs. RHE	CO (93%) HCOO ⁻ (85%)	68
		Sn-electrodeposited OD-Cu	0.1 M KHCO ₃	-0.6 V vs. RHE	CO (>~90%)	67
		Cu ₈₇ Sn ₁₃ Cu ₅₅ Sn ₄₅	0.1 M KHCO ₃	-0.99 V vs. RHE -1.09 V vs. RHE	CO (60%) HCOO ⁻ (89.5%)	66
	In	Cu-In alloy	0.1 M KHCO ₃	-0.5 V vs. RHE	CO (90%)	70
Group 3	Pd	Pd-decorated Cu	0.5 M KHCO ₃	-0.96 V vs. RHE	CH ₄ (46-40%), C ₂ H ₄ (7-11%)	97
		Disordered CuPd	1 M KOH	-0.89 V vs. RHE	CH ₄ (~7.5%)	81
		PhaseSep CuPd	1 M KOH	-0.74 V vs. RHE	C2 chemicals (~65%)	81
		CuPd ₃	1 M KOH	-0.55 V vs. RHE	CO (~90%)	81
		Pd ₇ Cu ₃	0.1 M KHCO ₃	-0.8 V vs. RHE	CO (~80%)	77
		Pd ₇ Cu ₃	0.1 M KHCO ₃	Bias -1.2 V	CO (~75%)	78
		CuPd nanoalloy (Cu ₂ Pd)	0.1 M KHCO ₃	-1.8 V vs. Ag/AgNO ₃	CH ₄ (~51%)	98
		Cu ₂ O-derived Cu with PdCl ₂	0.1 M KHCO ₃	-1.0 V vs. RHE	C ₂ H ₆ (30.1%), C ₂ H ₄ (3.4%)	99
Group 4	Pt	Cu-Pt (at. 3:1) nanocrystal	0.5 M KHCO ₃	-1.6 V vs. SCE	CH ₄ (21%)	84
		Cu/Pt(111)	0.1 M KHCO ₃	-1.3 V vs. RHE	CH ₄ (~7.5%)	83
	Ni	Cu-electrodeposited Ni	0.5 M KHCO ₃ water/MeOH solution	-1.9 V vs. Ag QRE	CH ₄ (20.2%), C ₂ H ₄ (7.5%)	100

2.6 Conclusion and Outlook

Design and fabrication of selective Cu-based CO₂RR electrocatalysts, especially ones selective for hydrocarbon production, remains a difficult task due to the relatively strong binding of the *CO intermediate during reaction. Surface and interface engineering through coupling Cu with a secondary metal has shown to be a successful initial strategy for reducing the reaction energy barrier to increase its activity. It has also shown to be successful in breaking the scaling relationship that exists between *COOH, *CO and *CHO/*COH to improve the selectivity of Cu. Here, we have reviewed recent examples of Cu-based alloy and bi-metallic materials, and how the O-affinity and H-affinity of the secondary metal affects selectivity. Overall, many examples show that the selectivity for CO/HCOOH and hydrocarbons/alcohols in Cu-M systems can be rationally tuned by modifying O- and/or H-adsorbing sites on the surface. The relationship between an alloy’s chemical composition and its CO₂RR activity/selectivity are systematically linked to its intrinsic intermediate binding energies. Along with some general trends, possible design strategies for future CO₂RR electrocatalysts are provided.

The ultimate goal in this field is to design catalysts selective for deep reduction products with high energy density. Therefore, it is crucial that the design of catalysts address the inherent scaling between *CO and *CHO intermediates. In some cases, it has been shown that the electronic characteristics of both parent metals are relatively preserved after alloying.⁸⁷ For these systems, the binding behaviour of the pure metals can be used to predict intermediate binding on the resultant material. Therefore, one such strategy that could be implemented is the limited growth or metal doping of a secondary metal on a Cu surface. The way that this could be achieved is by constructing single metal atom catalysts (SMAC) supported on a Cu substrate. By employing single M₃ or M₄ SMAC sites, hydrogenation of *CO to deeper products may be facilitated while the HER is limited. Additionally, bi-metallic dimers of Cu and a secondary metal could exhibit strong interfacial coupling which may enhance the selectivity for hydrocarbons, as has been shown theoretically for M₄ metals.⁹⁵ While Cu-M₃ alloys

have shown the best performance toward hydrocarbon production, limited studies exist for these cases. Therefore, more Group 3 metals should be identified and studied. Further, ternary alloys with Cu should be explored as combining specific O-adsorbing and H-adsorbing (*i.e.* M_2 and M_3) sites next to Cu may also prove beneficial for stabilizing and hydrogenating *CO to deeper products. In all these strategies, greater effort should also be focused on exposing more under-coordinated sites, *e.g.* steps and corner sites, in order to maximize the interfacial coupling of different active sites in these materials for optimized binding of intermediates.

To this end, we have provided a general view of the role that O-binding and H-binding sites play at the interface, as well as how they affect the binding of reaction intermediates. Nevertheless, a more profound basis for intermediate energetics is still required. From a theoretical perspective, computational electrochemistry remains to be the most direct and powerful tool to reveal the microscopic picture of the CO_2RR on different catalyst surfaces. For example, it was identified by computations that the first protonation step (*i.e.* CO_2 to *COOH) is the step which determines CO_2 activation in the CO_2RR pathway, while the second protonation step (*i.e.* *CO to *COH or *CHO) dominates the selectivity towards different products. Furthermore, electronic structure computation can reveal and direct the sub-atomic level and atomic level tuning of catalyst surfaces. Additionally, the effects of steps, terraces, islands, and single atom morphologies toward the CO_2RR can be visualized directly through computations. However, models used in DFT calculations are normally constrained to ideal and flat repeating units (this is natural when periodic boundary conditions are adopted). On some catalyst surfaces, it remains a challenge to efficiently identify the real active site(s) due to the complexity of materials which contain multiple structural features. In some cases, the opposite trend was found to occur on the actual alloy material, whereby instability of the surface can lead to morphological changes during reaction conditions.³⁰ Therefore, the chemical composition and physical structure stabilities of bi-metallic catalysts is a significant consideration and should also be experimentally studied both during and after the CO_2RR process (*e.g.* surface segregation may be an issue). In future, more advanced calculations, including high-throughput computation and

machine learning techniques, could be adopted in order to produce more representative models of these complex catalyst surfaces. Coupled with experimental studies, a route to rational design strategies for CO₂RR electrocatalysts appears possible. The concepts proposed in this review related to O-affinity and H-affinity are also very general and may be extended to other catalytic processes involving multiple reaction intermediates. Therefore, this general guidance could be adopted for the design of electrocatalysts and heterogeneous catalysts for the ORR, alkaline HER, CO₂ hydrogenation, *etc.*

2.7 Acknowledgement

The authors gratefully acknowledge financial support from the Australian Research Council (ARC) through the Discovery Project programs (DP160104866, DP170104464, DE160101163, and FL170100154) and the Linkage Project program (LP160100927), and the Australian Government through Research Training Program Scholarships.

2.8 References

1. Liu, J. L.; Guo, C. X.; Vasileff, A.; Qiao, S.-Z., *Small Methods* 2017, *1*, 1600006.
2. Wang, Y.; Liu, J.; Wang, Y.; Al-Enizi, A. M.; Zheng, G., *Small* 2017, *13*, 1701809.
3. Zhang, W.; Hu, Y.; Ma, L.; Zhu, G.; Wang, Y.; Xue, X.; Chen, R.; Yang, S.; Jin, Z., *Adv. Sci.* 2017, 1700275.
4. Zhu, D. D.; Liu, J. L.; Qiao, S.-Z., *Adv. Mater.* 2016, *28*, 3423-52.
5. Vasileff, A.; Zheng, Y.; Qiao, S.-Z., *Adv. Energy Mater.* 2017, *7*, 1700759.
6. Bagger, A.; Ju, W.; Varela, A. S.; Strasser, P.; Rossmeisl, J., *ChemPhysChem* 2017, *18*, 3266-3273.
7. Hori, Y.; Wakebe, H.; Tsukamoto, T.; Koga, O., *Electrochim. Acta* 1994, *39*, 1833-1839.
8. Kuhl, K. P.; Cave, E. R.; Abram, D. N.; Jaramillo, T. F., *Energy Environ. Sci.* 2012, *5*, 7050-7059.
9. Kim, D.; Kley, C. S.; Li, Y.; Yang, P., *PNAS* 2017, *114*, 10560-10565.
10. Hori, Y.; Takahashi, R.; Yoshinami, Y.; Murata, A., *J. Phys. Chem. B* 1997, *101*, 7075-7081.
11. Peterson, A. A.; Norskov, J. K., *J. Phys. Chem. Lett.* 2012, *3*, 251-258.
12. Hansen, H. A.; Varley, J. B.; Peterson, A. A.; Nørskov, J. K., *J. Phys. Chem. Lett.* 2013, *4*, 388-92.
13. Norskov, J. K.; Abild-Pedersen, F.; Studt, F.; Bligaard, T., *PNAS* 2011, *108*, 937-43.
14. Greeley, J.; Jaramillo, T. F.; Bonde, J.; Chorkendorff, I. B.; Norskov, J. K., *Nat. Mater.* 2006, *5*, 909-13.
15. Feaster, J. T.; Shi, C.; Cave, E. R.; Hatsukade, T.; Abram, D. N.; Kuhl, K. P.; Hahn, C.; Nørskov, J. K.; Jaramillo, T. F., *ACS Catal.* 2017, *7*, 4822-4827.
16. Jones, J. P.; Prakash, G. K. S.; Olah, G. A., *Isr. J. Chem.* 2014, *54*, 1451-1466.
17. Hori, Y.; Kikuchi, K.; Suzuki, S., *Chem. Lett.* 1985, *14*, 1695-1698.
18. Hori, Y., CO₂ reduction using electrochemical approach. In *Solar to Chemical*

- Energy Conversion*, Springer International Publishing, 2016; pp 191-211.
19. Kuhl, K. P.; Hatsukade, T.; Cave, E. R.; Abram, D. N.; Kibsgaard, J.; Jaramillo, T. F., *J. Amer. Chem. Soc.* 2014, *136*, 14107-13.
 20. Zheng, Y.; Jiao, Y.; Jaroniec, M.; Qiao, S.-Z., *Angew. Chem. Int. Ed.* 2015, *54*, 52-65.
 21. Lv, H. F.; Li, D. G.; Strmcnik, D.; Paulikas, A. P.; Markovic, N. M.; Stamenkovic, V. R., *Nano Energy* 2016, *29*, 149-165.
 22. Nie, Y.; Li, L.; Wei, Z., *Chem. Soc. Rev.* 2015, *44*, 2168-201.
 23. Shao, M.; Chang, Q.; Dodelet, J. P.; Chenitz, R., *Chem. Rev.* 2016, *116*, 3594-657.
 24. Huang, X. Q.; Zhao, Z. P.; Cao, L.; Chen, Y.; Zhu, E. B.; Lin, Z. Y.; Li, M. F.; Yan, A. M.; Zettl, A.; Wang, Y. M.; Duan, X. F.; Mueller, T.; Huang, Y., *Science* 2015, *348*, 1230-1234.
 25. Stamenkovic, V. R.; Fowler, B.; Mun, B. S.; Wang, G.; Ross, P. N.; Lucas, C. A.; Markovic, N. M., *Science* 2007, *315*, 493-7.
 26. Hori, Y.; Takahashi, I.; Koga, O.; Hoshi, N., *J. Phys. Chem. B* 2002, *106*, 15-17.
 27. Hori, Y.; Kikuchi, K.; Murata, A.; Suzuki, S., *Chem. Lett.* 1986, *15*, 897-898.
 28. Schouten, K. J. P.; Kwon, Y.; van der Ham, C. J. M.; Qin, Z.; Koper, M. T. M., *Chem. Sci.* 2011, *2*, 1902-1909.
 29. Hori, Y.; Murata, A.; Takahashi, R., *J. Chem. Soc. Farad. T. 1* 1989, *85*, 2309-2326.
 30. Jovanov, Z. P.; Hansen, H. A.; Varela, A. S.; Malacrida, P.; Peterson, A. A.; Norskov, J. K.; Stephens, I. E. L.; Chorkendorff, I., *J. Catal.* 2016, *343*, 215-231.
 31. Hashiba, H.; Sato, H. K.; Yotsuhashi, S.; Fujii, K.; Sugiyama, M.; Nakano, Y., *Sustain. Energy Fuels* 2017, *1*, 1734-1739.
 32. Durand, W. J.; Peterson, A. A.; Studt, F.; Abild-Pedersen, F.; Norskov, J. K., *Surf. Sci.* 2011, *605*, 1354-1359.
 33. Hansen, H. A.; Shi, C.; Lausche, A. C.; Peterson, A. A.; Nørskov, J. K., *Phys.*

- Chem. Chem. Phys.* 2016, *18*, 9194-201.
34. Peterson, A. A.; Abild-Pedersen, F.; Studt, F.; Rossmeisl, J.; Norskov, J. K., *Energy Environ. Sci.* 2010, *3*, 1311-1315.
 35. Nie, X.; Esopi, M. R.; Janik, M. J.; Asthagiri, A., *Angew. Chem. Int. Ed.* 2013, *52*, 2459-62.
 36. Nie, X. W.; Luo, W. J.; Janik, M. J.; Asthagiri, A., *J. Catal.* 2014, *312*, 108-122.
 37. Ulissi, Z. W.; Tang, M. T.; Xiao, J. P.; Liu, X. Y.; Torelli, D. A.; Karamad, M.; Cummins, K.; Hahn, C.; Lewis, N. S.; Jaramillo, T. F.; Chan, K. R.; Norskov, J. K., *ACS Catal.* 2017, *7*, 6600-6608.
 38. Abild-Pedersen, F.; Greeley, J.; Studt, F.; Rossmeisl, J.; Munter, T. R.; Moses, P. G.; Skulason, E.; Bligaard, T.; Norskov, J. K., *Phys. Rev. Lett.* 2007, *99*, 016105.
 39. Li, Y. W.; Sun, Q., *Adv. Energy Mater.* 2016, *6*, 1600463.
 40. Zhu, W.; Michalsky, R.; Metin, O.; Lv, H.; Guo, S.; Wright, C. J.; Sun, X.; Peterson, A. A.; Sun, S., *J. Amer. Chem. Soc.* 2013, *135*, 16833-6.
 41. Dutta, A.; Rahaman, M.; Luedi, N. C.; Broekmann, P., *ACS Catal.* 2016, *6*, 3804-3814.
 42. Raciti, D.; Livi, K. J.; Wang, C., *Nano Lett.* 2015, *15*, 6829-35.
 43. Sen, S.; Liu, D.; Palmore, G. T. R., *ACS Catal.* 2014, *4*, 3091-3095.
 44. Wang, Z. L.; Li, C. L.; Yamauchi, Y., *Nano Today* 2016, *11*, 373-391.
 45. He, J.; Dettelbach, K. E.; Salvatore, D. A.; Li, T.; Berlinguette, C. P., *Angew. Chem. Int. Ed.* 2017, *56*, 6068-6072.
 46. Kim, D.; Resasco, J.; Yu, Y.; Asiri, A. M.; Yang, P., *Nat. Commun.* 2014, *5*, 4948.
 47. Jiao, Y.; Zheng, Y.; Chen, P.; Jaroniec, M.; Qiao, S.-Z., *J. Amer. Chem. Soc.* 2017, *139*, 18093-18100.
 48. Norskov, J. K.; Bligaard, T.; Logadottir, A.; Kitchin, J. R.; Chen, J. G.; Pandelov, S.; Norskov, J. K., *J. Electrochem. Soc.* 2005, *152*, J23-J26.
 49. Greeley, J.; Stephens, I. E. L.; Bondarenko, A. S.; Johansson, T. P.; Hansen, H.

- A.; Jaramillo, T. F.; Rossmeisl, J.; Chorkendorff, I.; Nørskov, J. K., *Nat. Chem.* 2009, *1*, 552.
50. Trasatti, S., *J. Electroanal. Chem. Interf. Electrochem.* 1972, *39*, 163-184.
 51. Kepp, K. P., *Inorg. Chem.* 2016, *55*, 9461-70.
 52. Christophe, J.; Doneux, T.; Buess-Herman, C., *Electrocatalysis* 2012, *3*, 139-146.
 53. Jia, F. L.; Yu, X. X.; Zhang, L. Z., *J. Power Sources* 2014, *252*, 85-89.
 54. Kim, D.; Xie, C.; Becknell, N.; Yu, Y.; Karamad, M.; Chan, K.; Crumlin, E. J.; Nørskov, J. K.; Yang, P., *J. Amer. Chem. Soc.* 2017, *139*, 8329-8336.
 55. Ross, M. B.; Dinh, C. T.; Li, Y.; Kim, D.; De Luna, P.; Sargent, E. H.; Yang, P., *J. Amer. Chem. Soc.* 2017, *139*, 9359-9363.
 56. Monzo, J.; Malewski, Y.; Kortlever, R.; Vidal-Iglesias, F. J.; Solla-Gullon, J.; Koper, M. T. M.; Rodriguez, P., *J. Mater. Chem. A* 2015, *3*, 23690-23698.
 57. Shi, C.; Hansen, H. A.; Lausche, A. C.; Nørskov, J. K., *Phys. Chem. Chem. Phys.* 2014, *16*, 4720-7.
 58. Chen, K.; Zhang, X.; Williams, T.; Bourgeois, L.; MacFarlane, D. R., *Electrochim. Acta* 2017, *239*, 84-89.
 59. Chang, Z. Y.; Huo, S. J.; Zhang, W.; Fang, J. H.; Wang, H. L., *J. Phys. Chem. C* 2017, *121*, 11368-11379.
 60. Choi, J.; Kim, M. J.; Ahn, S. H.; Choi, I.; Jang, J. H.; Ham, Y. S.; Kim, J. J.; Kim, S.-K., *Chem. Eng. J.* 2016, *299*, 37-44.
 61. Gurudayal; Bullock, J.; Sranko, D. F.; Towle, C. M.; Lum, Y. W.; Hettick, M.; Scott, M. C.; Javey, A.; Ager, J., *Energy Environ. Sci.* 2017, *10*, 2222-2230.
 62. Clark, E. L.; Hahn, C.; Jaramillo, T. F.; Bell, A. T., *J. Amer. Chem. Soc.* 2017, *139*, 15848-15857.
 63. Ren, D.; Ang, B. S. H.; Yeo, B. S., *ACS Catal.* 2016, *6*, 8239-8247.
 64. Hori, Y.; Murata, A.; Ito, S.-Y., *Chem. Lett.* 1990, *19*, 1231-1234.
 65. Lv, W.; Zhang, R.; Gao, P.; Lei, L., *J. Power Sources* 2014, *253*, 276-281.
 66. Morimoto, M.; Takatsuji, Y.; Yamasaki, R.; Hashimoto, H.; Nakata, I.; Sakakura, T.; Haruyama, T., *Electrocatalysis* 2017, *8*, 1-10.
 67. Sarfraz, S.; Garcia-Esparza, A. T.; Jedidi, A.; Cavallo, L.; Takanabe, K., *ACS*

- Catal.* 2016, *6*, 2842-2851.
68. Li, Q.; Fu, J.; Zhu, W.; Chen, Z.; Shen, B.; Wu, L.; Xi, Z.; Wang, T.; Lu, G.; Zhu, J. J.; Sun, S., *J. Amer. Chem. Soc.* 2017, *139*, 4290-4293.
 69. Schreier, M.; Heroguel, F.; Steier, L.; Ahmad, S.; Luterbacher, J. S.; Mayer, M. T.; Luo, J. S.; Gratzel, M., *Nat. Energy* 2017, *2*, 17087.
 70. Rasul, S.; Anjum, D. H.; Jedidi, A.; Minenkov, Y.; Cavallo, L.; Takanabe, K., *Angew. Chem. Int. Ed.* 2015, *54*, 2146-50.
 71. Martin, R.; Buchwald, S. L., *Acc. Chem. Res.* 2008, *41*, 1461-73.
 72. Suh, D. J.; Park, T. J.; Ihm, S. K., *Ind. Eng. Chem. Res.* 1992, *31*, 1849-1856.
 73. Conrad, H.; Ertl, G.; Latta, E. E., *Surf. Sci.* 1974, *41*, 435-446.
 74. Jewell, L. L.; Davis, B. H., *Appl. Catal. A* 2006, *310*, 1-15.
 75. Kyriakou, G.; Boucher, M. B.; Jewell, A. D.; Lewis, E. A.; Lawton, T. J.; Baber, A. E.; Tierney, H. L.; Flytzani-Stephanopoulos, M.; Sykes, E. C. H., *Science* 2012, *335*, 1209-1212.
 76. Bai, S.; Shao, Q.; Wang, P.; Dai, Q.; Wang, X.; Huang, X., *J. Amer. Chem. Soc.* 2017, *139*, 6827-6830.
 77. Li, M.; Wang, J. J.; Li, P.; Chang, K.; Li, C. L.; Wang, T.; Jiang, B.; Zhang, H. B.; Liu, H. M.; Yamauchi, Y.; Umezawa, N.; Ye, J. H., *J. Mater. Chem. A* 2016, *4*, 4776-4782.
 78. Li, M.; Li, P.; Chang, K.; Liu, H.; Hai, X.; Zhang, H.; Ye, J., *Chem. Comm.* 2016, *52*, 8235-8.
 79. Takashima, T.; Suzuki, T.; Irie, H., *Electrochim. Acta* 2017, *229*, 415-421.
 80. Hammer, B.; Morikawa, Y.; Norskov, J. K., *Phys. Rev. Lett.* 1996, *76*, 2141-2144.
 81. Ma, S.; Sadakiyo, M.; Heima, M.; Luo, R.; Haasch, R. T.; Gold, J. I.; Yamauchi, M.; Kenis, P. J., *J. Amer. Chem. Soc.* 2017, *139*, 47-50.
 82. Long, R.; Li, Y.; Liu, Y.; Chen, S.; Zheng, X.; Gao, C.; He, C.; Chen, N.; Qi, Z.; Song, L.; Jiang, J.; Zhu, J.; Xiong, Y., *J. Amer. Chem. Soc.* 2017, *139*, 4486-4492.
 83. Varela, A. S.; Schlaup, C.; Jovanov, Z. P.; Malacrida, P.; Horch, S.; Stephens,

- I. E. L.; Chorkendorff, I., *J. Phys. Chem. C* 2013, *117*, 20500-20508.
84. Guo, X.; Zhang, Y.; Deng, C.; Li, X.; Xue, Y.; Yan, Y. M.; Sun, K., *Chem. Comm.* 2015, *51*, 1345-8.
 85. Ko, J.; Kim, B. K.; Han, J. W., *J. Phys. Chem. C* 2016, *120*, 3438-3447.
 86. Back, S.; Yeom, M. S.; Jung, Y., *ACS Catal.* 2015, *5*, 5089-5096.
 87. Back, S.; Kim, J. H.; Kim, Y. T.; Jung, Y., *ACS Appl. Mater. Interfaces* 2016, *8*, 23022-7.
 88. Han, B. C.; Miranda, C. R.; Ceder, G., *Phys. Rev. B* 2008, *77*, 075410.
 89. Adit Maark, T.; Nanda, B. R. K., *J. Phys. Chem. C* 2016, *120*, 8781-8789.
 90. Adit Maark, T.; Nanda, B. R. K., *J. Phys. Chem. C* 2017, *121*, 4496-4504.
 91. Hirunsit, P.; Soodsawang, W.; Limtrakul, J., *J. Phys. Chem. C* 2015, *119*, 8238-8249.
 92. Sun, X.; Kang, X.; Zhu, Q.; Ma, J.; Yang, G.; Liu, Z.; Han, B., *Chem. Sci.* 2016, *7*, 2883-2887.
 93. Resasco, J.; Chen, L. D.; Clark, E.; Tsai, C.; Hahn, C.; Jaramillo, T. F.; Chan, K.; Bell, A. T., *J. Amer. Chem. Soc.* 2017, *139*, 11277-11287.
 94. Singh, M. R.; Kwon, Y.; Lum, Y.; Ager, J. W., 3rd; Bell, A. T., *J. Amer. Chem. Soc.* 2016, *138*, 13006-13012.
 95. Li, Y. W.; Su, H. B.; Chan, S. H.; Sun, Q., *ACS Catal.* 2015, *5*, 6658-6664.
 96. Zhao, W. G.; Yang, L. N.; Yin, Y. D.; Jin, M. S., *J. Mater. Chem. A* 2014, *2*, 902-906.
 97. Weng, Z.; Zhang, X.; Wu, Y.; Huo, S.; Jiang, J.; Liu, W.; He, G.; Liang, Y.; Wang, H., *Angew. Chem. Int. Ed.* 2017, *56*, 13135-13139.
 98. Wu, J.; Shan, S.; Luo, J.; Joseph, P.; Petkov, V.; Zhong, C. J., *ACS Appl. Mater. Interfaces* 2015, *7*, 25906-13.
 99. Chen, C. S.; Wan, J. H.; Yeo, B. S., *J. Phys. Chem. C* 2015, *119*, 26875-26882.
 100. Kaneco, S.; Sakaguchi, Y.; Katsumata, H.; Suzuki, T.; Ohta, K., *Bull. Catal. Soc. India* 2007, *6*, 74-82.

Chapter 3

Bronze Alloys with Tin Surface Sites

for Selective Electrochemical Reduction of CO₂

This Chapter includes work published in the journal article *Chem. Comm.*, 2018, 54, 13965. As outlined in Chapter 2, Cu-M₂ systems show a significant enhancement to carbon monoxide and formate selectivity, yet a comprehensive understanding of this selectivity trend is lacking. Therefore, the aim of this Chapter is to characterize the electrochemical performance of Cu-M₂ alloys (M₂ = Sn) and determine their reaction kinetics. From this, a preliminary hypothesis could be made regarding the key reaction step and intermediates which govern selectivity in the system.

In this Chapter, a range of bronze (Cu-Sn) nanoparticle catalysts were studied to demonstrate this selectivity trend toward CO and formate. A CO selective alloy (α bronze) and a formate selective alloy (η' bronze) were then chosen to probe the reaction mechanism and pathway. Low concentration tin bronze alloys show high selectivity for CO₂ electroreduction to CO while high concentration tin bronze alloys show high selectivity for formate. While the Tafel slopes indicate both catalysts are limited by the initial electron transfer step, we postulate that the tin surface sites control selectivity by influencing the binding configuration of the first reaction intermediate.

Statement of Authorship

Title of Paper	Bronze Alloys with Tin Surface Sites for Selective Electrochemical Reduction of CO ₂
Publication Status	<input checked="" type="checkbox"/> Published <input type="checkbox"/> Accepted for Publication <input type="checkbox"/> Submitted for Publication <input type="checkbox"/> Unpublished and Unsubmitted work written in manuscript style
Publication Details	A. Vasileff, C.C. Xu, L. Ge, Y. Zheng, S.Z. Qiao, Bronze Alloys with Tin Surface Sites for Selective Electrochemical Reduction of CO ₂ , Chemical Communications, 2018, 54, 13965-13968

Principal Author

Name of Principal Author (Candidate)	Anthony Vasileff		
Contribution to the Paper	Conducted the majority of experiments, analysed all the data and wrote the majority of the paper		
Overall percentage (%)	76		
Certification:	This paper reports on original research I conducted during the period of my Higher Degree by Research candidature and is not subject to any obligations or contractual agreements with a third party that would constrain its inclusion in this thesis. I am the primary author of this paper.		
Signature		Date	05/02/2020

Co-Author Contributions

By signing the Statement of Authorship, each author certifies that:

- the candidate's stated contribution to the publication is accurate (as detailed above);
- permission is granted for the candidate to include the publication in the thesis; and
- the sum of all co-author contributions is equal to 100% less the candidate's stated contribution.

Name of Co-Author	Chaochen Xu		
Contribution to the Paper	3% Helped with some of the experiments and provided valuable insight into the paper discussion		
Signature		Date	05/02/2020

Name of Co-Author	Lei Ge		
Contribution to the Paper	5% Conducted all XPS experiments		
Signature		Date	05/02/2020

Name of Co-Author	Yao Zheng		
Contribution to the Paper	8% Provided guidance and supervision from conception through to submission and helped to revise the paper.		
Signature		Date	05/02/2020

Name of Co-Author	Shizhang Qiao		
Contribution to the Paper	8% Provided guidance and supervision from conception through to submission and helped to revise the paper.		
Signature		Date	05/02/2020

3.1 Introduction

Copper has long been known as a unique catalyst for the electrochemical CO₂ reduction reaction (CO₂RR) because it is the only known metal to produce hydrocarbons and alcohols with modest activity.¹ However, copper is also a non-selective catalyst as it produces various products concurrently.¹ Therefore, engineering copper for selective CO₂RR is a key issue in developing Cu-based electrocatalysts.

Copper bi-metallic materials and alloys have recently shown an improvement in CO₂RR selectivity compared to copper, where the secondary metal plays an important role in altering inherent adsorption energetics of a series of CO₂RR intermediates.² An interesting bi-metallic system for the CO₂RR is the copper-tin system, with some of these materials showing high selectivity for CO.³⁻⁵ From computational studies, this behaviour is likely the result of changes in binding strength of key intermediates (*H and *CO are primarily explored).^{3, 5} For increased tin coverage, the catalyst will exhibit binding characteristics more alike tin. As a result, these Cu-Sn materials are more selective for formate. There also appears to be a point where the effect of tin on binding characteristics becomes negligible for these alloys. This is evidenced for very low tin concentration alloys which exhibit product selectivity similar to copper. As aforementioned, most theoretical studies focus on the effects of tin on *H and *CO binding in Cu-Sn materials, but given the separate pathways toward formate and CO,⁶ this does not provide adequate explanation. Therefore, an experimental understanding at the atomic level regarding this selectivity trend for 2e⁻ products is required.

Here, we designed and synthesized a Cu-rich alloy (α bronze nanoparticles) and a Sn-rich alloy (η' bronze nanoparticles) to study the CO₂RR selectivity of the Cu-Sn alloy system in detail. We find that α bronze nanoparticles (NPs) are capable of reaching Faradaic Efficiencies (FE) above 90 % for CO production, while η' bronze NPs can produce formate at FE of up to 72 %. By kinetics analysis, we determine the rate limiting step and possible binding configuration of the first reaction intermediate in these two electrocatalyst systems. From this observed behaviour, we can link the alloy composition to the CO₂RR selectivity trend at the atomic level.

3.2 Results and Discussion

The bronze NPs were synthesized by the reduction of copper and tin salts with sodium borohydride. These nanoparticles were then annealed at 500 °C and cooled slowly (pseudo equilibrium cooling conditions) to limit phase transformation (see Appendix A for experimental details). Composition of the nanoparticles (~ 50 -100 nm; Figure S3.1) was studied by energy-dispersive X-ray (EDX) spectroscopy and Cu K-edge and Sn L-edge signals were collected across line scans of each alloy sample (Figure 3.1a-b). The alloy NPs were typically homogeneous in composition and α bronze NPs had an average Cu to Sn atomic ratio of $\sim 95.5:4.5$ (Cu_{22}Sn) while the η' bronze NPs had an average Cu to Sn atomic ratio of $\sim 54.5:44.5$ (Cu_6Sn_5).

The X-ray diffraction (XRD) pattern confirms the crystal phase of the η' bronze NPs (Figure S3.2a; JCPDS Card #45-1488). Another phase is also observed in the XRD pattern which can be indexed to ϵ bronze (JCPDS Card #01-1240). Results from Rietveld refinement indicate that this is present as a minor phase making up 11.4 wt % of the alloy (Figure 3.1c). For α bronze NPs, the XRD pattern is most closely indexed to α Cu (Figure S3.2b; JCPDS Cards #04-0836). However, on comparison with Cu NPs (Figure 3.1d), the (111), (200), and (220) peak positions are negatively shifted which suggests that α bronze has a slightly larger lattice spacing. The selected area electron diffraction (SAED) patterns show that α bronze NPs had a (111) lattice spacing of 2.10 Å (Figure S3.3), slightly larger than that of Cu NPs (2.08 Å). The lattice constant for cubic α bronzes scales with Sn content,⁷ therefore the larger lattice spacing of the α bronze NPs confirms the doping of Sn in the Cu lattice.

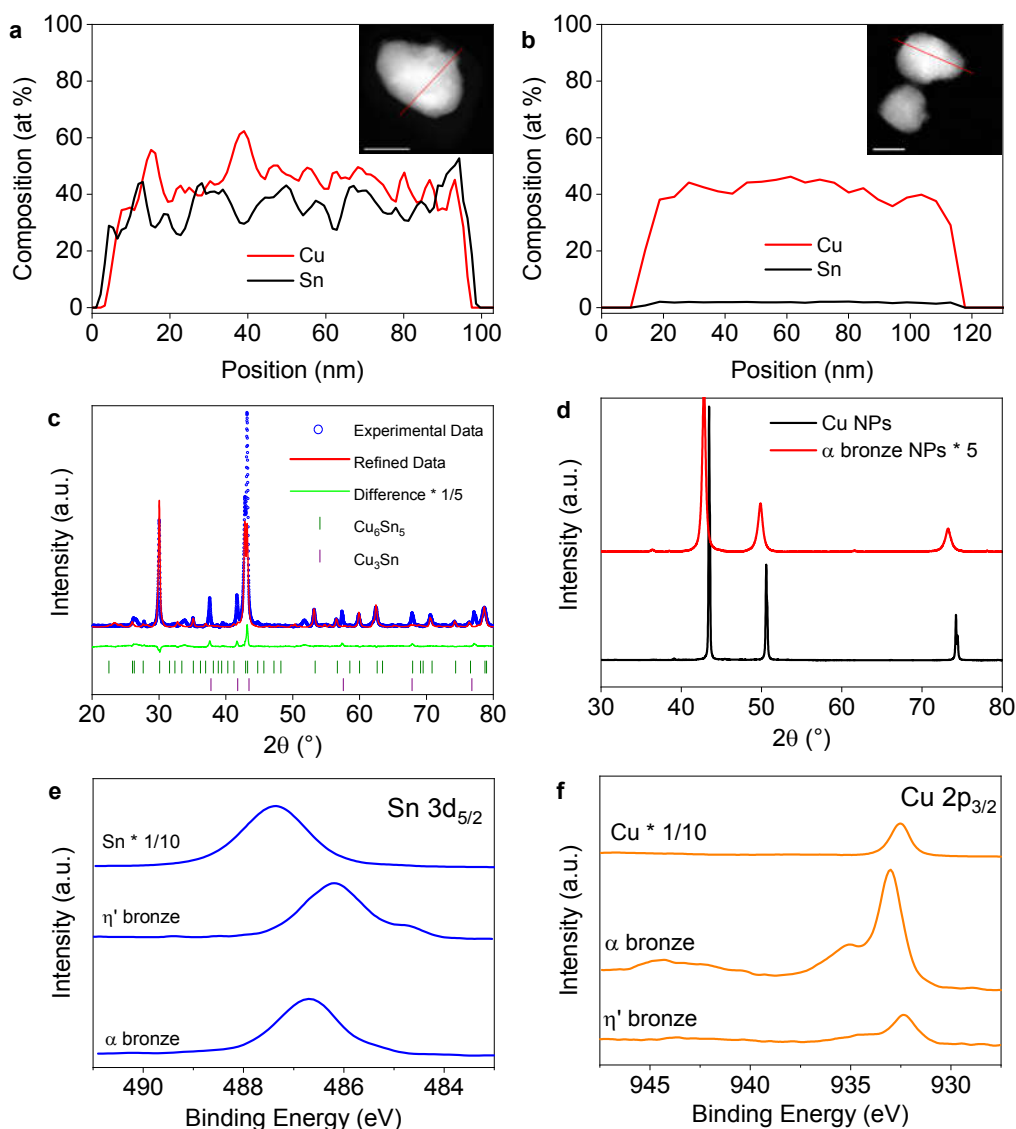


Figure 3.1 EDX line scan of a) η' bronze and b) α bronze NPs for Cu K-edge and Sn L-edge with STEM image of scanned particles inset. Scale bars are 50 nm. c) Rietveld refinement of η' bronze XRD data using theoretical profiles for Cu_6Sn_5 and Cu_3Sn to quantify phases. d) comparison of XRD spectra of α bronze NPs and Cu NPs. e) Sn 3d_{5/2} and f) Cu 2p_{3/2} XPS spectra for the bronze NPs, Cu NPs, and Sn NPs.

The X-ray Photoelectron Spectroscopy (XPS) survey spectra of the bronze NPs show distinct signals from Cu, Sn, and O (Figure S3.4). From the Sn 3d_{5/2} high resolution spectra (Figure 3.1e), the pure Sn sample exhibits a characteristic peak at 487.2 eV, which can be assigned to Sn^{IV} species,⁸ indicating the presence of a SnO_2 layer on the surface. For the bronze samples, the position of the Sn^{IV} peak shifts negatively to 486.7 eV and 486.2 eV for η' bronze and α bronze, respectively. A shift in this peak may result from the slightly larger electronegativity of Sn compared to Cu

causing charge redistribution within the alloy structures and result in different electrocatalytic properties.⁹ Further, a weak shoulder peak (centred around 485 eV) is observed to appear and can be attributed to $\text{Sn}^{(0)}$.¹⁰

In the Cu 2p region (Figure 3.1f), the bronze samples exhibit a characteristic Cu 2p_{3/2} peak at 932.8 eV, suggesting predominantly $\text{Cu}^{(0)}/\text{Cu}^{\text{I}}$ states.¹¹ Peaks observed around 934.9 eV and shake-up satellites can be attributed to Cu^{II} species, namely CuO and $\text{Cu}(\text{OH})_2$.¹¹ The O 1s spectra (Figure S3.5) also show the presence of oxide species on the sample surface, with the dominant contribution likely originating from Cu_2O (~531.7 eV) as the concentration of Sn decreases.¹¹ Under the reduction potentials utilized in this study, the active Cu and Sn sites likely exist in the zero valent state, as has been discussed previously.^{3, 12} From the above, we see that Sn doping causes charge re-distribution in the alloys, with η' bronze inducing a greater re-distribution compared to α bronze. As a result, the modified electronic structure caused by Sn doping likely plays a key role in changing the intermediate binding characteristics of the alloy.

To evaluate how altering surface properties through Sn doping affects the selectivity/activity of these copper-based alloy NPs, a range of Cu-Sn NPs were tested for the CO_2RR in CO_2 -saturated 0.1 M KHCO_3 electrolyte (Figure 3.2a). A clear selectivity trend can be observed with the decrease in tin concentration; as the tin concentration decreases, selectivity for formate decreases while selectivity for CO increases. However, for very low tin concentration alloys (Cu_{40}Sn), Sn-doping appears to have lesser effect on selectivity as selectivity appears to be similar to copper. Herein, we evaluate the performance of α phase and η' phase bronzes because they appear to exhibit the highest selectivity towards CO and HCOO^- , respectively.

From the linear scan voltammograms (LSV; Figure S3.6), α bronze NPs showed significantly higher catalytic current density (approximately double) compared to η' bronze. From Figure 3.2b, we see that α bronze reaches a maximum FE for CO production of 92 % at a potential of -0.81 V vs. RHE. For η' bronze (Figure 3.2c), a maximum FE for formate production of 73 % is achieved at -1.17 V vs. RHE. As shown in Figure 3.2d, the bronze NPs exhibited good stability over 6 h of continuous operation. CO production on α bronze NPs was maintained at FEs above 75 % while η' bronze

exhibited an average FE of 66 % towards formate production over 6 h. XRD spectra of the electrocatalysts before and after stability testing showed negligible change to the crystal structure of the NPs (Figure S3.7). No new peaks arising from metallic Cu or Sn were observed which suggests that surface segregation was unlikely.

To investigate how Sn surface sites in the Cu-based alloys affect the catalytic mechanism and pathway, Tafel analysis was performed to determine the possible reaction rate determining step (rds). Tafel slopes (Figure 3.3a-b) in the kinetically controlled potential region indicate that a one electron transfer step is the rds for both alloys.¹³⁻¹⁴ A comparison of Tafel plots between α bronze and Cu NPs (Figure S3.8) shows that Cu NPs have a significantly higher Tafel slope (149 mV dec^{-1}) for CO production in a similar potential region.

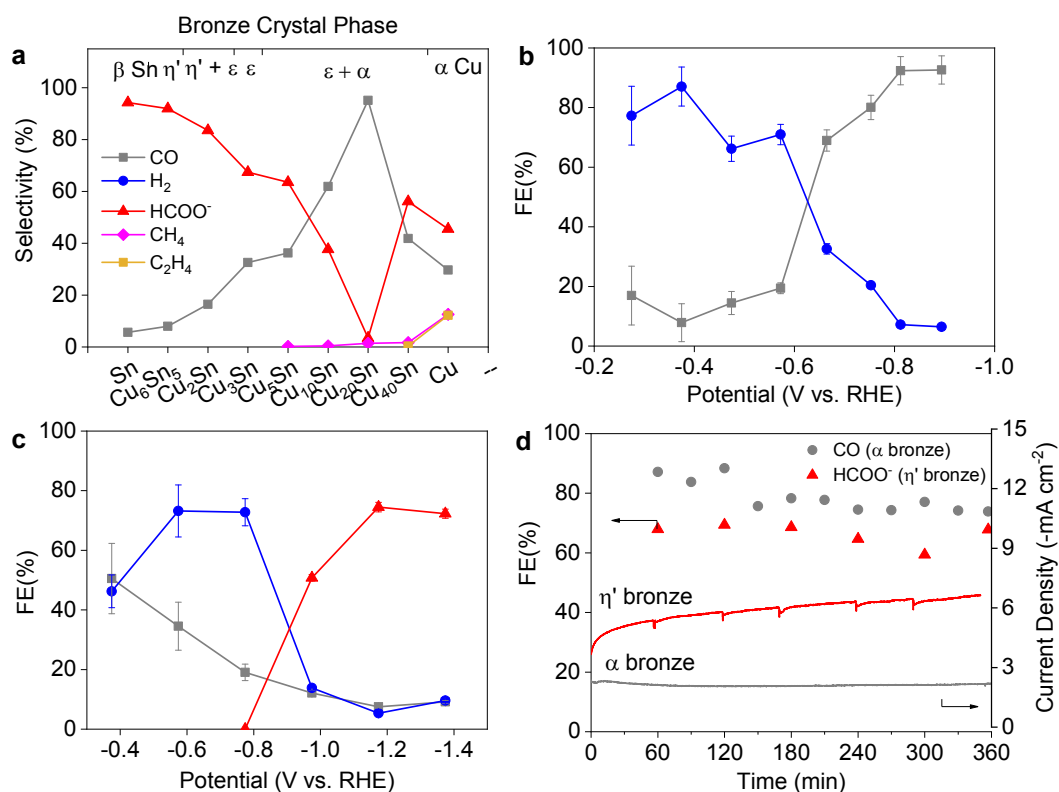


Figure 3.2 a) Selectivity of various bronze NP samples towards CO₂RR products at -1 V vs. RHE. Faradaic efficiency towards CO₂RR products for b) α bronze and c) η' bronze. d) Stability test of α bronze at -0.81 V vs. RHE and η' bronze -1.17 V vs. RHE with FE towards major products and current density over 6 h.

As outlined by Rosen et al.,¹³ a Tafel slope (Equation 1) for the CRR system can be derived:

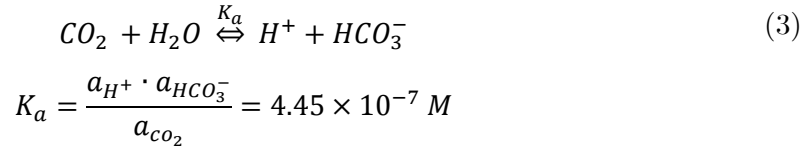
$$\text{Tafel Slope} = \frac{\partial \eta}{\partial \log(i)} = \frac{2.3RT}{F(\alpha + \theta_{C1})} \quad (1)$$

where η is the overpotential, i is the current density, R is the gas constant (8.314 J mol⁻¹ K⁻¹), T is temperature (K), F is the Faraday constant (96485 C mol⁻¹), α is the transfer coefficient, and θ_{C1} is the coverage of the *CO₂⁻ intermediate in the first step of the pathway. Assuming a similar transfer coefficient in both cases, the Tafel slope becomes dependent on θ_{C1} , with higher coverage resulting in a smaller Tafel slope, vice versa. Compared with pure Cu NPs, the smaller Tafel slope of both alloy NPs indicates increased θ_{C1} . Therefore, the presence of Sn in the cubic Cu lattice for both α and η' samples can better stabilize *CO₂⁻ intermediate during CO₂RR.¹⁵

For the first electron transfer step, the rate equation can be expressed as follows:

$$i = Fk^0 a_{CO_2} \theta^* \exp\left(\frac{\alpha F \eta}{RT}\right) \quad (2)$$

where k^0 is the rate constant (s⁻¹), a_{CO_2} (M) is the activity of CO₂, and θ^* is the fraction of unoccupied surface sites. To simplify the complexity of equilibrium processes occurring in the electrolyte near the catalyst surface,¹⁶ we impart the following equilibrium relationship for the CO₂ concentration near the catalyst surface:



We do this on the assumption that at lower overpotentials (when the total current density is relatively low), the local pH near the catalyst surface remains relatively neutral and therefore Equation 3 is the main equilibrium process occurring in the bulk and locally.¹⁶⁻¹⁷ Assuming diffusion between the bulk solution is not limiting in this low overpotential region, Equation 2 can be re-written as:

$$i = Fk^0 \left[\frac{\gamma_{H^+} [H^+] \gamma_{HCO_3^-} [HCO_3^-]}{K_a} \right] \theta^* \exp\left(\frac{\alpha F \eta}{RT}\right) \quad (4)$$

Based on Equation 4, we would expect to observe a first order dependency of cathodic current with respect to $[\text{HCO}_3^-]$. In Figure 3.3c-d, we indeed see that when CO_2 reduction was performed at constant potential in electrolytes of different $[\text{HCO}_3^-]$, both alloy catalysts exhibit a near first order dependency on $[\text{HCO}_3^-]$. Given both a Tafel slope $\sim 118 \text{ mV dec}^{-1}$ and a first order dependency on $[\text{HCO}_3^-]$, this further confirms that the first electron transfer step is the rds on both bronze NPs. Therefore, the role of Sn surface sites is likely critical at this first reaction step and lead to the observed differences in selectivity.

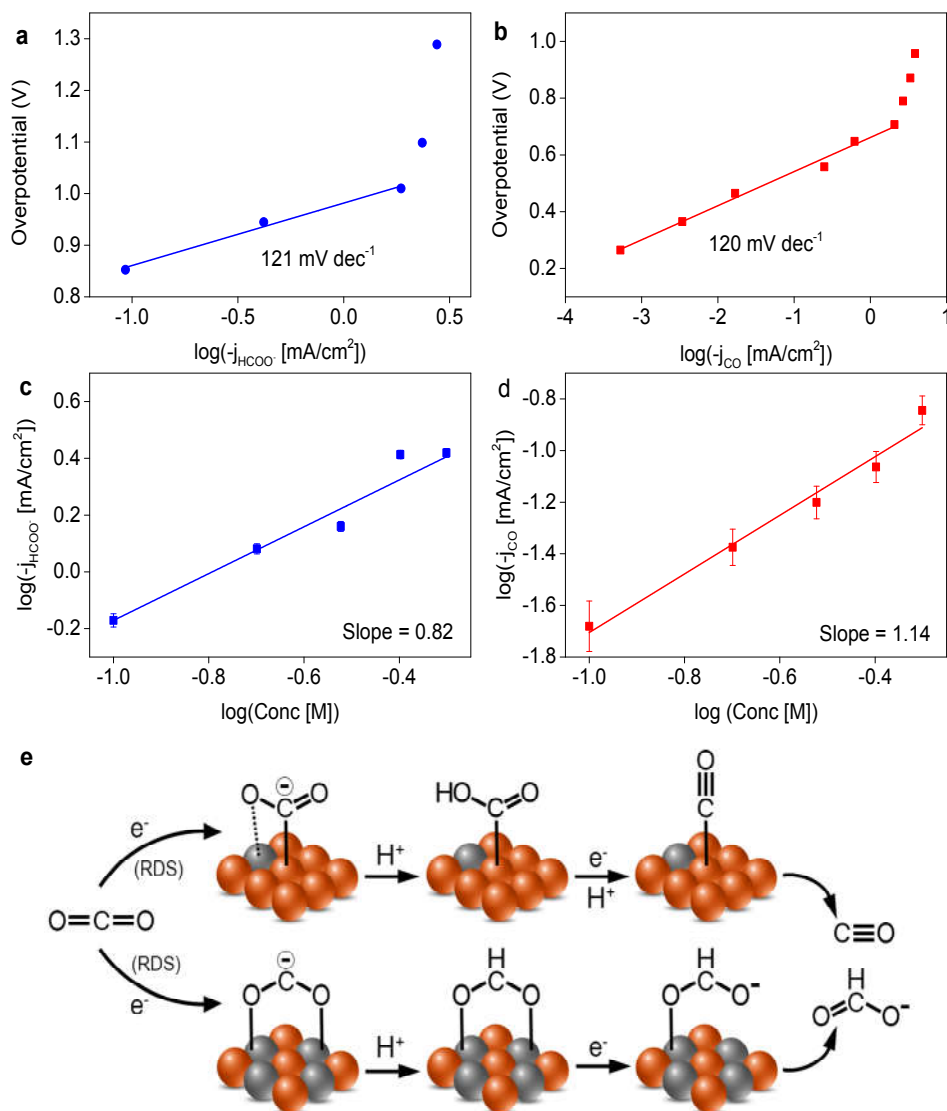


Figure 3.3 Tafel plots for a) α bronze and b) η' bronze. Rate dependency on $[\text{HCO}_3^-]$ for c) η' bronze at -0.97 V vs. RHE and d) α bronze at -0.57 V vs. RHE (corrected for changes in pH). KCl was added to the electrolyte to maintain constant ionic strength. e) Proposed reaction pathway with top route on low concentration Sn surfaces and bottom route on high concentration Sn surfaces.

To probe how Sn surface sites affect selectivity toward reaction pathways on both alloys, CO₂ reduction products were measured at different potentials in CO₂-saturated electrolytes with KHCO₃ concentrations of 0.1 M (pH 6.8), 0.5 M (pH 7.5), and 1.0 M (pH 7.8). Two alloys exhibit significantly different behaviour from one another. For η' bronze (Figure S3.9a-c), a significant increase in partial current for all observed reduction products (HCOO⁻, H₂, and CO) occurs when the [HCO₃⁻] is increased from 0.1 to 0.5 M. However, further increase to 1.0 M results in negligible change to partial currents, indicating a limiting reduction current on the electrode. Further, the FE towards CO and H₂ remains relatively consistent under all conditions (Figure S3.10a-c). Only a significant change in FE can be observed toward HCOO⁻, which is likely the result of increased CO₂ availability as discussed above. Therefore, a pathway to formate is dominant when increased Sn surface sites are present.

On the other hand, the pathway on α bronze appears to be far more electrolyte/pH sensitive as quite significant changes to partial current and FE towards all reduction products are observed. From Figure S3.9d-e and Figure S3.10d-e, we observe that with increasing bicarbonate concentration, the FE towards CO decreases at higher overpotentials while the FE and partial current towards hydrogen increases. The enhancement to HER partial current is likely due to the increased buffering capacity of the electrolytes maintaining a lower local pH.¹⁷⁻¹⁸ Interestingly, while no hydrocarbons (methane and ethylene) are observed in this potential range in 0.1 M KHCO₃, the partial current towards these products increases to approximately 8 % and 19 % of the total Faradaic current in 0.5 M and 1.0 M electrolyte, respectively. Therefore, by reducing the number of surface Sn sites, a pathway to formate is suppressed and a pathway to CO (and to hydrocarbons) is favored.¹⁹⁻²⁰

From the above experimental results, it appears that distinct pathways occur on the two alloy catalysts. We believe that this arises from different binding configurations of the initial reaction intermediate (i.e. C-bound vs. O-bound), as demonstrated in Figure 3.3e. On α bronze, the results suggest that the initial intermediate adsorbs in a C-bound configuration, given that CO is the main product and a pathway to hydrocarbons is possible. Further, an enhancement in kinetics for CO production

compared to copper indicates that the presence of Sn sites provides better stabilization of this intermediate, possibly through increased interaction with the O-ends.¹⁵ η' bronze exhibits behaviour more alike Sn electrodes, which leads us to believe that η' bronze binds the initial intermediate in an O-bound configuration.²¹⁻²² In addition, changing the electrolyte concentration does not have the same effect on product distribution as it does on α bronze, which supports the idea that formate production through an O-bound intermediate is a 'dead end' pathway.²³ Therefore, with increased Sn sites, the affinity for the C-bound intermediate decreases and a pathway to HCOO^- through the O-bound intermediate is favored. At higher overpotentials, HCOO^- was detected on α bronze indicating that both pathways can occur over low Sn concentration bronzes (Figure S3.11). This also suggests that lower potentials are required to drive the reaction through an O-bound intermediate.^{3, 22-23}

3.3 Conclusions

To summarize, we applied a Cu-rich bronze NP catalyst (α bronze) and a Sn-rich bronze NP catalyst (η' bronze) to explore the effect of alloy composition on product selectivity for CO₂ electroreduction. As expected from our preliminary observations, α bronze was selective for CO production, reaching FEs toward CO above 90 %, while η' bronze was selective for formate production, reaching FEs toward formate above 70 %. We used kinetic analysis to reveal the fundamental role of Sn surface sites toward product selectivity. For both alloys, the rds in the pathway is the first electron transfer to form the first reaction intermediate. On α bronze, this initial intermediate is likely C-bound and is better stabilized compared to copper, indicating that some Sn sites are beneficial for intermediate stabilization. For η' bronze, the initial intermediate is likely O-bound and the affinity for the C-bound intermediate is suppressed with increasing Sn surface sites. This Sn doping strategy realizes controlled selectivity of CO₂RR products and could be extended to other Cu-alloy systems.

3.4 Acknowledgement

The authors gratefully acknowledge financial support from the Australian Research Council (ARC) through Discovery Project programs (FL170100154, DP160104866, DP170104464 and DE160101163) and the Australian Government through Research Training Program Scholarships. The authors also thank Dr. Ashley Slattery at Adelaide Microscopy for help with STEM imaging and Dr. Wei Zhou for help with XRD refinement.

3.5 References

1. Hori, Y.; Takahashi, R.; Yoshinami, Y.; Murata, A., *J. Phys. Chem. B* 1997, *101*, 7075-7081.
2. Vasileff, A.; Xu, C.; Jiao, Y.; Zheng, Y.; Qiao, S.-Z., *Chem* 2018, *4*, 1809-1831.
3. Sarfraz, S.; Garcia-Esparza, A. T.; Jedidi, A.; Cavallo, L.; Takanabe, K., *ACS Catal.* 2016, *6*, 2842-2851.
4. Li, Q.; Fu, J.; Zhu, W.; Chen, Z.; Shen, B.; Wu, L.; Xi, Z.; Wang, T.; Lu, G.; Zhu, J. J.; Sun, S., *J. Amer. Chem. Soc.* 2017, *139*, 4290-4293.
5. Schreier, M.; Heroguel, F.; Steier, L.; Ahmad, S.; Luterbacher, J. S.; Mayer, M. T.; Luo, J. S.; Gratzel, M., *Nat. Energy* 2017, *2*, 17087.
6. Kortlever, R.; Shen, J.; Schouten, K. J. P.; Calle-Vallejo, F.; Koper, M. T. M., *J. Phys. Chem. Lett.* 2015, *6*, 4073-4082.
7. Sidot, E.; Kahn-Harari, A.; Cesari, E.; Robbiola, L., *Mater. Sci. Eng. A* 2005, *393*, 147-156.
8. Wang, D.; Miller Alfred, C.; Notis Michael, R., *Surf. Interface Anal.* 1996, *24*, 127-132.
9. Yang, N.; Zhang, Z.; Chen, B.; Huang, Y.; Chen, J.; Lai, Z.; Chen, Y.; Sindoro, M.; Wang, A. L.; Cheng, H.; Fan, Z.; Liu, X.; Li, B.; Zong, Y.; Gu, L.; Zhang, H., *Adv. Mater.* 2017, *29*, 1700769.
10. Naille, S.; Dedryvère, R.; Martinez, H.; Leroy, S.; Lippens, P. E.; Jumas, J. C.; Gonbeau, D., *J. Power Sources* 2007, *174*, 1086-1090.
11. Biesinger, M. C.; Lau, L. W. M.; Gerson, A. R.; Smart, R. S. C., *App. Surf. Sci.* 2010, *257*, 887-898.
12. Dutta, A.; Kuzume, A.; Rahaman, M.; Vesztergom, S.; Broekmann, P., *ACS Catal.* 2015, *5*, 7498-7502.
13. Rosen, J.; Hutchings, G. S.; Lu, Q.; Rivera, S.; Zhou, Y.; Vlachos, D. G.; Jiao, F., *ACS Catal.* 2015, *5*, 4293-4299.
14. Chen, Y.; Li, C. W.; Kanan, M. W., *J. Amer. Chem. Soc.* 2012, *134*, 19969-19972.

15. Hansen, H. A.; Shi, C.; Lausche, A. C.; Peterson, A. A.; Nørskov, J. K., *Phys. Chem. Chem. Phys.* 2016, *18*, 9194-201.
16. Zhong, H.; Fujii, K.; Nakano, Y.; Jin, F., *J. Phys. Chem. C* 2015, *119*, 55-61.
17. Gattrell, M.; Gupta, N.; Co, A., *J. Electroanal. Chem.* 2006, *594*, 1-19.
18. Zheng, J.; Sheng, W.; Zhuang, Z.; Xu, B.; Yan, Y., *Sci. Adv.* 2016, *2*, e1501602.
19. Nie, X. W.; Luo, W. J.; Janik, M. J.; Asthagiri, A., *J. Catal.* 2014, *312*, 108-122.
20. Schreier, M.; Yoon, Y.; Jackson, M. N.; Surendranath, Y., *Angew. Chem. Int. Ed.* 2018, *57*, 10221-10225.
21. Feaster, J. T.; Shi, C.; Cave, E. R.; Hatsukade, T.; Abram, D. N.; Kuhl, K. P.; Hahn, C.; Nørskov, J. K.; Jaramillo, T. F., *ACS Catal.* 2017, *7*, 4822-4827.
22. Gu, J.; Héroguel, F.; Luterbacher, J.; Hu, X., *Angew. Chem. Int. Ed.* 2018, *57*, 2943-2947.
23. Peterson, A. A.; Abild-Pedersen, F.; Studt, F.; Rossmeisl, J.; Nørskov, J. K., *Energy Environ. Sci.* 2010, *3*, 1311-1315.

Chapter 3

Supporting Information

3.6 Experimental Section

3.6.1 Materials

All chemicals (analytical reagent grade) used in this work, including copper (II) chloride dihydrate ($\text{CuCl}_2 \cdot 2\text{H}_2\text{O}$), tin (IV) chloride pentahydrate ($\text{SnCl}_4 \cdot 5\text{H}_2\text{O}$), sodium borohydride (NaBH_4), polyvinylpyrrolidone (PVP; 40000 MW), and potassium bicarbonate (KHCO_3) were purchased from Sigma-Aldrich and used without further purification. Carbon paper (CP, AvCarb MGL 190, Product Code: 1594008) was bought from FuelCellStore. Ultra-pure water ($18.2 \text{ M}\Omega \cdot \text{cm}$, PURELAB Option-Q) was used in all experiments. Scientific grade (HiQ) 5 % H_2/Ar was purchased from BOC. Ultra-high purity N_2 (99.999 %) and laser grade CO_2 (99.995 %) were purchased from BOC and used in all electrochemical experiments.

3.6.2 Synthesis of Electrocatalysts

Preparation of Bronze Alloy Nanoparticles:

30 ml of 1 mM PVP in water was added to a three-neck flask which was then purged with nitrogen for 30 min under stirring. Specific ratios of $\text{CuCl}_2 \cdot 2\text{H}_2\text{O}$ and $\text{SnCl}_4 \cdot 5\text{H}_2\text{O}$ were added to 5 ml of water and the mixture was sonicated for 10 min to form a homogenous solution. Excess NaBH_4 was dissolved in 5 ml of water and then added to the flask via syringe. Following this, the salt solution was added dropwise to the flask via syringe. The nanoparticles were then washed in water three times and then in ethanol three times by centrifugation (8500 rpm). The washed nanoparticles were dried under vacuum at 60°C for 12 h. The dried powder was then transferred to a silica boat

and annealed at 500°C (heating rate of 5 °C min⁻¹) for 5 h under a flow of 5 % H₂/Ar (30 ml min⁻¹) and cooled at a rate of 1 °C min⁻¹. The alloy nanoparticles were then collected and used for electrode fabrication.

Preparation of Cu Nanoparticles:

The method used to prepare the Cu nanoparticles was the same as that outlined for the alloy nanoparticles. However, no SnCl₄·5H₂O was used in the synthesis process.

Preparation of Sn Nanoparticles:

The method used to prepare the Sn nanoparticles was the same as that outlined for the alloy nanoparticles. However, no CuCl₂·2H₂O was used in the synthesis process and the nanoparticles were annealed at 200 °C instead of 500 °C.

Electrode Preparation:

CP (1 x 1 cm) was pre-treated by plasma cleaning and acid washing to remove metallic contaminants. The treated carbon paper was washed with water and dried in a vacuum oven at 60 °C. To prepare the catalyst suspensions, each alloy/metal nanoparticle powder was dispersed in ethanol at 20 mg ml⁻¹. The resultant mixtures were then sonicated for 1 h to form homogenous suspensions. 50 µl of catalyst suspension (loading of 1 mg cm⁻²) was then dropped on each side of a dried piece of carbon paper and dried in a vacuum oven for 12 h at 60°C.

3.6.3 Material Characterizations

The chemical composition of the nanoparticles was measured using EDS (SuperX) under STEM mode (FEI Titan Themis, 200 kV). SAED patterns were collected under TEM mode (Philips CM200, 200 kV). Crystal structure and chemical structure of the samples were characterized by XRD (Rigaku MiniFlex, Cu Kα), and by XPS (Kratos Axis Ultra, mono Al Kα (1486.6eV)).

3.6.4 Electrochemical Measurements

Electrochemical measurements were performed on a 760E bipotentiostat (CH Instruments, Inc., USA) using a gas tight three-electrode H-cell with anode and cathode compartments separated by a proton exchange membrane (Nafion 117). The alloy NP/CP samples were directly applied as the working electrodes. Ag/AgCl (4.0 M KCl) and a RuO₂ coated titanium mesh electrode (25 x 50 mm) were used as the reference and counter electrodes, respectively. All electrochemical measurements were conducted under stirring in KHCO₃ electrolyte which had been saturated with either N₂ or CO₂. CV scans at 100 mV s⁻¹ between -1.0 and -1.4 V vs. Ag/AgCl were first recorded until a stable current response was obtained and LSV scans were obtained at a scan rate of 5 mV s⁻¹. For chronoamperometric responses, the cell was first purged with CO₂ (10 min, 100 ml/min) and sealed. After applying a reduction potential, 100 µl of the head space was drawn using a gas tight syringe. The gas sample was manually injected into the inlet of a gas chromatograph (GC, 7890B, Agilent, USA) in splitless mode. The GC was fitted with a Plot-Q and a 5Å sieve column in series, TCD and methanizer/FID detectors, and Ar as the carrier gas. The catholyte was collected and analyzed using H¹ nuclear magnetic resonance spectroscopy (NMR, A500a DD2 500 MHz, Agilent, USA). H¹ chemical shifts were referenced to phenol and DMSO internal reference peaks in 10 vol% D₂O solvent. For the electrolyte concentration study, salinity of 1 M was maintained between the different bicarbonate solutions by adding KCl.

All electrochemical measurements were iR compensated and all potentials discussed in the results were given against the reversible hydrogen electrode (RHE). The conversion of reference potentials from Ag/AgCl to RHE was calculated using the following equation:

$$E_{RHE} = E_{Ag/AgCl} + 0.224 + 0.059pH$$

Overpotentials for CO and HCOO⁻ production were calculated using the following equation:

$$\eta = E_{RHE} - E^0$$

Where E⁰ is the equilibrium potential which is -0.11 V for CO production and -0.02 V for formate production.

3.7 Supplementary Figures

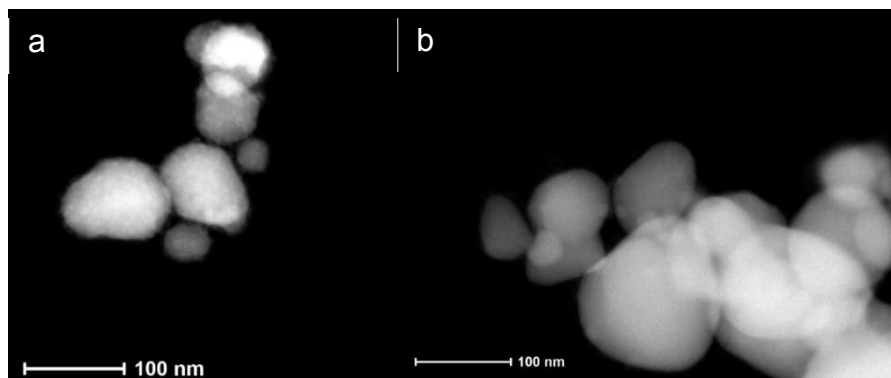


Figure S3.1 STEM images of a) α bronze and b) η' bronze nanoparticles.

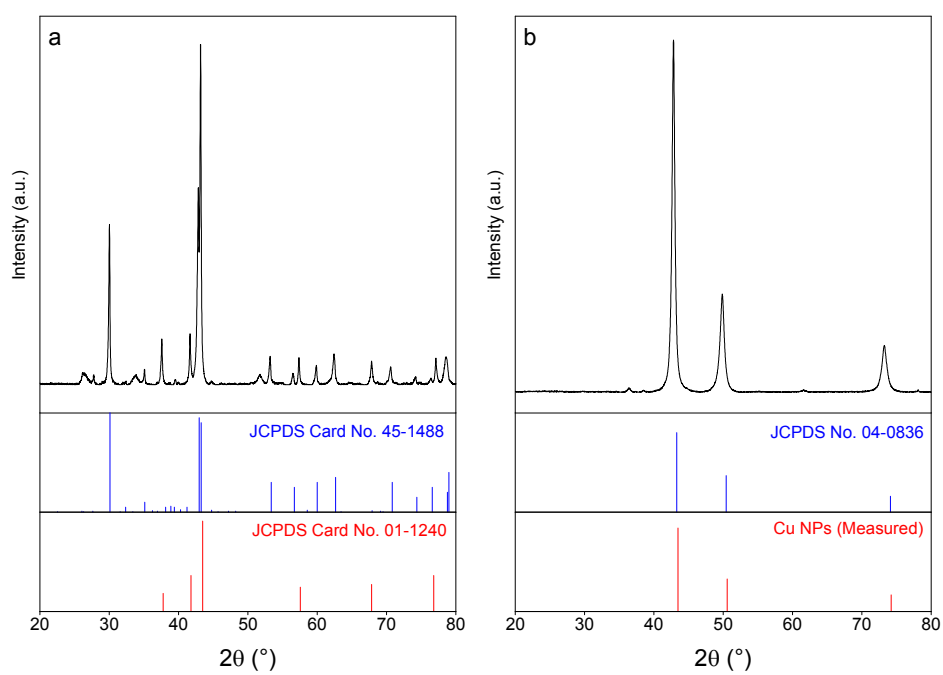


Figure S3.2 XRD spectra of a) η' bronze and b) α bronze nanoparticles.

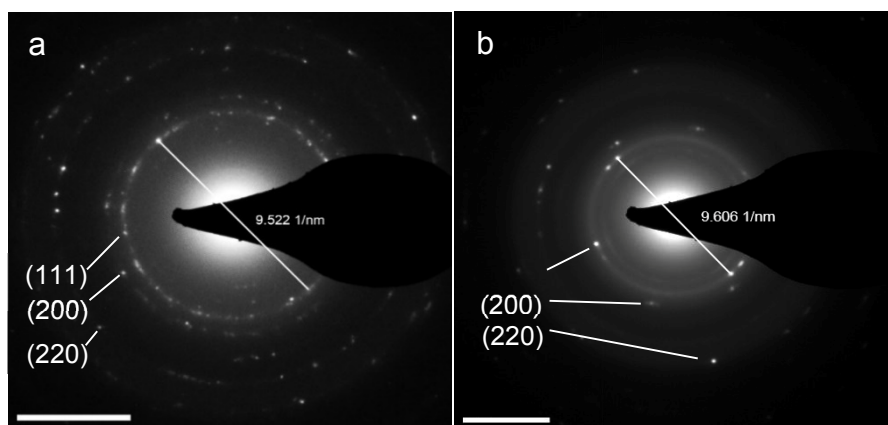


Figure S3.3 SAED image of a) α bronze NPs and b) Cu NPs. Scale bar is 5 nm^{-1} in each panel.

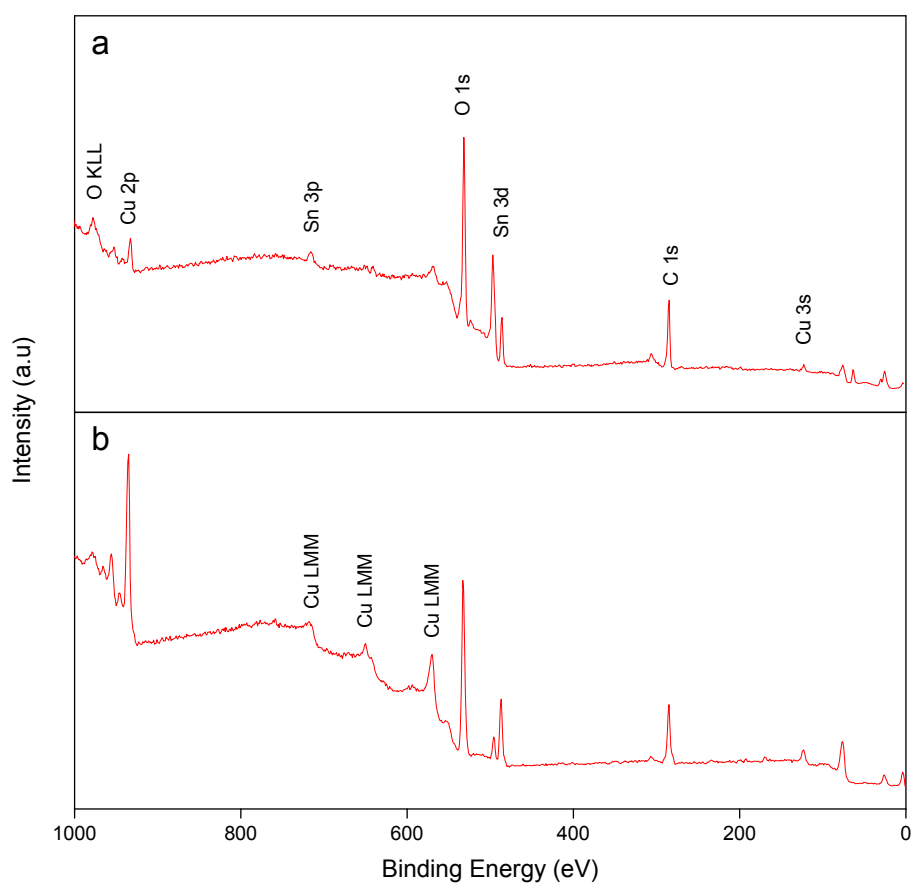


Figure S3.4 XPS Survey spectra for a) α bronze and b) η' bronze.

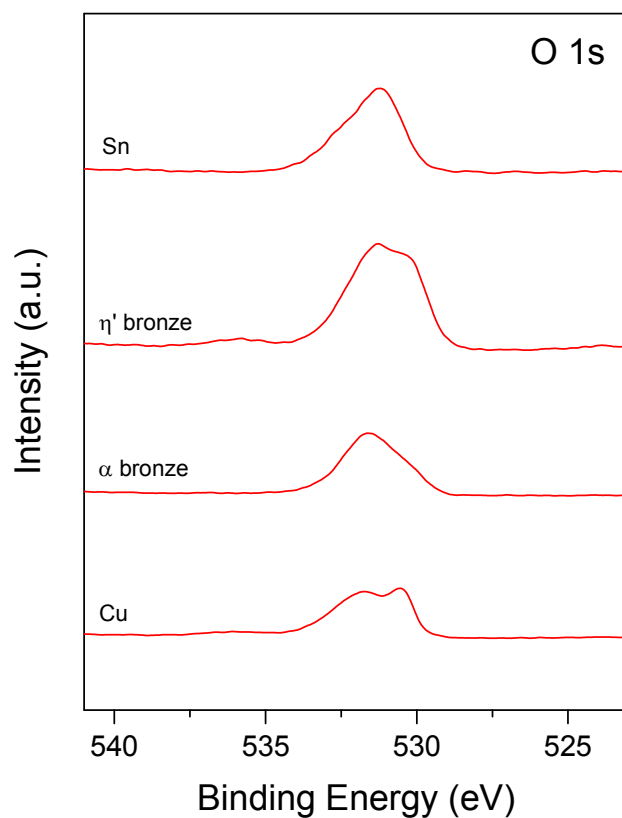


Figure S3.5 XPS O 1s spectra for the bronze NPs, Cu NPs, and Sn NPs.

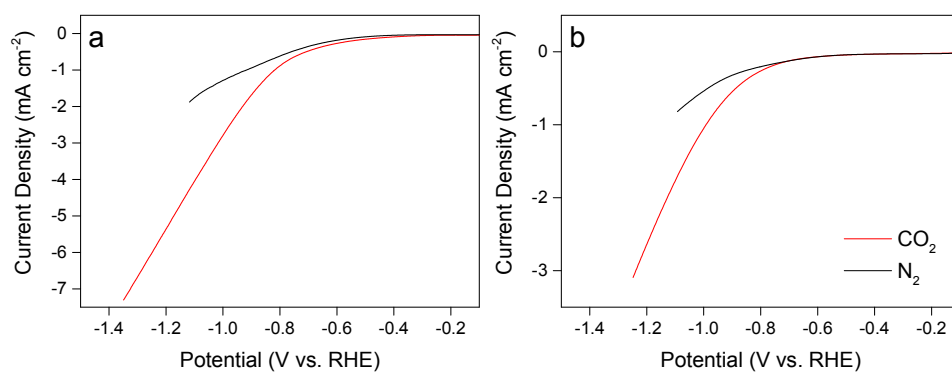


Figure S3.6 LSV plots in CO_2 (red line) and N_2 (black line) saturated 0.1 M KHCO_3 for a) α bronze and b) η' bronze.

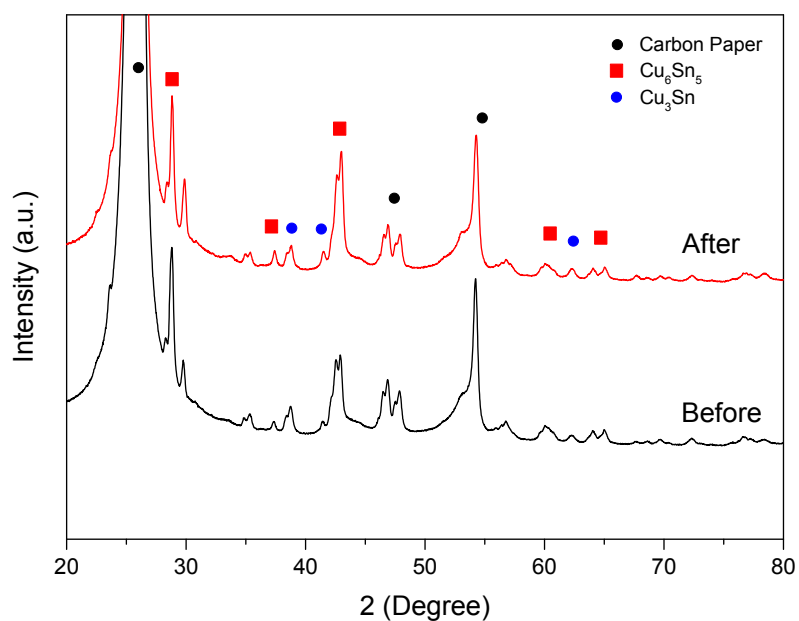


Figure S3.7 XRD spectra of η' bronze on carbon paper before and after the 6 h stability test.

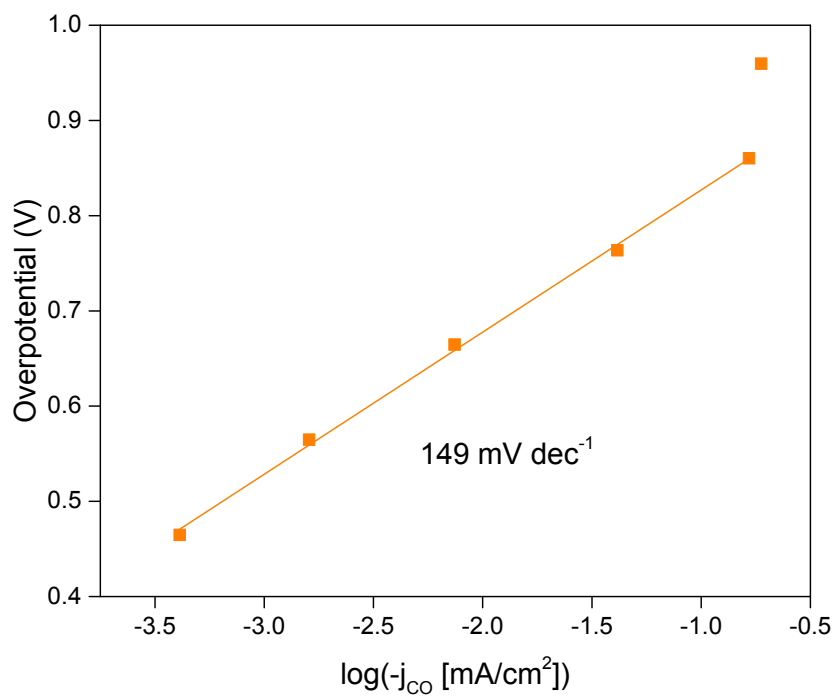


Figure S3.8 Tafel plot for CO formation on Cu NPs.

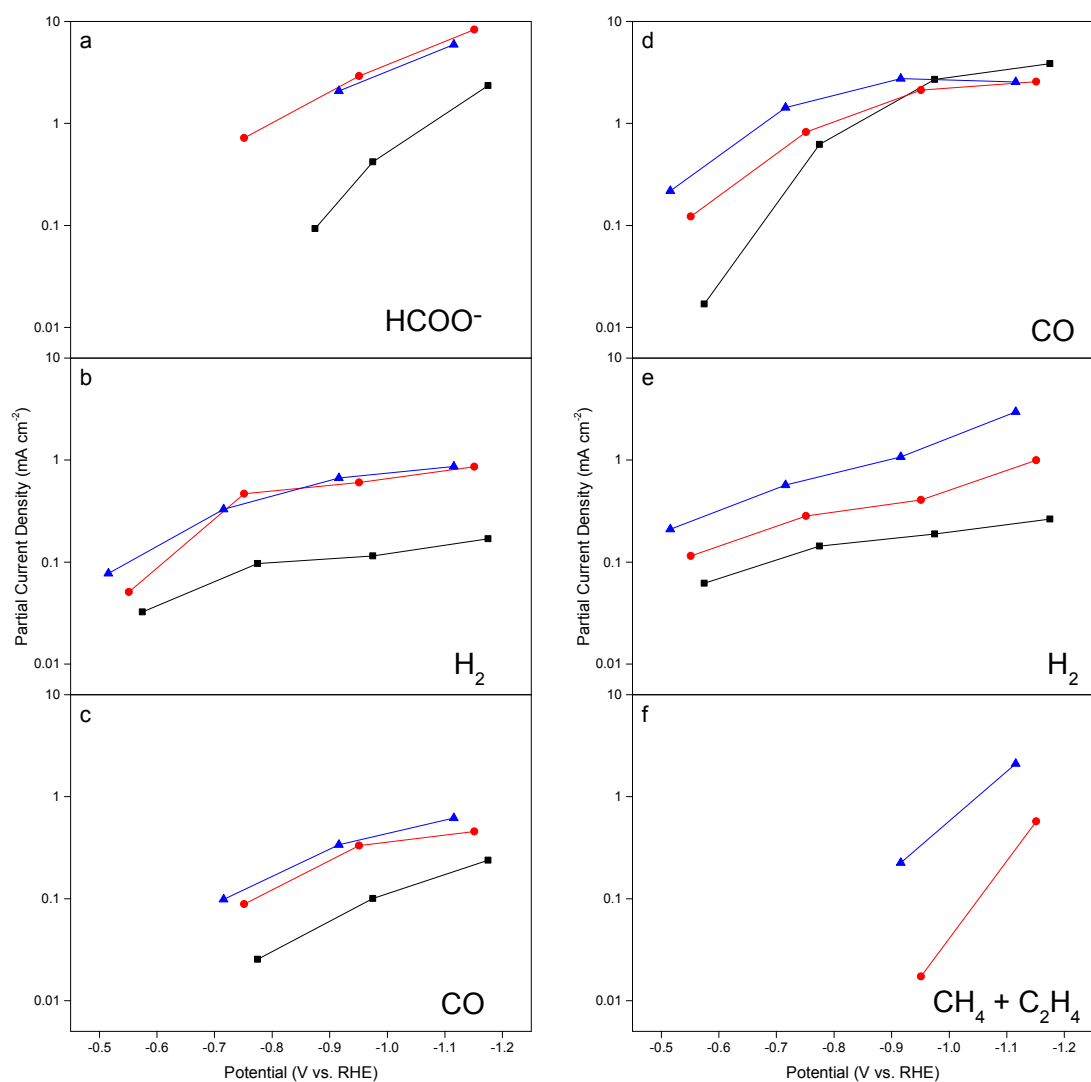


Figure S3.9 Plots of partial current in 0.1 M (black squares), 0.5 M (red circles), and 1.0 M (blue triangles) KHCO₃ electrolyte for various reduction products on a-c) η' bronze and d-f) α bronze. The ionic strength of the electrolyte was kept constant by the addition of KCl.

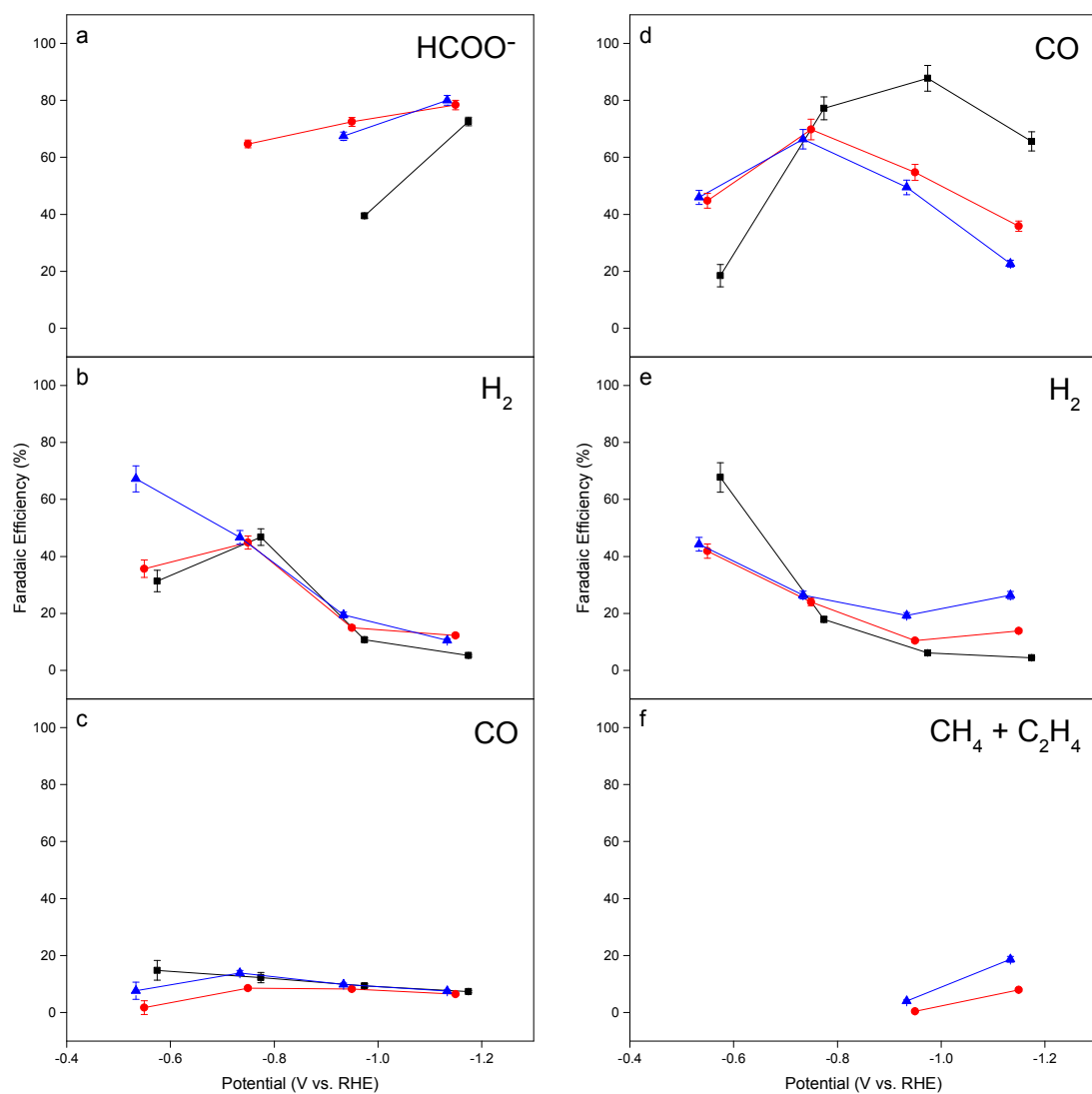


Figure S3.10 Plots of Faradaic efficiency in 0.1 M (black squares), 0.5 M (red circles), and 1.0 M (blue triangles) KHCO_3 electrolyte for various reduction products on a-c) η' bronze and d-f) α bronze. The ionic strength of the electrolyte was kept constant by the addition of KCl .

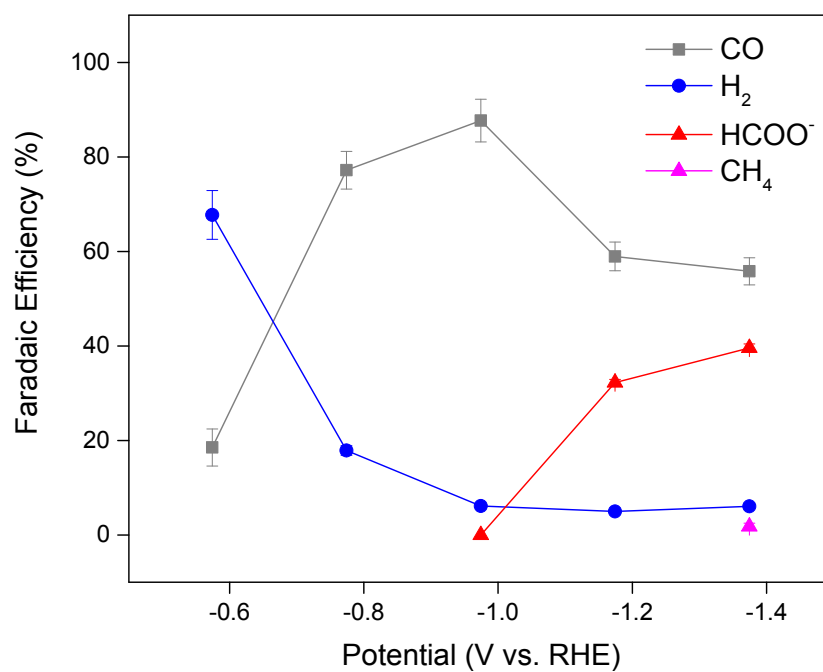


Figure S3.11 Faradaic efficiency profile for α bronze at higher overpotentials in 0.1 M KHCO₃ electrolyte for various reduction products.

Chapter 4

Selectivity Control for Electrochemical CO₂ Reduction by Charge Redistribution on the Surface of Copper Alloys

This Chapter includes work published in the journal article *ACS. Catal.*, 2019, 9, 9411. Chapter 3 explored how the Cu-Sn system exhibits a composition-dependent selectivity trend towards CO and formate products and it was hypothesized that this is governed by the catalyst binding of the first reaction intermediate. Additional work was required to investigate this hypothesis further. Therefore, the aim of this Chapter is to provide a fundamental basis for the behaviour observed.


In this Chapter, a multi-faceted approach combining computation with experiments was used to comprehensively understand the Cu-Sn system. Through controlling the introduction of tin surface sites into the alloy, the selectivity was steered toward CO or formate and an obvious selectivity trend was observed. Using in-situ Raman spectroscopy, it was found that this selectivity shift occurs due to a shift in adsorption preference from the C-bound *COOH intermediate to the O-bound *OCHO intermediate as predicted. Theoretical DFT calculations indicated that this selectivity shift is due to a gradual weakening of *COOH adsorption and strengthening of *OCHO that occurs with increasing Sn content. A combination of theoretical Bader charge analysis and experimental XPS revealed the origin of such transformation: upon

alloying, charge is redistributed from Sn to Cu which creates regions of localized positive charge on the Sn sites. Therefore, with increasing tin content, these localized positive sites hinder nucleophilic attack of the CO₂ carbon, making *COOH adsorption (and the CO pathway) less favorable.

Statement of Authorship

Title of Paper	Selectivity Control for Electrochemical CO ₂ Reduction by Charge Redistribution on the Surface of Copper Alloys
Publication Status	<input checked="" type="checkbox"/> Published <input type="checkbox"/> Accepted for Publication <input type="checkbox"/> Submitted for Publication <input type="checkbox"/> Unpublished and Unsubmitted work written in manuscript style
Publication Details	A. Vasileff, X. Zhi, C.C. Xu, L. Ge, Y. Jiao, Y. Zheng, S.Z. Qiao, Selectivity Control for Electrochemical CO ₂ Reduction by Charge Redistribution on the Surface of Copper Alloys, ACS Catalysis, 2019, 9, 9411-9417


Principal Author


Name of Principal Author (Candidate)	Anthony Vasileff		
Contribution to the Paper	Conducted the majority of experiments, analysed all the data and wrote the majority of the paper		
Overall percentage (%)	68		
Certification:	This paper reports on original research I conducted during the period of my Higher Degree by Research candidature and is not subject to any obligations or contractual agreements with a third party that would constrain its inclusion in this thesis. I am the primary author of this paper.		
Signature		Date	05/02/2020

Co-Author Contributions

By signing the Statement of Authorship, each author certifies that:

- the candidate's stated contribution to the publication is accurate (as detailed above);
- permission is granted for the candidate to include the publication in the thesis; and
- the sum of all co-author contributions is equal to 100% less the candidate's stated contribution.

Name of Co-Author	Xing Zhi		
Contribution to the Paper	6% Conducted DFT computations and wrote related sections of the paper.		
Signature		Date	05/02/2020

Name of Co-Author	Chaochen Xu		
Contribution to the Paper	2% Helped with some of the experiments and provided valuable insight into the paper discussion		
Signature		Date	05/02/2020

Name of Co-Author	Lei Ge		
Contribution to the Paper	5% Conducted all XPS experiments		
Signature		Date	05/02/2020

Name of Co-Author	Yan Jiao		
Contribution to the Paper	3% Provided specialist guidance regarding the DFT computations and helped with the discussion related to the DFT sections.		
Signature		Date	05/02/2020

Name of Co-Author	Yao Zheng		
Contribution to the Paper	8% Provided guidance and supervision from conception through to submission and helped to revise the paper.		
Signature		Date	05/02/2020

Name of Co-Author	Shizhang Qiao		
Contribution to the Paper	8% Provided guidance and supervision from conception through to submission and helped to revise the paper.		
Signature		Date	05/02/2020

4.1 Introduction

The electrochemical reduction of CO₂ is a potential route to a sustainable carbon cycle for industry given that it can couple carbon capture storage with renewable energy to produce fuels and chemical feedstocks. Most notable catalysts developed to date are very selective and active towards C₁ products (e.g. CO and formate).¹⁻³ However, energy dense fuels (C₂ and C₂₊) are better suited for existing infrastructure and provide more complex chemical feedstocks.¹ In this regard, copper is a unique catalyst because it is the only known metal to produce multi-carbon products.⁴⁻⁵ Mechanistically, evidence suggests that copper can adsorb *CO in quasi-equilibrium with free CO and such moderate adsorption of *CO may be the key to driving the CO₂ reduction reaction (CRR) to deeper reduction products.⁶ However, its moderate adsorption of *CO is likely the cause of its poor overall selectivity (towards both C₁ and C₂ products).⁷ To date, some strategies used to engineer the copper surface for selective catalysis appear promising and therefore, copper presents as a good platform for further development.⁸

It is generally accepted that CO and formate are produced by parallel pathways and selectivity for these pathways are determined by the binding configuration of the first stable reaction intermediate (i.e., *OCHO or *COOH).⁹ Specifically, CO₂ adsorbed on a catalyst surface via the carbon atom is prone to further reduction to CO while CO₂ absorbed via the oxygen atom(s) is prone to further reduction to formate.¹⁰ Given that formate is considered a dead-end pathway, while the CO pathway (and the *CO intermediate) forms the early stages of the pathway to multi-carbon products,¹¹ studying the reaction mechanism in the early stages of the CRR pathway is crucial to understanding how to limit the formate pathway and push the reaction to deeper reduction. At present in the literature, little has been done to understand this on real catalyst systems.¹²

The surface electronic properties of an electrocatalyst are inextricably linked to the adsorption behaviour of reaction intermediates on its surface. Consequently, there is a fine interplay between the electronic structure of a material and its reaction activity/selectivity.¹³⁻¹⁴ Alloying copper is a strategy that can alter its electronic structure and Cu-alloy systems have shown significantly different CRR selectivities

compared to Cu itself.⁸ For example, in a recent communication we experimentally demonstrated how the presence of tin surface sites on the copper surface can affect the CRR selectivity toward the first reaction intermediate in the pathway, *i.e.* to the C-bound *COOH intermediate for CO generation or O-bound *OCHO intermediate for formate generation.¹⁵ Therefore, this composition dependent selectivity observed on Cu-Sn alloys provides the perfect system to study the early stages of the CRR. Despite this, computational studies investigating Cu alloys have generally focused on *CO and *H intermediate binding characteristics but ignored the initial reaction intermediates.¹⁶⁻¹⁷ However, in order to comprehensively explain the selectivity trend observed for the Cu-based alloy system, investigation related to key surface properties (e.g. electronic structure) which govern *COOH and *OCHO intermediate selection is required. Insight into the surface electronic properties of these alloys is generally lacking in the literature but is highly needed to fully understand the dependency of composition – intermediate adsorption – selectivity, a crucial concept for the design of selective catalysts.¹⁸⁻¹⁹

In this work, we study the electrochemical reduction of CO₂ on a range of Cu-Sn alloy catalysts as a model to elucidate the relationship between surface electronic properties and the selectivity trend between CO and formate by electrochemical measurements, *in-situ* spectroscopy, and theoretical calculations. We find that as Sn content in the Cu-Sn alloy increases, selectivity is shifted from CO to formate generation. Spectroscopic measurements indicate that this selectivity shift coincides with a shift in intermediate adsorption preference from a C-bound intermediate to an O-bound intermediate. Thermodynamic analysis of the system suggests that this observed selectivity trend with composition occurs due to a gradual weakening of the *COOH intermediate and increased competitiveness of *OCHO and the formate pathway. A possible explanation for this gradual weakening to *COOH adsorption is a redistribution of charge from Sn to Cu sites upon alloying as found by Bader charge analysis and surface sensitive X-ray photoelectron spectroscopy characterization. Therefore, regions of localized positive charge may be present on the catalyst surface which hinders nucleophilic attack of the carbon in CO₂ and therefore makes reaction through a C-bound intermediate less favorable.

4.2 Results and Discussion

The Cu-Sn alloy powders were synthesized from the reduction of copper and tin salts in solution with sodium borohydride. The obtained precipitates were then annealed at high temperature and cooled slowly to form the desired crystal phase (see the experimental details in Section 4.6). X-ray diffraction (XRD) along with Inductively Coupled Plasma Mass Spectroscopy (ICP-MS) were used to determine the crystal phase and composition of each Cu-Sn alloy sample (Figure S4.1, Table S4.1). Surface compositions of the Cu-Sn alloys were also measured using X-ray photoelectron spectroscopy and the data is shown alongside the ICP-MS data in Table S4.1. Both techniques generally gave compositions within 2 % of each other. Therefore, the compositions of the alloys were relatively homogenous. The XRD spectra of the samples showed various intermetallic phases of bronze (Figure S4.1), predominantly with α -phase, δ -phase, ϵ -phase, and η' -phase bronzes. Specifically, Cu_5Sn_6 (naming of each sample herein is based on its composition) and Cu_4Sn_3 were predominantly η' -phase and ϵ -phase bronzes (JCPDS Cards #45-1488, #01-1240), Cu_3Sn_2 was predominantly ϵ -phase and δ -phase bronzes (JCPDS Cards #01-1240, #30-0511), Cu_7Sn_4 was predominantly δ -phase bronze (JCPDS Cards #31-0486), Cu_4Sn was predominantly δ -phase and α -phase bronzes (JCPDS Cards #31-0486, #44-1477), and Cu_{12}Sn was predominantly α -phase bronze (JCPDS Card #44-1477). Scanning electron microscopy (SEM, Figure S4.2) images show that the alloys show a similar micron level morphology and the distribution of Cu and Sn is homogenous throughout the alloys.

To systematically evaluate the electrocatalytic CRR performance of the alloy samples, the Cu-Sn powders were deposited on carbon paper at a loading of approximately 1 mg cm^{-2} . To normalize current responses between samples, mass loadings on each electrode were determined post electrochemical testing by acid leaching in hydrochloric acid and ICP-MS. From Figure 4.1a and Figure S4.3a, a clear trend in CO selectivity and partial current (j_{CO}) on a range of Cu-Sn alloys is observed (error bars for data presented in Figure 4.1a and 1b can be found in Table S4.2). Generally, all samples exhibit a maximum CO Faradaic efficiency (FE) around -0.8 V

vs. RHE while FE for the hydrogen byproduct typically declines with increasing overpotential (Figure S4.4). Interestingly, the tin content in the sample seems to have a direct effect on the gas-phase products (CO and H₂). Specifically, with decreasing tin content, significant enhancement to FE for CO is observed throughout the entire potential range (Figure 4.1a). Over the entire potential range, this resulted in an absolute average increase of 45 % FE between Cu₅Sn₆ and Cu₁₂Sn. It should be noted that despite the significant change to FE, the mechanisms of both CO and formate generation remains similar on all samples as evidenced by their similar Tafel slopes (Figure S4.5).

For liquid product efficiencies (only formate), it is generally observed that onset of significant FE and formate partial current ($j_{\text{HCOO-}}$) occurs around -0.8 V vs. RHE (around the maximum of CO efficiency), as shown in Figure 4.1b and Figure S4.3b. All samples exhibit somewhat similar FE and $j_{\text{HCOO-}}$, which suggests that formate generation is less sensitive to tin content in the Cu-Sn system compared to that of the CO product. Nevertheless, an enhancement of approximately 15 % FE for formate is observed with increasing tin content (Figure 4.1b), suggesting that formate is less favored on low tin alloys.¹⁵ To better visualize the selectivity trend, a linear relationship between formate selectivity (CRR products basis) and sample composition is observed (Figure 4.1c). From this we can clearly see that formate is favored over CO as the tin content in the alloy is increased. After long-term CRR, the Cu-Sn alloy powders were found to be somewhat more aggregated, but the micron-level morphology remained similar to the bulk powders (Figure S4.6). Further, no obvious changes to the crystal structures were observed (Figure S4.7 and Figure S4.8), which suggests that the Cu-Sn phases are stable under CRR conditions and provide the active sites for catalysis. We note that peak shifts in the XRD patterns before and after stability testing may be the result of sample misalignment between tests. Despite this, relative peak positions remain the same.

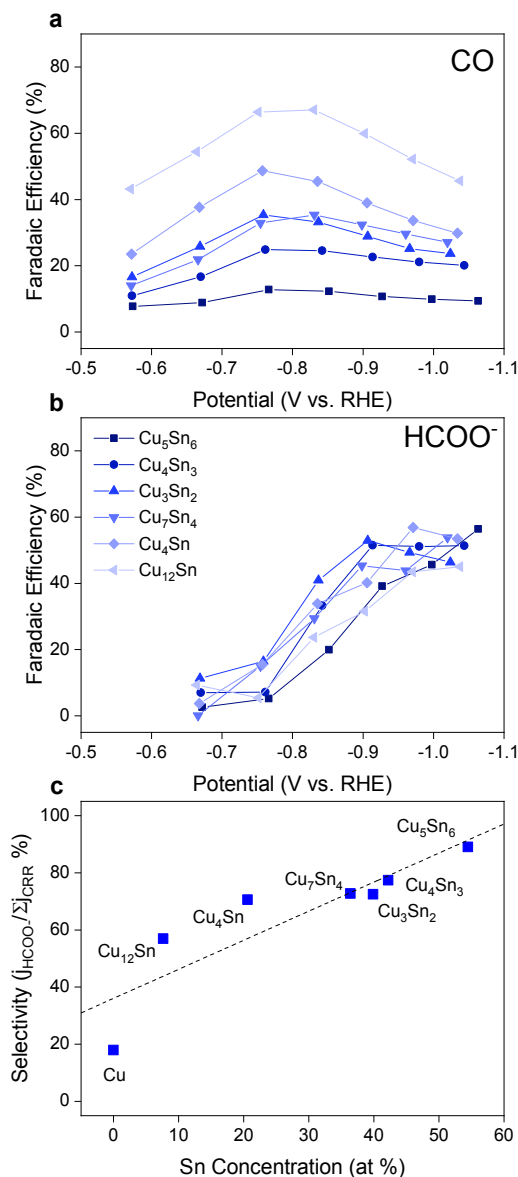


Figure 4.1 Electrochemical performances of various Cu-Sn alloy catalysts in 0.1 M KHCO₃ electrolytes. (a, b) Measured Faradaic efficiency towards CO and formate on various samples, (c) The selectivity towards formate (CRR products basis) vs. the alloy composition at approximately -1.0 V vs. RHE. Error bars in panels (a) and (b) were omitted for clarity but can be found separately in Table S4.2.

In order to better understand the reaction pathway observed for the Cu-Sn system, *in-situ* Raman spectroscopy was carried out using a confocal Raman microscope. The Cu-Sn powders were deposited on screen printed electrodes and studied using a thin electrolyte film (CO_2 saturated 0.1 M KHCO_3) while reduction potentials were applied. As probe samples, Cu_{12}Sn and Cu_5Sn_6 were chosen because they were the most selective samples toward CO and formate (Figure 4.1), respectively. From Figure 4.2a and Figure 4.2d, weak bands arising at 1295 cm^{-1} and 1436 cm^{-1} are observed when the potential applied to Cu_{12}Sn is stepped negatively from open-circuit potential (OCP). Given we observe no such peaks for control experiments with N_2 -saturated electrolyte or at OCP (Figure S4.9), it is likely these bands correspond to the $+\text{C-OH}$ and $+\text{C-O}$ stretching vibrations of $^*\text{COOH}$, which is the precursor to the CO product.²⁰⁻²¹ These bands are also observed for a Cu sample but appear broader and slightly blue shifted (Figure 4.2a), possibly indicating a weaker interaction of the surface with the carbon. Further, this intermediate is confirmed by a shoulder peak appearing around 1635 cm^{-1} with increasing overpotential, which can be attributed to the C=O asymmetric stretch associated with $^*\text{COOH}$ (Figure S4.10).²⁰⁻²¹ For Cu_5Sn_6 , only at more negative potentials (-0.66 V vs. RHE) does a broad band appear in Figure 4.2b at 1390 cm^{-1} . A single band in this region has been ascribed to the symmetric stretch of an $^*\text{OCHO}$ species (a general precursor to formate) adsorbed in a bidentate configuration.²¹⁻²³ Additionally, two other bands are observed for Cu_5Sn_6 which decrease in intensity with overpotential and are likely attributed to adsorbed carbonate (Figure 4.2c).^{20, 24}

These bands are also detected for Cu_{12}Sn (Figure 4.2d), but given the intensity and broadness of these bands, they may also be attributed to tin-carbonate species.²⁵ A sample with moderate tin concentration (Cu_7Sn_4) was also studied using Raman spectroscopy to see whether intermediates could be detected. From Figure S4.11, the sample shows features from both Cu_{12}Sn and Cu_5Sn_6 , with bands related to $^*\text{COOH}$ appearing at 1340 cm^{-1} and 1450 cm^{-1} and broader bands appearing around 1100 cm^{-1} and 1200 cm^{-1} similar to those of Cu_5Sn_6 . Bands related to $^*\text{COOH}$ quickly disappear with overpotential which suggests that the surface coverage of this intermediate drops with increasing overpotential (Figure 4.1a).

From the *in-situ* spectroscopy results combined with the electrochemical measurements, the following reaction scheme is devised. Cu-Sn samples with low tin content favour a pathway to CO via a C-bound *COOH intermediate. However, with increasing overpotential, the *OCHO intermediate becomes competitive with the *COOH intermediate and formate is produced parallel to CO. Affinity for the *COOH intermediate decreases for samples with higher tin content and therefore selectivity to CO decreases while a pathway to formate via *OCHO is preferred.

Density functional theory (DFT) was then employed to elucidate mechanistic details for *COOH and *OCHO intermediate adsorption experimentally observed for the Cu-Sn system. The thermodynamic energetics of the CRR were calculated for Sn-1 and Sn-2 alloys which we assign as models for Cu₁₂Sn and Cu₅Sn₆ experimental samples, respectively (see Computational Methods in Appendix B). Given our spectroscopic observations and the results from electrochemical measurements, the C-bound *COOH intermediate was used as the main intermediate in the CO production pathway, while the O-bound *OCHO intermediate was used in the formate production pathway.²⁶ The free energy diagrams of the CRR to CO and formate on the three Cu-based models are shown in Figure S4.13. From Figure 4.3a, we see that with addition of a Sn site to the Cu surface (Sn-1), *COOH shows weaker adsorption while *OCHO adsorption is not greatly affected. With the addition of another Sn site, there is a significantly stronger *OCHO interaction and further weakening to *COOH adsorption. This was found to manifest in a selectivity trend of free energy difference between *COOH and *OCHO intermediates ($\Delta G_{[*COOH-*OCHO]}$) across the models which agrees well with the experimental selectivity trend observed (Figure 4.3b).

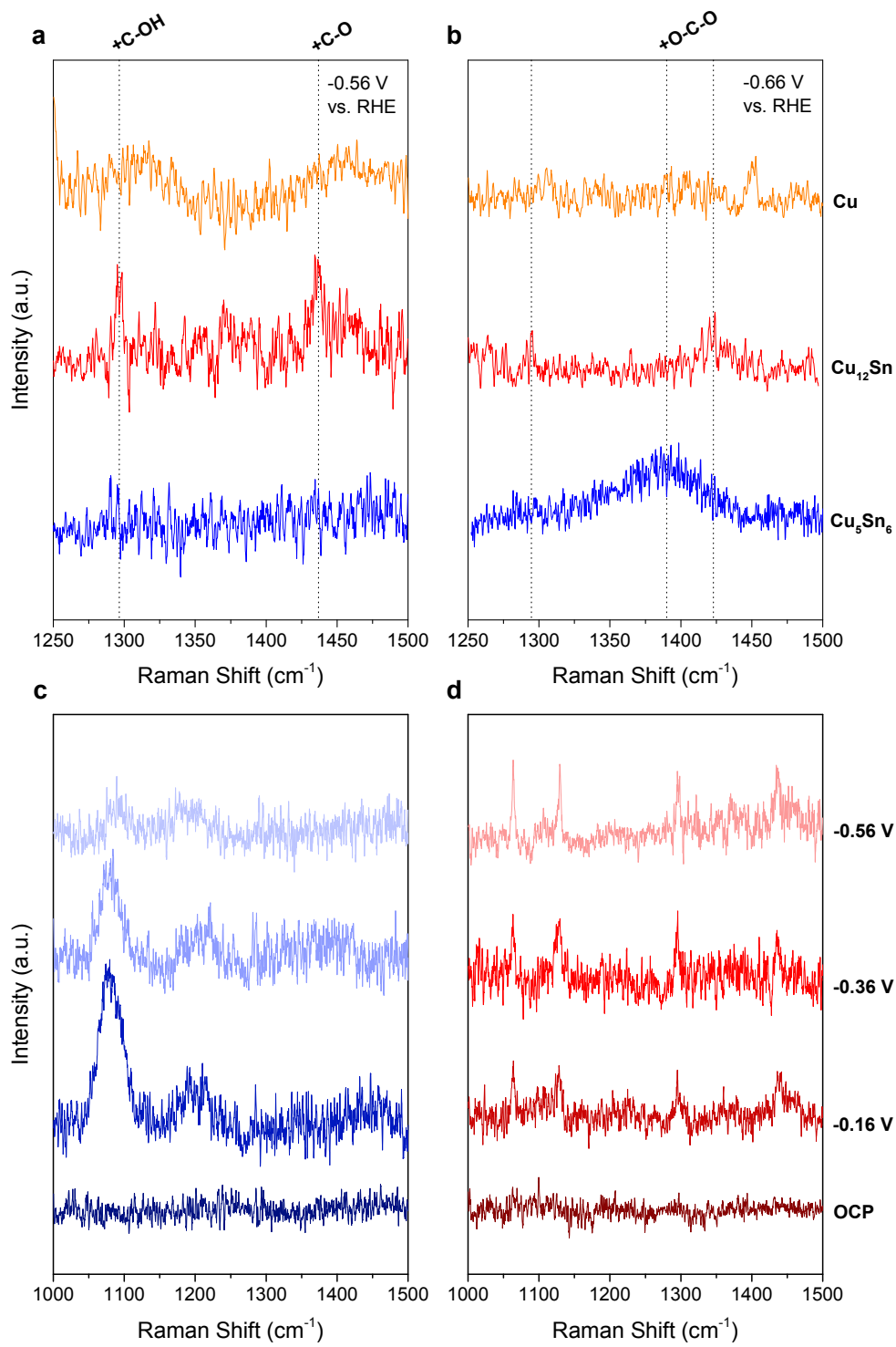


Figure 4.2 *In-situ* Raman spectroscopy study focusing on the carboxyl/formate intermediate vibrational range for a Cu sample (top), Cu_{12}Sn sample (middle), and Cu_5Sn_6 sample (bottom) at (a) -0.4 V vs. RHE and at (b) -0.5 V vs. RHE in CO_2 -saturated 0.1 M KHCO_3 electrolyte. (a) Potential dependent Raman spectra in CO_2 -saturated 0.1 M KHCO_3 electrolyte for (c) Cu_5Sn_6 and (d) Cu_{12}Sn .

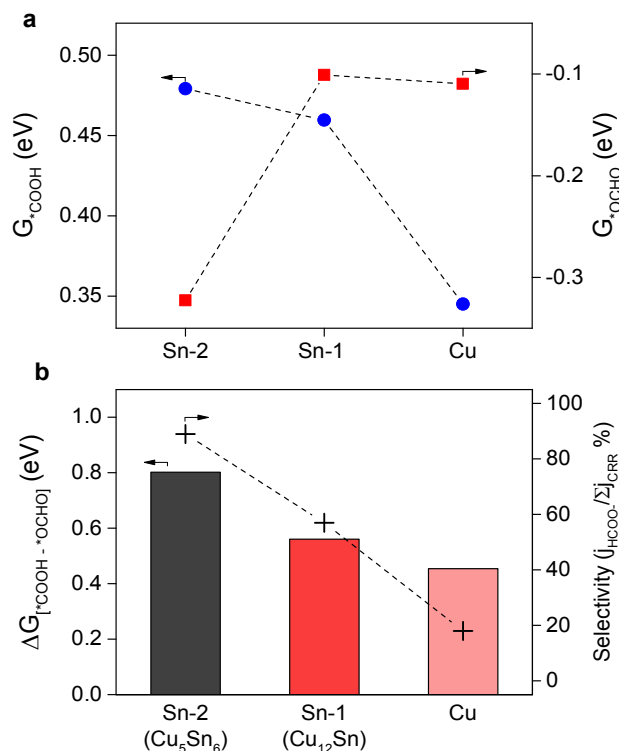


Figure 4.3 Thermodynamic analysis of the Cu-Sn system to elucidate formate pathway selectivity. (a) The free energy of $*COOH$ and $*OCHO$ intermediates on Cu, Sn-1, and Sn-2 extracted from the free energy pathways. (b) The free energy difference between $*COOH$ and $*OCHO$ intermediates on Cu, Sn-1, and Sn-2 with the experimental selectivity towards formate for the representative samples shown in brackets.

Density of states (DOS) analysis was performed on the three catalyst models to reveal the origin of this transformation to intermediate adsorption behaviour. From this, a better view on electronic structure and composition dependent selectivity could be devised for the system. As shown in Figure 4.4a, the d-orbital DOS position shifted negatively from the Fermi level (E_F) with increasing Sn concentration. The d-band centre of Cu, Sn-1, and Sn-2 was plotted against the free energy of $*COOH$, resulting in a linear trend (Figure 4.4b). A weaker $*COOH$ adsorption was related to a lower DOS position, indicating decreasing competition of $*COOH$ adsorption with higher Sn content, agreeing with Figure 4.3a. Furthermore, the variation of $*COOH$ adsorption strength was analysed to indicate the trend of CO selectivity. An experimental volcano relation is observed in Figure 4.4c by plotting CO partial current at -0.76 V vs. RHE

against the Sn content in the alloys. Clearly, Cu_{12}Sn appeared near the volcano top, suggesting its favourability for CO production, while alloys with more tin concentration and pure copper all showed lesser preference for CO. When using the free energy of $^*\text{COOH}$ as a descriptor for CO generation, a similar volcano plot was constructed treating Sn-1 and Sn-2 as models for Cu_{12}Sn and Cu_5Sn_6 , respectively (Figure 4.4d). With Cu on the strong binding leg, Sn-1 at the volcano peak and Sn-2 on the weak binding leg, the plots match well between experiments and theoretical calculations. Therefore, the addition of tin surface sites appears to gradually shift the d-band centre negatively from the Fermi level which causes a gradual weakening to $^*\text{COOH}$ adsorption.

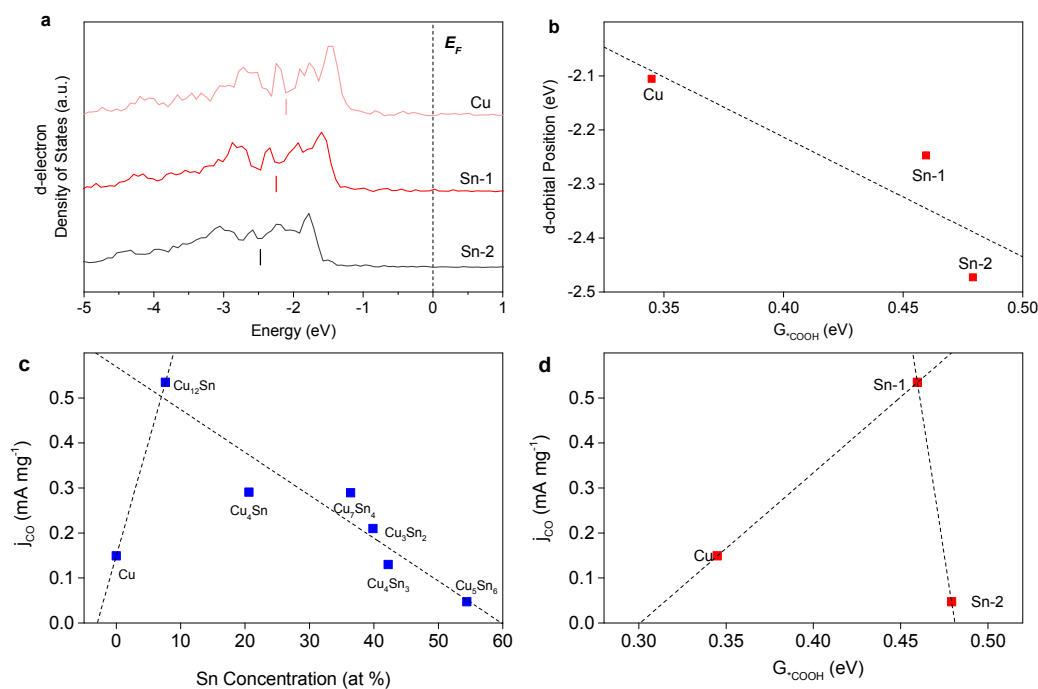


Figure 4.4 Electronic structure analysis of Cu-Sn models for CO generation behaviour across the system. (a) d-electron Density of States (DOS) of Cu, Sn-1, and Sn-2 models. Dashed line indicates the Fermi level and the vertical labels indicate the d-band centre position. (b) Plot of the d-band centre position for Cu, Sn-1, and Sn-2 against the binding strength of the $^*\text{COOH}$ intermediate. (c) Experimental volcano plot relating the alloy composition to the CO partial current at -0.76 V vs. RHE. (d) Volcano plot using the computed free energy of $^*\text{COOH}$ as a descriptor for CO partial current at -0.76 V vs. RHE

Bader charge analysis was conducted to study the charge distribution on the Cu-Sn surface to reveal electronic effects that may be responsible for the observed selectivity trend. It was found that the Sn donates charge to the Cu and is positively charged in the Cu-Sn alloys (Figure S4.14). This result is also consistent with a recent *in-situ* XAS study which found that Sn in a CuSn₃ alloy exists in a Sn^{δ+} state under reduction potentials.²⁷ Here we analyzed the chemical states of the Cu and Sn in the Cu-Sn alloys *ex situ* using X-ray Photoelectron Spectroscopy (XPS). High resolution Cu 2p spectra can be found in Figure S4.15. It should also be noted that electrochemically reduced Cu-based catalysts re-oxidize rapidly in air, which compromises the accuracy of *ex-situ* methods for determining the real active sites. Therefore, the samples were etched 20 nm with Ar plasma *in-situ* which appeared to significantly reduce the surface oxides present (Figure S4.16). In the Cu 2p region (Figure 4.5a), the characteristic Cu 2p_{3/2} peak around 932.4 eV is observed for the Cu sample which suggests predominantly zero valent Cu states present.²⁸ However, a negative shift in the Cu 2p_{3/2} peak is observed with increasing tin content which indicates some charge redistribution to the Cu.²⁹ In contrast, from the Sn 3d spectra (Figure S4.17), the characteristic Sn 3d_{5/2} peak appears to shift positively with increasing Cu content. This suggests that upon alloying Cu and Sn some charge is redistributed from the Sn to Cu sites.³⁰ We find that this is in agreement with the Bader charge analysis and we link a lower Cu 2p_{3/2} peak position to increased negative charge on the Cu sites (Figure 4.5b), leading to a positive charge on the Sn sites. This likely has significant impact to intermediate adsorption behaviour and reaction selectivity because when CO₂ is polarized, its lowest unoccupied molecular orbital (LUMO) is highly localized on the carbon, making it susceptible to nucleophiles.³¹ However, having regions of localized positive charge on the catalyst surface may hinder nucleophilic attack on the carbon and increase the thermodynamic barrier to *COOH adsorption. As a result, a pathway through the *OCHO intermediate is likely preferred over the *COOH intermediate, rendering CO formation less favourable for alloys with increased Sn content (Figure 4.5c).

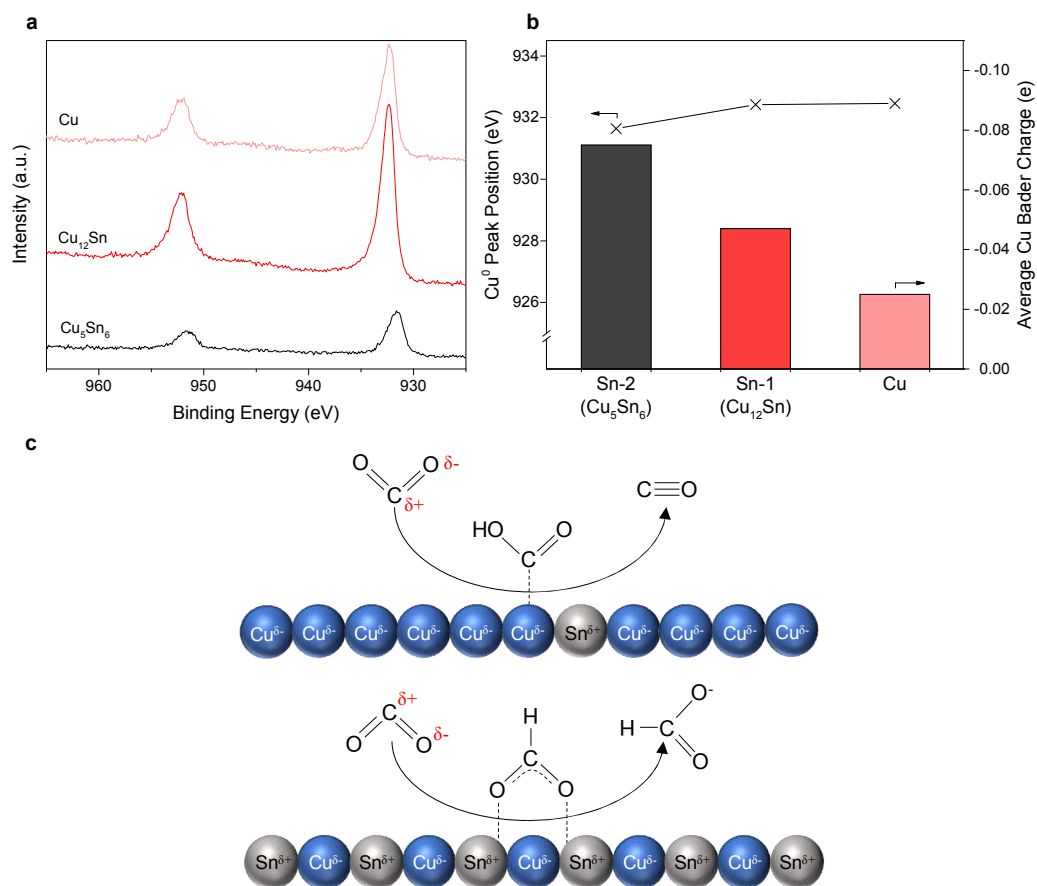


Figure 4.5 Analysis of charge redistribution in the alloys to elucidate the dependency of composition – intermediate adsorption – selectivity. (a) High resolution Cu 2p spectra for the Cu-Sn alloys and Cu etched 20 nm *in-situ*. (b) Average Bader charge and the Cu 2p_{3/2} peak position for the Cu, Sn-1, and Sn-2 model catalysts. (c) Proposed CRR pathway for the Cu-Sn alloy system due to the presence of localized positive charge on the Sn sites.

4.3 Conclusions

In summary, we have presented a range of Cu-Sn alloys as CRR electrocatalysts and studied the selectivity trend that exists between CO and formate from experimental electrochemistry, *in-situ* spectroscopy, and DFT calculations. We found that Cu-Sn alloys with low tin content favour a pathway to CO via a C-bound $\ast\text{COOH}$ intermediate. With increasing Sn content, affinity for the $\ast\text{COOH}$ intermediate decreases therefore selectivity to CO decreases while a pathway to formate via $\ast\text{OCHO}$ is preferred. DFT calculations suggest that alloying Sn with Cu leads to gradually weaker adsorption of $\ast\text{COOH}$ while $\ast\text{OCHO}$ is adsorbed more strongly. This ultimately leads to increased competitiveness by the formate pathway over the CO pathway as the Sn content in the alloy catalysts increases. Charge transfer from the Sn to Cu sites in the alloys may create regions of localized positive charge which hinder formation of the C-bound intermediate and thus results in decreased selectivity towards the CO pathway. The results demonstrate how alloying can modify local electronic environments in order to tune the binding of targeted reaction intermediates for selective electrocatalysis.

4.4 Acknowledgement

The authors gratefully acknowledge financial support from the Australian Research Council (ARC) through Discovery Project and Linkage project programs (FL170100154, DP160104866, DP170104464, DE160101163 and LP160100927) and the Australian Government through Research Training Program Scholarships. The authors also thank Mr. Philip Clements from the School of Chemistry, University of Adelaide for conducting NMR spectroscopy and Dr. Sarah Gilbert and Mr. Ken Neubauer from Adelaide Microscopy for conducting ICP-MS and SEM sample coating.

4.5 References

1. Bushuyev, O. S.; De Luna, P.; Dinh, C. T.; Tao, L.; Saur, G.; van de Lagemaat, J.; Kelley, S. O.; Sargent, E. H., *Joule* 2018, *2*, 825-832.
2. Verma, S.; Hamasaki, Y.; Kim, C.; Huang, W. X.; Lu, S.; Jhong, H. R. M.; Gewirth, A. A.; Fujigaya, T.; Nakashima, N.; Kenis, P. J. A., *ACS Energy Lett.* 2018, *3*, 193-198.
3. Lu, Q.; Rosen, J.; Zhou, Y.; Hutchings, G. S.; Kimmel, Y. C.; Chen, J. G.; Jiao, F., *Nat. Commun.* 2014, *5*, 3242.
4. Kuhl, K. P.; Cave, E. R.; Abram, D. N.; Jaramillo, T. F., *Energy Environ. Sci.* 2012, *5*, 7050-7059.
5. Jiao, Y.; Zheng, Y.; Chen, P.; Jaroniec, M.; Qiao, S.-Z., *J. Amer. Chem. Soc.* 2017, *139*, 18093-18100.
6. Wuttig, A.; Liu, C.; Peng, Q.; Yaguchi, M.; Hendon, C. H.; Motobayashi, K.; Ye, S.; Osawa, M.; Surendranath, Y., *ACS Cent. Sci.* 2016, *2*, 522-528.
7. Peterson, A. A.; Nørskov, J. K., *J. Phys. Chem. Lett.* 2012, *3*, 251-258.
8. Vasileff, A.; Xu, C.; Jiao, Y.; Zheng, Y.; Qiao, S.-Z., *Chem* 2018, *4*, 1809-1831.
9. Feaster, J. T.; Shi, C.; Cave, E. R.; Hatsukade, T.; Abram, D. N.; Kuhl, K. P.; Hahn, C.; Nørskov, J. K.; Jaramillo, T. F., *ACS Catal.* 2017, *7*, 4822-4827.
10. Kortlever, R.; Shen, J.; Schouten, K. J. P.; Calle-Vallejo, F.; Koper, M. T. M., *J. Phys. Chem. Lett.* 2015, *6*, 4073-4082.
11. Zheng, Y.; Vasileff, A.; Zhou, X.; Jiao, Y.; Jaroniec, M.; Qiao, S.-Z., *J. Amer. Chem. Soc.* 2019, *141*, 7646-7659.
12. Cheng, T.; Xiao, H.; Goddard, W. A., *J. Amer. Chem. Soc.* 2016, *138*, 13802-13805.
13. Jiao, Y.; Zheng, Y.; Jaroniec, M.; Qiao, S.-Z., *Chem. Soc. Rev.* 2015, *44*, 2060-2086.
14. Jin, H.; Guo, C.; Liu, X.; Liu, J.; Vasileff, A.; Jiao, Y.; Zheng, Y.; Qiao, S.-Z., *Chem. Rev.* 2018, *118*, 6337-6408.
15. Vasileff, A.; Xu, C.; Ge, L.; Zheng, Y.; Qiao, S.-Z., *Chem. Comm.* 2018, *54*, 13965-13968.

16. Sarfraz, S.; Garcia-Esparza, A. T.; Jedidi, A.; Cavallo, L.; Takanabe, K., *ACS Catal.* 2016, *6*, 2842-2851.
17. Schreier, M.; Heroguel, F.; Steier, L.; Ahmad, S.; Luterbacher, J. S.; Mayer, M. T.; Luo, J. S.; Gratzel, M., *Nat. Energy* 2017, *2*, 17087.
18. Ko, J.; Kim, B. K.; Han, J. W., *J. Phys. Chem. C* 2016, *120*, 3438-3447.
19. Zheng, Y.; Jiao, Y.; Qiao, S.-Z., *Adv. Mater.* 2015, *27*, 5372-5378.
20. Socrates, G., *Infrared and Raman Characteristic Group Frequencies: Tables and Charts*. 3rd ed.; John Wiley and Sons: Middlesex, 2001.
21. Firet, N. J.; Smith, W. A., *ACS Catal.* 2017, *7*, 606-612.
22. Bohra, D.; Ledezma-Yanez, I.; Li, G.; de Jong, W.; Pidko, E. A.; Smith, W. A., *Angew. Chem. Int. Ed.* 2019, *58*, 1345-1349.
23. Bando, K. K.; Sayama, K.; Kusama, H.; Okabe, K.; Arakawa, H., *Appl. Catal. A* 1997, *165*, 391-409.
24. Smith, B. D.; Irish, D. E.; Kedzierzawski, P.; Augustynski, J., *J. Electrochem. Soc.* 1997, *144*, 4288-4296.
25. Baruch, M. F.; Pander, J. E.; White, J. L.; Bocarsly, A. B., *ACS Catal.* 2015, *5*, 3148-3156.
26. Feaster, J. T.; Shi, C.; Cave, E. R.; Hatsukade, T. T.; Abram, D. N.; Kuhl, K. P.; Hahn, C.; Norskov, J. K.; Jaramillo, T. F., *ACS Catal.* 2017, *7*, 4822-4827.
27. Zheng, X.; Ji, Y.; Tang, J.; Wang, J.; Liu, B.; Steinrück, H.-G.; Lim, K.; Li, Y.; Toney, M. F.; Chan, K.; Cui, Y., *Nat. Catal.* 2019, *2*, 55-61.
28. Biesinger, M. C.; Lau, L. W. M.; Gerson, A. R.; Smart, R. S. C., *App. Surf. Sci.* 2010, *257*, 887-898.
29. Kuhn, M.; Sham, T. K., *Phys. Rev. B* 1994, *49*, 1647-1661.
30. Wang, D.; Miller Alfred, C.; Notis Michael, R., *Surf. Interface Anal.* 1998, *24*, 127-132.
31. Appel, A. M.; Bercaw, J. E.; Bocarsly, A. B.; Dobbek, H.; DuBois, D. L.; Dupuis, M.; Ferry, J. G.; Fujita, E.; Hille, R.; Kenis, P. J. A.; Kerfeld, C. A.; Morris, R. H.; Peden, C. H. F.; Portis, A. R.; Ragsdale, S. W.; Rauchfuss, T. B.; Reek, J. N. H.; Seefeldt, L. C.; Thauer, R. K.; Waldrop, G. L., *Chem. Rev.* 2013, *113*, 6621-6658.

Chapter 4

Supporting Information

4.6 Experimental Section

4.6.1 Materials

All chemicals (analytical reagent grade) used in this work, including copper (II) chloride dihydrate ($\text{CuCl}_2 \cdot 2\text{H}_2\text{O}$), tin (IV) chloride pentahydrate ($\text{SnCl}_4 \cdot 5\text{H}_2\text{O}$), sodium borohydride (NaBH_4), potassium bicarbonate (KHCO_3), denatured ethanol, concentrated hydrochloric acid (HCl 36 %), and concentrated nitric acid (HNO_3 70 %), were purchased from Sigma-Aldrich and used without further purification. Carbon paper (CP, AvCarb MGL 190, Product Code: 1594008) was bought from FuelCellStore. Ultra-pure water ($18.2 \text{ M}\Omega \cdot \text{cm}$, PURELAB Option-Q) was used in all experiments. Scientific grade (HiQ) 5 % H_2/Ar was purchased from BOC. Ultra-high purity N_2 (99.999 %) and laser grade CO_2 (99.995 %) were purchased from BOC and used in all electrochemical experiments.

4.6.2 Synthesis of Electrocatalysts

Preparation of Cu-Sn Alloy Powders:

To synthesize the Cu-Sn alloy powders, the chloride salts of copper and tin were reduced in the presence of NaBH_4 . Generally, various ratios of $\text{CuCl}_2 \cdot 2\text{H}_2\text{O}$ and $\text{SnCl}_4 \cdot 5\text{H}_2\text{O}$ were dissolved in 30 ml of water and added to a 250 ml three neck flask fitted with a septum stopper. The flask was then stirred with a magnetic stirrer bar and purged with nitrogen for 30 min. Excess NaBH_4 was dissolved in 5 ml of water and sonicated for a minute to dissolve it fully. The NaBH_4 solution was then drawn into a syringe and

added dropwise to the flask under continued nitrogen flow and stirring. Once all the NaBH_4 solution was added to the flask, the reaction mixture was left to react for 30 min. The precipitate was then collected and washed in water three times and then in ethanol three times by centrifugation (8500 rpm, 5 min). The washed precipitate was dried in a vacuum oven at 60°C for 12 h. To obtain the alloy powders, the dried precipitate was then transferred to a silica boat and annealed at 400°C (heating rate of 5°C min^{-1}) for 5 h under a flow of 5 % H_2/Ar (30 ml min^{-1}). The alloy powders were then cooled slowly under continued gas flow at $0.5^\circ\text{C min}^{-1}$ to limit phase transformation. The powders were then ground using an agate mortar and pestle and used for electrode fabrication and characterization.

Preparation of Cu Powders:

The method used to prepare the Cu powder is the same as that outlined for the alloy powder. The only difference is that no $\text{SnCl}_4 \cdot 5\text{H}_2\text{O}$ was used.

Electrode Preparation:

Carbon paper (1 x 1 cm) was treated in concentrated HNO_3 for 24 h. The treated carbon paper was then rinsed in water, washed three times by sonication (10 min), and dried in an oven at 60°C . To prepare the Cu-Sn/CP electrodes, each alloy/metal powder was added to anhydrous ethanol at a concentration of 20 mg ml^{-1} and sonicated for 1 h to form a homogenous suspension. $50 \text{ }\mu\text{l}$ of catalyst suspension (loading of 1 mg cm^{-2}) was then drop cast on each side of a dry piece of carbon paper and dried in a vacuum oven for 12 h at 60°C .

4.6.3 Material Characterization

The chemical composition of the alloy powders and electrode mass loadings were determined by inductively coupled plasma mass spectroscopy (ICP-MS, Agilent 7900x). For ICP-MS, the electrodes were first leached into 10 ml of 3 M HCl solution for 3 days. These samples were then diluted 200:1 with 1 M HCl solution and filtered through $0.22 \text{ }\mu\text{m}$ filters (Millipore) before testing. The crystal structure and chemical structure of the samples were characterized by powder X-ray diffraction spectroscopy (XRD, Cu-

target Bruker D8 Advance), and X-ray photoelectron spectroscopy (Kratos Axis Ultra, mono Al K α 1486.6eV). XPS samples were etched 20 nm *in-situ* under an Ar plasma to remove surface oxides. XPS spectra were calibrated to the carbon C-C peak using 284.5 eV.

4.6.4 Electrochemical Measurements

Electrochemical Measurements:

Electrochemical measurements were performed on a 760E potentiostat (CH Instruments, USA) using a gas tight three-electrode H-cell with anode and cathode compartments separated by a proton exchange membrane (Nafion 117). The Cu-Sn/CP electrodes were used directly as the working electrodes. Ag/AgCl electrode (4.0 M KCl) and RuO₂ coated titanium mesh electrode were used as the reference and counter electrodes, respectively. All electrochemical measurements were conducted in 0.1 M KHCO₃ electrolyte. In a typical electrochemical test, cyclic voltammetry (CV) and linear scan voltammetry (LSV) were first conducted in N₂-saturated electrolyte. The catholyte was stirred and bubbled with N₂ for 10 min at 100 ml min⁻¹ to remove air and saturate the electrolyte. Following this, 50 CV scans at 100 mV s⁻¹ between -1.0 and -1.4 V vs. Ag/AgCl were recorded (with stirring and N₂ bubbling, 10 ml min⁻¹) until a stable current response was obtained. An LSV scan was then obtained at a scan rate of 5 mV s⁻¹ (with stirring and N₂ bubbling, 10 ml min⁻¹) within a potential range of -1.0 and -1.8 V vs. Ag/AgCl. CV and LSV scans were subsequently conducted in CO₂ saturated electrolyte (pH = 6.8) in the same manner. For chronoamperometric responses, the catholyte was continuously stirred and bubbled with CO₂ at a rate of 10 ml min⁻¹. Chronoamperometry was performed for 1 h at potentials between -1.2 and -1.8 V vs. Ag/AgCl in 100 mV intervals.

All electrochemical measurements were iR compensated and all potentials discussed in the results were given against the reversible hydrogen electrode (RHE). The conversion of reference potentials from Ag/AgCl to RHE was calculated using the following equation:

$$E_{RHE} = E_{Ag/AgCl} + 0.224 + 0.059pH$$

For calculation of the Faradaic efficiencies towards gas-phase products (FE_g), ideal gas conditions were assumed, and the following equation was applied:

$$FE_g = \alpha \frac{PC_g \dot{V}}{RT} \cdot \frac{N_e F}{I}$$

where α is a conversion factor, P is the pressure, C_g is the concentration of the gas phase component, \dot{V} is the CO_2 flow rate, R is the gas constant, T is the temperature, N_e is the number of electrons transferred per mole product, F is the Faraday constant, and I is the instantaneous current. For liquid phase components, the Faradaic efficiency (FE_l) was calculated as follows:

$$FE_l = \beta C_l V \cdot \frac{N_e F}{Q}$$

where β is a conversion factor, C_l is the concentration of the liquid phase component, V is the total liquid volume, and Q is the total charge passed.

Product Analysis:

Gas products were sampled after 20 min while liquid products were sampled after the full hour of chronoamperometry. The cell head space was vented directly to the sampling loop of a gas chromatograph (GC, 7890B, Agilent, USA). The GC was fitted with Plot-Q and a 5Å sieve columns (Agilent) in series, TCD and methanizer/FID detectors, and UHP Ar as the carrier gas. The detection limit for CO by FID was approximately 1 ppm while the detection limit for H_2 by TCD was closer to 10 ppm. The FID and TCD detectors showed good linearity over a wide concentration range toward CO and H_2 , respectively, and calibration charts for both are shown below in Figure S4.18.

The catholyte samples were collected and analyzed using ^1H nuclear magnetic resonance spectroscopy (NMR, A500a DD2 500 MHz, Agilent, USA) as outlined in Kuhl (2012).¹ Formate present in samples was quantified from a calibration curve using known standards of potassium formate and an internal phenol standard. The formate calibration curve is shown in Figure S4.18. Samples were prepared for NMR immediately after collection and kept refrigerated at 4 °C until ready for testing.

4.7 *In-Situ* Raman Spectroscopy

4.7.1 Sample Preparation

The same alloy suspensions used for electrochemical performance measurements were also used for Raman spectroscopy. Screen-printed electrodes (Pine Research Instrumentation, RRPE1002C) were employed for the *in-situ* tests. These screen-printed electrodes use a 4 x 5 mm carbon working electrode (WE), Ag/AgCl reference electrode, and carbon counter electrode. The carbon WE would typically exhibit D and G bands in the 1200-1600 cm^{-1} range which would interfere with CRR relevant bands.² Given this, a 4 x 5 mm piece of smooth copper foil (0.025 mm, Sigma Aldrich) was adhered on the WE surface using conductive glue. The bare foils did not show any observable bands under CRR conditions (Figure S4.12). To prepare samples for *in-situ* tests, 20 μl of alloy suspension was deposited on the WE and dried in a vacuum oven at 60°C.

4.7.2 Raman Measurements

In-situ Raman spectroscopy was performed using a confocal Raman microscope (Horiba LabRAM HR Evolution) with a 50X (0.5 N.A) long working distance objective (Olympus). The screen-printed electrode was connected to a 760E potentiostat (CH Instruments, USA) and then laid flat and clipped to a microscope slide. 100 μl of CO_2 -saturated 0.1 M KHCO_3 was pipetted on the working end of the electrode and a No. 1 thickness cover glass was placed on top. A He-Ne laser (633 nm, CVI Melles Griot) and an 1800 gr cm^{-1} grating was used in all experiments. For a typical measurement, 40 CV cycles between -1.0 and -1.4 V vs. Ag/AgCl were first performed to obtain a stable current response. The electrolyte was then changed, and Raman spectra were collected at OCP and during chronoamperometry at various potentials. Fresh electrolyte was applied after each measurement to ensure a CO_2 saturated environment was maintained and to minimize interference from bubbles generated on the WE. For analysis, Raman spectra were baseline corrected.

All potentials discussed in the results were given against the reversible hydrogen electrode (RHE). Conversion of the reference potential from the screen-printed electrode (Ag/AgCl) to RHE was calibrated against an external Ag/AgCl electrode and calculated using the following equation:

$$E_{RHE} = E_{Ag/AgCl} + 0.442 + 0.059pH$$

4.8 Theoretical Calculations

All calculations were performed using density functional theory (DFT). The Perdew-Burke-Ernzerhof (PBE) functional was employed for electron exchange-correlation within the generalized gradient approximation (GGA), as implemented in the VASP code. The ionic cores were described by the projector-augmented wave (PAW) method. The cut-off energy for plane wave expansion was set to be 550 eV. During geometry optimization, the structures were relaxed to forces on the atoms smaller than 0.01 eV Å⁻¹. A 0.18 eV width of the smearing and (3 × 3 × 1) Gamma k-point grid were applied. The Tkatchenko-Scheffler method was adopted in all calculations to address van der Waals (vdW) interactions between atoms.

The Cu (111) surface was modeled with a four-layered slab of a (3 × 3) supercell with 15 Å of vacuum space. The Cu-Sn alloy models with different atom ratios were built by substituting one or two Cu atom(s) in the top layer with Sn atom(s), respectively. Cu-Sn models were denoted as Sn-1 and Sn-2. These models provide some reasonable insights into local reaction environments, suggesting consequent impact on reactivity and selectivity of Cu-Sn alloys with increasing Sn concentrations. Adsorption of reaction intermediates on the (111) facets of Cu, Sn-1 and Sn-2 were calculated with the bottom three layers fixed and the top layer allowed to relax freely. The computational hydrogen electrode model was employed for free energies calculations.³ The solvation effects were included for *COOH (0.25 eV), *OCHO (0.10 eV), and *CO (0.10 eV) according to previous studies.⁴⁻⁵

4.9 Supplementary Figures and Tables

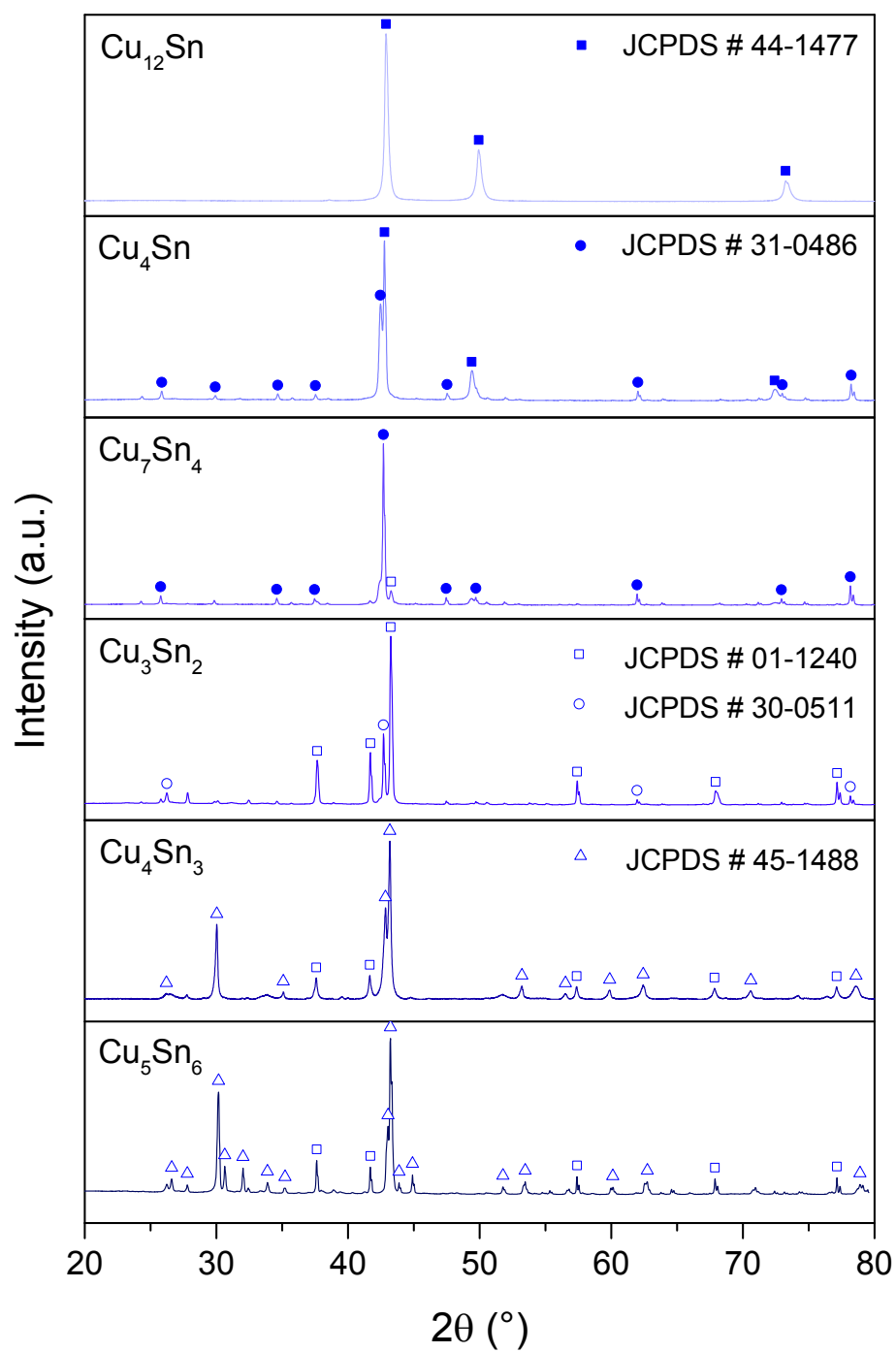


Figure S4.1 XRD patterns of the various Cu-Sn alloy samples with standard patterns for reference.

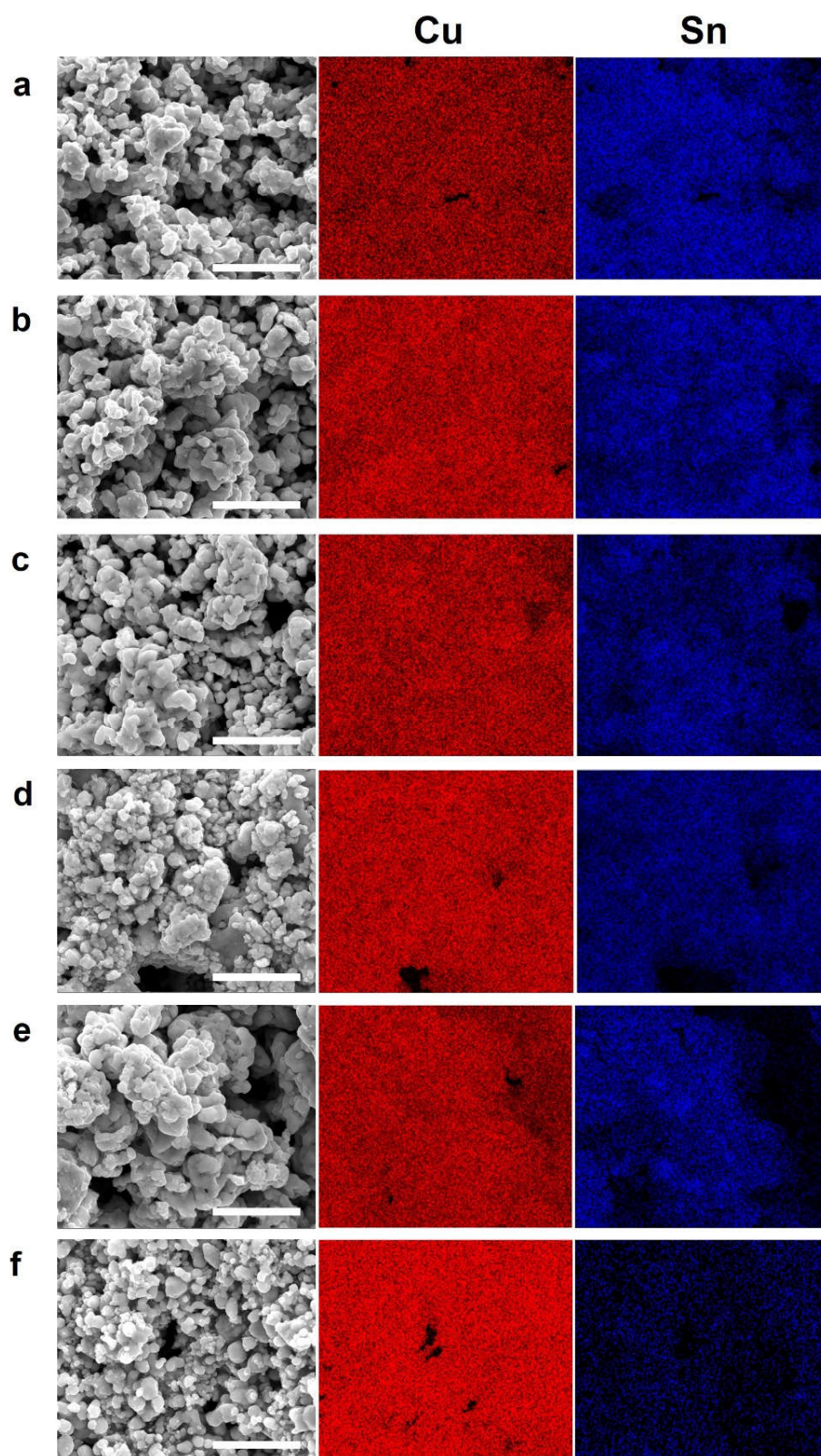


Figure S4.2 SEM images and elemental distribution of Cu and Sn in the bulk powders for (a) Cu_5Sn_6 , (b) Cu_4Sn_3 , (c) Cu_3Sn_2 , (d) Cu_7Sn_4 , (e) Cu_4Sn , and (f) Cu_{12}Sn . Scale bar is 5 μm .

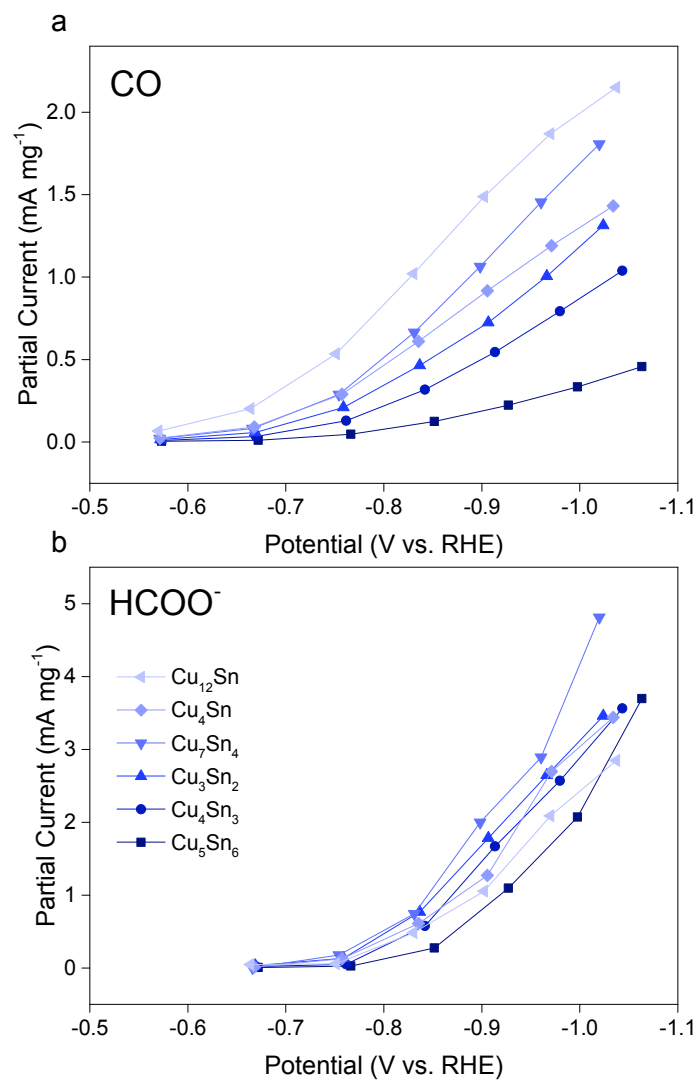


Figure S4.3 Partial current plots toward (a) CO and (b) formate over the potential range tested in CO₂-saturated 0.1 M KHCO₃ electrolyte.

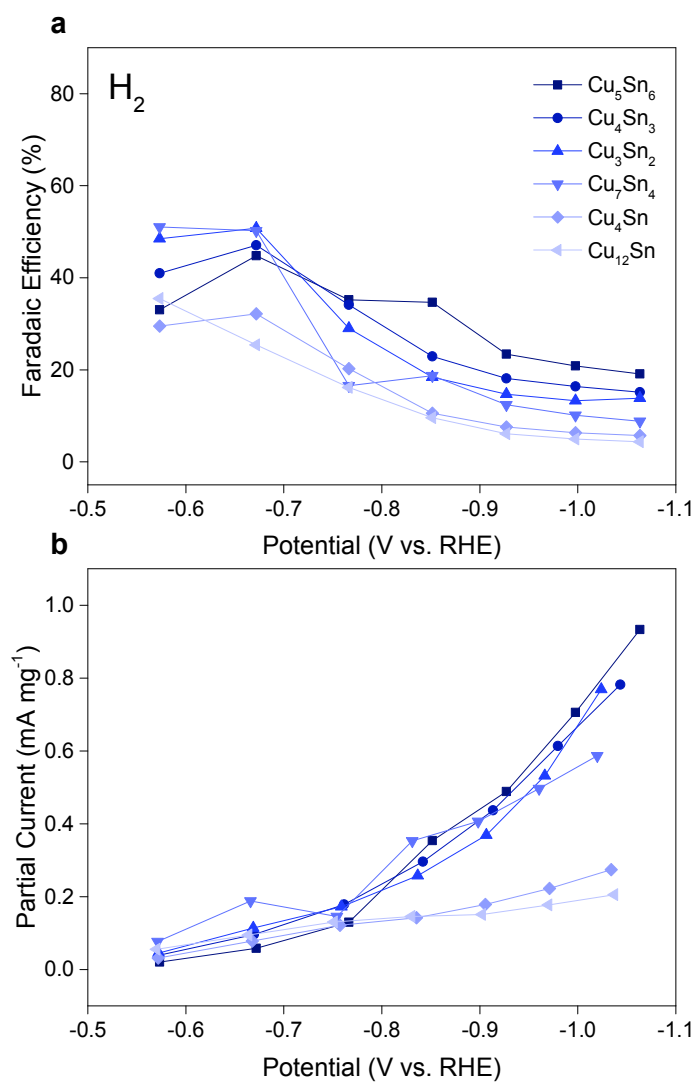


Figure S4.4 Electrochemical HER performance of the various Cu-Sn alloys in CO_2 -saturated 0.1 M $KHCO_3$ electrolyte measured as (a) Faradaic efficiency and (b) partial current.

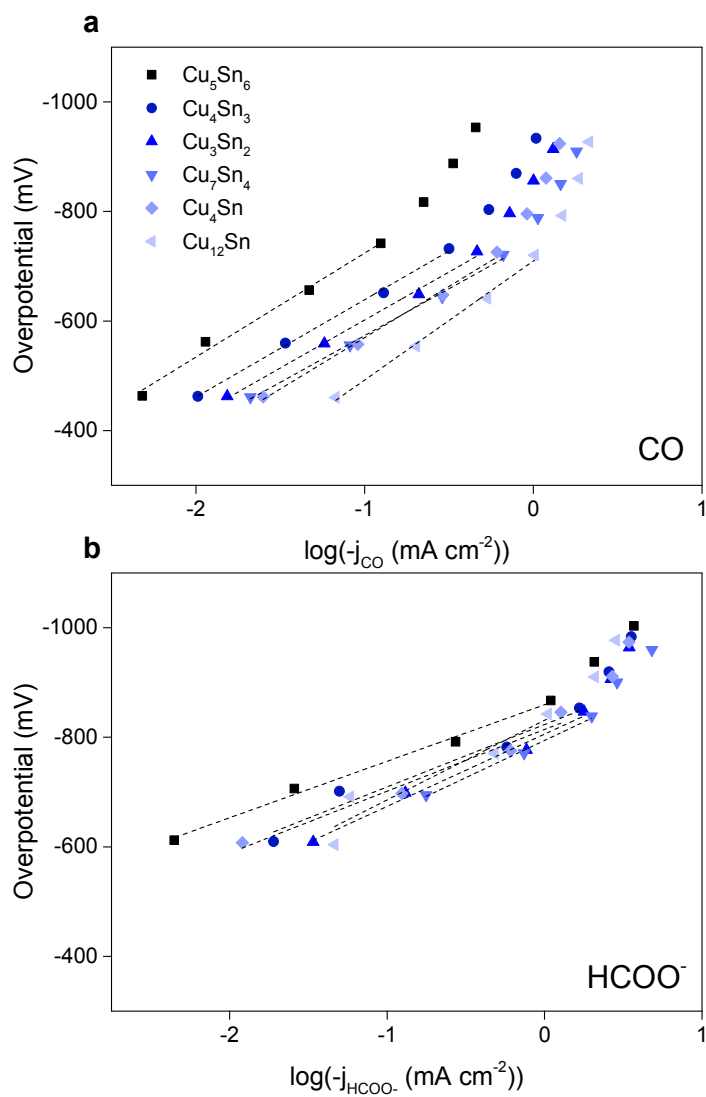


Figure S4.5 Tafel slopes of the Cu-Sn samples in CO_2 -saturated 0.1 M KHCO_3 electrolyte toward a) CO and b) formate.

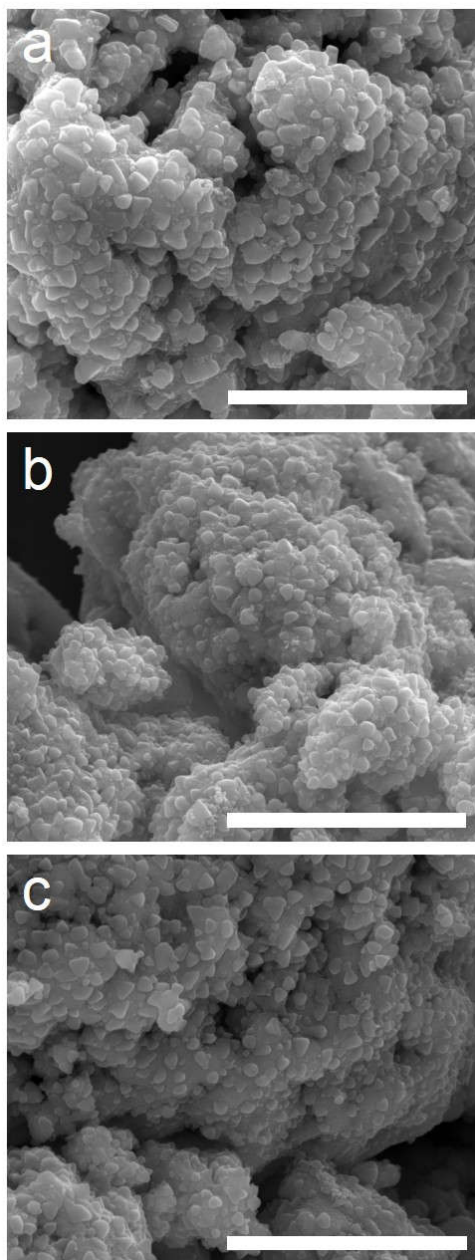


Figure S4.6 SEM images of a) Cu₅Sn₆, b) Cu₇Sn₄, and c) Cu₁₂Sn as-deposited on carbon paper supports after the CO₂ reduction reaction. The scale bars in each panel are 3 μm.

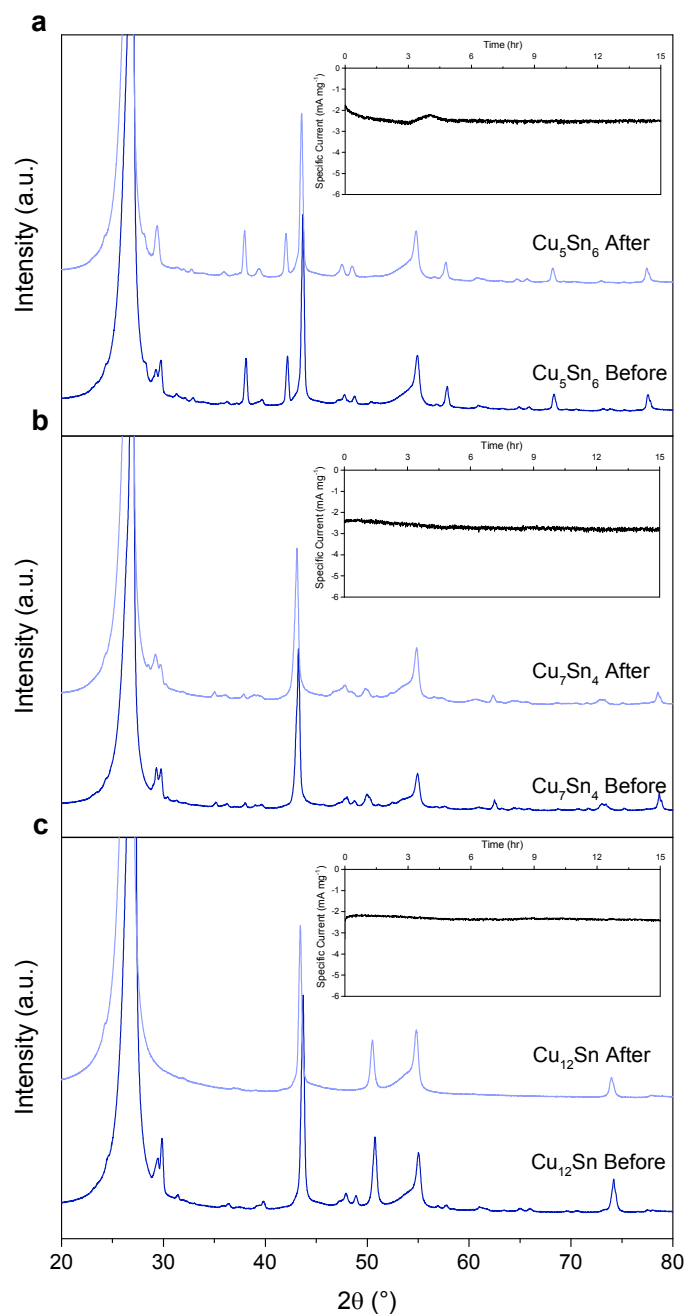


Figure S4.7 XRD patterns of the Cu-Sn/CP electrode before and after CRR stability testing with the amperometric i-t curve shown in the inset for (a) Cu_5Sn_6 , (b) Cu_7Sn_4 and (c) Cu_{12}Sn . Transient peaks observed for Cu_{12}Sn /CP were not observed on the Cu_{12}Sn powder and are likely related to reducible species of the carbon paper (Figure S4.8).

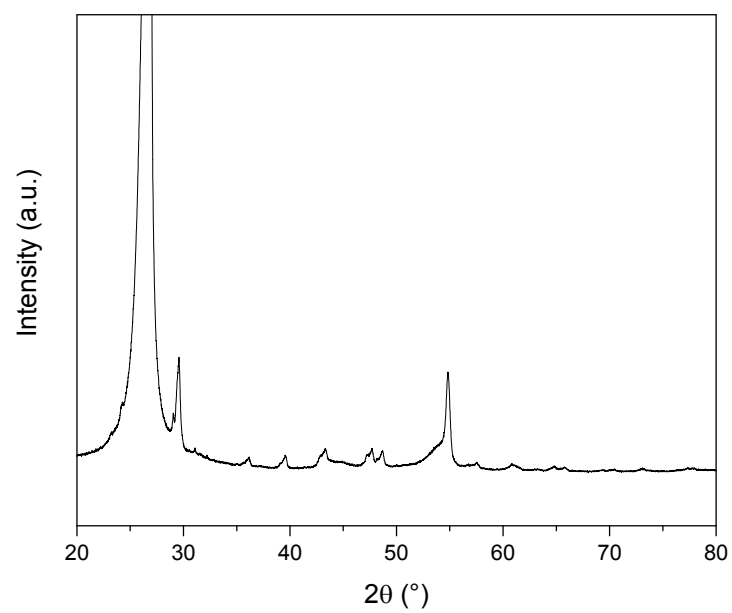


Figure S4.8 Typical XRD pattern of a carbon paper substrate.

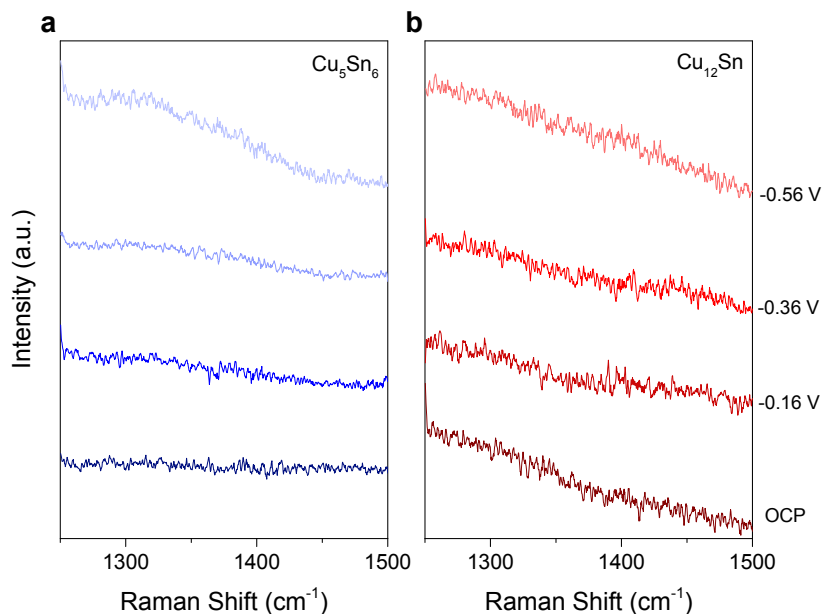


Figure S4.9 *In-situ* Raman spectra in N_2 -saturated 0.1 M KHCO_3 electrolyte at OCP and negative potentials for (a) Cu_5Sn_6 and (b) Cu_{12}Sn .

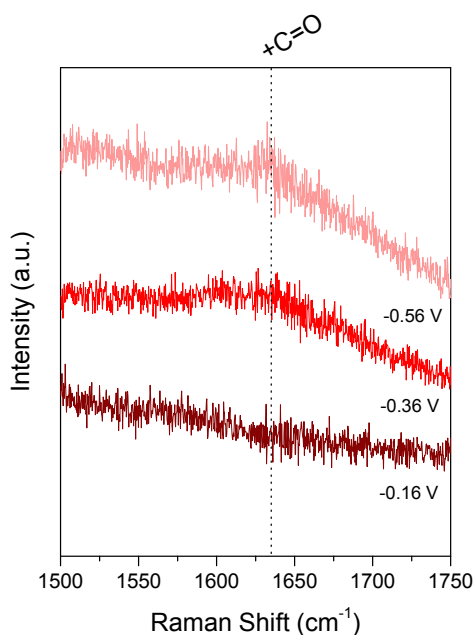


Figure S4.10 *In-situ* Raman spectra in CO_2 -saturated 0.1 M KHCO_3 electrolyte at negative potentials for the Cu_{12}Sn sample. The bending mode of adsorbed water ($+\text{H}-\text{O}-\text{H}$) is typically observed around 1600 cm^{-1} . A shoulder peak is observed at $\sim 1635\text{ cm}^{-1}$ which is assigned to the asymmetric stretch of the carbonyl group associated with $^*\text{COOH}$.

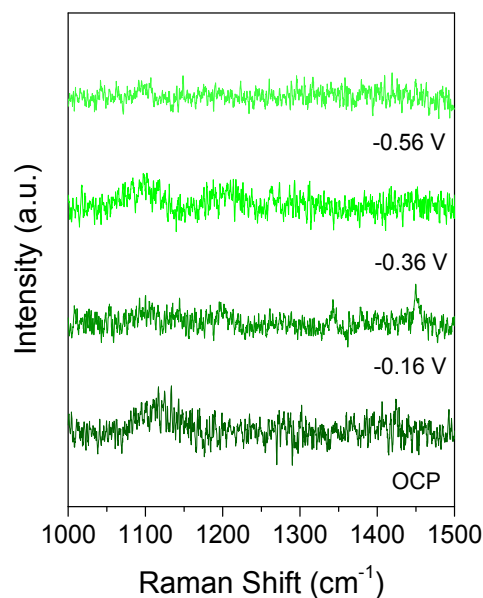


Figure S4.11 *In-situ* Raman spectra in CO₂-saturated 0.1 M KHCO₃ electrolyte at OCP and negative potentials for Cu₇Sn₄.

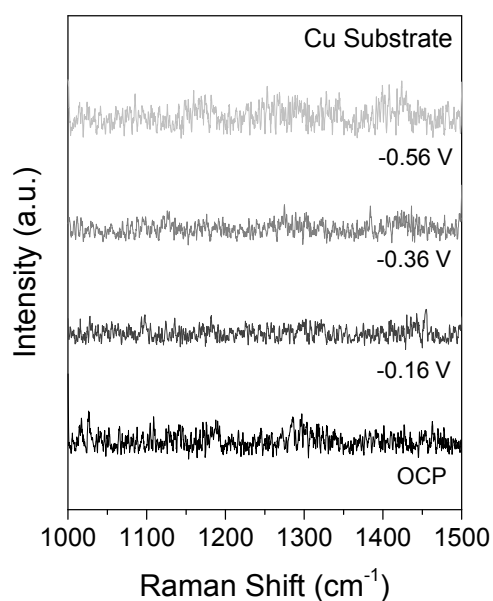


Figure S4.12 *In-situ* Raman spectra in CO₂-saturated 0.1 M KHCO₃ electrolyte at OCP and negative potentials for the bare Cu foil substrate. Note that the bare foil did not have the surface roughness generally needed for surface enhancement and therefore did not interfere with the collection of Raman spectra for the Cu-Sn samples.

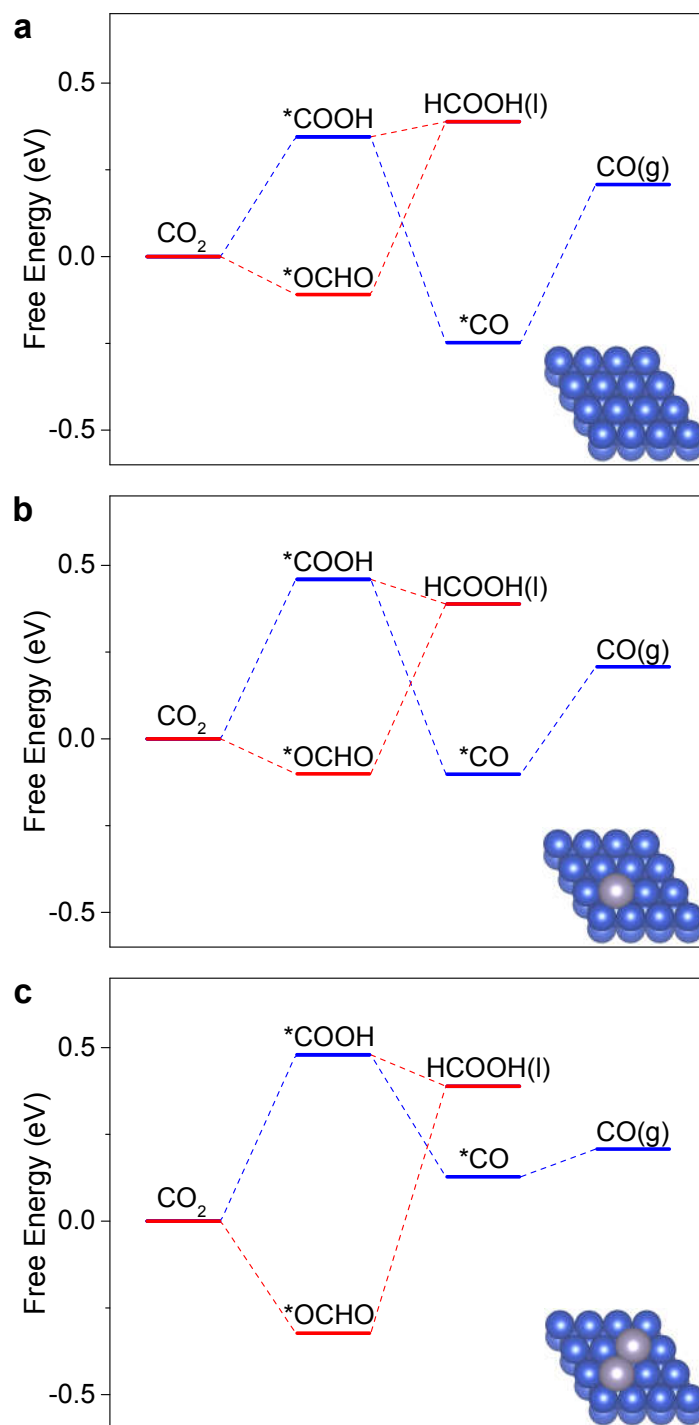


Figure S4.13 Free energy diagrams of CO₂ reduction pathways to CO and HCOOH on (a) Cu, (b) Sn-1, and (c) Sn-2. The insets show the optimized configurations of Cu, Sn-1, and Sn-2.

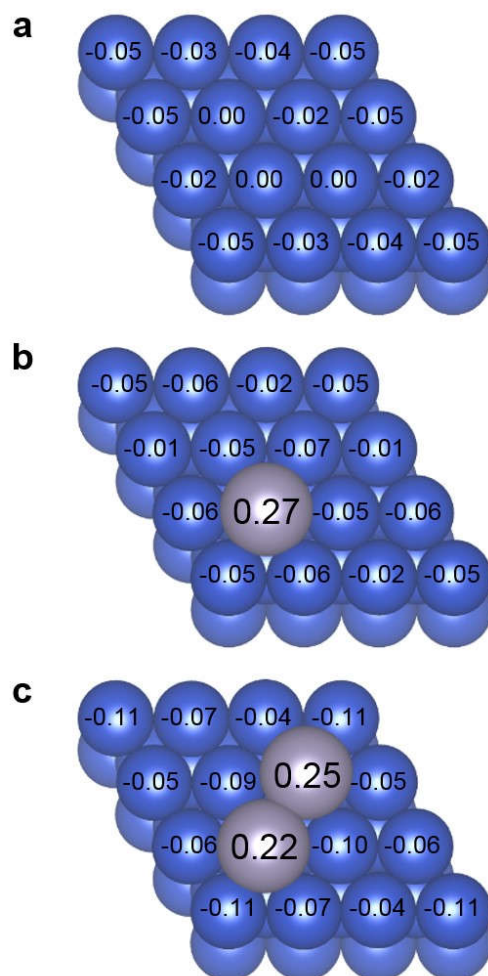


Figure S4.14 Bader charge analysis of plane catalysts for (a) Cu, (b) Sn-1, and (c) Sn-2. Negative values represent a negative charge on the atom. Blue and grey spheres indicate Cu and Sn atoms, respectively.

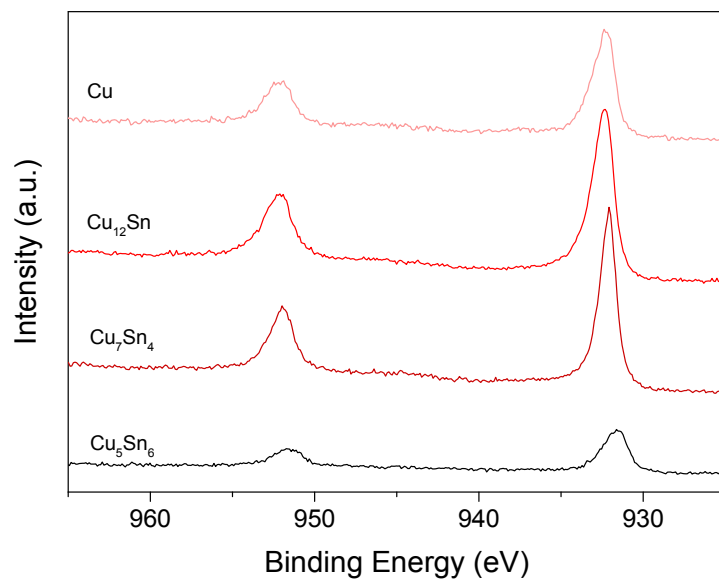


Figure S4.15 High resolution XPS Cu 2p spectra for Cu-Sn and pure Cu samples.

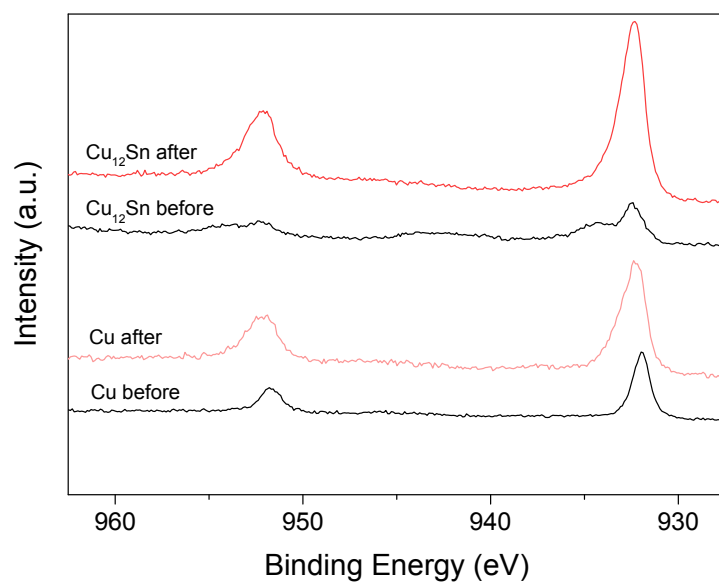


Figure S4.16 High resolution XPS Cu 2p spectra for Cu and Cu₁₂Sn samples both before and after being etched 20 nm *in-situ* by Ar plasma. Note the shift in the Cu 2p_{3/2} peak as surface oxides have been removed.

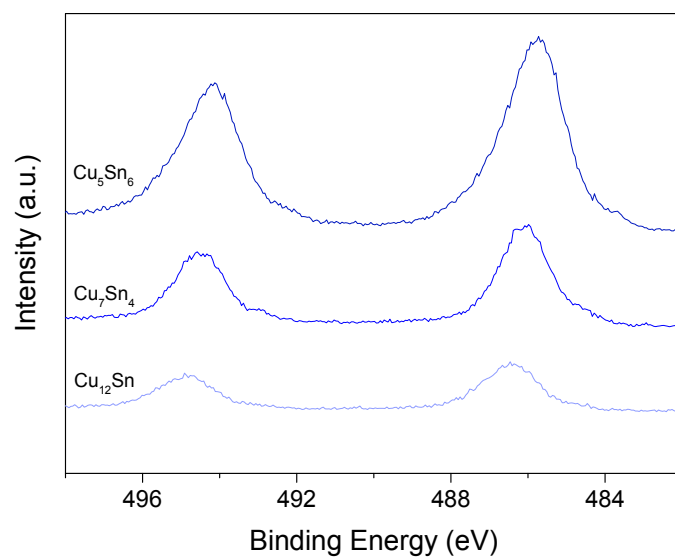


Figure S4.17 High resolution XPS Sn 3d spectra for Cu-Sn samples.

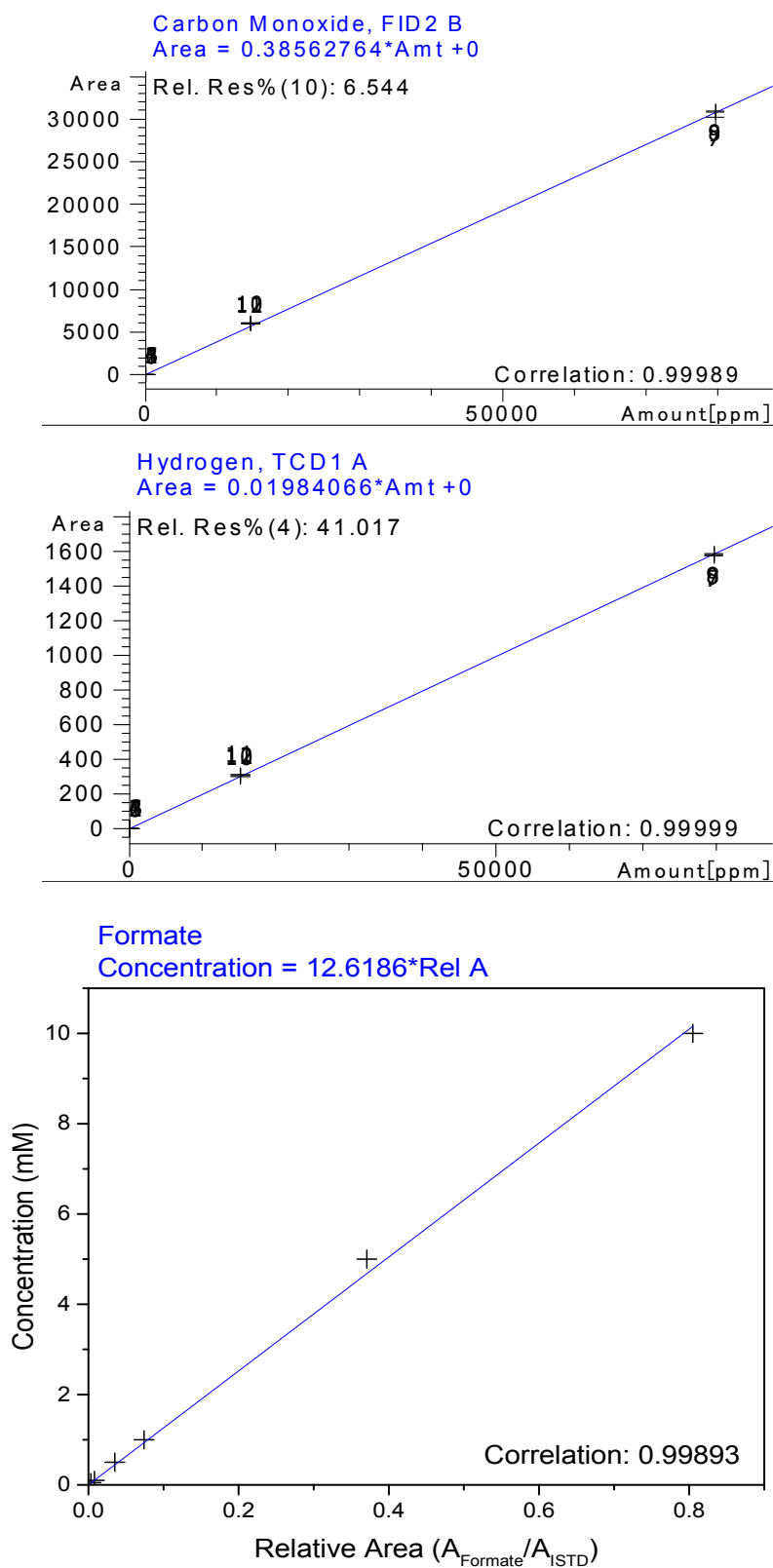


Figure S4.18 (top) GC-FID calibration curve for carbon monoxide, (middle) GC-TCD calibration curve for hydrogen, (bottom) ¹H-NMR calibration curve for formate.

Table S4.1 Bulk composition data of the Cu-Sn alloys obtained from ICP-MS and surface composition obtained from XPS.

Sample	Cu Conc. ICP-MS (at%)	Sn Conc. ICP-MS (at%)	Ratio Cu/Sn	Cu Conc. XPS (at%)	Sn Conc. XPS (at%)
Cu ₅ Sn ₆	45.6	54.4	0.84	47.2	52.8
Cu ₄ Sn ₃	57.8	42.2	1.37	56.0	44.0
Cu ₃ Sn ₂	60.1	39.9	1.51	59.8	40.2
Cu ₇ Sn ₄	63.6	36.4	1.75	70.0	30.0
Cu ₄ Sn	79.4	20.6	3.85	79.6	20.4
Cu ₁₂ Sn	92.4	7.6	7.24	90.8	9.18

Table S4.2 Error associated with Faradaic efficiency data presented in Figure 4.1 and Figure S4.4.

	V vs. Ag/AgCl	Cu₅Sn₆	Cu₄Sn₃	Cu₃Sn₂	Cu₇Sn₄	Cu₄Sn	Cu₁₂Sn
δFE_{CO} (%)	-1.2	29.3	17.4	16.5	11.9	13.3	9.1
	-1.3	14.1	8.0	6.8	4.8	5.9	3.9
	-1.4	5.0	3.1	2.6	2.1	2.4	1.9
	-1.5	1.8	1.3	1.1	1.0	1.1	1.1
	-1.6	0.9	0.7	0.7	0.6	0.7	0.8
	-1.7	0.5	0.5	0.5	0.5	0.5	0.7
	-1.8	0.4	0.4	0.4	0.4	0.4	0.5
δFE_{H₂} (%)	-1.2	36.7	21.7	20.7	14.8	16.6	11.4
	-1.3	17.7	10.1	8.6	6.0	7.3	4.8
	-1.4	6.2	3.9	3.2	2.5	3.0	2.2
	-1.5	2.3	1.6	1.4	1.2	1.3	1.2
	-1.6	1.1	0.9	0.8	0.7	0.8	0.7
	-1.7	0.7	0.6	0.5	0.5	0.5	0.5
	-1.8	0.5	0.4	0.4	0.3	0.4	0.4
δFE_{HCOO-} (%)	-1.3	2.0	6.4	11.5	22.5	4.2	11.6
	-1.4	15.9	5.7	11.2	10.2	9.7	5.4
	-1.5	3.2	1.3	11.2	4.5	16.5	9.9
	-1.6	11.7	20.2	16.4	10.4	3.2	9.8
	-1.7	7.3	11.0	7.7	7.5	11.6	10.1
	-1.8	10.5	11.3	5.7	12.8	11.4	11.1

4.10 Supplementary References

1. Kuhl, K. P.; Cave, E. R.; Abram, D. N.; Jaramillo, T. F., *Energy Environ. Sci.* 2012, 5, 7050-7059.
2. Ferrari, A. C., *Solid State Commun.* 2007, 143, 47-57.
3. Nørskov, J. K.; Rossmeisl, J.; Logadottir, A.; Lindqvist, L.; Kitchin, J. R.; Bligaard, T.; Jónsson, H., *J. Phys. Chem. B* 2004, 108, 17886-17892.
4. Peterson, A. A.; Abild-Pedersen, F.; Studt, F.; Rossmeisl, J.; Nørskov, J. K., *Energy Environ. Sci.* 2010, 3, 1311-1315.
5. Durand, W. J.; Peterson, A. A.; Studt, F.; Abild-Pedersen, F.; Nørskov, J. K., *Surf. Sci.* 2011, 605, 1354-1359.

Chapter 5

Electrochemical Reduction of CO₂ to Ethane through Stabilization of an Ethoxy Intermediate

This Chapter includes work that has been accepted for publication by *Angew. Chem. Int. Ed.* 2020, 10.1002/anie.20204846 (invited article). In previous Chapters, the early CO₂RR reaction mechanism was intensely studied and provided parameters to improve the selectivity towards CO, a precursor intermediate to multi-carbon products. The main aim of this Chapter is to focus on the late-stage reaction pathway to multi-carbon products (ethylene, ethane, ethanol, *etc.*) and determine the key properties of copper-based materials which influence their selectivity.

In this Chapter, iodide-derived (ID-Cu) and oxide-derived (OD-Cu) copper systems were studied to obtain a deeper understanding of the C₂ pathway. Ethane is a seldom observed product due to the higher selectivity towards ethylene and ethanol generally. Consequently, little experimental evidence for its reaction mechanism exists. Here, it was found that ID-Cu achieved higher selectivity and faster kinetics towards ethane production compared to OD-Cu, which was likely due to trace iodine species on the surface and positively charged Cu species. Through *in-situ* X-ray absorption fine structure and *in-situ* Raman techniques, it was experimentally found that the formation of ethane follows the same pathway to ethylene and ethanol, and better stabilization of the late stage ethoxy intermediate can steer the reaction to ethane over ethanol.

Statement of Authorship

Title of Paper	Electrochemical Reduction of CO ₂ to Ethane through Stabilization of an Ethoxy Intermediate
Publication Status	<input type="checkbox"/> Published <input checked="" type="checkbox"/> Accepted for Publication <input type="checkbox"/> Submitted for Publication <input type="checkbox"/> Unpublished and Unsubmitted work written in manuscript style
Publication Details	A. Vasileff, Y.P. Zhu, Y.Q. Zhao, X. Zhi, L. Ge, H.M. Chen, Y. Zheng, S.Z. Qiao, Electrochemical Reduction of CO ₂ to Ethane through Stabilization of an Ethoxy Intermediate, Angewandte Chemie International Edition, 2020, 10.1002/anie.20204846

Principal Author

Name of Principal Author (Candidate)	Anthony Vasileff		
Contribution to the Paper	Conducted the majority of experiments, analysed all the data and wrote the majority of the paper.		
Overall percentage (%)	68		
Certification:	This paper reports on original research I conducted during the period of my Higher Degree by Research candidature and is not subject to any obligations or contractual agreements with a third party that would constrain its inclusion in this thesis. I am the primary author of this paper.		
Signature		Date	05/02/2020

Co-Author Contributions

By signing the Statement of Authorship, each author certifies that:

- the candidate's stated contribution to the publication is accurate (as detailed above);
- permission is granted for the candidate to include the publication in the thesis; and
- the sum of all co-author contributions is equal to 100% less the candidate's stated contribution.

Name of Co-Author	Yanping Zhu		
Contribution to the Paper	6% Conducted the in-situ XAFS measurements and helped to process and analyse the data.		
Signature		Date	01/04/2020

Name of Co-Author	Yongqiang Zhao		
Contribution to the Paper	3% Assistance with electrode material fabrication for the experiments		
Signature		Date	05/02/2020

Name of Co-Author	Xing Zhi		
Contribution to the Paper	2% Conducted the DFT computations for the paper.		
Signature		Date	05/02/2020

Name of Co-Author	Lei Ge		
Contribution to the Paper	2% Conducted all XPS experiments		
Signature		Date	05/02/2020

Name of Co-Author	Hao Ming Chen		
Contribution to the Paper	3% Provided specialist guidance regarding the XAFS experiments and helped add valuable discussion to the paper related to those experiments.		
Signature		Date	07/04/2020

Name of Co-Author	Yao Zheng		
Contribution to the Paper	8% Provided guidance and supervision from conception through to submission and helped to revise the paper.		
Signature		Date	05/02/2020

Name of Co-Author	Shizhang Qiao		
Contribution to the Paper	8% Provided guidance and supervision from conception through to submission and helped to revise the paper.		
Signature		Date	05/02/2020

5.1 Introduction

In recent years, the field of electrochemical CO₂ reduction (CO₂RR) has seen significant progress in reactor and catalyst design such that commercially relevant reaction rates are becoming ever more obtainable.^{1, 2} However, the majority of these catalyst systems are highly selective for C1 products (CO, formate),³ which have limited applicability as fuels directly. Preferably, products with higher energy density are obtained from this process which can be utilized directly in existing energy infrastructure.⁴ Copper-based catalysts are known to be reasonably selective for C2 products, with ethylene (C₂H₄) and ethanol (C₂H₅OH) being obtained at higher faradaic efficiencies.^{5, 6} Ethane (C₂H₆), on the other hand, is seldom produced in this reaction, yet has the highest energy density of these C2 products (-1.43 MJ mol⁻¹ (C₂H₆); -1.32 MJ mol⁻¹ (C₂H₄); -1.24 MJ mol⁻¹ (C₂H₅OH)).⁷

Studies using polycrystalline copper generally report no production of ethane,⁸ however, compound-derived copper catalysts show an enhancement.⁹⁻¹³ This may be due to factors like increased grain boundaries and residual oxygen which favour C2 selectivity.^{14, 15} Given its infrequency as a CO₂RR product and negligible selectivity compared with other C1-C3 products, limited pathways and mechanisms have been proposed for the production of ethane from CO₂.^{10-12, 16} The most popular of these pathways are (i) hydrogenation of pre-generated ethylene in a tandem reaction and (ii) two *CH₃ intermediates, a precursor to methane, coupling to form ethane directly. Despite some evidence for these pathways, mechanistic inconsistencies related to important experimental observations persist: (i) the concurrent production of ethane with ethylene and ethanol and (ii) the near or complete absence of methane formation on ethane producing catalysts. The limitation of these pathways stems fundamentally from the requirement of two diligently designed active sites and the high barrier to *CO protonation as well as low barrier to *CH₃ protonation, which would preclude ethane formation.¹⁷ Furthermore, previous ethane formation mechanisms were mainly deduced by simple ex-situ product analysis, while *in-situ* spectroscopic evidence identifying the critical intermediates is lacking. Therefore, expanding our understanding

of the ethane pathway is required to better inform catalyst design and enable its production from CO₂.

In this work, using some model compound-derived copper electrocatalysts, namely iodide-derived copper (ID-Cu) and oxide-derived copper (OD-Cu) foams, we study the CO₂ to ethane pathway. ID-Cu exhibited significantly greater ethane selectivity and more favorable kinetics compared to OD-Cu. *In-situ* X-ray adsorption (XAS) and Raman studies suggest a mechanism involving an oxygen-bound ethoxy (*OCH₂CH₃) intermediate undergoes a selectivity determining step which can produce either ethane or ethanol. This intermediate appears to be better stabilized on ID-Cu due to trace iodine species in the copper lattice. As a result, we provide a rational strategy to engineer Cu-based catalysts that are selective towards products beyond ethylene and ethanol.

5.2 Results and Discussion

The ID-Cu foam was obtained using a two-step process involving calcination of Cu foam and iodine in a vacuum-sealed ampoule and subsequent electrochemical reduction (Figure 5.1a). The ampoule method excluded oxygen and yielded uniform CuI coatings,¹⁸ as seen in the high-resolution scanning transmission electron microscope (HR-STEM) image (Figure 5.1b). The HR-STEM image shows that the cubic form of CuI was obtained from the synthesis conditions with an interplanar distance for the (111) facets of 3.5 Å. Scanning electron microscopy (SEM) also shows that the uniform CuI coating had a thickness of approximately 30 µm (Figure S5.1). Elemental dispersive spectroscopy (EDS; Figure S5.1) mapping of the CuI coating confirms a stoichiometry of 1:1 between copper and iodine and the X-ray diffraction (XRD; Figure 5.1c) pattern shows that the CuI coating had a cubic structure (i.e. α -CuI). After electrochemical reduction of the CuI-coated foam at a potential of -0.8 V vs. Ag/AgCl, the light reddish foam was converted into the black iodine-derived copper (ID-Cu) sample. From the SEM and TEM images, we see that the uniform CuI coating was converted into a layered structure made up of Cu nanoparticles approximately 100 nm in diameter with a cubic structure (Figure S5.2). The XRD pattern of ID-Cu (Figure 5.1c) shows

predominantly polycrystalline copper phase with some cuprous oxide phase, likely formed from exposure to air. Although susceptible to ambient oxygen, this formed oxide is easily reduced under reduction potentials as evidenced by *in-situ* Raman measurements (Figure S5.3).¹⁹

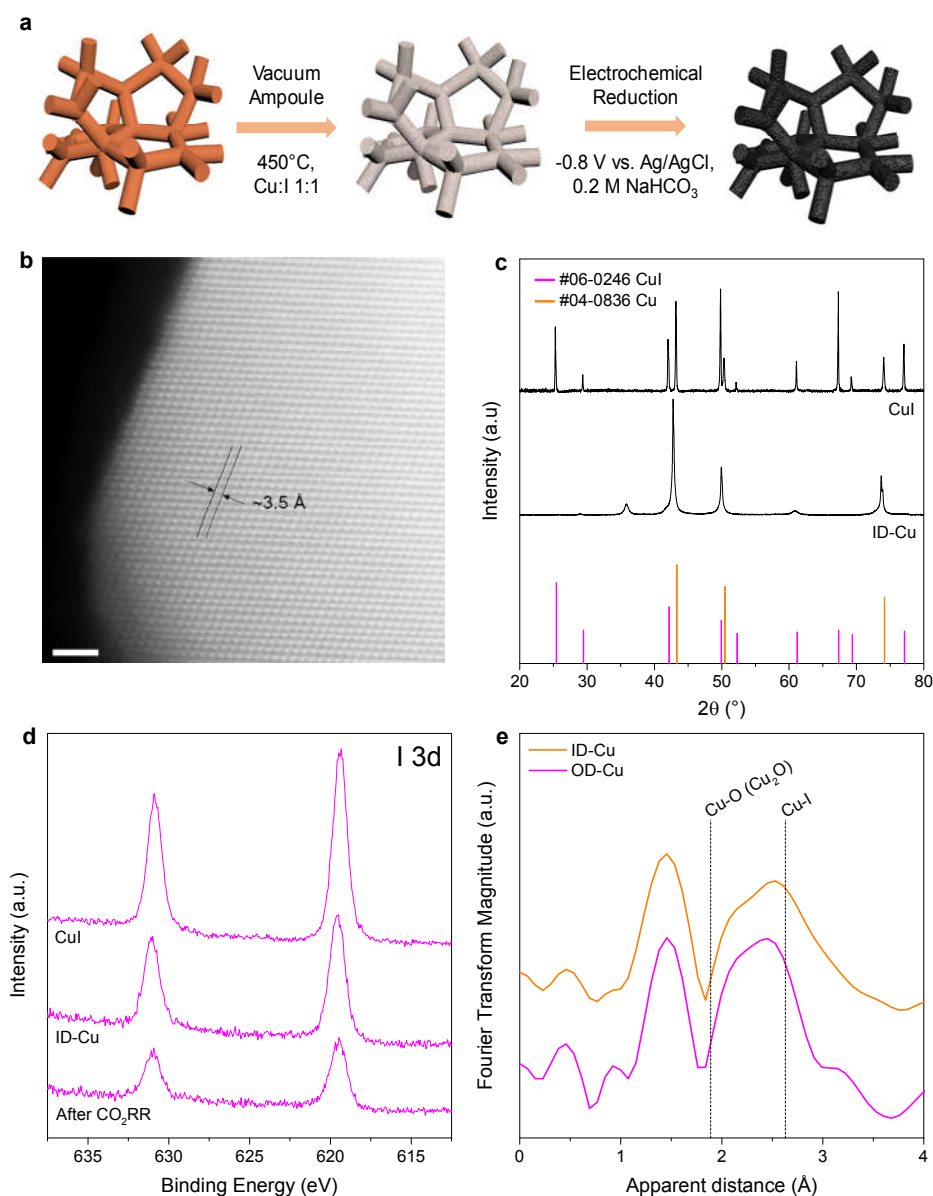


Figure 5.1 a) Two-step synthesis process for ID-Cu involving calcination in a vacuum ampoule and subsequent electrochemical reduction. b) HR-STEM image of CuI before electrochemical reduction (2 nm scale bar). c) Diffraction patterns and d) high-resolution I 3d XPS spectra of ID-Cu at various stages. e) Comparison of Cu K-edge EXAFS spectra without phase-correction between ID-Cu and OD-Cu in the dry state after electrochemical reduction.

From X-ray photoelectron spectroscopy (XPS), the I 3d spectra (Figure 5.1d) indicate that iodine species are present after electrochemical reduction and after CO₂ reduction reaction, and elemental analysis of the samples shows an iodine concentration of approximately 1.4 at % (s.d. 0.32%; Figure S5.4) which is homogeneously dispersed throughout ID-Cu (Figure S5.5). A positive shift of the I 3d peaks in ID-Cu compared to CuI indicate some charge increase on the I sites. This behaviour is similar to atomically dispersed iodine on an iodide-derived nickel surface.¹⁸ When analysing the Fourier transformed extended X-ray fine structure (EXAFS) spectra (Figure 5.1e), Cu-I coordination at 2.65 Å is observed for ID-Cu with a coordination number of about one. From these results, it is likely the iodine also exists as atomically dispersed species on the ID-Cu surface. The OD-Cu precursor coating, synthesized by an established method,⁹ was composed of mixed cuprous and cupric oxide phases which was converted to metallic Cu⁰ in the OD-Cu sample after electrochemical reduction, evidenced by the XRD pattern (Figure S5.6).

As shown in Figure 5.2a, both compound-derived samples were able to produce relevant C2 products across the range of potentials investigated while the copper sample generated predominantly methane at higher overpotentials (Figure S5.7). It is interesting to note that both ID-Cu and OD-Cu samples did not produce any methane at any of the potentials investigated, making it unlikely that *CH₃ intermediates (necessary for a *CH₃ coupling mechanism) were generated. When comparing the C2 product distribution, we find that OD-Cu is less selective compared to ID-Cu (Figure 5.2b), only reaching an ethane selectivity (normalized to the total C2+ products) of 27 % at -1.6 V vs. Ag/AgCl. By comparison, ID-Cu reached a normalized ethane selectivity of 72 % (maximum absolute Faradaic efficiency of 5.2 % of all CO₂ reduction products and hydrogen; Figure S5.8) at the same condition (Figure 5.2c). Tafel slopes also indicate that ethane generation was significantly more kinetically favourable on ID-Cu (116 mV dec⁻¹) compared to OD-Cu (196 mV dec⁻¹; Figure 5.2d). In addition, ethylene generation shows a smaller Tafel slope compared to ethane (77 mV dec⁻¹; Figure S5.9), which suggests the rate determining step (rds) to ethane occurs after ethylene generation if the two share a common pathway. Computational evidence has

shown that the adsorption of ethylene is weak on Cu, and the adsorption mode becomes significantly destabilized with high H^* coverage.²⁰ Given this condition is likely met here as the Faradic efficiency towards the HER exceeds that of the CO_2RR (Figure S5.8), we exclude a pathway through ethylene re-adsorption and hydrogenation.

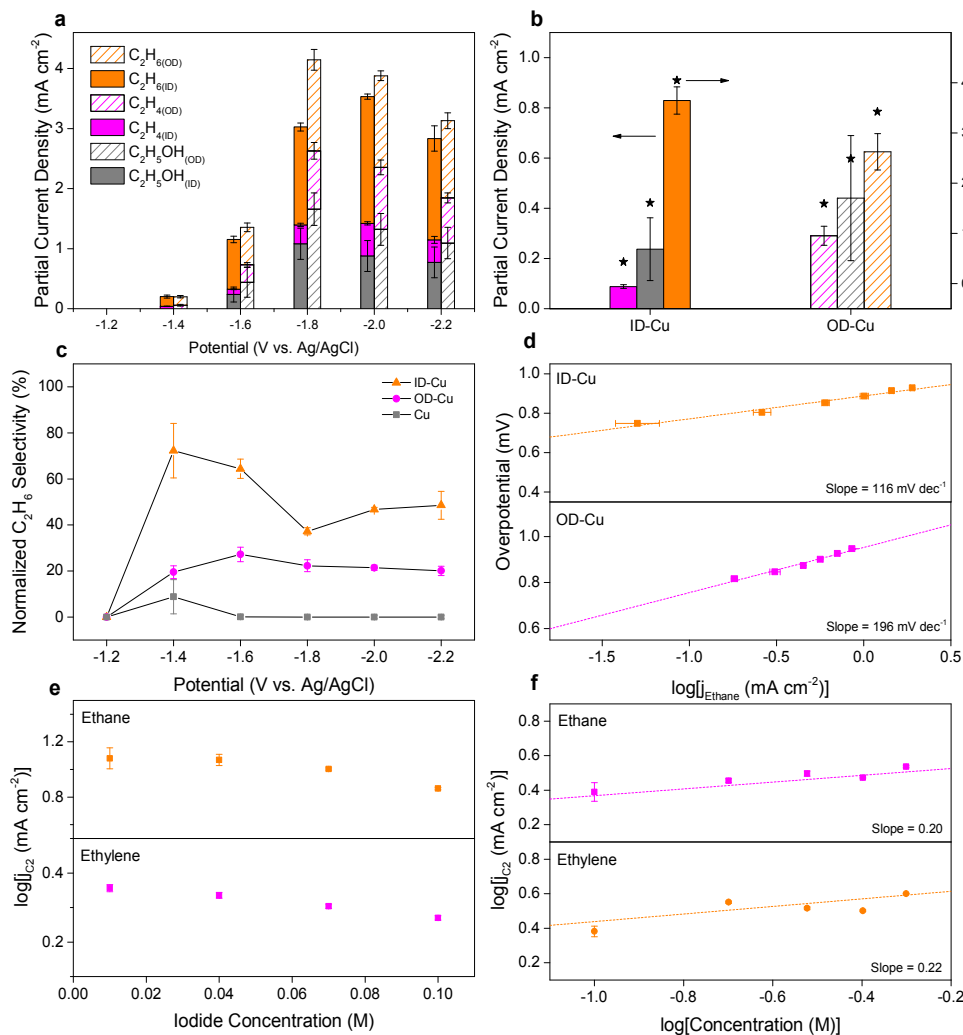


Figure 5.2 a) Partial current densities toward ethane, ethylene, and ethanol on ID-Cu and OD-Cu. b) C₂ product distribution for ID-Cu and OD-Cu samples at -1.6 V vs. Ag/AgCl. c) Ethane selectivity normalized to the total C₂ + C₃ production for various samples. d) Tafel slopes toward ethane production for ID-Cu and OD-Cu samples. Electrolyte study showing the ethane and ethylene dependence on e) iodide concentration and f) bicarbonate concentration.

To determine whether electrolyte specific factors influence the generation of ethane, bicarbonate and iodide studies were conducted as these factors have been shown to stabilize key intermediates and favour hydrocarbon production on copper catalysts.^{21, 22} Here, it was found that electrolyte iodide concentration had no (possibly slightly negative) correlation to ethane generation (Figure 5.2e), while bicarbonate dependency was also found to be close to zero order (slight dependency; Figure 5.2f). This result possibly indicates a zero-order dependence on bicarbonate for the ethane pathway and a rds which is not pH dependent.²³ For example, a $^*\text{CO}$ coupling step (widely accepted as the rds to ethylene)^{24, 25} or a $^*\text{CH}_3$ coupling step as the rds would show no pH dependence. As $^*\text{CH}_3$ is believed to be an intermediate in the methane pathway, a pathway to ethane through $^*\text{CH}_3$ coupling is not likely here as we observe no methane generation. However, we consistently observed the concurrent production of ethane with ethylene and ethanol (Figure 5.2a).¹¹ Therefore, we believe these C2 products share a pathway with common reaction intermediates.

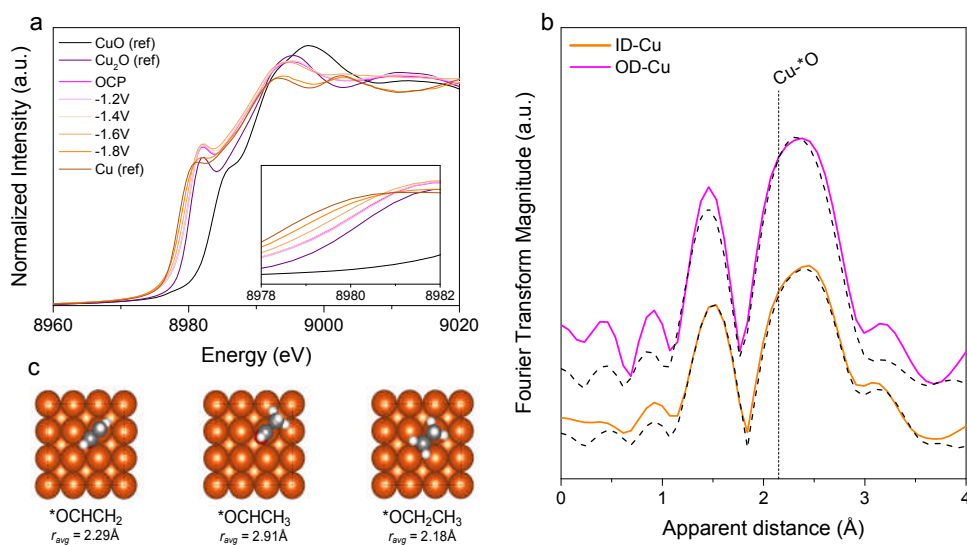


Figure 5.3 a) Potential dependent XANES data for ID-Cu with Cu references. b) Comparison of Fourier transformed EXAFS data at -1.4 V with the fitting result shown as a dashed line. All potentials are referenced to Ag/AgCl. c) DFT calculated bond lengths for relevant O-bound intermediates in the C2 pathway.

In order to probe this C2 reaction mechanism further, we performed *in-situ* X-ray absorption fine structure (XAFS) spectroscopy on the ID-Cu and OD-Cu samples under CO₂RR conditions. From the Cu K-edge X-ray absorption near-edge structure (XANES), we find that the sample surface existed predominantly in Cu^I state under open circuit potential (OCP) conditions but maintained an oxidation state of $0 > n > 1$ under CO₂RR conditions (Figure 5.3a and Figure S5.10). It is likely that the trace iodine or oxygen species were stable in the nanostructure under reduction potentials and contributed to the higher oxidation state of Cu sites. While Cu sites in OD-Cu maintained a higher oxidation state compared to ID-Cu (Figure 5.3a and S10), OD-Cu was also more selective towards formate (Figure S5.11), whose production also proceeds via an oxygen-bound *OCHO intermediate.²⁶ It is important to note that many oxygen-bound intermediates are better stabilized on sites with charge depletion.²⁷ Therefore, a pathway through *OCHO to formate is possibly a significant competing reaction to the C2 pathway. Consequently, optimizing the oxidation state of the Cu active sites, e.g. by trace iodine species, is critical to optimizing the binding of key oxygen-bound intermediates in the C2 pathway.

From the EXAFS, a fitting model was established to identify the main coordination peaks under reaction conditions (Figure S5.12, Table S5.1 and C.2). As shown in Figure 5.3b, lattice oxygen from Cu₂O (~ 1.9 Å) persists at negative potentials for ID-Cu and OD-Cu.²⁸ However, another path with slightly longer Cu-O bond length (~ 2.15 Å) is observed at -1.4 V vs. Ag/AgCl for ID-Cu, which corresponds to the potential of maximum ethane selectivity. Using density functional theory (DFT), we calculated the Cu-O bond length for O-bound reaction intermediates in the latter stages of the ethanol pathway, i.e. *OCH₂CH₃, *OCHCH₃, and *OCHCH₂ (Figure 5.3c and Table S5.3).²⁴ We find that an adsorbed ethoxy intermediate (Cu-OCH₂CH₃) has a bond length of ~ 2.18 Å which matches well with the EXAFS result (Figure 5.3b). Therefore, we attribute the new Cu-O path to this adsorbed ethoxy intermediate under CO₂RR conditions. Note that with further increase of the cathodic potential (< -1.6 V), the Cu^I was further reduced to metallic Cu⁰ as illustrated by the intensified scattering path at ~ 2.2 Å that is attributed to the single-scattering metallic Cu⁰-Cu⁰ path. This could

also suggest the formation of metallic Cu leads to a significant decline in ethane selectivity (Figure 5.2c). This finding further shows that I species are of paramount importance for enhancing the production of ethane from the CO₂RR.

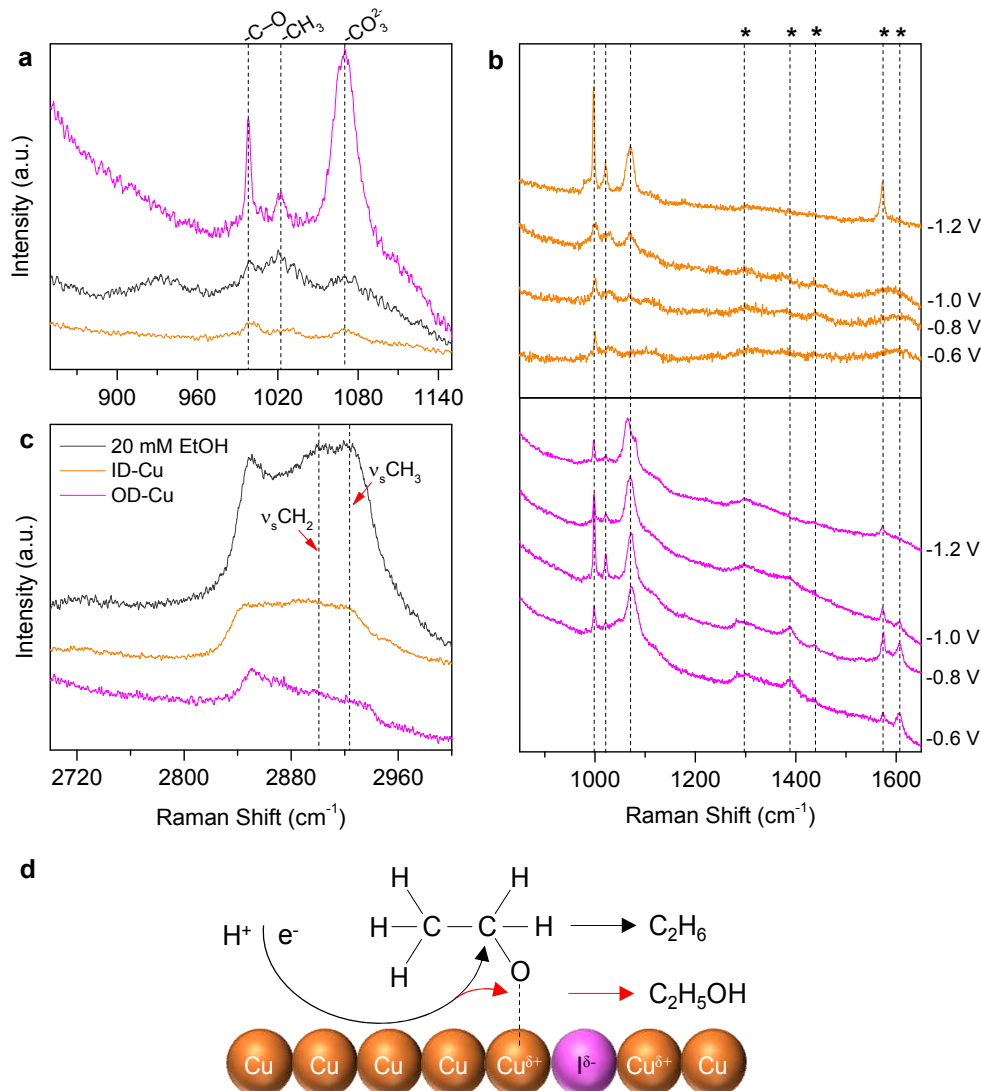


Figure 5.4 *In-situ* Raman spectra in CO₂-saturated 0.2 M NaHCO₃ for ID-Cu and OD-Cu samples shown for the a) enlarged region between 850-1150 cm⁻¹ at -1.0 V and b) potential dependent spectra. Vibrational bands denoted with * are related to carboxyl and formate intermediates. c) The -CH_x stretching region between 2700-3000 cm⁻¹ at -0.8 V. d) C₂ reaction pathway outlining the selectivity determining ethoxy intermediate between ethane and ethanol.

Potential-dependent Raman spectra were then collected for ID-Cu and OD-Cu to identify the critical reaction intermediate(s) for ethane generation proposed above. Compared with N₂-saturated control tests (Figure S5.13), spectra collected in CO₂-saturated electrolyte exhibit bands around 1000 cm⁻¹, 1020 cm⁻¹, and 1573 cm⁻¹ for both ID-Cu and OD-Cu samples (Figure 5.4a and Figure S5.14). Other vibrational bands denoted with * in Figure 5.4b are likely attributed to early reaction intermediates like carboxylate and formate.²⁶ Bands at 1000 and 1020 cm⁻¹ are not usually observed in Raman studies for CO₂RR on copper.²⁹ It is possible that the band at 1020 cm⁻¹ is related to the bicarbonate ion.³⁰ However, it is also possible that they correspond to +C-O stretching and +CH₃ rock vibrations, which would be consistent with the presence of an ethoxy intermediate.³¹ To confirm the identity of these bands, a control experiment using 20 mM of ethanol in 0.2 M NaCl was conducted under similar potential conditions on ID-Cu. From Figure 5.4a and Figure S5.15, we find that bands related to the +C-O stretching and +CH₃ rock vibrational modes of adsorbed ethanol appear as the potential is stepped negatively.^{31, 32} These bands increase in intensity as the potential decreases on ID-Cu (Figure 5.4b), corresponding to the onset and increase in ethane generation on ID-Cu (Figure 5.2). In comparison, the intensity of these bands on OD-Cu decreases with increasing overpotential. This may be due to the relative increase in ethylene generation on the catalyst which removes vinyl oxide intermediates for further reduction to ethane.¹¹

The -CH_x stretching region is another prominent region in the Raman spectra related to CO₂RR intermediates. From Figure 5.4c and Figure S5.16, we observe very different peak shapes when comparing ID-Cu with OD-Cu. Most noticeably, we see that ID-Cu has features around 2890 and 2920 cm⁻¹, while the most prominent features on OD-Cu are at 2850 cm⁻¹ and 2940 cm⁻¹. When compared with adsorbed ethanol, we see that bands related to symmetric -CH₂ (ν_s CH₂) and -CH₃ (ν_s CH₃) stretching are apparent around 2900 and 2925 cm⁻¹. This further supports the existence of an ethoxy intermediate in the C2 pathway. More importantly, the optimal Cu oxidation state of ID-Cu may be responsible for better stabilization of *OCH₂CH₃ and lead to the stronger ν_s CH₂ and ν_s CH₃ features compared to OD-Cu. Further, by taking into consideration

the enhanced ethane selectivity on ID-Cu, we believe stabilization of this intermediate is key to the production of ethane from CO₂.

To clearly demonstrate this, the mechanism scheme in Figure 5.4d summarizes the following: (1) ethylene, ethane and ethanol share a common pathway originating from the *CO-CO coupling step, (2) a selectivity step involving an O-bound ethoxy (*OCH₂CH₃) intermediate leads to either ethane or ethanol, (3) an optimal charge state of the Cu active sites (e.g. through iodine surface species) leads to better stabilization of *OCH₂CH₃ bound at the oxygen favoring hydrogenation of the carbon to produce ethane. Otherwise, hydrogenation of the oxygen will occur and lead to ethanol.

5.3 Conclusions

To summarize, we have synthesized compound derived copper foams, namely ID-Cu and OD-Cu, and studied their C2 mechanism for CO₂ electroreduction. Interestingly, ID-Cu is significantly more selective toward ethane production, a product seldom observed for CO₂ reduction. Ethane production is found to be kinetically more favorable on ID-Cu which may be correlated to trace iodine species which are persistent under reaction conditions and lead to an optimal oxidation state of the Cu sites. As evidenced by *in-situ* XAFS and Raman spectroscopy, an O-bound ethoxy intermediate is observed during ethane production and is a significant intermediate. Further, the optimized oxidation state of the Cu active sites is critical to stabilize this key O-bound intermediate and to enhance the selectivity toward C2 products.

5.4 Acknowledgement

The authors gratefully acknowledge financial support from the Australian Research Council (ARC) through Discovery Project and Linkage project programs (FL170100154, DP160104866, and DP170104464) and the Australian Government through Research Training Program Scholarships. XAFS measurements were undertaken at BL-17C1 at the National Synchrotron Radiation Research Center (NSRRC, Hsinchu, Taiwan).

5.5 References

1. D. Higgins, C. Hahn, C. Xiang, T. F. Jaramillo, A. Z. Weber, *ACS Energy Lett.* 2019, *4*, 317.
2. T. Burdyny, W. A. Smith, *Energy Environ. Sci.* 2019, *12*, 1442.
3. B. Endrődi, G. Bencsik, F. Darvas, R. Jones, K. Rajeshwar, C. Janáky, *Prog. Energy Combust. Sci.* 2017, *62*, 133.
4. Y. Zheng, A. Vasileff, X. Zhou, Y. Jiao, M. Jaroniec, S.-Z. Qiao, *J. Amer. Chem. Soc.* 2019, *141*, 7646.
5. K. P. Kuhl, E. R. Cave, D. N. Abram, T. F. Jaramillo, *Energy Environ. Sci.* 2012, *5*, 7050.
6. Y. Hori, I. Takahashi, O. Koga, N. Hoshi, *J. Phys. Chem. B* 2002, *106*, 15.
7. D. W. Green, R. H. Perry, *Perry's Chemical Engineers' Handbook, Eighth Edition*, McGraw-Hill Education, 2007.
8. Y. Hori, A. Murata, R. Takahashi, *J. Chem. Soc. Farad. T. 1* 1989, *85*, 2309.
9. D. Raciti, K. J. Livi, C. Wang, *Nano Lett.* 2015, *15*, 6829.
10. A. D. Handoko, K. W. Chan, B. S. Yeo, *ACS Energy Lett.* 2017, *2*, 2103.
11. M. Ma, K. Djanashvili, W. A. Smith, *Angew. Chem. Int. Ed.* 2016, *55*, 6680.
12. A. Dutta, M. Rahaman, N. C. Luedi, P. Broekmann, *ACS Catal.* 2016, *6*, 3804.
13. F.-S. Ke, X.-C. Liu, J. Wu, P. P. Sharma, Z.-Y. Zhou, J. Qiao, X.-D. Zhou, *Catal. Today* 2017, *288*, 18.
14. J. E. Pander III, D. Ren, Y. Huang, N. W. X. Loo, S. H. L. Hong, B. S. Yeo, *ChemElectroChem* 2018, *5*, 219.
15. X. Feng, K. Jiang, S. Fan, M. W. Kanan, *ACS Cent. Sci.* 2016, *2*, 169.
16. K. D. Yang, W. R. Ko, J. H. Lee, S. J. Kim, H. Lee, M. H. Lee, K. T. Nam, *Angew. Chem. Int. Ed.* 2017, *56*, 796.
17. J. Hussain, H. Jónsson, E. Skúlason, *ACS Catal.* 2018, *8*, 5240.
18. Y. Zhao, T. Ling, S. Chen, B. Jin, A. Vasileff, Y. Jiao, L. Song, J. Luo, S.-Z. Qiao, *Angew. Chem. Int. Ed.* 2019, *131*, 12380.
19. Y. Deng, A. D. Handoko, Y. Du, S. Xi, B. S. Yeo, *ACS Catal.* 2016, *6*, 2473.

20. C. J. Heard, S. Siahrostami, H. Grönbeck, *J. Phys. Chem. C* 2016, *120*, 995.
21. A. S. Varela, W. Ju, T. Reier, P. Strasser, *ACS Catal.* 2016, *6*, 2136.
22. Y. Huang, C. W. Ong, B. S. Yeo, *ChemSusChem* 2018, *11*, 3299.
23. M. Dunwell, W. Luc, Y. Yan, F. Jiao, B. Xu, *ACS Catal.* 2018, 8121.
24. F. Calle-Vallejo, M. T. M. Koper, *Angew. Chem. Int. Ed.* 2013, *52*, 7282.
25. E. Pérez-Gallent, M. C. Figueiredo, F. Calle-Vallejo, M. T. M. Koper, *Angew. Chem. Int. Ed.* 2017, *56*, 3621.
26. A. Vasileff, X. Zhi, C. Xu, L. Ge, Y. Jiao, Y. Zheng, S.-Z. Qiao, *ACS Catal.* 2019, *9*, 9411.
27. Y. Jiao, Y. Zheng, P. Chen, M. Jaroniec, S.-Z. Qiao, *J. Amer. Chem. Soc.* 2017, *139*, 18093.
28. L. Yuan, S.-F. Hung, Z.-R. Tang, H. M. Chen, Y. Xiong, Y.-J. Xu, *ACS Catal.* 2019, *9*, 4824.
29. B. D. Smith, D. E. Irish, P. Kedzierzawski, J. Augustynski, *J. Electrochem. Soc.* 1997, *144*, 4288.
30. A. R. Davis, B. G. Oliver, *J. Solution Chem.* 1972, *1*, 329.
31. S. Burikov, T. Dolenko, S. Patsaeva, Y. Starokurov, V. Yuzhakov, *Mol. Phys.* 2010, *108*, 2427.
32. J. Eng, K. Raghavachari, L. M. Struck, Y. J. Chabal, B. E. Bent, G. W. Flynn, S. B. Christman, E. E. Chaban, G. P. Williams, K. Radermacher, S. Mantl, *J. Chem. Phys.* 1997, *106*, 9889.

Chapter 5

Supporting Information

5.6 Material Synthesis and Characterization

5.6.1 Materials

Iodine powder ($\geq 99.8\%$), concentrated nitric Acid (70 %) and concentrated phosphoric acid (85 %) were purchased from Sigma-Aldrich and used without further purification. Undenatured ethanol (anhydrous, $\geq 99.5\%$) and sodium carbonate ($\geq 99.7\%$) were purchased from Chem-Supply and used without further purification. C-10100 grade copper foam (2 mm thickness) was purchased from KYL Scientific and C-10100 grade copper rod (32 mm) was purchased from Austral Wright Metals. Ultra-pure water (18.2 M Ω ·cm, PURELAB Option-Q) was used in all experiments and laser grade CO₂ (99.995 %) was purchased from BOC and used in all electrochemical experiments.

5.6.2 Electrocatalyst Synthesis

Copper Foam Preparation:

To prepare the copper foam for electrocatalyst synthesis, the copper foam was first sonicated in ethanol for 30 min and then rinsed with copious water. The cleaned copper foam was then sonicated in 1 M nitric acid solution for 30 min to remove surface oxides. Once rinsed with sufficient water to remove the acid, the copper foam was dried overnight in a vacuum oven at 60°C.

Preparation of CuI Precursors:

The CuI precursors were fabricated by calcination of copper foam with iodine powder in a vacuum sealed ampoule. Typically, a prepared piece of copper foam (20×5 mm) and iodine powder were placed in an ampoule in a 1:1 mass ratio and flame-sealed under vacuum. The ampoule and contents were then heated in a muffle furnace to $450\text{ }^{\circ}\text{C}$ for 3 h. The heating rate was $5\text{ }^{\circ}\text{C min}^{-1}$ and the cooling rate was $1\text{ }^{\circ}\text{C min}^{-1}$. The CuI precursors were kept in the sealed ampoules and covered with aluminium foil to prevent air and light exposure until further use.

Preparation of CuO Precursors:

The CuO precursors were fabricated by the calcination of copper foam in air. Typically, a piece of prepared copper foam (20×5 mm) was placed in an alumina boat and then heated in a muffle furnace to $450\text{ }^{\circ}\text{C}$ for 3 h. The heating rate was $5\text{ }^{\circ}\text{C min}^{-1}$ and the cooling rate was $1\text{ }^{\circ}\text{C min}^{-1}$.

Preparation of ID-Cu and OD-Cu Samples:

To obtain the usable catalysts, the CuI and CuO precursors underwent the same electrochemical reduction step. Typically, either a CuI or CuO precursor was applied directly as the working electrode in a three-electrode system as described in Section 5.7.1. The CuI and CuO samples were converted to ID-Cu and OD-Cu samples, respectively, by applying a potential of -0.8 V vs. Ag/AgCl for one hour. The catalysts were then rinsed carefully with water, dried with a low stream of nitrogen gas and applied directly as electrocatalysts.

5.6.3 Material Characterization

The crystal structure and chemical structure of the samples were characterized by X-ray diffraction (Rigaku MiniFlex, Cu K α), and X-ray photoelectron spectroscopy (Kratos Axis Ultra, mono Al K α 1486.6eV). XPS spectra were calibrated to the carbon C-C peak using 284.5 eV. Electron imaging was carried out using scanning electron microscopy (FEI Quanta 450, 20 kV) with 5 nm Pt sample coating and transmission electron microscopy under STEM mode (FEI Titan Themis, 200 kV). Elemental mapping of the samples were conducted with SDD EDS detector (Oxford Instruments).

5.7 Electrochemical Characterization

5.7.1 Electrochemical Measurements

Electrochemical measurements were performed on a 760E potentiostat (CH Instruments). The compound-derived copper foam samples were applied directly as the working electrode in a three-electrode cell with Ag/AgCl reference electrode (4.0 M KCl) and RuO₂ coated titanium mesh counter electrode. Cathode and anode compartments were separated by a Nafion 117 cation exchange membrane and the electrolyte was 0.2 M sodium bicarbonate which had been derived from bubbling CO₂ overnight through a solution of 0.1 M sodium carbonate. In a typical electrochemical test, the catholyte was stirred and bubbled with CO₂ for 10 min at 100 sccm to remove air and saturate the electrolyte. Following this, the gas flow rate was reduced to 10 sccm and chronoamperometry was performed for 1 h at potentials between -1.2 and -2.2 V vs. Ag/AgCl.

85% of the iR drop was compensated for within the cell and calculated overpotentials for Tafel slopes were calculated using the following equation:

$$\eta = E^0 - E_{Ag/AgCl} + 0.217 + 0.059pH$$

where η is the overpotential, E^0 is the reversible potential ($E^0(C_2H_6) = 0.143$ V, $E^0(C_2H_4) = 0.08$ V, calculated using tabulated free energies), $E_{Ag/AgCl}$ is the applied potential, and pH is the measured electrolyte pH.

For calculation of the Faradaic efficiencies towards gas-phase products (FE_g), ideal gas conditions were assumed, and the following equation was applied:

$$FE_g = \alpha \frac{PC_g \dot{V}}{RT} \cdot \frac{N_e F}{I}$$

where α is a conversion factor, P is the pressure, C_g is the concentration of the gas phase component, \dot{V} is the CO_2 flow rate, R is the gas constant, T is the temperature, N_e is the number of electrons transferred per mole product, F is the Faraday constant, and I is the instantaneous current. For liquid phase components, the Faradaic efficiency (FE_l) was calculated as follows:

$$FE_g = \alpha \frac{PC_g \dot{V}}{RT} \cdot \frac{N_e F}{I}$$

where β is a conversion factor, C_l is the concentration of the liquid phase component, V is the total liquid volume, and Q is the total charge passed.

5.7.2 Product Analysis

Gas products were sampled every 20 min while liquid products were sampled after the full hour of chronoamperometry. The cell head space was vented directly to the sampling loop of a gas chromatograph (GC, 7890B, Agilent). The GC was fitted with Plot-Q and a 5Å sieve columns (Agilent) in series, TCD and methanizer/FID detectors, and UHP Ar (BOC) as the carrier gas.

The catholyte samples were collected and analyzed using ^1H nuclear magnetic resonance spectroscopy (NMR, A500a DD2 500 MHz, Agilent). Liquid products present in samples were quantified from a calibration curve using known standards and internal phenol and DMSO standards. Samples were prepared for NMR immediately after collection and kept refrigerated at 4 °C until ready for testing.

5.8 *In-situ* Raman Spectroscopy

5.8.1 Sample Preparation

The Raman studies were carried out in a customized cell using current collectors machined from C-10100 copper rod. The current collector served not only as the electrical contact, but also as the substrate for the active catalyst. To prepare the current collector, the exposed face was wet-polished with 3000 grit sandpaper and then with 5 μm colloidal alumina using a plastic lap followed by a polishing pad. The current collector was thoroughly rinsed with water and sonicated in ethanol for 10 min between each stage to remove abrasive media. The current collector was finally electropolished for 5 min in concentrated phosphoric acid at 1.9 V vs. a large copper counter electrode. To deposit the precursor coating (CuI or CuO) and obtain the active catalyst (ID-Cu or OD-Cu) on the prepared surface, a similar method to that described above was employed. For the CuI coatings, typically only 20 mg of iodine powder was used to limit thickness.

5.8.2 Raman Measurements

In-situ Raman spectroscopy was performed using a confocal Raman microscope (Horiba LabRAM HR Evolution) with a 60X (1.0 N.A) water-immersion objective (Olympus). A He-Ne laser (633 nm, CVI Melles Griot) and an 1800 gr cm^{-1} grating was used in all experiments. The potentiostatic tests were carried out using a customized Teflon cell with a leakless Ag/AgCl reference electrode and Pt wire counter electrode connected to a 760E potentiostat (CH Instruments). CO_2 -saturated 0.2 M sodium bicarbonate electrolyte was flowed through the cell via a peristaltic pump.

5.9 *In-situ* XAFS Measurements

X-ray absorption near edge spectra (XANES) and extended X-ray absorption fine structure (EXAFS) at Cu K-edge were collected at BL-17C1 at the National Synchrotron Radiation Research Center (NSRRC, Hsinchu, Taiwan). A customized reaction cell was adopted to carry out in-situ absorption spectroscopy measurements of

the Cu K-edge (8979 eV) in total-fluorescence-yield mode at ambient conditions. The measurements were conducted using a typical three-electrode setup with the same conditions as the electrochemical characterizations but performed in a specially designed Teflon container with a window sealed by Kapton tape. REX2000 software using ab initio-calculated phases and amplitudes from the program FEFF 8.2 was used for EXAFS fitting.

5.10 Theoretical Bond Length Calculations

All calculations were performed using density functional theory (DFT). The Perdew-Burke-Ernzerhof (PBE) functional was employed for electron exchange-correlation within the generalized gradient approximation (GGA), as implemented in the VASP code. The ionic cores were described by the projector-augmented wave (PAW) method. The cut-off energy for plane wave expansion was set to be 500 eV. During geometry optimization, the structures were relaxed to forces on the atoms smaller than 0.05 eV Å⁻¹. A smearing width of 0.18 eV and a (4 × 4 × 1) Monkhorst-Pack k-point grid were applied. The Tkatchenko-Scheffler method was adopted in all calculations to address Van der Waals (VdW) interactions between atoms.

The Cu (100) surface was modeled with a four-layered slab of a (3 × 3) supercell with 15 Å of vacuum space. Adsorption of reaction intermediates on the Cu (100) surface were calculated with the bottom two layers fixed. The bond lengths between O-bound intermediates and the catalytic Cu (100) surface were calculated by measuring the distance along the z direction between the coordinate of O atom and the average coordinate of the nearest four Cu atoms. Calculated bond lengths between the O-bound intermediates and individual coordinates of four nearest copper atoms along with the average Cu-O bond lengths are found in Table S5.3.

5.11 Supplementary Figures and Tables

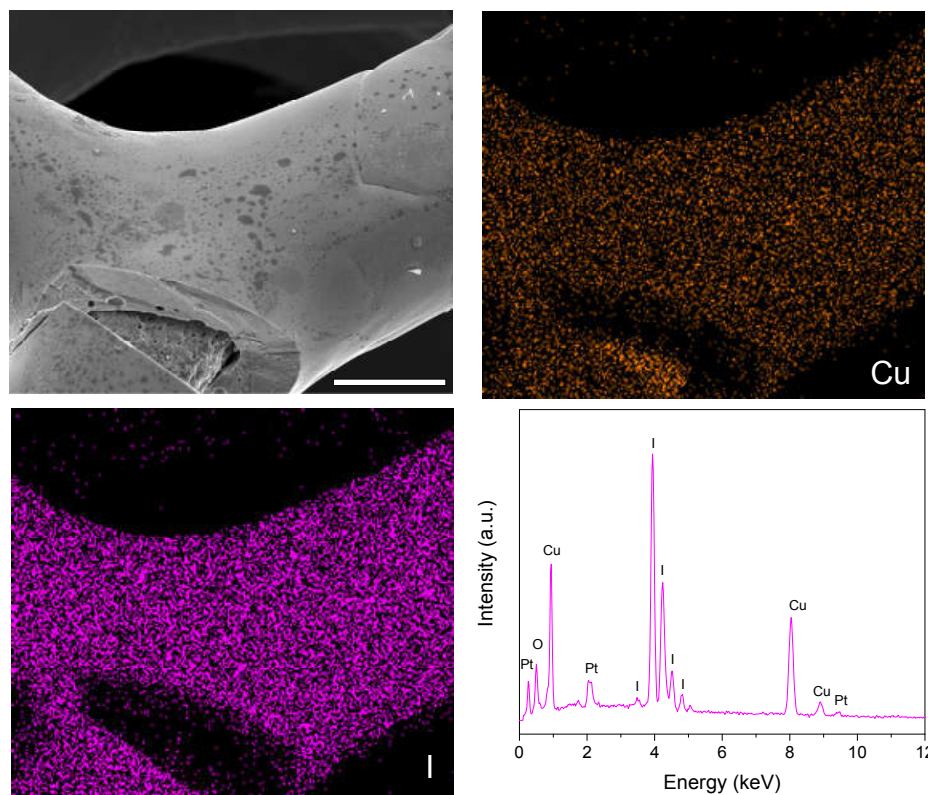


Figure S5.1 a) SEM image of the CuI precursor foam (scale bar = 50 μm) and elemental mapping of b) copper and c) iodine. d) Resultant EDS spectra of the mapping showing a composition of 50.60 at% copper and 49.40 at% iodine (Cu:I = 1:1).

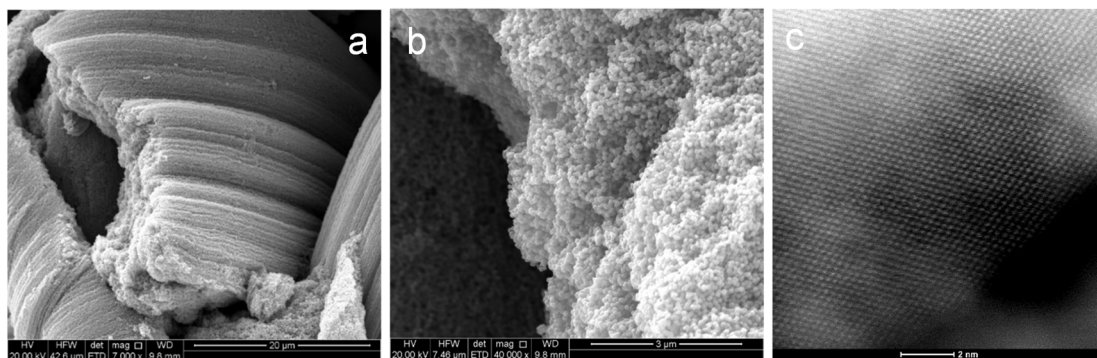


Figure S5.2 a) SEM image of the ID-Cu sample after the electrochemical reduction step (scale bar = 20 μm). The smooth CuI coating was converted into a layered structure made of nanoparticles depicted in panel b) of approximately 100 nm in size (scale bar = 3 μm). c) Representative HR-STEM image of the nanoparticles in the ID-Cu sample showing the cubic copper lattice (scale bar = 2 nm).

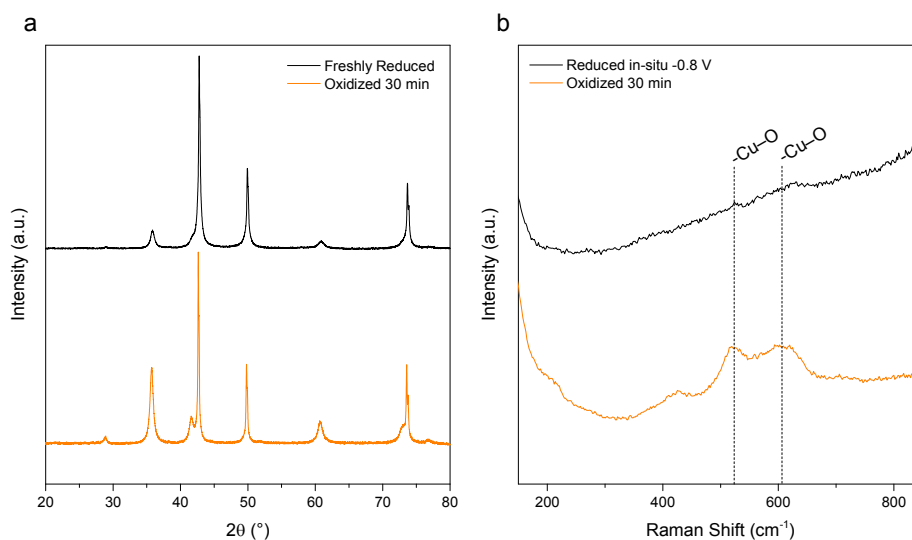


Figure S5.3 a) XRD patterns of ID-Cu showing the effects of 30 min air exposure. Reflections at $\sim 36^\circ$, 42° , and 61° are related to cuprous oxide (JCPDS Card No. 05-0667). b) In-situ Raman spectra of ID-Cu at OCP and at -0.8 V vs. Ag/AgCl demonstrating the reduction of oxides generated by 30 min air exposure.

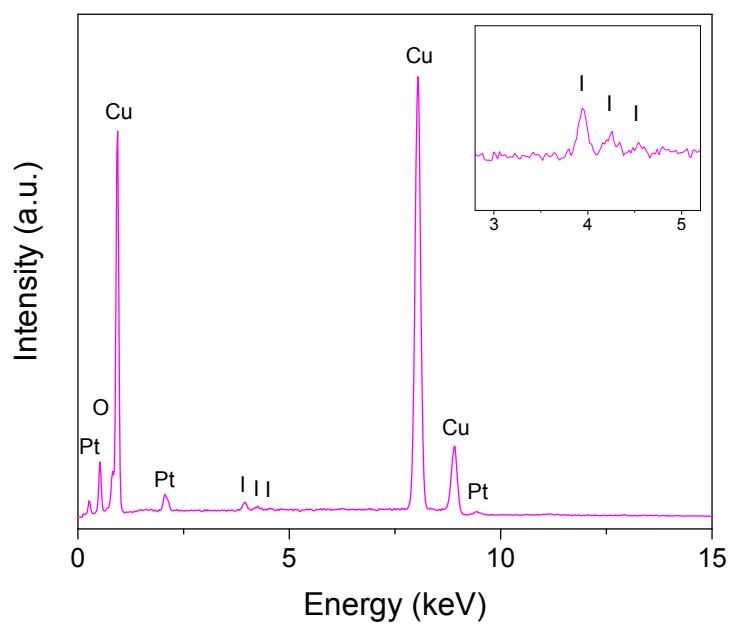


Figure S5.4 EDS spectra of ID-Cu after the electrochemical reduction step and after CO₂RR conditions (inset; enlarged region showing iodine peaks).

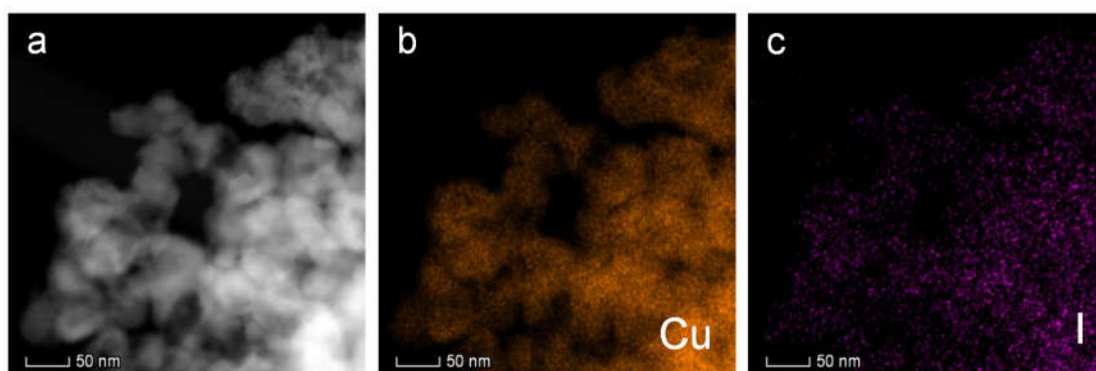


Figure S5.5 a) STEM image of ID-Cu and EDX elemental map exhibiting the distribution of b) copper and c) iodine throughout the sample.

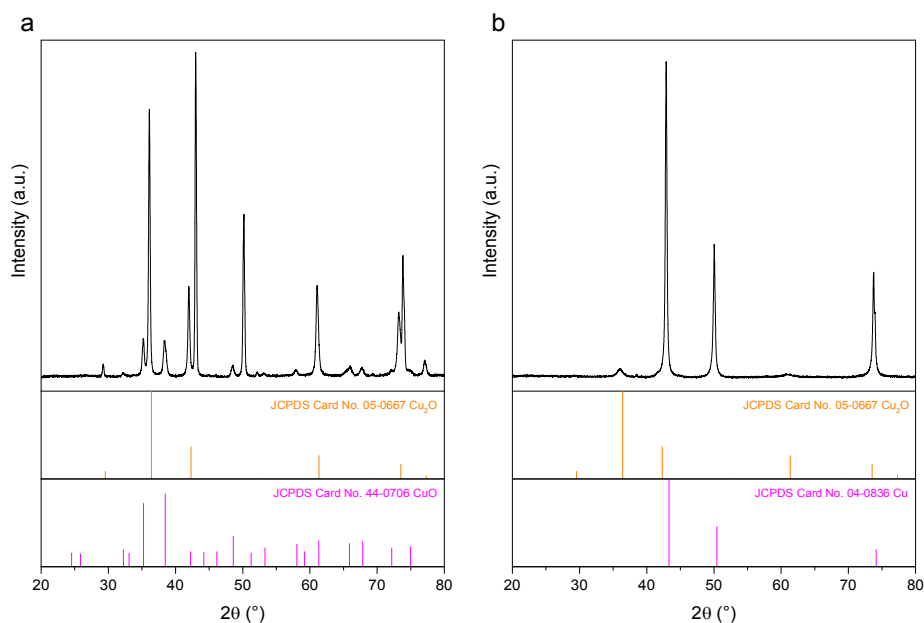


Figure S5.6 XRD patterns of a) the CuO precursor sample and b) the OD-Cu sample after the electrochemical reduction step.

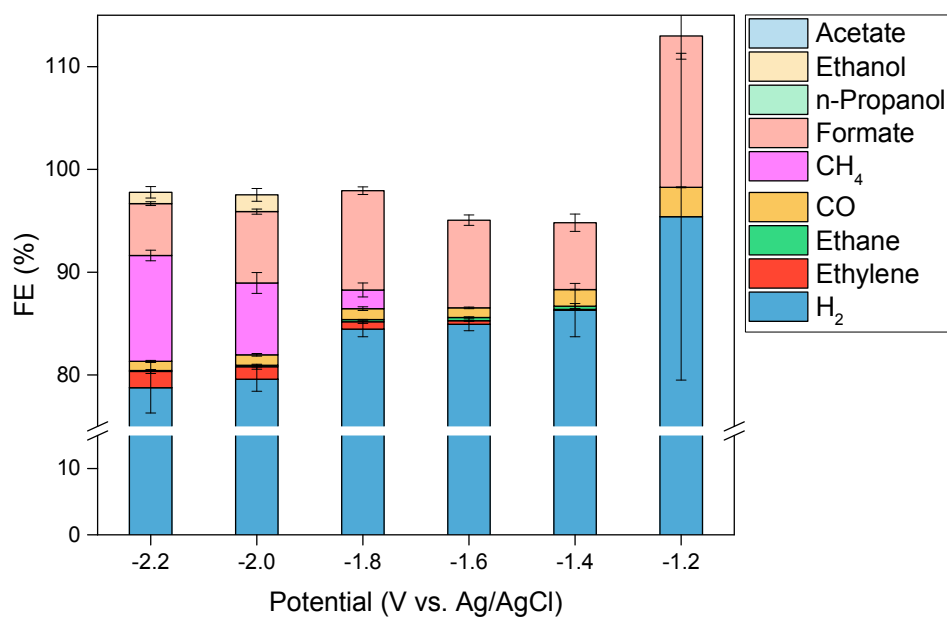


Figure S5.7 Faradaic efficiencies for various CO_2RR products and hydrogen over the entire potential range for the Cu support sample.

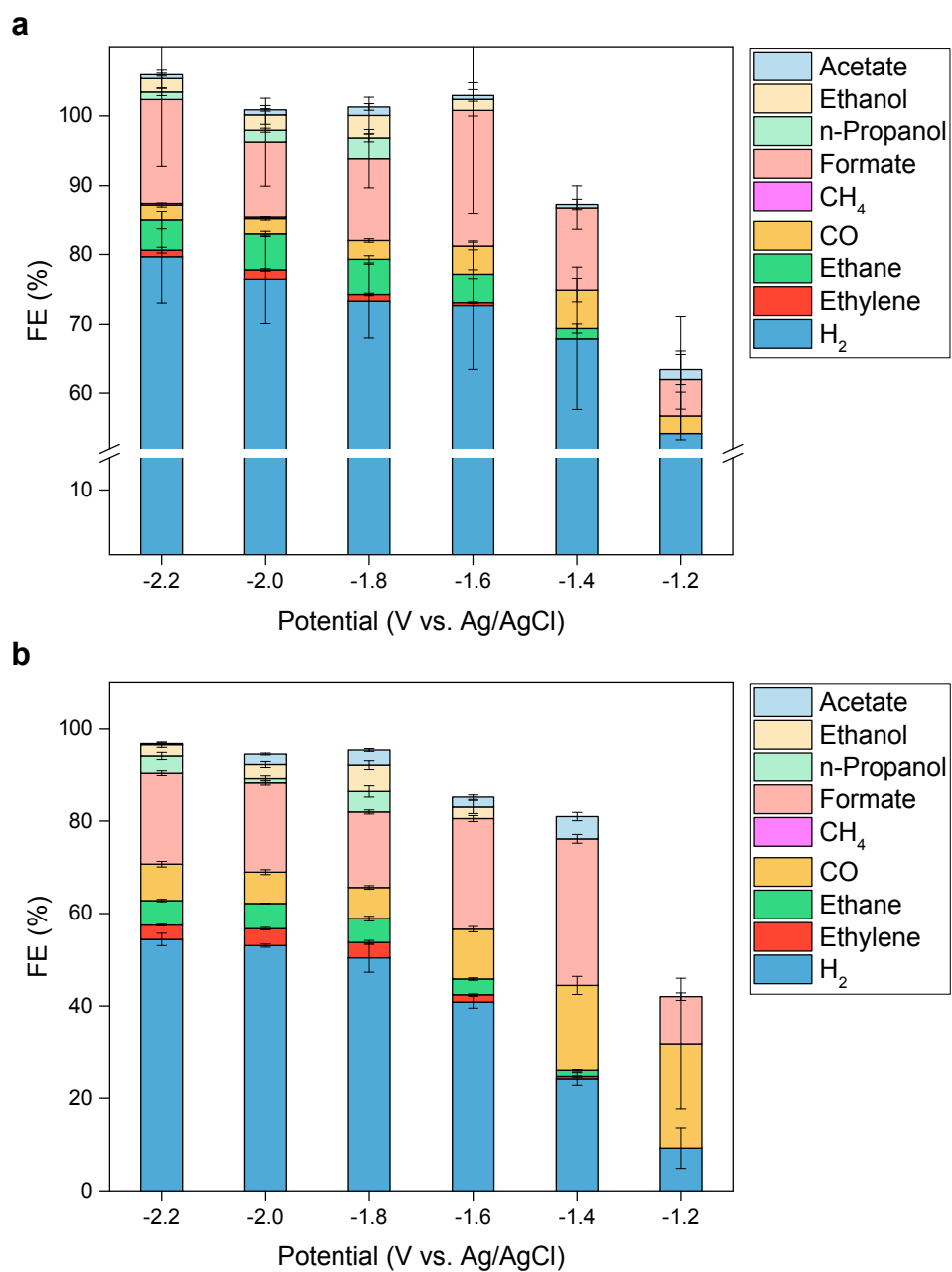


Figure S5.8 Faradaic efficiencies for various CO₂RR products and hydrogen over the entire potential range for a) ID-Cu and b) OD-Cu.

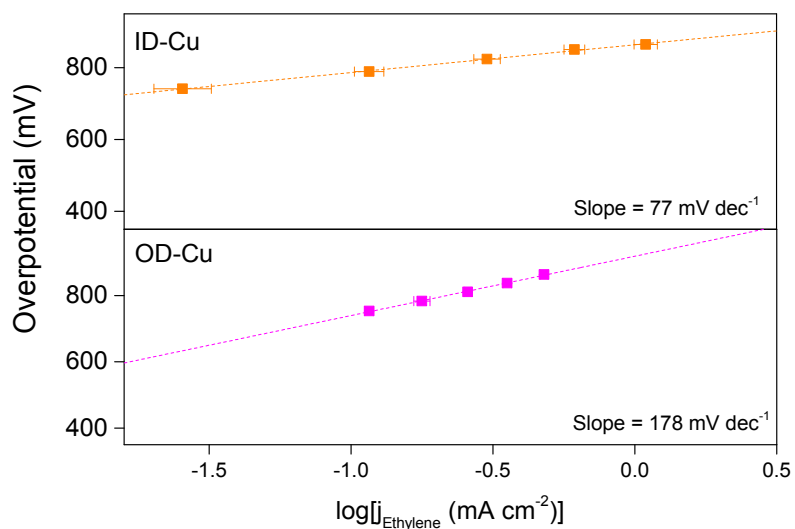


Figure S5.9 Tafel slopes of ID-Cu (top) and OD-Cu (bottom) samples towards ethylene production during CO_2RR conditions.

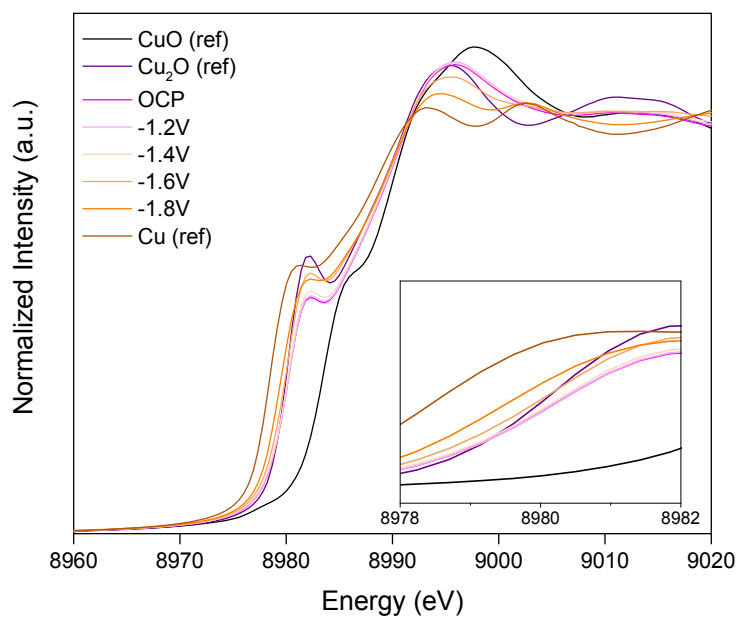


Figure S5.10 Potential dependent XANES spectra of the OD-Cu sample in CO_2RR conditions. Inset is a zoomed in frame showing the shift in absorption-edge position.

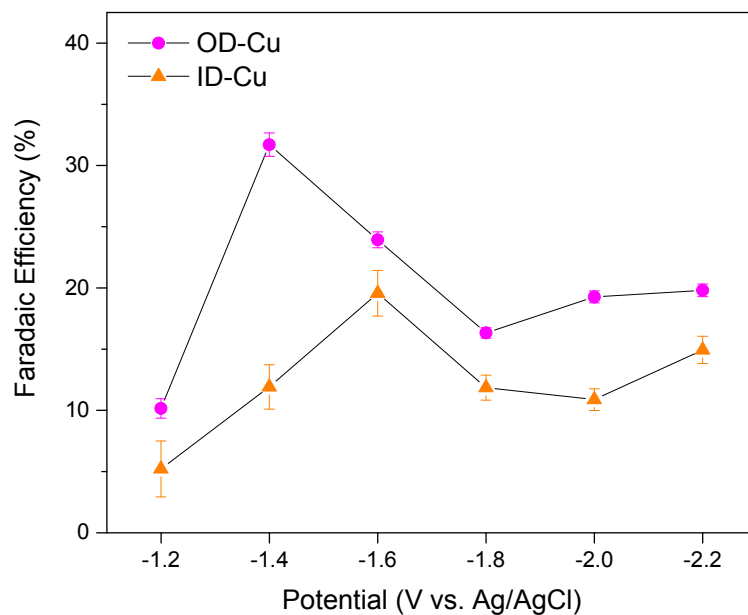


Figure S5.11 Potential dependent Faradaic efficiencies of ID-Cu and OD-Cu samples toward formate during CO₂RR conditions.

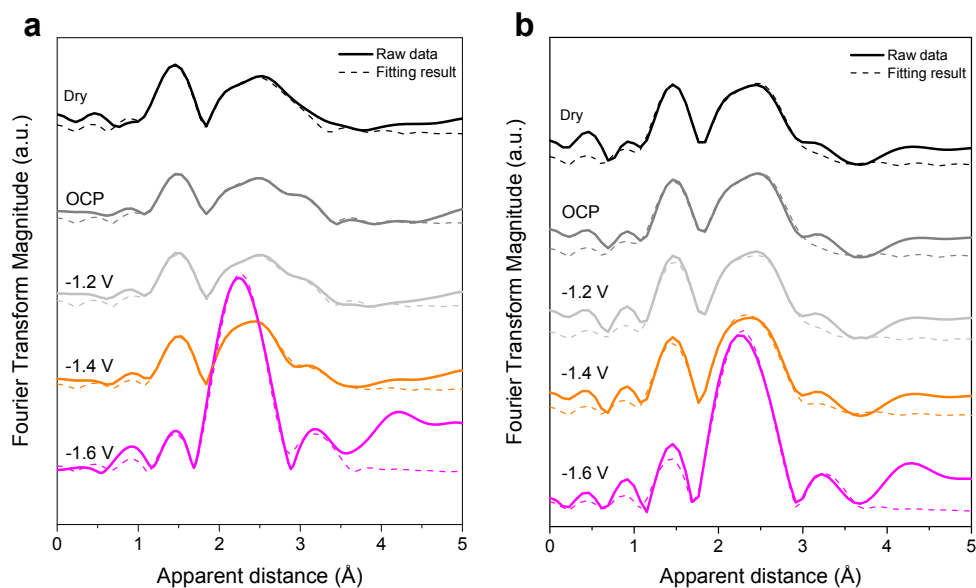


Figure S5.12 Potential dependent EXAFS spectra of a) ID-Cu and b) OD-Cu in the dry state and during CO₂RR conditions. Fitting results are also shown and fitting parameters for ID-Cu and OD-Cu can be found in Table S5.1 and Table S5.2, respectively.

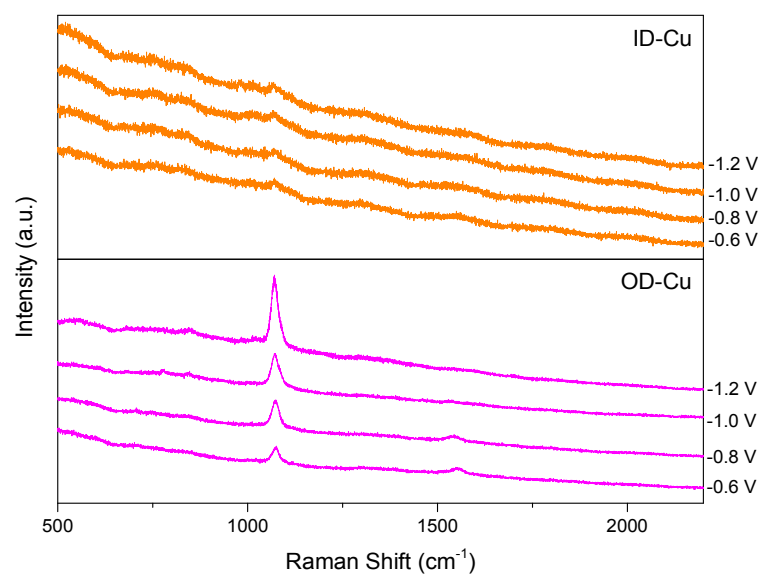


Figure S5.13 Potential dependent Raman spectra of ID-Cu (top) and OD-Cu (bottom) in N₂-saturated 0.2 M NaHCO₃.

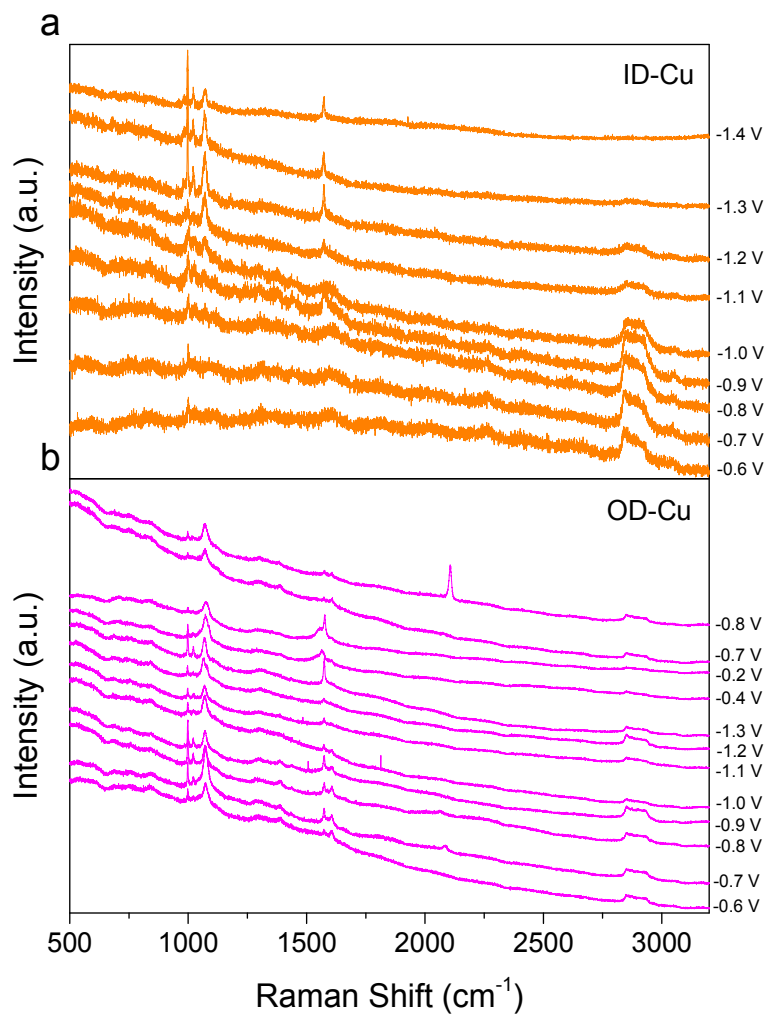


Figure S5.14 Potential dependent Raman spectra of ID-Cu (top) and OD-Cu (bottom) in CO_2 -saturated 0.2 M NaHCO_3 .

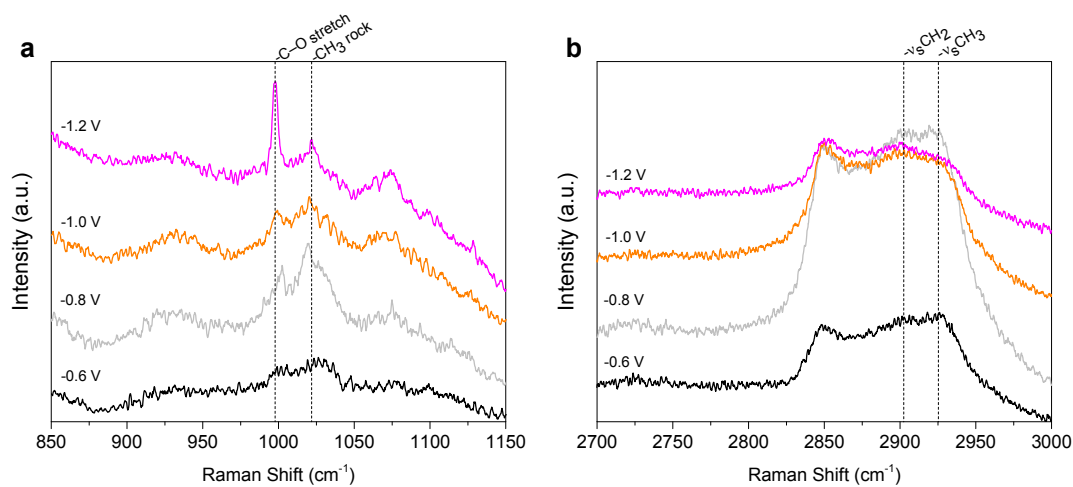


Figure S5.15 Potential dependent Raman spectra of an ID-Cu sample where the supporting electrolyte (N_2 -saturated 0.2 M NaCl) contains 20 mM of ethanol.

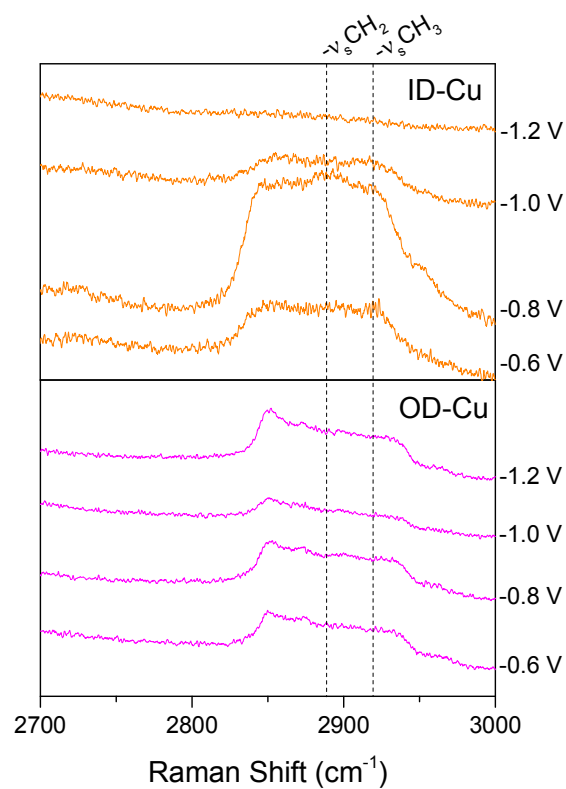


Figure S5.16 Comparison of the $-\text{CH}_x$ stretching region between ID-Cu (top) and OD-Cu (bottom) in CO_2 -saturated 0.2 M NaHCO_3 .

Table S5.1 EXAFS curve fitting results for ID-Cu.

Condition	Path	CN	R (Å)	ΔE	DW
ID-Cu: Dry	CU-O (Cu_2O)	1.0 (2)	1.84 (1)	3.1 (9)	0.0058 (3)
	CU-I	1.3 (3)	2.63 (2)	11.6 (9)	0.0082 (5)
	CU-CU (Cu_2O)	6.2 (8)	2.96 (2)	-5.2 (9)	0.012 (8)
ID-Cu: OCP	CU-O (Cu_2O)	1.1 (2)	1.89 (2)	8.1 (2)	0.0089 (5)
	CU-I	1.0 (4)	2.65 (2)	13.3 (1)	0.0068 (3)
	CU-CU(Cu_2O)	6.6 (8)	2.99 (3)	-1.1 (1)	0.012 (7)
ID-Cu: -1.2 V	CU-O (Cu_2O)	1.2 (2)	1.89 (1)	8.2 (9)	0.0085 (2)
	CU-O	0.1 (1)	2.13 (1)	-2.3 (1)	0.051 (1)
	CU-I	1.1 (3)	2.65 (1)	13.4 (2)	0.0073 (9)
	CU-CU (Cu_2O)	7.1 (9)	2.99 (2)	-1.5 (8)	0.012 (4)
ID-Cu: -1.4 V	CU-O (Cu_2O)	0.8 (1)	1.89 (3)	9.7 (1)	0.005 (7)
	CU-O	0.3 (2)	2.15 (1)	16.5 (1)	0.0073 (1)
	CU-CU (CU)	1.0 (2)	2.59 (2)	7.9 (1)	0.01 (8)
	CU-I	0.8 (3)	2.66 (2)	14.8 (1)	0.0057 (3)
	CU-CU (Cu_2O)	4.9 (7)	3.01 (2)	1.7 (8)	0.01 (7)
	CU-CU(CU)	0.5 (1)	3.59 (8)	-1.6 (5)	0.0059 (2)
ID-Cu: -1.6 V	CU-O (Cu_2O)	0.4 (1)	1.88 (2)	7.8 (2)	0.0065 (2)
	CU-CU (CU)	3.5 (3)	2.56 (1)	4.7 (1)	0.0073 (3)
	CU-CU (CU)	1.7 (1)	3.56 (2)	0.3 (7)	0.0096 (13)

Table S5.2 EXAFS curve fitting results for OD-Cu.

Condition	Path	CN	R (Å)	ΔE	DW
OD-Cu: Dry	CU-O (Cu ₂ O)	1.3 (1)	1.88 (1)	4.7 (7)	0.0065 (9)
	CU-CU (CU)	1.4 (4)	2.53 (2)	-2.7 (1)	0.0087 (6)
	CU-CU (Cu ₂ O)	7.5 (1)	2.97 (2)	3.6 (9)	0.015 (7)
OD-Cu: OCP	CU-O (Cu ₂ O)	1.3 (2)	1.89 (1)	5.5 (7)	0.0071 (1)
	CU-CU (CU)	1.3 (3)	2.52 (2)	-5.5 (9)	0.0086 (6)
	CU-CU (Cu ₂ O)	7.5 (1)	2.96 (1)	2.7 (7)	0.015 (6)
OD-Cu: -1.2 V	CU-O (Cu ₂ O)	1.3 (1)	1.89 (2)	7.3 (4)	0.0061 (2)
	CU-CU (CU)	1.3 (1)	2.52 (2)	-4.9 (4)	0.008 (6)
	CU-CU (Cu ₂ O)	7.8 (6)	2.98 (7)	4.0 (8)	0.015 (1)
OD-Cu: -1.4 V	CU-O (Cu ₂ O)	1.0 (1)	1.87 (3)	4.9 (5)	0.005 (2)
	CU-CU (CU)	1.8 (1)	2.55 (8)	1.8 (8)	0.0083 (5)
	CU-CU (Cu ₂ O)	5.3 (5)	3.00 (8)	3.5 (6)	0.015 (7)
OD-Cu: -1.6 V	CU-O (Cu ₂ O)	0.6 (1)	1.84 (2)	4.7 (7)	0.005 (6)
	CU-CU (CU)	3.8 (3)	2.56 (7)	4.7 (9)	0.0085 (3)
	CU-CU (CU)	1.9 (1)	3.56 (9)	0.03 (9)	0.0098 (1)
	CU-CU (Cu ₂ O)	3.0 (3)	3.00 (8)	9.1 (1)	0.015 (8)

Table S5.3 DFT calculated bond lengths for O-bound intermediates (*OCHCH₂, *OCHCH₃, *OCH₂CH₃) with an active Cu (100) facet.

O → Cu Distance (Å)	*OCHCH ₂	*OCHCH ₃	*OCH ₂ CH ₃
Cu1	2.200	2.993	2.181
Cu2	2.023	2.122	2.183
Cu3	2.649	3.531	2.171
Cu4	2.295	2.991	2.184
Cu centre	1.352	2.082	1.202
Average	2.292	2.909	2.180
Minimum	2.023	2.122	2.171

Chapter 6

Improving Ethylene Selectivity of Copper-Based Electrocatalysts for CO₂ Reduction by Gold Deposition

This Chapter includes work in preparation for publication by the authors. The aim of this Chapter is to explore design features of copper bi-metallic electrocatalysts and how to exploit these to improve selectivity towards multi-carbon products, namely ethylene. Oxide-derived copper (OD-Cu) materials are known to possess high electrocatalytic activity for C₂ products. However, improving their selectivity is still challenging. Here, electrochemistry combined with *in-situ* spectroscopy was used to determine the key reaction intermediates on OD-Cu and how introducing a secondary metal can help steer the reaction pathway to ethylene.

In this Chapter, OD-Cu nanocubes served as a platform for the improvement of selectivity towards ethylene. Improvement to ethylene selectivity was achieved through the electrodeposition of gold nanoparticles on the (110) edges and (111) corners of the nanocubes (OD-Cu-Au). The OD-Cu-Au nanocubes achieved a 26 % increase in faradaic efficiency towards ethylene and markedly better kinetics with a significantly smaller Tafel slope. From *in-situ* ATR-FTIR, we identified that OD-Cu-Au could maintain a higher population of linear-bonded *CO (CO_L) on its surface compared to OD-Cu, whose surface was dominated by bridge-bonded *CO (CO_B). Consequently, we believe that the deposited gold in OD-Cu-Au plays a key role in providing CO_L for spillover and coupling in a kinetically more favorable process.

Statement of Authorship

Title of Paper	Improving Ethylene Selectivity of Copper-Based Electrocatalysts for CO ₂ Reduction by Gold Deposition
Publication Status	<input type="checkbox"/> Published <input type="checkbox"/> Accepted for Publication <input type="checkbox"/> Submitted for Publication <input checked="" type="checkbox"/> Unpublished and Unsubmitted work written in manuscript style
Publication Details	A. Vasileff, Y. Zheng, S.Z. Qiao, Improving Ethylene Selectivity of Copper-Based Electrocatalysts for CO ₂ Reduction by Gold Deposition, 2020, <i>In Preparation</i>

Principal Author

Name of Principal Author (Candidate)	Anthony Vasileff		
Contribution to the Paper	Conducted the majority of experiments, analysed all the data, and wrote the majority of the paper.		
Overall percentage (%)	84		
Certification:	This paper reports on original research I conducted during the period of my Higher Degree by Research candidature and is not subject to any obligations or contractual agreements with a third party that would constrain its inclusion in this thesis. I am the primary author of this paper.		
Signature		Date	09/04/2020

Co-Author Contributions

By signing the Statement of Authorship, each author certifies that:

- the candidate's stated contribution to the publication is accurate (as detailed above);
- permission is granted for the candidate to include the publication in the thesis; and
- the sum of all co-author contributions is equal to 100% less the candidate's stated contribution.

Name of Co-Author	Yao Zheng		
Contribution to the Paper	8% Provided guidance and supervision from conception through to writing of the paper.		
Signature		Date	09/04/2020

Name of Co-Author	Shizhang Qiao		
Contribution to the Paper	8% Provided guidance and supervision from conception through to writing of the paper.		
Signature		Date	09/04/2020

6.1 Introduction

The electrochemical reduction of CO_2 to useful fuels, such as carbon monoxide, methane, and ethylene, is considered to be an elegant solution for closing the carbon cycle because it has the potential to couple renewable energy with CO_2 sequestration and conversion. Copper has been widely studied as an electrocatalyst for the CO_2 reduction reaction (CO_2RR) because of its low activity towards hydrogen evolution and its ability to drive carbon-carbon coupling towards multi-carbon products (ethylene, ethanol, etc.).^{1, 2} However, a crucial issue surrounding copper for this reaction is its generally poor selectivity. This has largely been explained by its relatively moderate binding of the carbon-bound intermediates involved in key reaction steps.³ Therefore, given the multitude of possible pathways and reaction intermediates involved in the CO_2RR process, it becomes very difficult to tune the selectivity of copper, and CO_2RR electrocatalysts generally.

Carbon monoxide (CO) is known to be a key intermediate in the CO_2RR pathway to multi-carbon products and work by Koper’s group strongly suggests that a coupling step involving adsorbed CO intermediates ($^*\text{CO}$) is the key carbon-carbon coupling mechanism.^{4, 5} CO usually binds to the copper surface in a linear mode (CO_L ; to one Cu) or in a bridge-bonded mode (CO_B ; to two or more Cu),⁶ and recent evidence suggests that a mixture of adsorption modes is preferable for $^*\text{CO}$ coupling.⁷ This is because calculated kinetic barriers for a $^*\text{CO}$ coupling step are larger when involving two CO_B .⁷ Therefore, optimizing the $^*\text{CO}$ coupling step will likely require specific morphologies and electronic characteristics which allow for the steady-state adsorption of CO in mixed adsorption modes and at a high coverage.^{1, 4}

Recently, oxide-derived copper (OD-Cu) electrocatalysts, i.e. copper oxides reduced to metallic copper, have become a large focus in this field due to their enhanced selectivity towards C_2 products.^{8, 9} Although it is not entirely clear why OD-Cu shows such an enhancement to C_2 selectivity, it may be due to factors like increased grain boundaries, residual oxygen, and/or the creation of favourable active sites.^{8, 10, 11} Therefore, OD-Cu presents as an ideal platform for optimizing the adsorption energetics

towards the key $^*\text{CO}$ intermediate, as discussed above. One such way to do this is through alloying of a secondary metal with the OD-Cu.¹² Further, if the secondary metal has a high selectivity towards CO (e.g. gold and silver) and can be deposited discretely on the surface of the OD-Cu, it is possible that CO can be generated and spill over to the OD-Cu for $^*\text{CO}$ coupling.¹³

In this study, we compare the selectivity of electrochemical CO_2 reduction to ethylene for OD-Cu nanocubes with and without electrodeposited gold nanoparticles (OD-Cu-Au). The gold nanoparticles, characterized using high-resolution scanning transmission electron microscopy (HR-STEM), were found to deposit predominantly on the (110) edges and (111) corners rather than on the (100) faces of the nanocubes. As a result of the deposited gold, a 26 % increase in Faradaic efficiency towards ethylene generation was achieved on OD-Cu-Au compared to OD-Cu. Significantly better kinetics towards ethylene generation were also achieved on OD-Cu-Au as evidenced by its smaller Tafel slope (240 mV dec^{-1} compared to 351 mV dec^{-1} for OD-Cu). In-situ attenuated total reflectance Fourier-transformed infrared (ATR-FTIR) spectroscopy identified key CO_L and CO_B intermediates on both catalysts. However, it was found that while CO_B was the dominant binding mode of CO on OD-Cu, both CO_B and CO_L binding modes were present on the OD-Cu-Au at potentials relevant to ethylene generation. Therefore, we believe that the deposited gold in OD-Cu-Au provided CO_L for spillover to the OD-Cu surface which could couple with CO_B in a kinetically more favorable process.

6.2 Results and Discussion

The OD-Cu and OD-Cu-Au nanocubes used in this study were derived from Cu_2O nanocubes which were electrochemically reduced and electrodeposited with gold in solution (Figure 6.1a). To begin with, the precursor Cu_2O nanocubes were obtained from a chemical co-precipitation approach.¹⁴ Briefly, copper (II) hydroxide precipitate was formed in solution from copper (II) sulfate which was then reduced to copper (I) oxide by sodium ascorbate. Crystal shape and growth was controlled using sodium dodecyl sulfate to produce nanocubes with six (100) facets. As shown in the scanning electron image (SEM; Figure 6.1b and Figure S6.1), the Cu_2O nanocubes were relatively homogeneous in size with an average edge length of 57.0 nm (s.d. 6.6 nm) and HR-STEM identified the Cu_2O (100) facets with lattice spacing of 2.2 Å (Figure 6.1c).

After electrochemical reduction of the Cu_2O nanocubes at -0.8 V vs. Ag/AgCl, conversion to metallic copper is evidenced by the X-ray diffraction patterns (Figure 6.1d). Reduction of the Cu_2O nanocubes was also a homomorphic process as the OD-Cu nanocubes maintained a similar cubic morphology (Figure 6.1e and Figure S6.2). When gold (III) chloride was introduced into the electrochemical cell during reduction of the Cu_2O nanocubes, we observed deposition of nanoparticles on the OD-Cu nanocubes (Figure S6.3). Gold nanoparticles of approximately 3-5 nm were identified from the HR-STEM images with (111) lattice spacing of 2.4 Å (Figure 6.2a-b). Interestingly, the gold nanoparticles tended to deposit on the edges of the nanocubes rather than the faces which was clearly observed from the STEM elemental mapping (Figure 6.2c-d). Formation of (110) and (111) facets occurs on the edges and corners, respectively, of the nanocubes as perfect corner geometry is generally not obtainable. These are of higher surface energy compared to the (100) facets,¹⁵ and can preference galvanic replacement and deposition of such nanoparticles in order to reduce the surface energy.^{16, 17} Experimental studies have shown that (100) facets are the most active facet for CO_2 reduction to ethylene.^{18, 19} Therefore, deposition of gold nanoparticles on the edges which blocks the (110) and (111) facets, rather than on the nanocube faces, may be beneficial for providing CO spillover to the highly selective (100) facets.

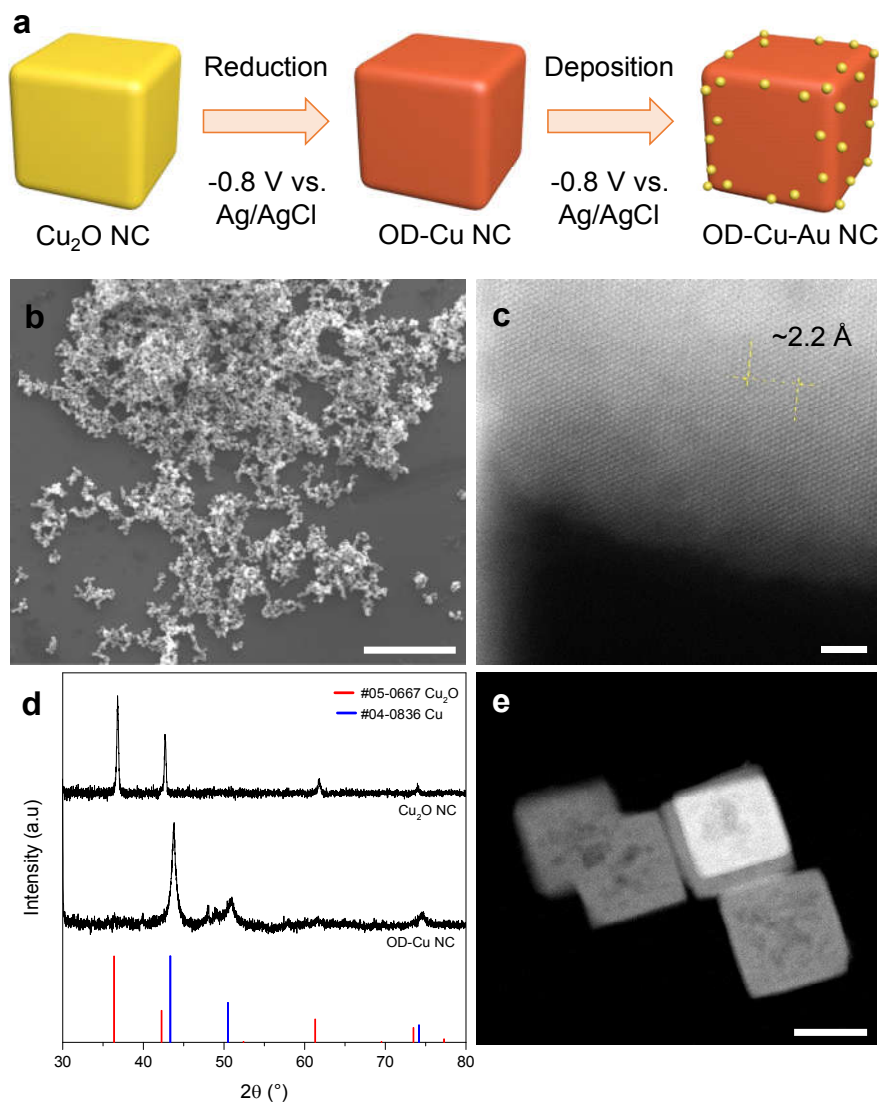


Figure 6.1 a) Synthesis process for OD-Cu and OD-Cu-Au involving electrochemical reduction of Cu_2O nanocubes and subsequent electrochemical deposition of Au. b) SEM image of a representative sample of the Cu_2O nanocubes (scale bar is 2 μm) and c) HR-STEM image of the Cu_2O nanocubes showing the (100) lattice spacing over 10 atomic columns (scale bar is 2 nm). d) Diffraction patterns of the Cu_2O nanocubes and the OD-Cu nanocubes after electrochemical reduction. e) STEM image of the OD-Cu nanocubes after electrochemical reduction (scale bar is 50 nm).

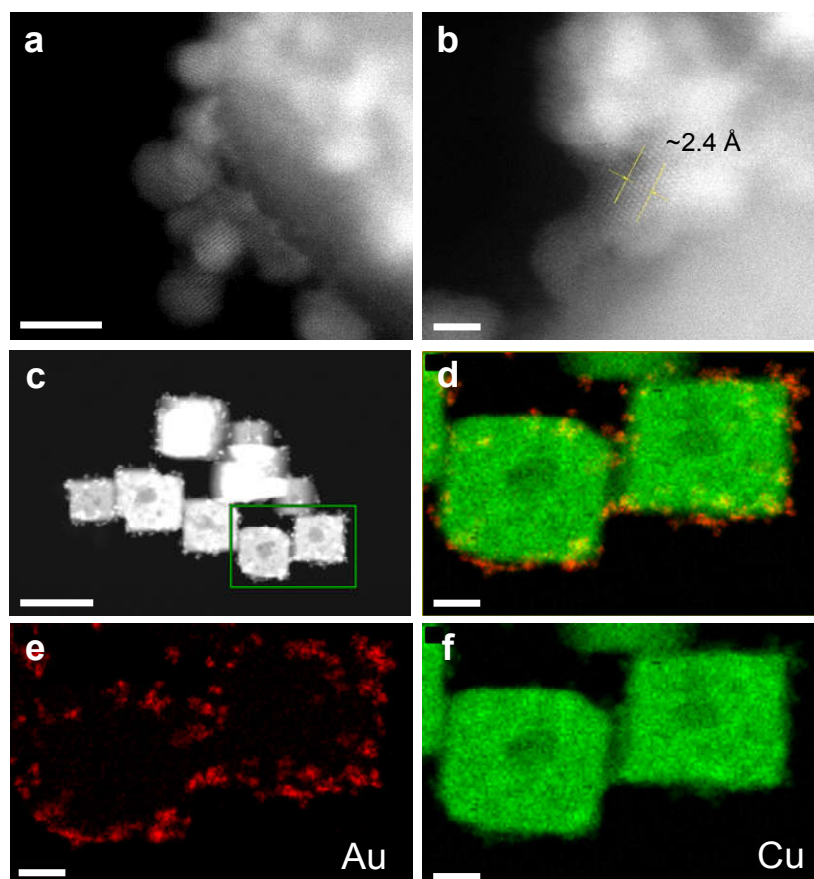


Figure 6.2 HR-STEM images of the OD-Cu-Au nanocubes showing a) the interface between the OD-Cu and gold nanoparticles (scale bar is 5 nm) and b) the spacing of the gold (111) lattice over 5 atomic columns (scale bar is 2nm). c) EDX mapping area (outlined with a green box) performed on OD-Cu-Au for d) combined gold and copper mapping, e) gold and f) copper. The scale bar in panel c is 100 nm, and 20 nm for panels d-f.

The electrocatalytic activity of the catalysts towards CO₂ reduction to ethylene was assessed in a typical H-cell with 0.1 M KHCO₃ as the supporting electrolyte. We found that OD-Cu-Au not only had a larger cathodic current density in the range of potentials investigated (Figure S6.4), but also achieved significantly different Faradaic efficiencies (FE) to various reduction products (Figure 6.3a-b). While OD-Cu reached a maximum FE of 27.7 % towards ethylene (Figure 6.3a), OD-Cu-Au reached an FE of 35.0 % (Figure 6.3b) which is a ~26 % increase in efficiency. Interestingly, OD-Cu-Au was also significantly less selective towards hydrogen evolution. A sharp increase in FE for hydrogen evolution is observed for OD-Cu (28 to 50 %) at potentials more negative than -2.0 V vs. Ag/AgCl, while they remained relatively constant (19 to 23

%) on OD-Cu-Au. This demonstrates the significant increase in selectivity towards CO₂ reduction products from the deposition of gold on the nanocubes.

When analysing the ethylene partial current on both catalysts (Figure 6.3c), we observe that it increased across the entire potential range for OD-Cu-Au while it began to decrease for OD-Cu at -2.1 V vs. Ag/AgCl. This loss in ethylene partial current for OD-Cu may be caused by onset of diffusion limits in the system, preventing further increases to transport and reduction of CO₂ on the surface. This may also explain the increase in hydrogen evolution at these potentials. From Figure 6.3d, the Tafel slopes also indicate that ethylene generation was significantly more kinetically favourable on OD-Cu-Au (240 mV dec⁻¹) compared to OD-Cu (351 mV dec⁻¹). It is widely accepted that a *CO coupling step is the rate determining step in the ethylene pathway.⁴ In this system, we also observe that the FE and partial current towards CO are generally higher on OD-Cu-Au compared to OD-Cu (Figure S6.5). This is not surprising, given the high selectivity of gold for CO₂ reduction to CO.² However, increased generation of *CO on OD-Cu-Au (due to the deposition of gold) may result in spill over of *CO intermediates and enhance *CO coupling kinetics as observed here.

To gain a better mechanistic insight into this catalyst system, in-situ ATR-FTIR studies were conducted on OD-Cu and OD-Cu-Au under CO₂RR conditions. The in-situ infrared spectra were collected during chronoamperometric tests in CO₂ saturated 0.1 M KHCO₃ solution between -1.0 and -2.2 V vs. Ag/AgCl (100 mV steps) and are shown in Figure 6.4. Full infrared spectra can be found in Figure S6.6. From these spectra, we observe two bands of interest arise around 1876 and 2080 cm⁻¹, which likely correspond to C≡O stretching of bridge-bonded (CO_B) and linear/terminal (CO_L) adsorption modes of CO, respectively.^{6, 20} The other prominent band observed (~2340 cm⁻¹), is likely due to dissolved carbon dioxide.²¹ In Figure 6.4a-b, onset of CO_L begins around -1.0 V for OD-Cu and increases significantly in intensity to -1.3 V. At this point, the CO_B band begins to appear and becomes increasingly more intense as the potential is stepped more negatively. At the same time, the CO_L band decays almost to zero. Therefore, it is apparent that CO_B becomes the dominant adsorption mode on OD-Cu at high overpotentials.

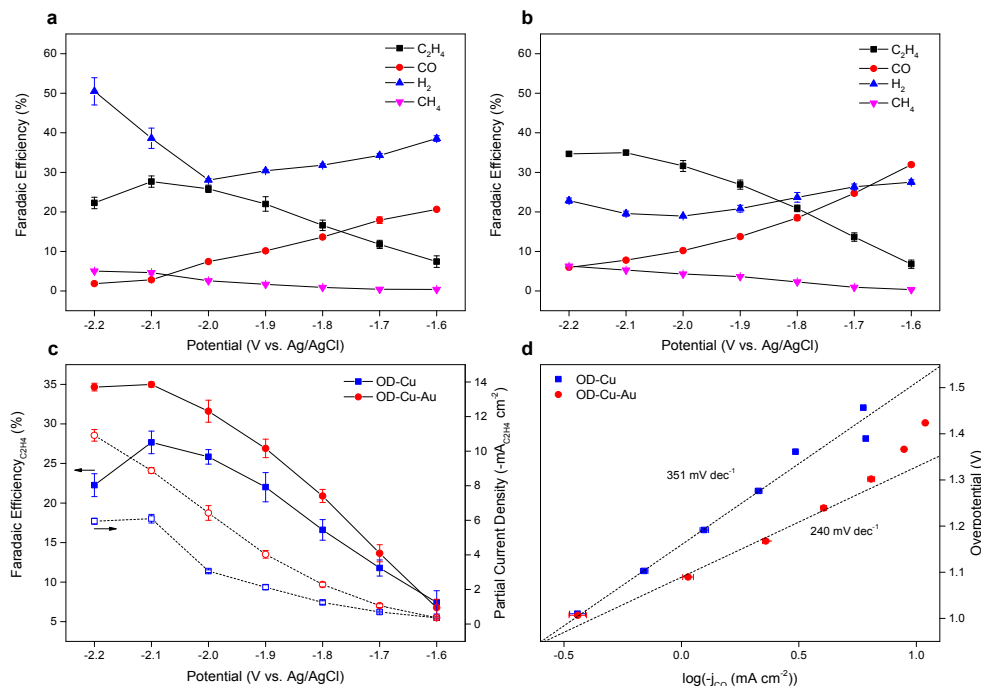


Figure 6.3 Measured Faradaic efficiencies towards gas products on a) OD-Cu and b) OD-Cu-Au. c) Comparison of partial current densities and Faradaic efficiencies towards ethylene on OD-Cu and OD-Cu-Au across the potential range studied. d) Comparison of Tafel slopes towards ethylene production for OD-Cu and OD-Cu-Au samples.

For OD-Cu-Au, we observe in Figure 6.4c-d that the CO_L band similarly appears at lower overpotentials with the absence of the CO_B band. However, in contrast to OD-Cu, the CO_L band maintained significant intensity with increasing overpotential. As a result, a mixture of CO_L and CO_B adsorption states were present on OD-Cu-Au at high overpotentials, corresponding to conditions where onset and significant generation of ethylene occurred (Figure 6.3). From Figure S6.7, it is also clear that the fraction of $*CO$ bound as CO_L was greater on OD-Cu-Au compared to OD-Cu throughout the entire potential range. As shown in a previous study, the kinetic barrier for coupling a linear-bonded $*CO$ with a bridge-bonded $*CO$ (0.72 eV) is smaller compared to coupling of two bridge-bonded $*CO$ (0.82 eV).⁷ Others have also suggested that bridge-bonded $*CO$ is inert to further reduction, although here they focused on $*CO$ hydrogenation to formyl ($*CHO$) and not $*CO$ coupling.⁶ Therefore, it is possible that the deposited gold in OD-Cu-Au can effectively provide $*CO$ (in the form of CO_L) to

the OD-Cu surface for either direct coupling or for reaction with the local CO_B population. This in turn could reduce the kinetic barrier to *CO coupling and improve the rate and selectivity towards ethylene, as observed in Figure 6.3d.

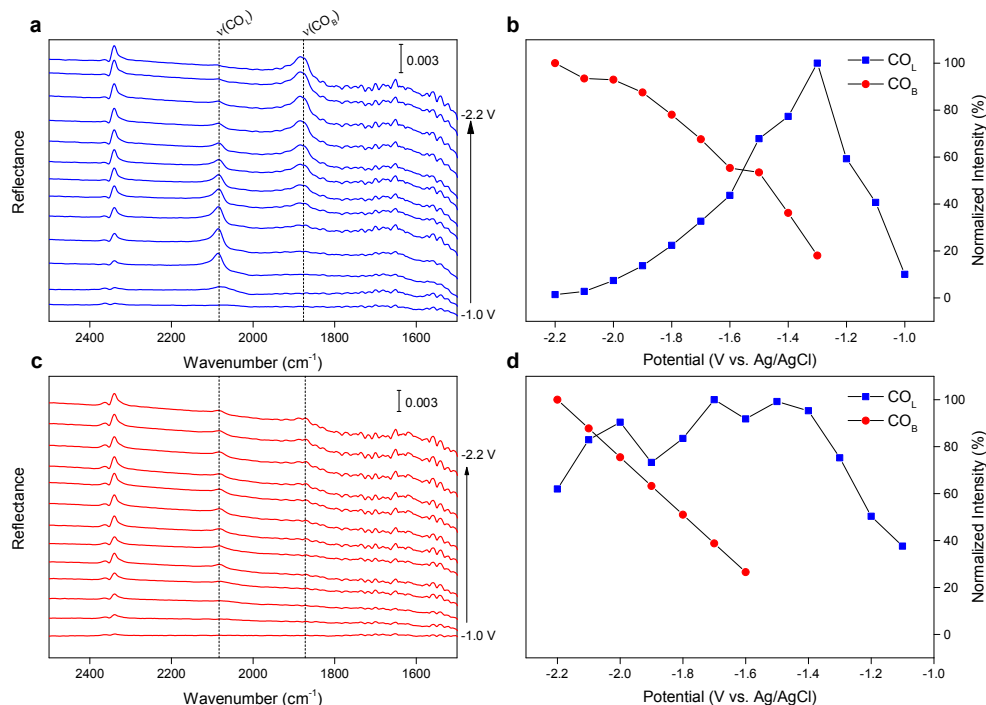


Figure 6.4 In-situ ATR-FTIR spectra in CO₂-saturated 0.1 M KHCO₃ for a-b) OD-Cu and c-d) OD-Cu-Au samples. Panels b and d show the corresponding normalized intensities (normalized to the potential of greatest intensity) of the integrated CO_L and CO_B peaks across the entire potential range studied. Background spectra were obtained at -0.8 V v. Ag/AgCl and all potentials are referenced to Ag/AgCl.

6.3 Conclusion

In summary, oxide-derived copper (OD-Cu) nanocubes with electrodeposited gold nanoparticles (OD-Cu-Au) were synthesized and utilized for the electrocatalytic reduction of CO₂ to ethylene. Compared to the OD-Cu nanocubes without gold deposition, the OD-Cu-Au nanocubes achieved a greater overall cathodic current and a 26 % increase in Faradaic efficiency towards ethylene generation. The OD-Cu-Au nanocubes also exhibited a significantly smaller Tafel slope towards the generation of ethylene (240 mV dec⁻¹) compared to that of the OD-Cu nanocubes (351 mV dec⁻¹). This indicated a significant enhancement to the kinetics governing ethylene formation as a result of gold deposition. From in-situ ATR-FTIR, it was found that while bridge-bonded *CO became the dominant CO adsorption mode on OD-Cu nanocubes at high overpotentials, a mixture of linear and bridge-bonded *CO was present on the surface of OD-Cu-Au. We postulate that the deposited gold in OD-Cu-Au provided linear *CO for spillover to the OD-Cu surface and coupling with the local population of bridge-bonded *CO. As a result of this, the kinetic barrier to *CO coupling (the rate determining step of ethylene generation) was reduced which in turn increased the rate and selectivity to ethylene formation.

6.4 Acknowledgment

The authors gratefully acknowledge financial support from the Australian Research Council (ARC) through Discovery Project and Linkage project programs (FL170100154, DP160104866, DP170104464, DE160101163 and LP160100927) and the Australian Government through a Research Training Program Scholarship. Coating of the silicon prism for ATR-FTIR was performed at the South Australian Node of the Australian National Fabrication Facility.

6.5 References

1. Y. Zheng, A. Vasileff, X. Zhou, Y. Jiao, M. Jaroniec, S.-Z. Qiao, *J. Amer. Chem. Soc.* 2019, *141*, 7646.
2. Y. Hori, H. Wakebe, T. Tsukamoto, O. Koga, *Electrochim. Acta* 1994, *39*, 1833.
3. A. A. Peterson, J. K. Norskov, *J. Phys. Chem. Lett.* 2012, *3*, 251.
4. F. Calle-Vallejo, M. T. M. Koper, *Angew. Chem. Int. Ed.* 2013, *52*, 7282.
5. E. Pérez-Gallent, M. C. Figueiredo, F. Calle-Vallejo, M. T. M. Koper, *Angew. Chem. Int. Ed.* 2017, *56*, 3621.
6. C. M. Gunathunge, V. J. Ovalle, Y. Li, M. J. Janik, M. M. Waegele, *ACS Catal.* 2018, *8*, 7507.
7. F. Li, A. Thevenon, A. Rosas-Hernández, Z. Wang, Y. Li, C. M. Gabardo, A. Ozden, C. T. Dinh, J. Li, Y. Wang, J. P. Edwards, Y. Xu, C. McCallum, L. Tao, Z.-Q. Liang, M. Luo, X. Wang, H. Li, C. P. O'Brien, C.-S. Tan, D.-H. Nam, R. Quintero-Bermudez, T.-T. Zhuang, Y. C. Li, Z. Han, R. D. Britt, D. Sinton, T. Agapie, J. C. Peters, E. H. Sargent, *Nature* 2020, *577*, 509.
8. J. E. Pander III, D. Ren, Y. Huang, N. W. X. Loo, S. H. L. Hong, B. S. Yeo, *ChemElectroChem* 2018, *5*, 219.
9. D. Raciti, C. Wang, *ACS Energy Lett.* 2018, *3*, 1545.
10. X. Feng, K. Jiang, S. Fan, M. W. Kanan, *ACS Cent. Sci.* 2016, *2*, 169.
11. Y. Lum, J. W. Ager, *Nat. Catal.* 2019, *2*, 86.
12. A. Vasileff, C. Xu, Y. Jiao, Y. Zheng, S.-Z. Qiao, *Chem* 2018, *4*, 1809.
13. J. Gao, H. Zhang, X. Guo, J. Luo, S. M. Zakeeruddin, D. Ren, M. Grätzel, *J. Amer. Chem. Soc.* 2019, *141*, 18704.
14. S. Thoka, A.-T. Lee, M. H. Huang, *ACS Sustain. Chem. Eng.* 2019, *7*, 10467.
15. Z. Wang, G. Yang, Z. Zhang, M. Jin, Y. Yin, *ACS Nano* 2016, *10*, 4559.
16. X.-W. Liu, *Langmuir* 2011, *27*, 9100.
17. Z. Zhang, J. Ahn, J. Kim, Z. Wu, D. Qin, *Nanoscale* 2018, *10*, 8642.
18. Y. Huang, A. D. Handoko, P. Hirunsit, B. S. Yeo, *ACS Catal.* 2017, *7*, 1749.
19. N.-T. Suen, Z.-R. Kong, C.-S. Hsu, H.-C. Chen, C.-W. Tung, Y.-R. Lu, C.-L.

- Dong, C.-C. Shen, J.-C. Chung, H. M. Chen, *ACS Catal.* 2019, 9, 5217.
20. G. Socrates, *Infrared and Raman Characteristic Group Frequencies: Tables and Charts*, John Wiley and Sons, Middlesex 2001.
21. B. Z. Nikolic, H. Huang, D. Gervasio, A. Lin, C. Fierro, R. R. Adzic, E. Yeager, *J. Electroanal. Chem. Interf. Electrochem.* 1990, 295, 415.

Chapter 6

Supporting Information

6.6 Material Synthesis and Characterization

6.6.1 Materials

Copper (II) sulfate pentahydrate ($\geq 98\%$), L(+)-sodium ascorbate ($\geq 98\%$), sodium dodecyl sulfate ($\geq 99\%$), sodium hydroxide ($\geq 98\%$), gold (III) chloride trihydrate ($\geq 99.9\%$), and potassium bicarbonate ($\geq 99.7\%$) were purchased from Sigma-Aldrich and used without further purification. Undenatured ethanol (anhydrous, $\geq 99.5\%$) was purchased from Chem-Supply and used without further purification. Carbon paper (Toray 030) used for electrode fabrication was purchased from Fuel Cell Store. Ultra-pure water ($18.2\text{ M}\Omega\cdot\text{cm}$, PURELAB Option-Q) was used in all experiments and laser grade CO_2 (99.995 %) was purchased from BOC and used in all electrochemical experiments.

6.6.2 Electrocatalyst Synthesis

Preparation of Copper (I) Oxide Nanocubes:

Cu_2O nanocubes of approximately 50 nm in size were prepared using a reported method.

¹ In a typical synthesis, 9.36 mL of water was added to a specimen container containing 58 mg of sodium dodecyl sulfate. The contents were stirred (magnetic stirring, 600 rpm) for 5 min to dissolve the sodium dodecyl sulfate to which 100 μL of 0.1 M copper (II) sulfate was then added. After the solution was stirred for a subsequent 5 min, 40 μL of 1.0 M sodium hydroxide solution was added and allowed to stir for another minute. Finally, 0.5 mL of 0.2 M sodium ascorbate solution was added to the container, stirred for 5 min, and then allowed to age (without stirring) for 10 min. The Cu_2O nanocubes

were collected via centrifugation (10,000 rpm, 10 min) and then washed via centrifugation with three aliquots of water (2 mL each) and three aliquots of ethanol (2 mL each). The nanocubes were then stocked at 2 mg mL⁻¹ in ethanol for electrochemical tests and 1.25 mg mL⁻¹ in water for ATR-FTIR tests.

Preparation of OD-Cu and OD-Cu-Au Nanocubes:

To obtain the usable catalysts, the Cu₂O nanocubes were first deposited on carbon paper cut to 15 x 5 mm. On either side of a 5 x 5 mm working area of the carbon paper, 20 μ L of the nanocube suspension in ethanol (2 mg mL⁻¹) was deposited. The deposited nanocubes were then dried in a vacuum oven at 50°C for 12 h. The Cu₂O nanocubes on carbon paper were applied directly as the working electrode in a three-electrode system as described in the Section 6.7.1. The OD-Cu nanocubes were then obtained by applying a potential of -0.8 V vs. Ag/AgCl for one hour. The OD-Cu-Au nanocubes were obtained in a similar manner, except that after 30 min of applying the reduction potential, 160 μ L of 0.1 mM gold (III) chloride solution was added to the cathode compartment.

6.6.3 Material Characterization

The crystal structure of the samples was characterized by X-ray diffraction (Rigaku MiniFlex, Cu K α). Electron imaging was carried out using scanning electron microscopy (FEI Quanta 450, 20 kV) and transmission electron microscopy under STEM mode (FEI Titan Themis, 200 kV). Elemental mapping of the samples was conducted with SDD EDS detector (Oxford Instruments).

6.7 Electrochemical Characterization

6.7.1 Electrochemical Measurements

Electrochemical measurements were performed on a 760E potentiostat (CH Instruments). The catalysts as described above in Section 6.6.2 were applied directly as the working electrode in a three-electrode cell with Ag/AgCl reference electrode (4.0 M KCl) and RuO₂ coated titanium mesh counter electrode. Cathode and anode compartments were separated by a Nafion 117 cation exchange membrane and 0.1 M potassium bicarbonate solution was used as the electrolyte in all electrochemical experiments. In a typical electrochemical test, the catholyte was stirred and bubbled with CO₂ for 10 min at 100 sccm to remove air and saturate the electrolyte. Following this, the gas flow rate was reduced to 10 sccm and chronoamperometry was performed for 1 h at potentials between -1.6 and -2.2 V vs. Ag/AgCl.

For calculation of the Faradaic efficiencies towards ethylene and other gas-phase products (FE_g), ideal gas conditions were assumed, and the following equation was applied:

$$FE_g = \alpha \frac{PC_g \dot{V}}{RT} \cdot \frac{N_e F}{I}$$

where α is a conversion factor, P is the pressure, C_g is the concentration of the gas phase component, \dot{V} is the CO₂ flow rate, R is the gas constant, T is the temperature, N_e is the number of electrons transferred per mole product, F is the Faraday constant, and I is the instantaneous current.

6.7.2 Product Analysis

Gas products were sampled every 20 min during chronoamperometry. The cell head space was vented directly to the sampling loop of a gas chromatograph (GC, 7890B, Agilent). The GC was fitted with Plot-Q and a 5Å sieve columns (Agilent) in series, TCD and methanizer/FID detectors, and UHP Ar (BOC) as the carrier gas.

6.8 *In-situ* ATR-FTIR

6.8.1 Sample Preparation

ATR-FTIR measurements were conducted using a 60° silicon prism (Pike Technologies). To establish an electrical contact on the reflecting pane of the silicon prism, a 50 nm layer of gold was sputter coated under ultra-high vacuum conditions. To adhere the gold layer to the silicon, a 10 nm chromium adhesion layer was coated first. Gold was chosen for the electrical contact due to its inertness and because it does not show adsorption bands under normal CO₂RR conditions.²

On this gold layer, 50 μ L of the Cu₂O nanocube suspension in water (1.25 mg mL⁻¹) was deposited and left to dry slowly to form an even layer of nanocubes on the surface. The silicon prism was then assembled into a modified Teflon electrochemical cell (Pike Technologies) fitted with a low-profile leakless Ag/AgCl electrode (Pine Research) and Pt wire serving as the reference and counter electrodes, respectively. The cell was filled with 5.5 mL of 0.1 M potassium bicarbonate solution and the active OD-Cu nanocubes were obtained using a similar electrochemical reduction technique to that above. To obtain the OD-Cu-Au nanocubes, similar to that above, gold (III) chloride solution was introduced into the cell during the reduction step. An amount of 0.2 mmol mg⁻¹ (gold ions to Cu₂O nanocubes deposited) was maintained between electrochemical tests and ATR-FTIR tests.

6.8.2 ATR-FTIR Measurements

In-situ ATR-FTIR was performed with a Thermo-Fisher Nicolet iS20 equipped with a liquid nitrogen cooled MCT-A detector and purged with high purity nitrogen (BOC). The Pike electrochemical cell was mounted on a VeeMax III ATR accessory (Pike Technologies) and was connected to a 760E potentiostat (CH Instruments) for chronoamperometric tests. All ATR-SEIRAS measurements were collected with a spectral resolution of 4 cm⁻¹, optical velocity of 1.8988, and gain of 1.0. Initially, the potential was held at -0.8 V vs. Ag/AgCl for 30 min to both saturate the electrolyte with CO₂ and collect background spectra. The potential was subsequently stepped

negatively from -1.0 V to -2.2 V vs. Ag/AgCl in 100 mV increments with sample spectra recorded at each potential. All spectra were collected within a period of 50 s and 74 interferograms were co-added to obtain each spectrum. A CO₂ flow rate of 10 sccm was maintained throughout the experiment.

6.9 Supplementary Figures

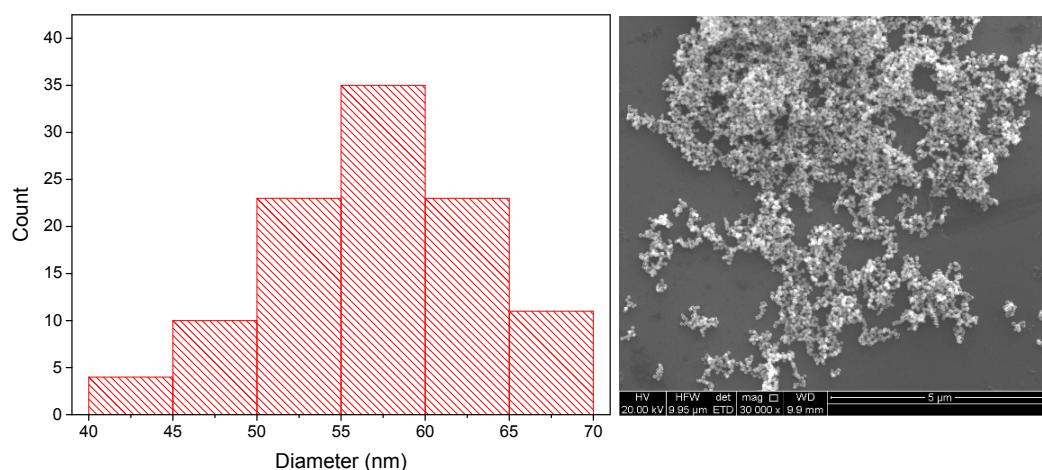


Figure S6.1 Size distribution data for the Cu₂O nanocubes. The mean size was 57.0 nm with a standard deviation of 6.6 nm and the mode size was 60.5 nm.

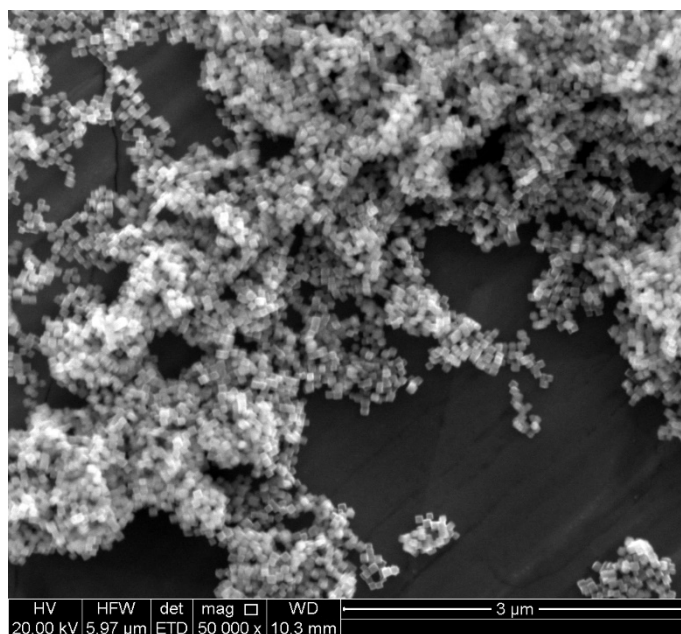


Figure S6.2 SEM image of the OD-Cu nanocubes after the electrochemical reduction step. Note they retained a cubic morphology, indicating that it was a homomorphic process.

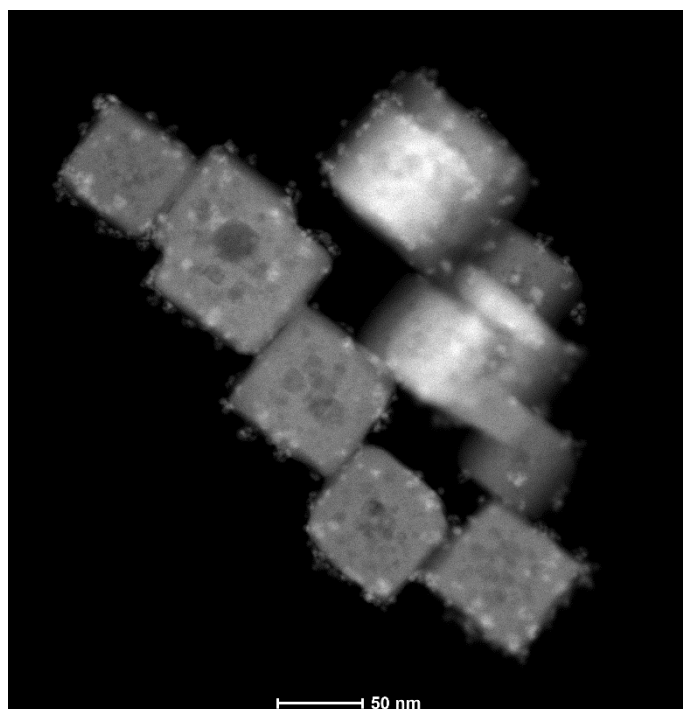


Figure S6.3 STEM image of the OD-Cu-Au nanocubes highlighting the deposition of gold nanoparticles on the OD-Cu.

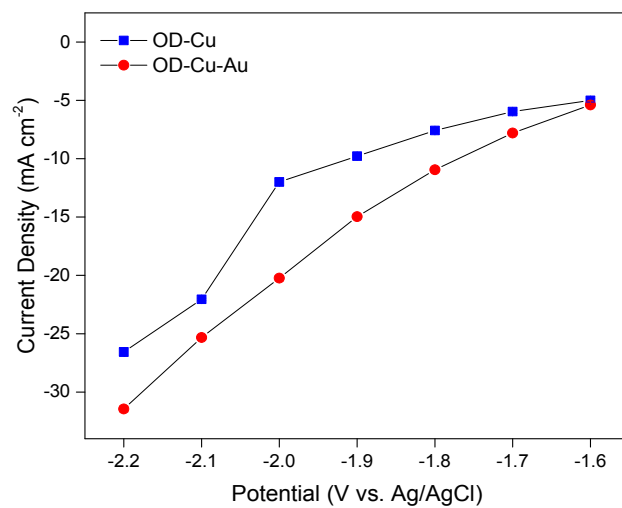


Figure S6.4 Potential-current plot for OD-Cu and OD-Cu-Au obtained from the steady-state CO₂RR currents at each potential tested.

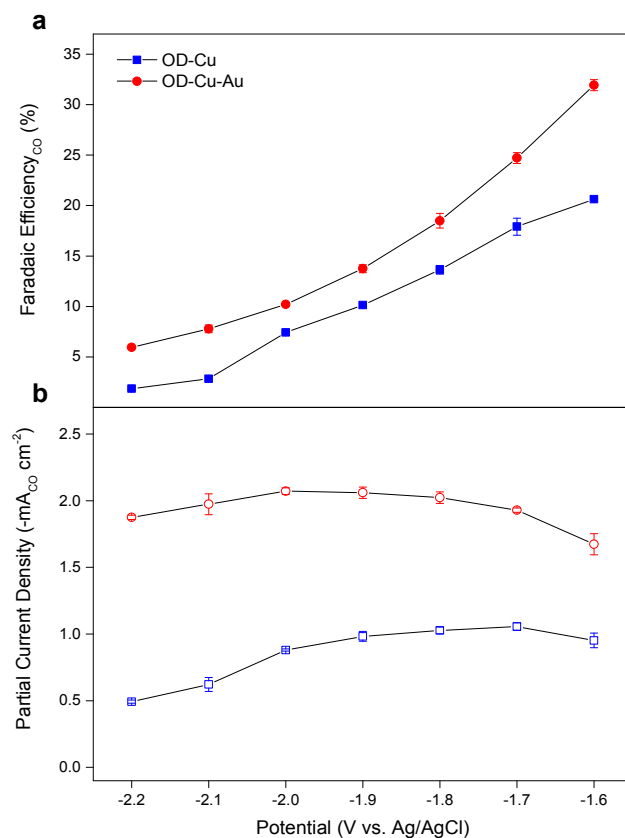


Figure S6.5 Comparison of a) Faradaic efficiencies and b) partial current densities towards carbon monoxide on OD-Cu and OD-Cu-Au across the potential range studied.

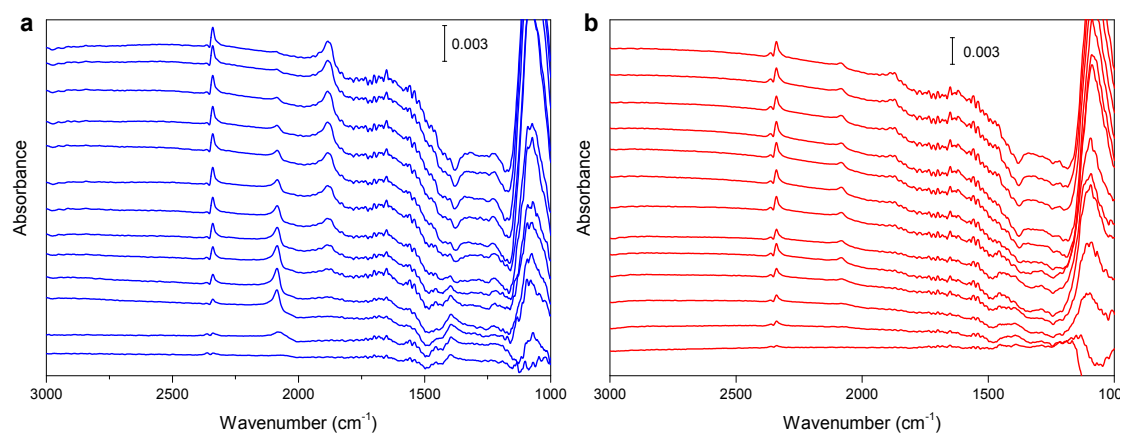


Figure S6.6 Potential dependent ATR-FTIR spectra of a) OD-Cu and b) OD-Cu-Au in CO₂-saturated 0.1 M KHCO₃.

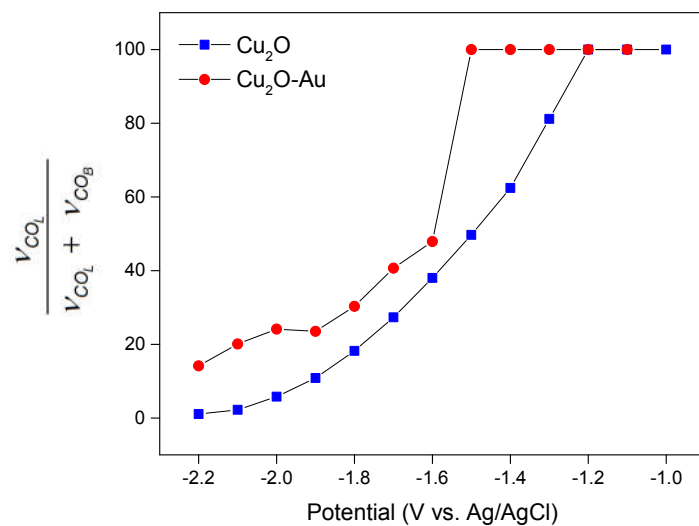


Figure S6.7 Proportion of adsorbed *CO intermediates in the COL binding mode as a function of potential for OD-Cu and OD-Cu-Au.

6.10 Supplementary References

1. S. Thoka, A.-T. Lee, M. H. Huang, *ACS Sustain. Chem. Eng.* 2019, 7, 10467.
2. M. Dunwell, Q. Lu, J. M. Heyes, J. Rosen, J. G. Chen, Y. Yan, F. Jiao, B. Xu, *J. Amer. Chem. Soc.* 2017, 139, 3774.

Chapter 7

Conclusions and Outlook

The body of work presented in this Thesis has demonstrated the use of copper as an electrocatalyst platform for the CO₂RR and improving its selectivity through alloying and introduction of a secondary element. By using a multi-faceted approach which combined electrochemistry with *in-situ* spectroscopy techniques and computational studies, a fundamental understanding of the intrinsic effects of the secondary element towards reaction selectivity was gained.

In Chapter 2, a classification for copper alloys was developed based on the oxygen and hydrogen affinities of the bulk secondary metal. From this classification, predictions could be made regarding the CO₂RR products selectivity of the alloy catalysts. In Chapters 3 and 4, Cu-Sn alloys were studied as CO₂RR electrocatalysts because from the classification presented in Chapter 2, they were predicted to have high selectivities toward CO and formate, which was important for investigation of the early reaction pathway. In these Chapters, a composition-dependent selectivity trend was observed which shows that as Sn concentration in the alloy increases, selectivity for formate increases over CO. While it was found that the initial electron transfer step was limiting to both CO and formate, *in-situ* Raman spectroscopy found that this selectivity trend was accompanied with a shift in intermediate binding preference from a carbon-bound *COOH intermediate to an oxygen-bound *OCHO intermediate. Further, theoretical calculations suggested that an increase in Sn concentration leads to a weakening of *COOH adsorption and strengthening of *OCHO adsorption. These observations were explained fundamentally by the resultant charge redistribution which occurs from Sn to Cu upon alloying. Consequently, local positive charge on the Sn sites hinders

nucleophilic attack of the carbon in the CO₂ molecule, which preferences *OCHO adsorption in the first reaction step.

Chapters 5 and 6 then begun to explore copper-based electrocatalysts and the late reaction pathway. The focus of these chapters was the effects of secondary elements (non-metal and metal) on selectivity towards multi-carbon products. Using copper-based electrocatalysts (ID-Cu and OD-Cu), it was found that ID-Cu exhibited significantly greater ethane selectivity and more favorable kinetics compared to OD-Cu. *In-situ* X-ray adsorption and Raman spectroscopies suggested that an oxygen-bound ethoxy intermediate is a key intermediate in the mechanism and determines selectivity towards ethane or ethanol. It was shown that this intermediate is likely better stabilized on ID-Cu due to trace iodine species in the copper lattice. As a result, a rational design strategy involving the introduction of secondary elements to improve the C₂ selectivity beyond ethylene and ethanol of copper-based catalysts was demonstrated.

In-situ spectroscopy was further utilized in Chapter 6 to explore the design features of copper bi-metallic electrocatalysts and how they affect selectivity towards multi-carbon products. Using *in-situ* ATR-FTIR to study OD-Cu nanocubes, it was found that bridge-bonded *CO (CO_B) was the dominant binding mode of CO at overpotentials relevant to C₂ product generation. However, OD-Cu nanocubes with electrodeposited gold (OD-Cu-Au) maintained a higher population of linear-bonded *CO (CO_L) in conjunction with greater selectivity and faster kinetics towards ethylene generation. Consequently, the ability to introduce a secondary metal to affect the adsorption dynamics of key reaction intermediates and improve the selectivity of copper-based electrocatalysts was achieved.

The work presented in this Thesis provides insight into the CO₂RR performance of copper alloy and bi-metallic electrocatalysts and demonstrates their importance in the field. This Thesis also demonstrates the importance of using *in-situ* techniques in order to meaningfully understand the reaction mechanisms and how selectivity is affected by the secondary element. Therefore, rational design strategies which positively affect the performance of copper-based electrocatalysts can be formulated. Although

these systems show great potential as active catalysts for CO₂ reduction, much of the work conducted is still at the fundamental lab-scale. For example, the H-cell reactors used throughout this Thesis can provide insight into the reaction process, but severely limit CO₂ diffusion and are not practical for high reaction rates. Therefore, future studies should adopt flow-cell reactors as a standard because they can greatly improve diffusion of reactants and accommodate high currents. However, a catalyst system characterized in a conventional H-cell may not perform as expected in a flow-cell due to changes in factors like pH gradient. Therefore, there is great need to perform *in-situ* spectroscopic studies on catalysts applied in this configuration. With this also calls for the development of flow-cells which can allow for spectrometer sampling.

The focus of this Thesis is the study and improvement of copper-based materials for CO₂ reduction electrocatalysis. However, another interesting area of investigation for this field is the development of carbon-based electrocatalysts. Carbon-based materials are significant because they are cost effective, have large surface areas, and can be synthesized with a variety of morphologies and dopants. Carbon materials can also be utilized as supports to increase the effective surface area for metal catalysts. To demonstrate the potential of these materials, a review of the recent development of carbon-based materials for this field was conducted and included in Appendix A. Overall, the future of this field will require investigation into material design which involves a variety of different catalyst systems. Further, the ability to perform advanced characterization studies will be critical to their development and facilitate overcoming the challenges currently facing electrocatalytic CO₂ reduction.

Appendix A

Supplementary Literature Review

Carbon Solving Carbon's Problems: Recent Progress of Nanostructured Carbon-Based Catalysts for the Electrochemical Reduction of CO₂

This Appendix includes work published in the journal article *Adv. Energy Mater.* 2017, 7, 1700759. The aim of this Appendix is to review nanostructured carbon materials which have recently shown promise as high performing materials for CO₂ electroreduction and present as possible alternatives to copper. The materials included in this review include graphene materials, carbon nanotubes, porphyrin materials, nanodiamond, and glassy carbon. Along with discussion regarding materials synthesis, structural characterisation, and electrochemical performance characterisation techniques used, this report will discuss the findings of recent computational CO₂RR studies which have been key to elucidating active sites and reaction mechanisms and developing strategies to break conventional scaling relationships. Lastly, challenges and future perspective of these carbon-based materials for CO₂ reduction applications will be given. Much work is still required to realise the commercial viability of the technology, but advanced experimental techniques coupled with theoretical calculations are expected to facilitate its future development.

Statement of Authorship

Title of Paper	Carbon Solving Carbon's Problems: Recent Progress of Nanostructured Carbon-Based Catalysts for the Electrochemical Reduction of CO ₂
Publication Status	<input checked="" type="checkbox"/> Published <input type="checkbox"/> Accepted for Publication <input type="checkbox"/> Submitted for Publication <input type="checkbox"/> Unpublished and Unsubmitted work written in manuscript style
Publication Details	A. Vasileff, Y. Zheng, S.Z. Qiao, Carbon Solving Carbon's Problems: Recent Progress of Nanostructured Carbon-Based Catalysts for the Electrochemical Reduction of CO ₂ , <i>Adv. Energy Mater.</i> 2017 , 7, 1700759-1700780

Principal Author

Name of Principal Author (Candidate)	Anthony Vasileff		
Contribution to the Paper	Devised the idea of the paper with supervisors, gathered the bulk of the information and wrote the bulk of the paper.		
Overall percentage (%)	84		
Certification:	This paper reports on original research I conducted during the period of my Higher Degree by Research candidature and is not subject to any obligations or contractual agreements with a third party that would constrain its inclusion in this thesis. I am the primary author of this paper.		
Signature		Date	09/04/2020

Co-Author Contributions

By signing the Statement of Authorship, each author certifies that:

- the candidate's stated contribution to the publication is accurate (as detailed above);
- permission is granted for the candidate to include the publication in the thesis; and
- the sum of all co-author contributions is equal to 100% less the candidate's stated contribution.

Name of Co-Author	Yao Zheng		
Contribution to the Paper	8% Provided guidance and supervision from conception through to submission and helped to revise the paper.		
Signature		Date	09/04/2020

Name of Co-Author	Shizhang Qiao		
Contribution to the Paper	8% Provided guidance and supervision from conception through to submission and helped to revise the paper.		
Signature		Date	09/04/2020

A.1 Introduction

In the last century, conventional fossil fuels have been the primary feedstock for global energy production due to their unmatched energy and power density. In addition, the rich composition of mined petroleum has lent itself in the production of many products and industrial chemicals. As a result, fossil fuels have underpinned the entire global economy. However, environmental concerns and socioeconomic instability associated with major fossil fuel producing nations has caused much concern within the global community regarding long-term sustainability and security of these commodities.^[1, 2]

With the global population in 2016 at 7.42 billion,^[3] and with unprecedented growth in the middle class of the world's two most populous nations, China and India, global energy demand has never been higher and will continue to rise. In 2013, China's activities produced 2.8 million tonnes of carbon dioxide (CO₂) emissions which is a 400 % increase on its emissions 20 years prior.^[3] This growing need for energy has only recently been supplemented by renewable sources with 10.3 % of total global energy sourced by modern renewable methods.^[4] Of that, wind, solar and geothermal make up 1.4 %, hydroelectric 3.9 % and the balance made up by biomass, biofuels and solar-thermal.^[4] Although much research and development has been conducted on these energy sources, there is still much improvement to be made regarding the technology and renewable energy policies in order to achieve a fully renewable energy society.

A major hurdle in the development and proliferation of renewable energy involves energy conversion and storage technologies. Much of the criticism regarding renewable energy points to issues of intermittency and baseload power capability, aspects that advanced conversion and storage technologies can address.^[5] However, the relatively high cost and low energy densities of current energy conversion/storage devices greatly hinders their commercial integration into renewable energy systems. A long-proposed method of energy conversion and storage is through the CO₂ reduction reaction (CO₂RR) into useful molecules such as: methane, formic acid, carbon monoxide (CO) *etc.* coupled with renewable energy sources, such as wind and solar. Methods proposed in the literature for the conversion of CO₂ are primarily: electrocatalytic reduction, photocatalytic reduction, chemical and biochemical,^[6] and have all been extensively studied in recent years.^[7-9] Of all processes studied, electrocatalytic reduction appears

to be the most feasible as it can be conducted in ambient conditions whilst having a highly controllable reaction step and relatively high conversion efficiency, and can be driven by renewable energy/integrated into renewable energy systems.^[6, 10] An integrated CO₂RR system is attractive because: (1) it sequesters carbon from the atmosphere, (2) it provides an energy storage solution for intermittent renewable sources with high energy density and (3) it can be used to produce industrial chemicals and fuels. The third point is particularly interesting because as society decreases its dependency on conventional fossil fuels, a void will be left for the materials and petrochemical industries. However, if petroleum feedstock can be derived from CO₂ conversion, then the feedstock could potentially be produced anywhere and directly implemented into conventional downstream industries.

However, every CO₂ conversion process is faced with the ultimate challenge of an extremely stable molecule,^[6] and hence large kinetic barrier due to the first electron transfer to the adsorbed CO₂ molecule.^[11] Further, conducting the CO₂RR in aqueous electrolyte is more appealing because it reduces the need for harsh solvents and chemicals but presents challenges with the competing hydrogen evolution reaction (HER). This is due to the adsorbed *H intermediate (necessary for hydrogen evolution) being more stable than adsorbed CO or *COOH intermediates (necessary for the reduction of CO₂).^[11] Therefore, very effective catalysts are required in order to drive the conversion process without the cost of huge overpotential/low energy efficiency.

In order to electrochemically reduce CO₂ at ambient conditions, there are several catalyst characteristics that are necessary in developing effective catalysts. These are: low activity to the competing HER, optimal binding of CO at the catalyst surface, high selectivity and activity toward CO₂ reduction, and robustness and long term stability.^[12] In the fields of nanotechnology and materials engineering, nanostructured carbon-based materials, such as graphene, have had much attention in recent years and have been extensively applied in energy conversion technologies, such as water splitting. The reason for carbon's newfound attention in this area is because these nanomaterials have incredibly high surface area, allow for compositional fine tuning and heteroatom doping, allow for structural fine tuning, have excellent conductivity and are cost effective. Being metal-free materials, they also have the potential to eliminate or reduce the usage of metals in these technologies, making them environmentally friendly.

At present, a large volume of new research, on both computational and experimental CO₂RR studies, has emerged which is expanding research opportunities and driving fast development within the field. In this progress report, we present recent achievements made regarding novel carbon nanostructures used as electrocatalysts and supports for the CO₂RR. Specifically, we will first provide a brief overview of the electrochemistry, and then review various recent CO₂RR electrocatalysts in the following categories: graphene materials, carbon nanotubes (CNTs) and nanofibers, porphyrin materials, and nanodiamond and glassy carbon. Our discussion of these various electrocatalysts focuses on electrochemical performance characterisation in comparison to benchmark precious metal catalysts and the role of nanotechnology in chemical and structure design for performance optimisation objectives. We will also address advances in the determination of the true active sites in these carbon-based electrocatalysts, strategies to break conventional CO₂RR scaling relationships, and the synergistic effects between carbon support and metal nanoparticles on inherent activity through recent computational studies. Finally, we will discuss the current challenges faced in the design of these electrocatalysts and the bottlenecks in the fundamental knowledge and provide some future perspective on these carbon-based materials in CO₂RR technology. Although there are a few review articles in the literature regarding non-metal and non-precious electrocatalysts for the CO₂RR,^[10, 13-15] even in the past year, impetus to study heterogeneous catalysts for the CO₂RR has significantly increased and a lot of quality research on the development of non-metal catalysts has recently been published. Therefore, we believe this progress report to be timely in order to discuss recent developments made concerning carbon-based materials employed as electrocatalysts and supports for the CO₂RR and their future in the technology.

A.2 Electrochemistry of Carbon Catalysts and the CO₂RR

In recent years, carbon-based electrocatalysts have been studied and exploited for various electrochemical processes such as the Hydrogen Evolution Reaction (HER), the Oxygen Evolution Reaction (OER) and the Oxygen Reduction Reaction (ORR).^[16, 17] The main driver behind studying and developing these materials for electrocatalysis is that they offer a low cost alternative to conventional precious metal catalysts such as Platinum (Pt) and Iridium Oxide (IrO₂), used as benchmark electrocatalysts for the HER and OER, respectively.

A.2.1 Nanostructured Carbon Electrocatalysts

For the CO₂RR, bulk metal and metal structured catalysts have been the primary focus for CO₂RR electrocatalysts.^[18, 19] These metals can be separated into three distinct groups: formic acid producing metals (Sn, Hg, Pb, Bi), CO producing metals (Au, Ag and Zn) and Cu in its own group due to its ability to produce a range of higher order hydrocarbons.^[5, 20] However, these metal electrocatalysts face many issues; primarily poor selectivity, loss of efficiency toward competing hydrogen evolution, poor stability and inactivation by CO.^[10]

For the CO₂RR and other processes, carbon based electrocatalysts and supports have shown to be very stable and efficient in operation.^[13, 16, 21, 22] Whether applied as totally metal free or as carbon-metal composites, development of cost effective carbon based material with equal or better activity to precious metal benchmarks could potentially realise energy storage/conversion devices for mainstream applications. However, carbon materials generally possess negligible inherent CO₂RR activity for the electroreduction of CO₂ and catalyse the competing HER in preference.^[23] Despite this, CO₂RR active sites can be introduced into the carbon framework through chemical treatments like heteroatom doping. By introducing one or more types of heteroatoms (N, P, S *etc.*) into the carbon network, the charge and spin density of the carbon atoms will be altered by the more electronegative dopants adjacent to them.^[24] This in turn induces regions where adsorption and activation of reaction intermediates can take place to drive electrocatalysis. Metal nanoparticles (NPs) active to certain electrochemical processes can also be effectively anchored to the carbon surface.^[24] Due to the large surface area and excellent electrical properties of carbon materials, like graphene,^[25] the NPs can be anchored and confined on the surface which minimises agglomeration and enhances interfacial contact. Consequently, this accommodates an increased density of active sites and promotes enhanced catalytic activity.^[26-28]

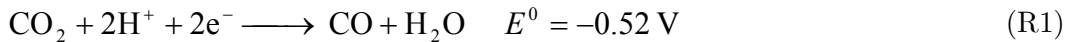
A disadvantage of this strong interaction between metal species and carbon materials is that many carbon materials which are claimed to be “metal-free” actually have significant metal impurities.^[23] These metal species can partake in electrocatalysis and cause ambiguity when determining the activity origins of such carbon materials. Many studies are aware of this fact and have taken necessary experimental steps to avoid the presence of significant metal impurities in order to make clear claims about

the performance of metal-free materials. Techniques like chemical vapour deposition (CVD) and electrospinning have been employed and demonstrated the synthesis of carbon materials without metal contamination.^[29, 30] Further, recent studies have shown that some common trace metal contaminants, like Fe found in CNTs, are not selective to CO₂ reduction and catalyse the HER in preference.^[31]

Additional to compositional fine tuning, the many allotropes of carbon (graphene, fullerenes, carbon nanotubes *etc.*) possess highly tuneable morphologies which can be nanostructured to obtain desired electrocatalytic properties.^[32-34] Nanostructuring has been found to be an effective strategy to enhance the activity of bulk electrodes.^[35, 36] Namely, by fabricating electrocatalysts with well-developed nanostructures, their surface areas can be significantly increased, which results in a higher density of active sites without altering their inherent properties. Various carbon structures can also be coupled to form novel nanostructures with precise control over physical properties, such as pore size, pore type, particle size, and layer thickness, which is beneficial for rational optimisation of performance.^[37, 38] Further, it has been found that edge site carbons are more catalytically active than those carbon within the basal plane,^[39] and so strategies employed to increase the density of edge sites within these carbon materials can significantly increase activity.^[37, 40] Presented in Section A.2.2 is a brief overview of the CO₂RR pathway and general mechanism.

A.2.2 Simple Thermodynamics but Difficult Kinetics of CO₂RR

The cathodic CO₂RR is generally represented by the half-cell Reaction (R1), with standard cell potential for pH 7 *vs.* the Normal Hydrogen Electrode (NHE).^[8]



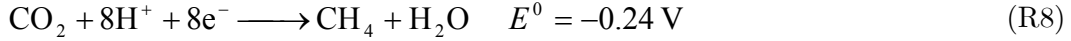
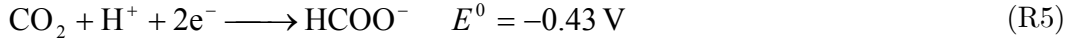
The corresponding anodic reaction is the oxidation of water to molecular oxygen (OER) which is represented as Reaction (R2) at pH 7 *vs.* NHE.^[6, 41]



Combining these two half-cell reactions, we obtain Reaction (R3), the overall electrochemical cell reaction.



Unlike other electrochemical processes like the OER and HER, the CO₂RR differs because it can proceed *via* different multi-step pathways, involving a different number of electrons depending on the end product. Generally, a two, four, six, or eight electron pathway is involved in the CO₂RR mechanism.^[15, 42] Reducing CO₂ electrochemically proceeds quite simply from a thermodynamic standpoint with standard electrode potentials toward aqueous reduction products (pH 7) referenced to NHE shown in Reaction (R1) and (R4) – (R8).^[5, 8]



However, the electrochemical reduction of CO₂ to hydrocarbons is difficult and generally proceeds at more negative potentials compared to the equilibrium potentials shown above. There are three main reasons for the difficulty associated with reducing CO₂ electrochemically. The first reason is that the rate determining step (RDS) for the CO₂RR process is most likely the first electron transfer to an adsorbed CO₂ molecule to form the CO₂^{•−} intermediate (Reaction (R4)).^[42] This occurs at a highly negative potential of approximately -1.9 V *vs.* NHE because it involves the bending of the CO₂ molecule which is linear and extremely stable,^[5, 8] in turn presenting a large kinetic barrier. The second reason is that when conducted in aqueous media, the CO₂RR competes with the HER due to their similar equilibrium potentials. Further, adsorbed *H intermediates are more stable than adsorbed *CO or *COOH intermediates, causing the HER to dominate at more negative potentials.^[11, 43, 44] Lastly, the CO₂RR usually proceeds *via* the adsorption of a CO₂ molecule at the interface between the electrode and electrolyte. Given that CO₂ is largely insoluble in aqueous media, diffusion and mass transfer limitations can limit the reaction rate and turnover frequency.^[45] Therefore, effective catalysts and advantageous reaction conditions are key to efficient CO₂RR operation.

A.3 Carbon-Based Electrocatalysts

A.3.1 Graphene Materials

Ever since its first laboratory synthesis in 2004 by Geim and Novoselov,^[46] graphene has secured itself as a leading research interest in materials science and nanotechnology due to its remarkable electronic and mechanical properties. Graphene has also found a promising role in the field of catalysis due to the ability to fine tune its electronic structure through techniques like heteroatom doping and its excellent stability during catalytic operation.^[47-49] Although graphene itself has been shown to possess no intrinsic catalytic activity toward CO₂ reduction,^[50] by introducing atomic defects (through doping with heteroatoms like N, S, B *etc.*) which alter local electron density, active sites for the CO₂RR can be formed.^[29, 50, 51] Graphene materials have also been used as effective supports for metal nanoparticles active toward the CO₂RR due to their large surface areas and excellent network conductivities, affording a metal-support synergy that enhances catalytic activity.

A.3.1.1. Nitrogen Doped Graphene

At present, nitrogen has been the main dopant used in graphene materials for synthesis of CO₂RR electrocatalysts due to its high electronegativity and, thus, ability to polarise carbon atoms in the graphitic lattice.^[29, 31, 52, 53] Density Functional Theory (DFT) calculations have shown that a critical step in the CO₂RR pathway is the adsorption of the *COOH intermediate, which presents an up-hill energy barrier.^[29] While pristine graphene provides a large free energy barrier towards this, introduction of N defects provides much stronger binding of *COOH and subsequent enhancement of CO₂RR activity. Similar findings have also been found for boron doped graphene (B-graphene).^[50] Synthesis of graphene for CO₂ reduction catalysts has largely been *via* high temperature pyrolysis of GO,^[50, 51] but CVD methods have also been used,^[29] and doping of heteroatoms has been performed with post treatment methods. N-doping in this way provides better control over final N content and moiety type and has direct implications on electrochemical performance. However, a balance must be found in order to provide sufficient active sites to improve electrocatalytic activity but also not induce too much doping to the detriment of network conductivity and charge transfer.

Very recently, Wu *et al.* used a CVD technique to grow microporous graphene foams (Figure A.1a and b) which were then post-doped with nitrogen (N) using graphitic carbon nitride (g-C₃N₄).^[29] The resultant N-graphene had an N content of 6.5 at% and was active and selective toward CO production. Maximum Faradaic efficiency (FE) and current density towards CO was 85% and 1.8 mA cm⁻² respectively, at a potential of -0.58 V *vs.* the Reversible Hydrogen Electrode (RHE; corresponding to an overpotential of -0.47 V). Production of formate was also observed but at a very small FE of ~3% (at -0.58 V), which suggests that the CO₂RR proceeds *via* a 2e⁻ pathway on this catalyst material.

Other examples of N-graphene have shown significant performance toward formate production with a very small onset overpotential of 240 mV.^[51] Maximum FE toward formate production reached 73% at -0.84 V *vs.* RHE, which is comparable to that of the high performing metal-free polyethylenimine/N-doped carbon nanotube composites (PEI-NCNT; Figure A.1c).^[53] Shown in Figure A.1d, the Tafel slope for the N-graphene electrode was found to be 135 mV dec⁻¹, which is similar to a rate-limited single e⁻ transfer (118 mV dec⁻¹) and suggests that the rate determining step is the first e⁻ transfer to adsorbed CO₂ molecules on the electrode surface. Following this, it is likely that a proton transfer from dissolved HCO₃⁻ occurs and produces the adsorbed formate ion, which is then desorbed, causing the reduced carbon atom to proceed back to its initial oxidised state. Wang *et al.* note that pyridinic-N form the highest N functionality in their N-graphene (Figure A.1e and f) which results in high bond polarity and hence, oxidised adjacent carbon atoms.^[51] However, these oxidised carbon atoms are reduced through redox cycling and it is this reduction-oxidation cycling of active carbon atoms which they attribute to the high activity and stability.

Only very recently have examples of metal free electrocatalysts been shown to catalyse the CO₂RR through reaction pathways involving more than two electrons. By employing N-doped graphene materials in ionic liquid (IL) 1-butyl-3-methylimidazolium tetrafluoroborate ([Bmim]BF₄) electrolyte, CO₂ was reduced to methane at a maximum FE of 93.5% and potential of -1.4 V *vs.* SHE.^[54] Addition of small amounts (1-5 wt%) of water to the IL was also found to significantly increase the partial current density of CH₄, but at a small expense to its selectivity. This demonstrates role of the IL electrolyte in the mechanism and its ability to suppress

hydrogen evolution. Given this, it is likely the [Bmim]BF₄ is fundamental in driving the reduction of CO₂ to the CO₂^{•-} intermediate, possibly through a complex formed between the IL and CO₂ as evidenced by Kumar *et al.*^[30]

N-doped graphene synthesised as quantum dots (NGQDs) have also exhibited CO₂ reduction to higher order hydrocarbons.^[55] Remarkably, the NGQDs could highly suppress hydrogen evolution over the CO₂RR potential range studied (-0.2 to -1.0V *vs.* RHE) in an aqueous electrolyte (1M KOH). The NGQDs, deposited on a gas diffusion electrode (GDE), were very active toward the CO₂RR, achieving a maximum total FE of 90%, with highest selectivities toward ethanol and ethylene. Further, they could catalyse CO₂ reduction to a range of hydrocarbons, including *n*-propanol which requires an 18e⁻ transfer (Figure A.2a). Whereas the 2e⁻ pathway products dominated on undoped graphene quantum dots (GQDs) and N-doped reduced graphene oxide (NRGO; Figure A.2b and c). The activity and faster kinetics of the NGQDs was attributed to the presence of rich pyridinic-N defects within the graphene, unique morphology, and small lateral size (Figure A.2d-f). Of most importance is the density of exposed edge sites, as it was found that the nanometre sized NGQDs possessed three orders of magnitude greater exposed edges sites when compared to micron sized NRGO. Given the lower energy of formation for pyridinic-N at an edge site, it is likely that most of the N defects in the NGQDs formed at edge sites. Evidence suggests that edge site dopants are more active for electrochemistry than dopants located within the basal plane.^[39] Therefore, engineering of rich edge sites in carbon-based electrocatalysts should be comprehensively considered in future studies.

Stability in operation is also an important factor for rational catalyst design and N-graphene materials have shown significantly better stabilities to bulk metal electrodes. As demonstrated by Wang *et al.*, their N-graphene achieved a stable chronoamperometric response over 12 h operation, with negligible change to the material's morphology as evidenced by SEM.^[51] Similar observations have been made for other N-graphene materials, displaying very stable operation over long term operation and achieving better stability than polycrystalline metal electrodes like Au and Ag.^[29, 54] One reason for this improved stability and reduction in performance attenuation over polycrystalline metals is that N-graphene has been shown to be largely insensitive to CO and, therefore, it is not poisoned by CO₂ reduction products.^[56]

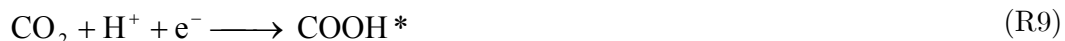
A.3.1.2 Boron Doped Graphene

Doping graphene with other heteroatoms, such as boron (B), has also recently been explored. Sreekanth *et al.* synthesised B-graphene for the reduction of CO₂ to formic acid.^[50] In 0.1 M KHCO₃ aqueous solutions, B-graphene was shown to be active and selective to the formation of formate with an FE of 66% at -1.4 V vs. SCE. DFT shows an asymmetric distribution of spin density throughout the graphene lattice when boron is doped. It suggests that both B and C atoms are catalytically active, both affording chemisorption of CO₂ and facilitating CO₂ reduction due to positive spin densities. As formate was the only appreciable reduction product detected, it is likely that the mechanism is a similar 2e⁻ pathway to that of N-graphene,^[51] whereby formic acid production proceeds *via* the *COOH intermediate. With the success of single doped carbons for CO₂RR applications, multiple heteroatom doping strategies could also prove to be feasible for enhancing catalytic activity, as seen for other electrochemical processes.^[57, 58] However, such strategies have yet to be employed for carbon-based CO₂RR electrocatalysts.

A.3.1.3. Graphene Supported Nanoparticles

The synergistic effects between graphene and metal NPs has been extensively studied due to the ability of graphene to effectively anchor and stabilise nanoparticles for electrocatalytic applications.^[59] Even trace levels of metal nanoparticles on carbon supports like graphene have shown to significantly enhance CO₂RR activity,^[23] therefore better utilising the metal component. The types of graphene supported metal nanoparticles/nanostructures recently synthesised for CO₂RR application can be broadly categorised into the following two types: (I) supported NPs with synergistic effects, (II) layer by layer/core shell structure. A third category covering supported dispersed single metal atoms has been theorised by computational studies and is discussed in Section A.4.4. However, no such materials have been synthesised for CO₂ reduction as synthesis of single atom catalysts is often quite difficult and requires appropriate support structures for the particular application.^[60-62]

For Type I materials, trace levels of metal nanoparticles have shown to significantly enhance the CO₂RR activity of graphene^[23] and recent studies have also extended this to N-graphene.^[63, 64] Monodisperse Cu NPs supported by pyridinic-N graphene (p-NG) and were found to be selective for CO₂ reduction to ethylene.^[63] Electrochemical tests show that maximum FE achieved toward ethylene production on the Cu/p-NG composite was 19% at -0.9 V, which is significantly better than that of the Cu NPs on their own (6.3% at -1.1 V); p-NG itself produced no ethylene but was highly active and selective to formate which is in agreement with Wang *et al.*^[51] Similarly, the rate limiting step is likely the single electron transfer and reduction of an adsorbed CO₂ molecule to CO₂^{•-}. However, it seems that when Cu NPs are coupled with N-graphene, particularly with pyridinic moieties, the COOH* intermediate is formed and undergoes a secondary protonation/dehydration step which forms CO*. It is believed that this surface absorbed CO* can undergo further protonation and is responsible for the production of higher hydrocarbons. Reaction (R9) to (R13) summarises the proposed reaction mechanism on Cu/p-NG.



For Type II materials, a highly textured N-graphene, in the form of carbon nano-spikes (CNS), supported Cu NPs was formed as a core-shell like structure. This material was found to be very active toward the CO₂RR and could reduce CO₂ to ethanol with a high selectivity (84%) and FE (63%) at -1.2 V *vs.* RHE.^[64] Figure A.3a demonstrates the highly controlled size and distribution of the NPs, which was facilitated by the graphene surface. As ethanol is an unexpected reduction product, it is believed that the unique morphology of the nano-spikes embedded and wrapped around the NPs (quasi core-shell) which provided close contact between the NPs and support (Figure A.3b), facilitating C-C coupling to a C2 intermediate (likely coupling of CO* to form OCCO*). Further, it may be that oxygen on one side of the C2 intermediate is reduced fully on the copper to form -CH₃, while the other O is adsorbed and prevented to fully reduce on the less reactive CNS.

Graphene has been shown by DFT and experimental techniques to prevent clustering of active nanoparticles and is well known to improve their chemical stability.^[28, 65] Xie *et al.* used a very novel approach to encapsulate Sn quantum sheets within sheets of graphene, as a Type II layer by layer structure, for the CO₂RR.^[66] Their method produced a two dimensional (2D) material that very precisely confined the dispersed Sn quantum sheets of approximately nanometre size within two layers of graphene (Figure A.3c-e). While such metallic nanostructures would oxidise in ambient conditions, compromising electronic and conductive properties, thermogravimetric analysis (TGA) was used and showed that the graphene envelopment was able to prevent oxidation of the Sn quantum sheets in air up to a temperature of 570°C. X-Ray Absorption Fine Structure (XAFS) also confirmed that the Sn quantum sheets were well protected from oxidation within the graphene sheets as no peaks related to oxides of tin were detected in the catalyst material. In terms of CO₂RR performance, Sn quantum sheets confined in graphene produced a catalytic current density of 21.1 mA cm⁻² at -1.8 V *vs.* SCE. This is an enhancement in current density of 2.5 and 13 times that of 15 nm Sn NPs and bulk Sn respectively, along with better FE across the entire potential range (Figure A.3f and g). The authors suggest that a reason for this enhancement in catalytic activity is due to the size reduction of the Sn nanostructures, as compared to the 15 nm NPs, and an increase in the disorder and distortion of the Sn surface. However, they also found that the coupling with graphene markedly reduced the interfacial charge transfer resistance which improved the overall conductivity of the catalyst. As a result, electron transfer to adsorbed CO₂ molecules (RDS) was improved which in turn improves the CO₂RR kinetics. A similar result was observed for Cu NPs on reduced graphene oxide (rGO) supports,^[67] in which the presence of surface functional groups stabilises the NPs by decreasing the interfacial energy between the Cu and rGO.^[28]

A.3.2 Carbon Nanotubes and Nanofibres

A.3.2.1. Nitrogen Doped Carbon Nanotubes

It has been hypothesised that the curvature effect in the graphitic lattice can tune limiting potentials for certain desired reduction products.^[11] Computational methods have shown that for planar N-graphene, no stable adsorption states for *CO or

*HCOOH exist and accordingly, the $2e^-$ pathway to CO or HCOOH production dominates on these materials, which is supported by previous experimental works.^[29, 50, 51] However, the effect of curvature causes partial sp^3 hybridisation in the graphitic lattice and as a result, can bind these intermediates more strongly. Given this result, it is possible that synthesis of curved structures like carbon nanotubes (CNTs) could produce higher order hydrocarbons.

Despite this, the $2e^-$ CO₂RR pathway also dominates on CNT based electrocatalysts and the literature shows that some are selective toward CO while others toward formate. In one example, N-doped CNT (NCNT) electrocatalysts synthesised by Wu *et al.* were CO selective.^[31] In 0.1 M KHCO₃ electrolyte, their NCNTs deposited on carbon paper were able to reduce CO₂ with a remarkably low onset overpotential of -0.18 V (Figure A.4a). In addition, at a low overpotential of -0.26 V, this catalyst was able to achieve a maximum FE of 80% toward CO and sustain this performance for 10 h of continuous operation. This is significantly higher than that of un-doped CNTs (~3.5%; Figure A.4b) and shows that NCNTs are a durable catalyst for CO₂ reduction. Through DFT analysis, they explain that NCNTs have very strong binding to COOH but weak binding to CO. Therefore, CO is desorbed too rapidly for subsequent proton and electron transfer to take place. Therefore, it may be that partial sp^3 hybridisation due to the curvature effect may cause an excessive binding of higher intermediates which prevents the production of higher order hydrocarbons.

Other NCNT examples have shown to be very selective towards formate, with a FE of 59% and only 2% towards CO.^[53] Further, applying a polyethylenimine (PEI) over-layer can significantly enhance catalytic activity and reduce catalytic overpotential, achieving a maximum FE of 85% towards formate with a current density (electroactive area) of 2.2 mA cm⁻². This performance was enhanced further with the use of graphenated NCNTs (GNCNTs). Due to increased conductivity and greater edge density, FE was slightly improved to 87% but catalytic current density (electroactive area) was almost doubled to 3.8 mA cm⁻². Pristine and O-doped CNTs were also studied but showed small FE toward formate (5% and 7% respectively), producing mainly hydrogen, and demonstrated no catalytic enhancement when a PEI over-layer was applied. This is an interesting result and suggests mechanistically that while a CO₂ molecule is adsorbed and reduced to the CO₂^{•-} intermediate at an N active site, the

resultant charge is stabilised by an H-bond interaction on the PEI. Due to this stabilisation, the overpotential is greatly reduced and subsequent electron and proton transfer to the $\text{CO}_2^{\bullet-}$ is facilitated. Given this result, it may be pertinent to further study the role of co-catalysts like PEI for producing higher order hydrocarbons at reduced overpotentials.

To understand the affect that N defects have and the origin of CO_2RR performance in NCNTs, Sharma *et al.* conducted a study utilising different N precursors and reaction conditions.^[68] By using a liquid CVD method, they grew NCNTs with three different precursors (acetonitrile, dimethylformamide and triethylamine) and at three different temperatures (750°C, 850°C and 950°C). They found that although the various NCNT samples contained similar total nitrogen content, electrochemical performance was vastly different. They hypothesised that this disparity in CO_2RR activity between samples was due to the different N functionalities. While total N content plays an important role in CO_2RR activity, they found that an increase in pyridinic and graphitic N greatly improve both the onset potential and faradaic efficiency toward CO (Figure A.4c). Interestingly, it was observed that an increase in pyrrolic N within the NCNTs caused a cathodic shift in onset potential and greatly reduced maximum FE. They explain that although pyrrolic N have an available lone e^- pair, the geometry of pyrrolic N defects situates the N atom inward the CNT. This restricts access to these lone pairs for CO_2 binding and binding to adjacent pyridinic N defects is favoured because much of the negative charge in the basal plane is localised around these defects. As a result, pyridinic N provides the lowest overpotential of 200 mV for the formation of COOH^* . Since the electrons available for binding CO_2 in graphitic N are located in the π^* antibonding orbital, graphitic N imposes a 1 eV higher barrier compared to pyridinic N toward the formation of COOH^* (Figure A.4d). However, graphitic N still provide a significant reduction in overpotential (~ 1 V) when compared to pristine CNTs.

A.3.2.2. Carbon Nitride/Carbon Nanotube Composites

Experimentally, porous carbon nitride (g- C_3N_4) has shown selective adsorption ability of large amounts of CO_2 .^[69, 70] Through an induced dipole interaction, g- C_3N_4 can effectively polarise CO_2 molecules, leading to enhanced adsorption which could facilitate the CO_2RR process. As a result, carbon nitride has been coupled with multi-walled carbon nanotubes (MWCNTs) and used as electrocatalysts for the CO_2RR ,

demonstrating high selectivity towards CO production.^[71] This catalyst achieved a total FE of 98%, with CO and H₂ being the only detectable products, and was able to effectively suppress the HER, with a HER onset overpotential of about 500 mV. While required overpotentials would probably impede economic viability, the novel synthesis technique of this catalyst is cost effective and simple. This is owing largely to the relatively low temperatures required to produce MWCNT/g-C₃N₄ composites, short reaction times and simple synthesis techniques, all of which are important factors for scalable production.

Jhong *et al.* also coupled carbon nitride with MWCNTs (CN/MWCNT) in the form of a thin coating.^[52] This MWCNT composite deposited onto carbon paper, forming a GDE, produced a catalytic current density of 90 mA cm⁻² at -1.62 V vs. Ag/AgCl. Their electrodes afforded relatively high catalyst loading (2.39 mg cm⁻²) and provided a marked increase in performance over Ag NPs (Figure A.5a) and other NCNT electrocatalysts.^[53, 71] Further, their CN/MWCNT achieved a maximum FE (at -1.62 V vs. Ag/AgCl) of 98% toward CO and 2% toward H₂ which demonstrates excellent selectivity toward CO and suppression of the HER. A unique feature of the CN/MWCNT is that it formed agglomerates of about a micron in size to produce a microporous morphology. It could be that this microstructure facilitates diffusion of electrolyte and CO₂ to and products away from the active sites, enhancing catalytic activity. Further, computational studies have shown that negatively polarised conductive g-C₄N₃ has the ability to capture and stabilise significant amounts of CO₂, owing to the absence of an energy barrier and large stabilisation energy of 1.08 eV under negative polarisation (Figure A.5b). Under reduction potentials, the fast charge transfer of the carbon network coupled with the CO₂ capture ability of the g-C₄N₃ could have provided synergistic effects and resulted in enhanced CO₂RR activity.

A.3.2.3. Carbon Nanofibers

Small overpotential, high activity and high selectivity are all necessary performance criteria for any successful electrocatalyst. One such material that is advancing all three of these criteria are the carbon nanofibers (CNFs) synthesised by Kumar *et al.* and have gained much attention.^[13, 14, 30] The studied CNFs had an average length of 500 nm and were produced using polyacrylonitrile (PAN) nanofibre mats. Two distinct reduction peaks (Figure A.6a) were observed at -0.573 V and -1.14 V (*vs.* SHE)

corresponding to the CO₂RR and HER, respectively. This was revealed after reduction products were collected at -0.573 V *vs.* SHE and it was found that CO was selectively produced with a FE of 98%. The CNFs produced a current density significantly higher than bulk Ag and Ag nanoparticles (Figure A.6b) and they attribute the inherent catalytic activity of the CNFs to their corrugated morphology resulting from the introduction of N defects. By conducting XPS before and after 9 h of continuous CO₂RR, it was discovered that the peak for pyridinic N remains relatively constant (Figure A.6c-f). Because of this, they postulate that pyridinic N species do not directly participate in the reaction as the two possible mechanisms (either permanent protonation or weak CO₂ binding) would alter the peak. Rather, pyridinic N shifts charge density away from adjacent C atoms and CO₂RR activity arises from the positively charged carbon. An interesting aspect of their study is that their material provides a large enough potential displacement between CO₂RR and HER cathodic peaks and can therefore selectively produce either CO or H₂ for syngas applications, depending on the applied voltage. In comparison, this potential displacement is smaller for benchmark Ag NPs which almost always leads to the suppression of hydrogen evolution.

3.2.4. CNT Supported Metal Nanoparticles

While only CO and formate have been produced on heteroatom doped CNTs, the production of higher order hydrocarbons has been achieved on CNT supported metal nanoparticles.^[72-74] Recently, CNTs have been used to support nanoparticles of Pd and Cu and have reduced CO₂ to acetic acid and methanol, respectively.^[73, 74] With an average particle size of 5.7 nm, Pd NPs supported on MWCNTs (Pd-MWCNTs) were able to produce formic and acetic acid with at maximum FE of 34.5% and 52.3%, respectively. However, these maximum efficiencies occurred at relatively high cell potentials (-4 V), did not occur concurrently and were dependent on electrolyte concentration. It was found that in 0.5 M KHCO₃, the Pd-MWCNTs were more selective toward formic acid while in 0.8 M KHCO₃, they were more selective toward acetic acid. This could be due to the ability of a higher concentration electrolyte dissolving more CO₂ into solution. Given Pd can adsorb CO₂ on its surface strongly,^[75] more dissolved CO₂ available for surface adsorption may facilitate multi-intermediate coupling steps.

When Cu NPs were loaded onto acid functionalised MWCNTs, methanol was produced with a maximum FE of 38.4% at a cell potential of -1.7 V *vs.* SCE.^[74] Again, this required potential is relatively high and reminds us of the direct consequence of multi-step, multi-intermediate reaction pathways in the formation of more complex end products.^[76] The optimum Cu loading was found to be 20 wt% as catalytic current density was maximised and loss in catalytic activity was observed for higher loadings. This was likely due to the agglomeration of Cu NPs that occurred at higher loadings which caused less uniform particle distribution and larger and less uniform particle sizes. Although the overall Cu content increased, these factors actually reduce the specific density of active sites due to the reduction in surface area and hinder their accessibility. Therefore, the mass loading of NPs onto support structures, carbon-based or otherwise, must be carefully considered in the rational design of CO₂RR catalysts.

A.3.3 Porphyrin Materials

Organo-metallic compounds like porphyrins have been long studied for the CO₂RR and were some of the first materials to address the issues associated with metal electrodes.^[10, 77, 78] Most commonly, metal-functionalised porphyrin materials used as CO₂RR electrocatalysts have been synthesised as molecular homogeneous catalysts. Consequently, a range of porphyrins are able to be functionalised with a range of transition metal centres (Co, Fe, Zn, Cu *etc.*),^[10, 79-83] and the resultant electrocatalysts have well-defined active centres which can be finely tuned for high activity and selectivity towards the CO₂RR. Regarding heterogeneous electrocatalysts, the active centres are often hard to define and performance optimisation is often challenging. However, heterogeneous electrocatalysts offer stability in electrocatalytic operation, especially in aqueous environments, which is paramount for practical application of these materials.

Generally speaking, however, in addition to catalyst-electrolyte separation issues, these molecular catalysts tend to be unstable and degenerate after only a few catalytic cycles.^[82] Usually, a co-catalyst must be employed in solution with homogenous porphyrin-based catalysts, such as a weak Lewis and Brønsted acids, in order to synergistically enhance their stability and efficiency.^[84-86] A recent example addressing some of these issues is the synthesis of Fe porphyrin dimers with finely tuned spacing of the Fe centres.^[82] Presence of two metal centres exhibited concerted stabilisation and

binding of CO₂ molecules which improved activity and stability without the need of co-catalysts.

In an effort to combine the exemplary features of both homogenous and heterogeneous electrocatalysts, transition metal porphyrin and other organometallic materials have recently been synthesised and constructed as metal organic frameworks (MOFs) and covalent organic frameworks (COFs), and have been functionalised on other nanostructured supports such as graphene and MWCNTs.^[79-81, 87, 88] The preparation of these porphyrin-based materials is generally through solvothermal or hydrothermal approaches, with the resultant materials deposited on conductive substrates to form the CO₂RR electrodes. Constructing the electrocatalysts in this way requires no high temperature steps which preserves the structure of the porphyrins and their well-defined active metal centres. Deposition on conductive substrates also improves stability and electron transfer to these active sites, enhancing electrocatalytic performance.

Transition metal (Zn, Cu and Co) centred porphyrins were linked to an alumina (Al₂O₃) layer to form MOFs for CO₂ reduction.^[79] Of these three transition metals, they all displayed typical CV plots for metalloporphyrin electrocatalysts with primary and secondary reduction peaks associated with metal centre reduction and proton/CO₂ reduction, respectively. However, the Co-centred porphyrin displayed the greatest increase in catalytic performance after CO₂ saturation and it was found that the MOF thickness affects performance, reaching maximum activity within 30-70 nm thickness. Cobalt loading also had direct implications on catalytic performance, as excess loading led to a decrease in performance, probably due to limitations in charge transfer from the electrode to the MOF, and as found elsewhere, tuning the catalyst coverage on the electrodes can be advantageous for efficiency and selectivity.^[89]

Cobalt porphyrins constructed into COFs were studied in order to utilise the unique features of such frameworks such as charge carrier mobility originating from the π conjugation and π - π stacking and the stability afforded by covalent bonding and reticular geometries.^[80] Deposited on porous carbon fabric for electrochemical tests, the COFs exhibited a catalytic onset potential of -0.42 V *vs.* RHE in CO₂ saturated carbonate electrolyte and demonstrated maximum activity at -0.67 V *vs.* RHE, producing mainly CO at a FE of 90%. At more negative potentials, this high selectivity

toward the CO₂RR begins to decline with hydrogen evolution being promoted. In order to optimise the performance of the COFs, they were instead synthesised with longer linkage molecules in order to increase the spacing between porphyrins for increased pore volume, as shown in Figure A.7a. This allowed for greater electrolyte access and CO₂ adsorption and in turn, reduced onset potential (-0.40 V; Figure A.7b) and increased catalytic activity by 2.2 times at -0.67 V (Figure A.7c). For Graphene supported Re-porphyrins, CO₂ diffusion limitations were also found to significantly affect activity.^[89] By utilising stirring to increase CO₂ diffusion into the electrolyte, reaction rate was found to increase by three times, while selectivity was maintained, as compared to non-stirring conditions. This is inexorably linked to the fact that while active centres are well defined in these materials, active site density is generally low and therefore need to be utilised effectively.

Recent computational studies have predicted that metal-functionalised porphyrin structures are capable of reducing CO₂ to methane and methanol.^[43] By immobilising cobalt protoporphyrins (CoPP) on pyrolytic graphite electrodes, Shen *et al.* were able to reduce CO₂ at relatively low overpotentials to CO and methane.^[81] Electrochemical tests were carried out in the pH range of 1-3 with CO₂ saturated electrolyte. At pH of 1, hydrogen evolution dominated with approximately 1% of FE utilised for CO and CH₄, while at pH of 3, production of CO and CH₄ occurred at less negative potentials compared to the HER and with significantly higher Faradaic efficiencies. Although the findings suggest that the CO₂RR and HER proceed *via* different pH dependent pathways, they explain that with their proposed mechanism (Figure A.7d), the rate of CO₂RR itself is not pH dependent, rather its relative rate to the rate of HER. Interestingly, the implication is that the hydrogenation of activated CO₂ is largely unaffected by H⁺ concentration. Instead, the CO₂^{•-} radical acts as a strong Brønsted base which can react with water molecules as a source of hydrogen. Cu-based porphyrin have also recently catalysed the reduction of CO₂ to methane and ethylene with significantly high current densities and stability.^[83] Conducted in a CO₂ saturated KHCO₃ electrolyte, the Cu-porphyrin achieved maximum CO₂RR activity at -0.976 V vs. RHE with partial current densities of 13.2 and 8.4 mA cm⁻² toward methane and ethylene, respectively. In both Co- and Cu-based catalysts, the oxidation state of the metal centre is key to activity. Additionally, although overpotential is significantly

affected by the electron transfer ability to the active metal centres, relative stabilities of $^*\text{CO}$ and $^*\text{COOH}$ intermediates are also important for catalytic activity.

A.3.4 Nanodiamond and Glassy Carbon

Conductive nanodiamond materials have been applied for the CO_2RR because of their excellent charge transfer and stability in harsh environments. By exploiting these properties, these materials have been used as supports to anchor molecules active toward the CO_2RR , such as cobalt porphyrins.^[90] The resultant catalyst showed sustained catalytic activity over long term operation, demonstrating the stabilising effect of the nanodiamond support. Most importantly, these materials are exploited for their high HER overpotentials.^[91] As a result, nanodiamond materials can provide a larger potential window to conduct CO_2 reduction, affording faster kinetics and higher efficiencies. In an effort to introduce CO_2RR active sites with low onset potentials, doping of boron and nitrogen into nanodiamond materials has recently been studied for CO_2RR application.^[92, 93] As shown in Figure A.8a, N-doped nanodiamond (NDD) was deposited on a silicon rod array using a microwave plasma enhanced CVD method and applied directly as an electrocatalyst for CO_2 reduction.^[92] The CO_2RR onset potential was -0.36 V vs. RHE and it was found that the NDD could preferentially produce acetate under any applied potential within the CO_2RR potential range. Remarkably, between cell potentials of -0.8 and -1.0 V vs. RHE , the NDD achieved Faradaic efficiencies of approximately 77% and 14% toward acetate and formate respectively (Figure A.8b), making it one of the best acetate producing electrocatalysts in the literature. Effects of deposition temperature were also studied with NDD being deposited at temperatures of 450 and 500°C to produce NDD_L and NDD_H , respectively. It was found that NDD_L afforded a $+0.24\text{ V}$ shift in onset potential and significantly greater acetate formation rates over NDD_H . Although both NDD_L and NDD_H had similar N content, crystal structure, and morphologies, XPS revealed that NDD_L had dominant pyridinic N moieties while NDD_H had dominant pyrrolic N moieties. Therefore, it is likely that pyridinic N is more active for CO_2 reduction and control of N configurations in resultant materials is crucial for enhancing the performance of N-doped carbon materials.

The excellent stability of nanodiamond materials was shown by the small CO₂RR performance attenuation of boron doped diamond (BDD) in continuous electrochemical testing (Figure A.8c). In CO₂ saturated methanol electrolyte, BDD exhibited CO₂RR activity toward formaldehyde production with highest FE of 74% achieved at -1.7 V *vs.* Ag/Ag⁺.^[93] Formic acid was also produced with a maximum FE of ~ 15% (Figure A.8d). To confirm formaldehyde production from the reduction of CO₂ on BDD, methanol was replaced with formic acid and was reduced to formaldehyde with FE of 85% at -1.5 V. From this, Nakata *et al.* deduced that the mechanism on BDD consists of two 2H⁺/2e⁻-coupled transfer steps, the first being the reduction of CO₂ to formic acid and then to formaldehyde. In both NDD and BDD, the high activity and Faradaic activities of these electrocatalysts was attributed to the presence of sp³ hybridised carbon within the diamond structure, especially the dopant-sp³C moieties. Indeed, the importance of nitrogen moieties was shown with metal-functionalised N-doped carbon black materials (M-N-C).^[94] Although N-C (M-N-C without metal) exhibited lower catalytic activities, they maintained similar selectivity to M-N-C. Further, CO and H₂ selectivity seemed to be independent of the metal species which indicates the importance of the nitrogen as the active sites and for intermediate stabilisation.

Glassy carbon has also been utilised as an electrocatalyst support for the CO₂RR.^[95-97] Although glassy carbon itself can catalyse CO₂ reduction in ambient conditions, it usually requires sufficiently negative reduction potentials to do so.^[96] Inspired by methanogenic cofactors like methanopterin, Xiang *et al.* functionalised glassy carbon electrodes with mercaptopteridine (PTE) and demonstrated one of the first examples of a totally metal free electrocatalyst for methanol production.^[95] The main products observed for CO₂ reduction were formic acid, formaldehyde, and methanol. Given that these are the only detectable products and that a reduction peak was also observed for PTE in formic acid, it was suggested that the mechanism on PTE proceeds *via* two successive two electron/proton coupled reduction steps, similar to BDD. In this case, the likely reaction pathway involves a two-electron reduced PTE-carbamate intermediate which was detected by FTIR. Although the PTE afforded modest FE toward methanol (10-23%), they note that better stabilisation of the cyclic methylene intermediate may increase efficiency past the first two-electron transfer step.

A.4 Computational CO₂RR Studies on Nanostructured Carbon Catalysts

Unlike the HER, where H* is the only reaction intermediate and therefore adsorption energy of this intermediate can be optimally tuned, the consequence of multiple CO₂RR reaction intermediates within the CO₂RR mechanism is that the adsorption energy of a certain intermediate cannot be optimally tuned without affecting another.^[98] The scaling relationships between the binding energies of these different CO₂RR intermediates therefore makes it difficult to operate at non-negligible overpotentials. Recent DFT studies have been pivotal in understanding the CO₂RR mechanism, elucidating CO₂RR active sites and developing new strategies for breaking these scaling relations in order to achieve better performance. In this section, computational studies of CO₂RR on metal free carbons, metal-porphyrin, metal-N/C composites, and nanostructured carbons as supports will be discussed.

A.4.1 Metal-Free Electrocatalysts

For metal catalysts, it has been found that the scaling relationships of CO₂RR intermediates are closely related to their d-band structure.^[99, 100] Therefore, synthesising metal-free electrocatalysts with only s- and p-orbital contribution could prove beneficial for breaking conventional scaling relationships. The most commonly studied metal-free materials for the CO₂RR are N-doped carbon materials. However, the mechanism and active sites on these materials are generally ambiguous and not fully understood, and recent fundamental studies have focused on these issues.

In order to elucidate the true active sites in N-doped carbon materials, Chai and Guo performed DFT calculations and *ab initio* molecular modelling to calculate free energy barriers for the activation of CO₂ on N-doped graphene (Figure A.9).^[11] They note that “the C sites that possess high electronic density of states (DOS) just below the Fermi level are most likely candidates for the active sites”,^[11] as electrons must be donated from the catalyst electrode to an adsorbed CO₂ molecule. It was found that pristine graphene has no stable adsorption state of CO₂, as the free energy barrier approaches 3.0 eV, which explains why graphene itself has no intrinsic CO₂RR activity. However, this free energy barrier was significantly reduced with the addition of N defects (Figure A.9b). Particularly for a graphitic N (gN) doped on the edge of a sheet, this barrier was reduced to 0.58 eV. It was also found that while the activation barrier

of gN was smaller than that of pyridinic N (pN), a reduction in the adsorption barrier can be achieved for both by increasing the concentration of edge doped N as an electron is donated to the unoccupied electronic states just above the Fermi level in an adjacent carbon atom (Figure A.9c). The result is a doubling of occupied electronic states just below the Fermi level in that carbon, as shown in Figure A.9a as C1, with a shift of states toward the Fermi level as compared to a carbon atom far away from the dopant site (C1'; Figure A.9a). Consequently, electron transfer to a CO₂ molecule is facilitated by this increase in occupied electronic states.

The role of pyridinic-N in the catalytic mechanism has also been discussed.^[63] Pyridinic-N replaces a carbon at a terminal end of a C6 ring in the graphene lattice and leaves an electron pair at 120° to the sigma bonds between nitrogen and carbon, and perpendicular to the pi-bonding network of the graphitic plane. Graphitic and pyrrolic N have their p-electrons conjugated with the pi-bonding network of the graphitic plane and therefore do not allow for localised electron pairs. It is this localised electron density, allowing for strong proton and CO₂ binding, which is attribute to enhancing CO₂RR activity. Given this, it may be that overall CO₂RR activity is a product of the combined effects, namely CO₂ binding and electron transfer, produced by the different N functionalities together.

A.4.2 Metal-Porphyrin Electrocatalysts

Metallo-porphyrins can be classified as single metal atom catalysts given the metal active centres are well defined and well dispersed. The DOS for these single metal atom sites is significantly different from that of metal surfaces, however, they present as the link between molecular and bulk metal catalysts.^[43] One advantage of single active sites in porphyrin materials elucidated by DFT is that a larger kinetic barrier to *H adsorption exists.^[101] This is due to *H having to adsorb to the metal centre in a position directly above it,^[102] as opposed to the more favourable binding at a metal hollow site in bulk metals, which causes the HER to progress *via* the Heyrovsky mechanism rather than the thermodynamically favourable Tafel mechanism. As a result, the HER is less competitive on these materials and allows the CO₂RR to proceed at higher Faradaic efficiency. Despite this, change in free energy for *COOH adsorption (ΔG_{*COOH}) is generally always larger than that of *H (ΔG_{*H}) which means the HER will be favoured and proceed at smaller overpotentials.^[103] For preferential and selective reduction of CO₂, a few computational studies have been conducted with tailored

nanostructures, such as introducing curvature in the form of porphyrin nanotubes.^[104] It has also been found that co-ordination of axial ligands to the metal centre can bind *OCHO in preference to both *H and *COOH.^[103] This is because the weaker binding of OCHO to the metal causes a decrease in energy of the 3d_{z2} orbital which causes greater binding to the ligands and hence, stabilises *OCHO. Whereas, the stronger relative binding of H and COOH to the metal leads to an increase in energy of the 3d_{z2} which destabilises the metal-ligand interaction.

A.4.3 Other Metal-N/C Composites

Functionalising transition metals with nitrogen/carbon as a class of M-N-C materials has proven to be an effective strategy for producing high performing bifunctional electrocatalysts for processes like the OER and ORR.^[105] Given d-band theory, that the binding of an intermediate is largely dependent on the electronic states of the metal surface, introducing s and p states for either disruption or hybridisation of the metal d orbitals alters the intermediate adsorption states and can break scaling relationships.^[98] Therefore, these materials appear promising for reducing overpotential. Few CO₂RR studies on such materials exist, but recent studies suggest that *COOH binding is dominated by the p orbital interaction of the intermediate with the N sites,^[94] which generally results in CO formation and desorption. Interestingly, due to the presence of d states contributed by the metal in M-N-C, subsequent *CO binding and protonation can occur, depending on the affinity of the metal species for CO. Given the high activity afforded by these carbon-based materials, it is cause for further exploration in the future.

A.4.4 Nanostructured Carbon Supports

Recently, DFT studies have been conducted in order to understand the synergy and underlying mechanism between metal NPs and carbon supports toward the reduction of CO₂. Lim *et al.* used DFT to study Cu nanoparticles (Cu₅₅; diameter of approximately 0.9 nm) on a defective graphene system.^[106] The Cu₅₅ exhibited strong adsorption on the graphene with adsorption energy of -4.26 eV. This was attributed to the dangling bonds of carbon atoms adjacent to the 5-8-5 vacancy site interacting with the copper atoms and is thought to be key in preventing sintering of the nanoparticles. To reveal the intrinsic activity of this composite system, they investigated the projected DOS of adsorbed CO* and CHO* intermediates with surface Cu atoms. Both Cu(111)

surfaces and the C₅₅-graphene systems show strong hybridisation of molecular orbitals for CO adsorption, however, when CHO is adsorbed, Cu₅₅-graphene shows much stronger hybridisation of molecular orbitals which represents better stabilisation of the CHO* intermediate on the Cu₅₅-graphene system.

Studies on single metal atom catalysts in graphene frameworks have also shown promise for enhancing CO₂RR activity with preferential pathways over the HER.^[99, 107] Due to strong metal-support interactions, namely metal d-orbitals with graphene p-orbitals, re-distribution of charge from the metal centre occurs, which was found to be the primary cause of deviation from conventional scaling relationships and improvements to CO₂RR activity. Similar observations have also been made for single dispersed metal atoms on metal carbide supports.^[108] Further, these materials maximise metal utilisation and can greatly improve catalytic efficiency.^[109, 110] Motivated by the work of He *et al.*,^[60] DFT studies were extended to investigate transition metal dopant pairs (dimers) on graphene supports in order to reveal whether these dispersed metal centres can be tuned to CO₂RR.^[107] The computational hydrogen electrode (CHE) was utilised to elucidate free energy profiles, electrocatalytic performance and reaction pathways and it was found that dimer geometry and configuration on the graphene support plays a very important role in the adsorption of intermediate species. Interestingly, the adsorption energy of CO and COOH species on iron (Fe) dimers at tri- and quadro-vacancies in the graphene (where two Fe atoms are on opposite sides of the graphene plane) shows a linear scaling relationship comparable to packed metal surfaces. This suggests that reducing the required overpotentials for CO₂RR on single metal atom sites is difficult. However, for Fe dimers at two adjacent single vacancies (2SV) in the graphene support (both Fe atoms on the same side of the graphene plane), COOH experiences greater stabilisation as it is co-ordinated in a bidentate configuration. As a result of this additional stabilisation, it is likely that adsorption energies of intermediates do not follow a linear scaling relationship on this metal dimer-2SV configuration. Additionally, the graphene support plays an important role as the high dispersion of metal dimers is achieved by the strong binding afforded by the vacancy sites within the defective graphene which prevents clustering. Given this result, it is clear that using carbon supports facilitates the synthesis of CO₂RR electrocatalysts with better metal utilisation and produces synergistic effects for enhanced activity.

A.5 Summary and Outlook

In this report, we have presented a summary of recent progress regarding nanostructured carbon-based materials for use as heterogeneous CO₂RR electrocatalysts. We have discussed the many advantages that carbon materials present in these applications such as tuneable compositions and morphologies, cost effectiveness, and durability in operation. Further, these materials used as catalyst supports for active metal nanoparticles provide many benefits like stabilisation and prevention of agglomeration of the nanoparticles, leading to enhanced CO₂RR activity. Thus far, carbon materials have shown potential as CO₂RR electrocatalysts with appreciable activity and selectivity, and recent examples of totally metal-free electrocatalysts facilitating C-C coupling to higher order hydrocarbons with high selectivity are very promising. However, despite efforts exerted in developing new electrocatalysts for commercial CO₂ reduction, electrically effective and economically feasible CO₂RR processes still remain to be seen. Although carbon-based electrocatalysts have addressed some of the issues associated with metal electrocatalysts, namely stability, these materials still deliver inadequate activity and require relatively high overpotentials. Further, the binding of different reaction intermediates is highly dependent on the material and its surface morphology. Therefore, products selectivity and yield are highly variable between materials.

At this stage in the technology’s development, further fundamental computational and experimental studies are required, with the following three main areas needing to be addressed: elucidation of active sites, the control of product selectivity and the role of the electrolyte. On heteroatom doped carbon, the true active sites are still ambiguous, so it is necessary to elucidate and confirm the active sites that are introduced by dopants. Once we have a better understanding of the moieties and morphological features that facilitate CO₂ reduction, we will be able to better engineer materials with an optimum distribution and density of active sites. Along with the active sites, product selectivity must also be examined more closely through combination of DFT studies and experimental confirmation. Given intermediates binding is dependent on the specific material, even varying between seemingly similar materials (see Refs [51] & [29] for example), better determining intermediate binding trends could significantly

increase our predictive capability for activity and selectivity. Table A.1 presents a summary of the performance of recent carbon-based CO₂RR electrocatalysts (grouped as: graphene materials, carbon nanotubes and nanofibers, nanodiamond, and porphyrin materials) and details the varying products distribution between them. Additionally, the role of the electrolyte (type and concentration) has been explored to some extent but is a factor which warrants greater focus as it directly affects CO₂RR performance. For instance, some studies have employed ionic liquids and found that they contribute directly to the reaction mechanism and are effective in suppressing hydrogen evolution. Although ionic liquids may not lend themselves to scale up, use of new electrolytes may provide much needed insight into the CO₂RR mechanism.

Looking forward, using a combination of computational results with experimental data can effectively screen and assess the performance of a multitude of materials, from which rational design strategies can be developed to tune physicochemical properties for optimum performance. Design strategies such as surface engineering of catalysts will play a crucial role in increasing electrocatalytic activities for commercially viable CO₂RR. Especially for doped metal free catalysts, producing materials with a greater density of exposed edge sites is likely to facilitate the formation of edge site dopants in greater number which will in turn enhance activity as shown by previous studies.^[39] Further, for anchored metal nanoparticles, improved surface engineering of carbon supports can accommodate smaller and better defined nanoparticles which can increase the utilisation efficiency of the metal.

Another crucial design strategy to consider for commercially viable operation is the suppression of the HER. As shown by DFT, single metal atom dopants may provide a larger kinetic barrier to H^{*} adsorption.^[101] Therefore, the design of supported single metal atom catalysts may provide effective suppression of the HER and increase selectivity towards CO₂ reduction. Some recent strategies proposed for suppressing the HER and improving the selectivity towards the electrochemical reduction of nitrogen could also be applied to CO₂RR.^[111] These strategies involve limiting the proton and electron transfer rate to the active sites and by doing this, target adsorbates can better compete with H^{*} and develop appreciable surface coverage. However, the option of hydrogen evolution simultaneously with CO₂ reduction for Fisher-Tropsch type application should not be ruled out and it would be appropriate to review the feasibility

of producing Fisher-Tropsch feedstock *via* electrochemical CO₂ reduction.

In summary, the electrochemical reduction of CO₂ provides an elegant solution to long term global energy needs. Although the technology still faces many challenges, recent progress in the field, with the constant production of new knowledge through the combination of advanced computational and experimental tools, appears promising. Through sustained efforts, a fully sustainable route to conventional fuels and chemicals, by utilising totally metal free catalysts driven by renewable energy, could be achieved.

A.6 References

1. L. Mihăescu, S. Mărginean, E. A. Stoica, J. Grabara, M.-F. Popescu, *Procedia Econ. Finan.* 2015, *27*, 467.
2. C. McGlade, P. Ekins, *Nature* 2015, *517*, 187.
3. PRB, *2016 World Population Data Sheet*, Population Reference Bureau, Washington, DC, USA 2016.
4. REN21, *Renewables 2016 Global Status Report*, REN21 Secretariat, Paris, France 2016.
5. Y. Hori, in *Handbook of Fuel Cells*, Wiley, Chichester, England 2003.
6. E. V. Kondratenko, G. Mul, J. Baltrusaitis, G. O. Larrazabal, J. Perez-Ramirez, *Energy Environ. Sci.* 2013, *6*, 3112.
7. J. Low, J. Yu, W. Ho, *J. Phys. Chem. Lett.* 2015, *6*, 4244.
8. A. M. Appel, J. E. Bercaw, A. B. Bocarsly, H. Dobbek, D. L. DuBois, M. Dupuis, J. G. Ferry, E. Fujita, R. Hille, P. J. A. Kenis, C. A. Kerfeld, R. H. Morris, C. H. F. Peden, A. R. Portis, S. W. Ragsdale, T. B. Rauchfuss, J. N. H. Reek, L. C. Seefeldt, R. K. Thauer, G. L. Waldrop, *Chem. Rev.* 2013, *113*, 6621.
9. S. G. Jadhav, P. D. Vaidya, B. M. Bhanage, J. B. Joshi, *Chem. Eng. Res. Des.* 2014, *92*, 2557.
10. J. Qiao, Y. Liu, F. Hong, J. Zhang, *Chem. Soc. Rev.* 2014, *43*, 631.
11. G.-L. Chai, Z.-X. Guo, *Chem. Sci.* 2016, *7*, 1268.
12. T. Hatsukade, K. P. Kuhl, E. R. Cave, D. N. Abram, T. F. Jaramillo, *Phys. Chem. Chem. Phys.* 2014, *16*, 13814.
13. N. Yang, S. R. Waldvogel, X. Jiang, *ACS Appl. Mater. Interfaces* 2016, *8*, 28357.
14. X. Mao, T. A. Hatton, *Ind. Eng. Chem. Res.* 2015, *54*, 4033.
15. D. D. Zhu, J. L. Liu, S. Z. Qiao, *Adv. Mater.* 2016, *28*, 3423.
16. X. Liu, L. Dai, *Nat. Rev. Mater.* 2016, *1*, 16064.
17. J. Zhang, Z. Xia, L. Dai, *Sci. Adv.* 2015, *1*, e1500564.
18. Z.-L. Wang, C. Li, Y. Yamauchi, *Nano Today* 2016, *11*, 373.
19. Q. Lu, F. Jiao, *Nano Energy* 2016, *29*, 439.
20. J. P. Jones, G. K. S. Prakash, G. A. Olah, *Isr. J. Chem.* 2014, *54*, 1451.
21. T. Asefa, *Acc. Chem. Res.* 2016, *49*, 1873.

22. W. Chen, Q. Xin, G. Sun, Q. Wang, Q. Mao, H. Su, *J. Power Sources* 2008, *180*, 199.
23. Y. Lum, Y. Kwon, P. Lobaccaro, L. Chen, E. L. Clark, A. T. Bell, J. W. Ager, *ACS Catal.* 2016, *6*, 202.
24. H. Wang, T. Maiyalagan, X. Wang, *ACS Catal.* 2012, *2*, 781.
25. A. A. Balandin, S. Ghosh, W. Bao, I. Calizo, D. Teweldebrhan, F. Miao, C. N. Lau, *Nano Lett.* 2008, *8*, 902.
26. Y. Liu, J. Li, W. Li, Y. Li, Q. Chen, F. Zhan, *J. Power Sources* 2015, *299*, 492.
27. S. Mao, G. Lu, J. Chen, *Nanoscale* 2015, *7*, 6924.
28. R. Kou, Y. Shao, D. Mei, Z. Nie, D. Wang, C. Wang, V. V. Viswanathan, S. Park, I. A. Aksay, Y. Lin, Y. Wang, J. Liu, *J. Am. Chem. Soc.* 2011, *133*, 2541.
29. J. Wu, M. Liu, P. P. Sharma, R. M. Yadav, L. Ma, Y. Yang, X. Zou, X.-D. Zhou, R. Vajtai, B. I. Yakobson, J. Lou, P. M. Ajayan, *Nano Lett.* 2016, *16*, 466.
30. B. Kumar, M. Asadi, D. Pisasale, S. Sinha-Ray, B. A. Rosen, R. Haasch, J. Abiade, A. L. Yarin, A. Salehi-Khojin, *Nat. Commun.* 2013, *4*, 2819.
31. J. Wu, R. M. Yadav, M. Liu, P. P. Sharma, C. S. Tiwary, L. Ma, X. Zou, X.-D. Zhou, B. I. Yakobson, J. Lou, P. M. Ajayan, *ACS Nano* 2015, *9*, 5364.
32. H. T. Chung, J. H. Won, P. Zelenay, *Nat. Commun.* 2013, *4*, 1922.
33. S. Zhang, H. Zhang, Q. Liu, S. Chen, *J. Mater. Chem. A* 2013, *1*, 3302.
34. S. Ratso, I. Kruusenberg, M. Vikkisk, U. Joost, E. Shulga, I. Kink, T. Kallio, K. Tammeveski, *Carbon* 2014, *73*, 361.
35. S. E. F. Kleijn, S. C. S. Lai, M. T. M. Koper, P. R. Unwin, *Angew. Chem. Int. Ed.* 2014, *53*, 3558.
36. H. Mistry, A. S. Varela, S. Köhl, P. Strasser, B. R. Cuenya, *Nat. Rev. Mater.* 2016, *1*, 16009.
37. J. Benson, Q. Xu, P. Wang, Y. Shen, L. Sun, T. Wang, M. Li, P. Papakonstantinou, *ACS Appl. Mater. Interfaces* 2014, *6*, 19726.
38. L. Zhang, X. Yang, F. Zhang, G. Long, T. Zhang, K. Leng, Y. Zhang, Y. Huang, Y. Ma, M. Zhang, Y. Chen, *J. Am. Chem. Soc.* 2013, *135*, 5921.
39. A. Shen, Y. Zou, Q. Wang, R. A. W. Dryfe, X. Huang, S. Dou, L. Dai, S. Wang, *Angew. Chem. Int. Ed.* 2014, *53*, 10804.

40. L. Tao, Q. Wang, S. Dou, Z. Ma, J. Huo, S. Wang, L. Dai, *Chem. Comm.* 2016, 52, 2764.
41. M. W. Kanan, D. G. Nocera, *Science* 2008, 321, 1072.
42. R. Kortlever, J. Shen, K. J. P. Schouten, F. Calle-Vallejo, M. T. M. Koper, *J. Phys. Chem. Lett.* 2015, 6, 4073.
43. V. Tripkovic, M. Vanin, M. Karamad, M. E. Björketun, K. W. Jacobsen, K. S. Thygesen, J. Rossmeisl, *J. Phys. Chem. C* 2013, 117, 9187.
44. M. Karamad, V. Tripkovic, J. Rossmeisl, *ACS Catal.* 2014, 4, 2268.
45. H. Li, C. Oloman, *J. Appl. Electrochem.* 2005, 35, 955.
46. K. S. Novoselov, A. K. Geim, S. V. Morozov, D. Jiang, Y. Zhang, S. V. Dubonos, I. V. Grigorieva, A. A. Firsov, *Science* 2004, 306, 666.
47. D. Higgins, P. Zamani, A. Yu, Z. Chen, *Energy Environ. Sci.* 2016, 9, 357.
48. M. Liu, R. Zhang, W. Chen, *Chem. Rev.* 2014, 114, 5117.
49. B. Xia, Y. Yan, X. Wang, X. W. Lou, *Mater. Horiz.* 2014, 1, 379.
50. N. Sreekanth, M. A. Nazrulla, T. V. Vineesh, K. Sailaja, K. L. Phani, *Chem. Comm.* 2015, 51, 16061.
51. H. Wang, Y. Chen, X. Hou, C. Ma, T. Tan, *Green Chem.* 2016, 18, 3250.
52. H.-R. M. Jhong, C. E. Tornow, B. Smid, A. A. Gewirth, S. M. Lyth, P. J. A. Kenis, *ChemSusChem* 2016, 10, 1094.
53. S. Zhang, P. Kang, S. Ubnoske, M. K. Brennaman, N. Song, R. L. House, J. T. Glass, T. J. Meyer, *J. Am. Chem. Soc.* 2014, 136, 7845.
54. X. Sun, X. Kang, Q. Zhu, J. Ma, G. Yang, Z. Liu, B. Han, *Chem. Sci.* 2016, 7, 2883.
55. J. Wu, S. Ma, J. Sun, J. I. Gold, C. Tiwary, B. Kim, L. Zhu, N. Chopra, I. N. Odeh, R. Vajtai, A. Z. Yu, R. Luo, J. Lou, G. Ding, P. J. A. Kenis, P. M. Ajayan, *Nat. Commun.* 2016, 7, 13869.
56. L. Qu, Y. Liu, J.-B. Baek, L. Dai, *ACS Nano* 2010, 4, 1321.
57. R. Li, Z. Wei, X. Gou, *ACS Catal.* 2015, 5, 4133.
58. H. Jiang, Y. Zhu, Y. Su, Y. Yao, Y. Liu, X. Yang, C. Li, *J. Mater. Chem. A* 2015, 3, 12642.
59. Q. Li, N. Mahmood, J. Zhu, Y. Hou, S. Sun, *Nano Today* 2014, 9, 668.
60. Z. He, K. He, A. W. Robertson, A. I. Kirkland, D. Kim, J. Ihm, E. Yoon, G.-

- D. Lee, J. H. Warner, *Nano Lett.* 2014, *14*, 3766.
61. B. Qiao, A. Wang, X. Yang, L. F. Allard, Z. Jiang, Y. Cui, J. Liu, J. Li, T. Zhang, *Nat. Chem.* 2011, *3*, 634.
 62. M. Yang, L. F. Allard, M. Flytzani-Stephanopoulos, *J. Am. Chem. Soc.* 2013, *135*, 3768.
 63. Q. Li, W. Zhu, J. Fu, H. Zhang, G. Wu, S. Sun, *Nano Energy* 2016, *24*, 1.
 64. Y. Song, R. Peng, D. K. Hensley, P. V. Bonnesen, L. Liang, Z. Wu, H. M. Meyer, M. Chi, C. Ma, B. G. Sumpter, A. J. Rondinone, *ChemistrySelect* 2016, *1*, 6055.
 65. B. Wu, D. Hu, Y. Yu, Y. Kuang, X. Zhang, J. Chen, *Chem. Comm.* 2010, *46*, 7954.
 66. F. Lei, W. Liu, Y. Sun, J. Xu, K. Liu, L. Liang, T. Yao, B. Pan, S. Wei, Y. Xie, *Nat. Commun.* 2016, *7*, 12697.
 67. D. C. B. Alves, R. Silva, D. Voiry, T. Asefa, M. Chhowalla, *Mater. Renew. Sustain. Energy* 2015, *4*, 1.
 68. P. P. Sharma, J. Wu, R. M. Yadav, M. Liu, C. J. Wright, C. S. Tiwary, B. I. Yakobson, J. Lou, P. M. Ajayan, X.-D. Zhou, *Angew. Chem. Int. Ed.* 2015, *54*, 13701.
 69. Y. Oh, V.-D. Le, U. N. Maiti, J. O. Hwang, W. J. Park, J. Lim, K. E. Lee, Y.-S. Bae, Y.-H. Kim, S. O. Kim, *ACS Nano* 2015, *9*, 9148.
 70. X. Tan, L. Kou, H. A. Tahini, S. C. Smith, *Sci. Rep.* 2015, *5*, 17636.
 71. X. Lu, T. H. Tan, Y. H. Ng, R. Amal, *Chem. Eur. J.* 2016, *22*, 11991.
 72. M. Gangeri, S. Perathoner, S. Caudo, G. Centi, J. Amadou, D. Bégin, C. Pham-Huu, M. J. Ledoux, J. P. Tessonnier, D. S. Su, R. Schlögl, *Catal. Today* 2009, *143*, 57.
 73. G. Lu, H. Wang, Z. Bian, X. Liu, *Scientific World J.* 2013, *2013*, 8.
 74. S. Safdar Hossain, S. u. Rahman, S. Ahmed, *J. Nanomater.* 2014, *2014*, 10.
 75. R. P. S. Chaplin, A. A. Wragg, *J. Appl. Electrochem.* 2003, *33*, 1107.
 76. M. T. M. Koper, *J. Electroanal. Chem.* 2011, *660*, 254.
 77. J. Hawecker, J.-M. Lehn, R. Ziessel, *J. Chem. Soc., Chem. Commun.* 1984, 328.
 78. J. Y. Becker, B. Vainas, R. Eger, L. Kaufman, *J. Chem. Soc., Chem. Commun.* 1985, 1471.
 79. N. Kornienko, Y. Zhao, C. S. Kley, C. Zhu, D. Kim, S. Lin, C. J. Chang, O. M.

- Yaghi, P. Yang, *J. Am. Chem. Soc.* 2015, *137*, 14129.
80. S. Lin, C. S. Diercks, Y.-B. Zhang, N. Kornienko, E. M. Nichols, Y. Zhao, A. R. Paris, D. Kim, P. Yang, O. M. Yaghi, C. J. Chang, *Science* 2015, *349*, 1208.
 81. J. Shen, R. Kortlever, R. Kas, Y. Y. Birdja, O. Diaz-Morales, Y. Kwon, I. Ledezma-Yanez, K. J. P. Schouten, G. Mul, M. T. M. Koper, *Nat. Commun.* 2015, *6*, 8177.
 82. E. A. Mohamed, Z. N. Zahran, Y. Naruta, *Chem. Comm.* 2015, *51*, 16900.
 83. Z. Weng, J. Jiang, Y. Wu, Z. Wu, X. Guo, K. L. Materna, W. Liu, V. S. Batista, G. W. Brudvig, H. Wang, *J. Am. Chem. Soc.* 2016, *138*, 8076.
 84. I. Bhugun, D. Lexa, J.-M. Saveant, *J. Am. Chem. Soc.* 1994, *116*, 5015.
 85. I. Bhugun, D. Lexa, J.-M. Savéant, *J. Am. Chem. Soc.* 1996, *118*, 1769.
 86. I. Bhugun, D. Lexa, J.-M. Savéant, *J. Phys. Chem.* 1996, *100*, 19981.
 87. S. Aoi, K. Mase, K. Ohkubo, S. Fukuzumi, *Chem. Comm.* 2015, *51*, 10226.
 88. J. J. Walsh, C. L. Smith, G. Neri, G. F. S. Whitehead, C. M. Robertson, A. J. Cowan, *Faraday Discuss.* 2015, *183*, 147.
 89. X. Zhou, D. Micheroni, Z. Lin, C. Poon, Z. Li, W. Lin, *ACS Appl. Mater. Interfaces* 2016, *8*, 4192.
 90. S. A. Yao, R. E. Ruther, L. Zhang, R. A. Franking, R. J. Hamers, J. F. Berry, *J. Am. Chem. Soc.* 2012, *134*, 15632.
 91. Y. Liu, S. Chen, X. Quan, X. Fan, H. Zhao, Q. Zhao, H. Yu, *Appl. Catal., B* 2014, *154-155*, 206.
 92. Y. Liu, S. Chen, X. Quan, H. Yu, *J. Am. Chem. Soc.* 2015, *137*, 11631.
 93. K. Nakata, T. Ozaki, C. Terashima, A. Fujishima, Y. Einaga, *Angew. Chem. Int. Ed.* 2014, *53*, 871.
 94. A. S. Varela, N. Ranjbar Sahraie, J. Steinberg, W. Ju, H.-S. Oh, P. Strasser, *Angew. Chem. Int. Ed.* 2015, *54*, 10758.
 95. D. Xiang, D. Magana, R. B. Dyer, *J. Am. Chem. Soc.* 2014, *136*, 14007.
 96. P. A. Christensen, A. Hamnett, A. V. G. Muir, *J. Electroanal. Chem.* 1990, *288*, 197.
 97. K. Hara, A. Kudo, T. Sakata, *J. Electroanal. Chem.* 1997, *421*, 1.
 98. Y. Li, Q. Sun, *Adv. Energy Mater.* 2016, *6*, 1600463.
 99. S. Back, J. Lim, N.-Y. Kim, Y.-H. Kim, Y. Jung, *Chem. Sci.* 2017, *8*, 1090.

- 100. F. Abild-Pedersen, J. Greeley, F. Studt, J. Rossmeisl, T. R. Munter, P. G. Moses, E. Skúlason, T. Bligaard, J. K. Nørskov, *Phys. Rev. Lett.* 2007, *99*, 016105.
- 101. A. Bagger, W. Ju, A. S. Varela, P. Strasser, J. Rossmeisl, *Catal. Today* 2017, *288*, 74.
- 102. I. M. B. Nielsen, K. Leung, *J. Phys. Chem. A* 2010, *114*, 10166.
- 103. M.-J. Cheng, Y. Kwon, M. Head-Gordon, A. T. Bell, *J. Phys. Chem. C* 2015, *119*, 21345.
- 104. G. Zhu, Y. Li, H. Zhu, H. Su, S. H. Chan, Q. Sun, *ACS Catal.* 2016, *6*, 6294.
- 105. Y. Zheng, Y. Jiao, Y. Zhu, Q. Cai, A. Vasileff, L. H. Li, Y. Han, Y. Chen, S.-Z. Qiao, *J. Am. Chem. Soc.* 2017, *139*, 3336.
- 106. D.-H. Lim, J. H. Jo, D. Y. Shin, J. Wilcox, H. C. Ham, S. W. Nam, *Nanoscale* 2014, *6*, 5087.
- 107. Y. Li, H. Su, S. H. Chan, Q. Sun, *ACS Catal.* 2015, *5*, 6658.
- 108. S. Back, Y. Jung, *ACS Energy Lett.* 2017, *2*, 969.
- 109. J. M. Thomas, R. Raja, D. W. Lewis, *Angew. Chem. Int. Ed.* 2005, *44*, 6456.
- 110. X.-F. Yang, A. Wang, B. Qiao, J. Li, J. Liu, T. Zhang, *Acc. Chem. Res.* 2013, *46*, 1740.
- 111. A. R. Singh, B. A. Rohr, J. A. Schwalbe, M. Cargnello, K. Chan, T. F. Jaramillo, I. Chorkendorff, J. K. Nørskov, *ACS Catal.* 2017, *7*, 706.

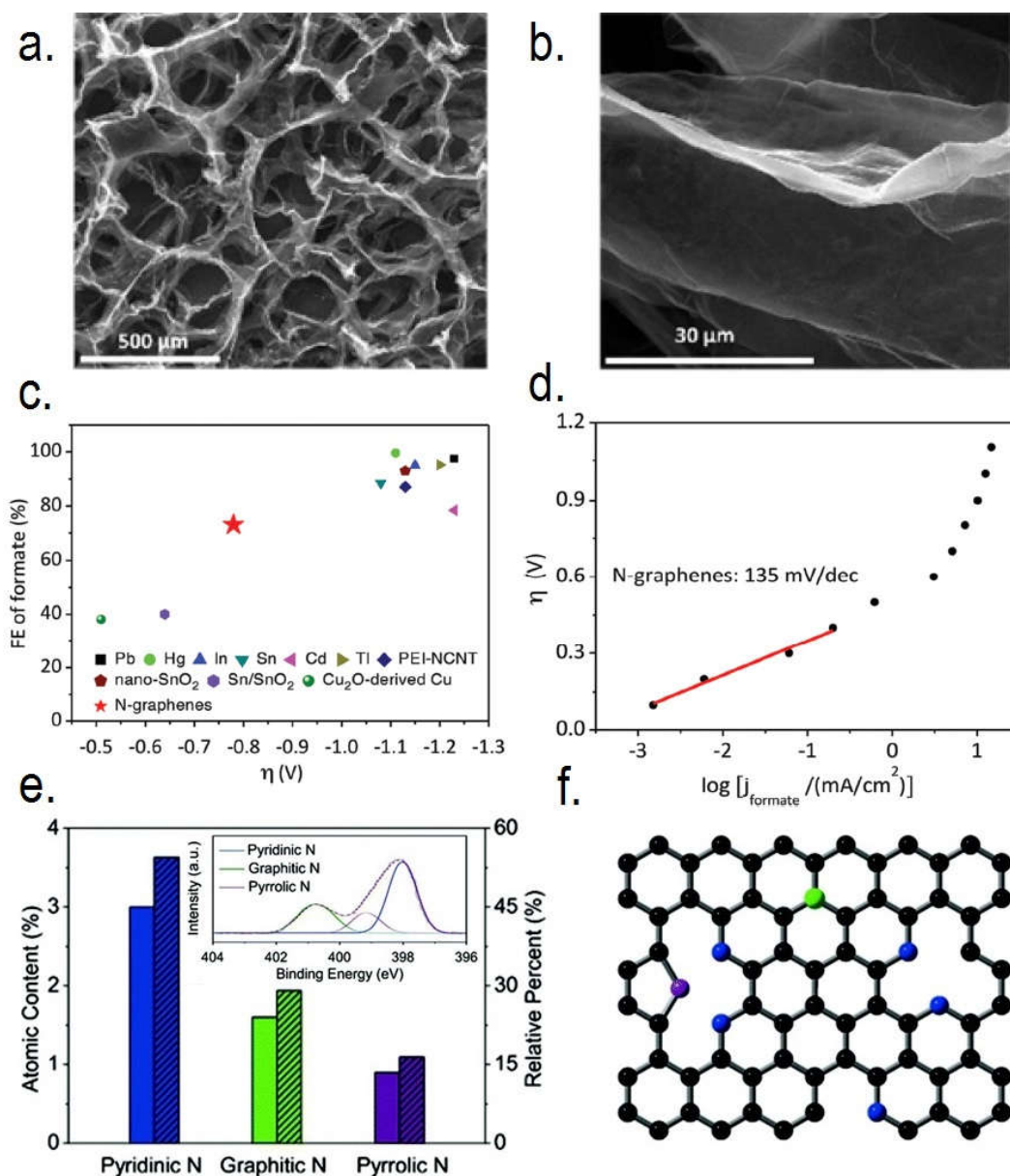


Figure A.1 Material characteristaion of N-graphene. (a) SEM image showing the microporous structure of the graphene foam. (b) Higher resolution SEM image of the characteristic crinkles and folds of an N-graphene sheet. Adapted with permission.^[29] Copyright 2015, The American Chemical Society. (c) Maximum Faradaic efficiency at corresponding overpotential for N-graphenes (red star) compared with other reported CO₂RR electrocatalysts. (d) Tafel plot for N-graphenes. (e) Statistic atomic content and relative percentage of the N functionalities in N-graphene. Inset shows the deconvoluted N 1s spectrum for N-graphene. (f) Representation of N functionalities in the graphene framework with pyridinic (blue), graphitic (green), and pyrrolic (purple) N configurations. Adapted with permission.^[51] Copyright 2016, The Royal Society of Chemistry.

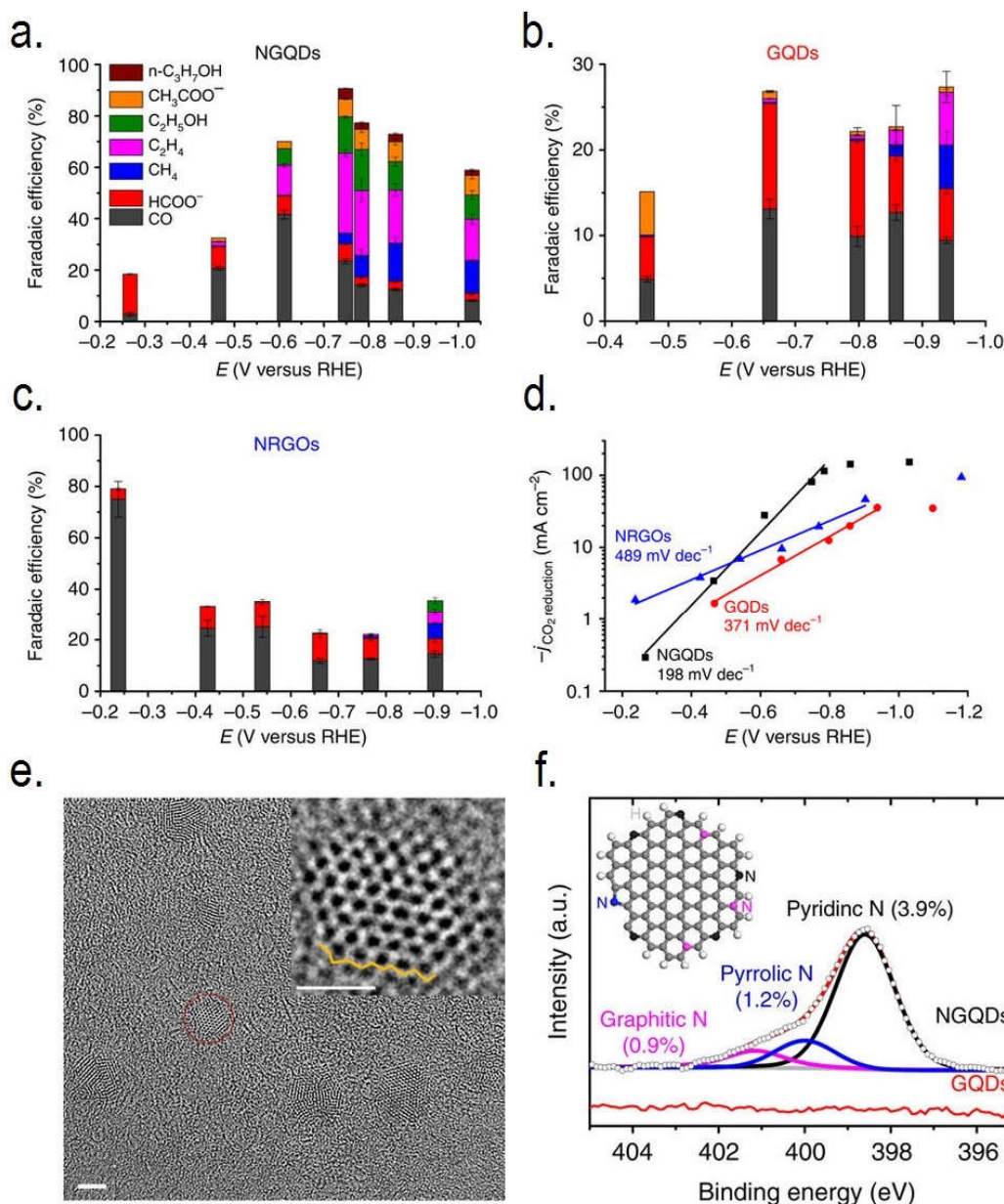


Figure A.2 Faradaic efficiencies at various potentials toward: carbon monoxide (grey), formate (red), methane (blue), ethylene (purple), ethanol (green), acetate (orange), and *n*-propanol (brown) on (a) N-doped graphene quantum dots (NGQDs), (b) Pristine graphene quantum dots (GQDs), and (c) N-doped reduced graphene oxide sheets (NRGO). (d) Tafel slopes for NGQDs, GQDs, and NRGO. (e) High magnification TEM image displaying the nanostructure of the NGQDs. Scale bar: 2 nm. Inset shows the zigzag edge of the graphene. Inset scale bar: 1 nm. (f) Deconvoluted high resolution N 1s spectrum for the NGQDs with the atomic concentration of each N functionality shown. The inset schematic represents the structure of the NGQDs with pyridinic (black), pyrrolic (blue), and graphitic (pink) N configurations. Adapted with permission.^[55] Copyright 2016, Nature Publishing Group.

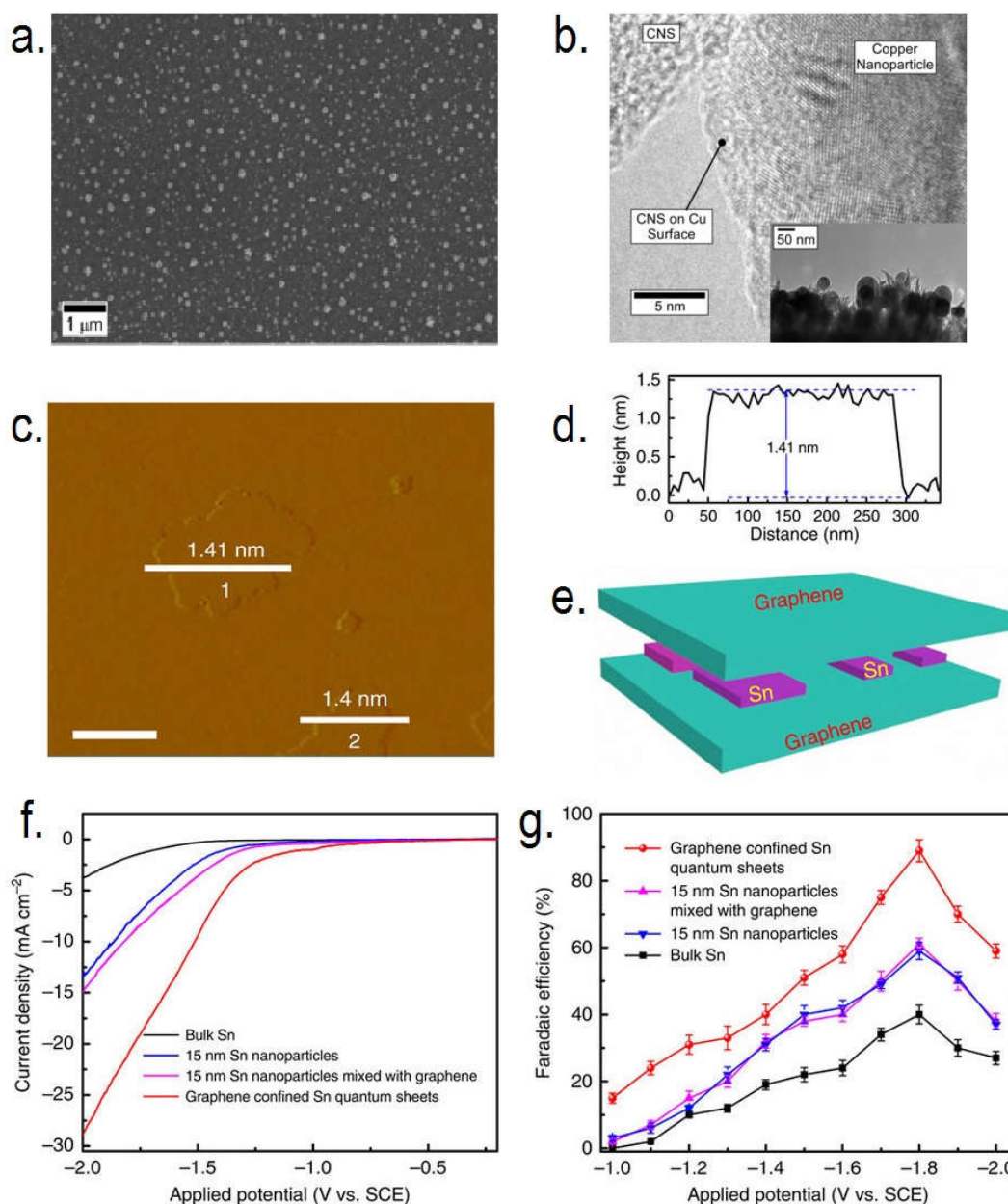


Figure A.3 (a) Low magnification SEM displaying the uniform distribution and size of copper nanoparticles on the carbon nano-spike material (Cu/CNS). (b) High resolution TEM image of the Cu/CNS. Inset shows the close contact the copper nanoparticles have with the CNS. Adapted with permission.^[64] Copyright 2016, Wiley-VCH Verlag GmbH & Co. (c) Atomic Force Microscopy (AFM) image of the confined tin quantum sheets. (d) Corresponding height profile to the AFM. (e) Schematic representation of the tin quantum sheets confined between sheets of graphene. Electrochemical performance of tin quantum sheets confined in graphene, 15 nm Sn nanoparticles/graphene mixture, 15 nm Sn nanoparticles, and bulk Sn, represented by (f) Linear sweep voltammetry (LSV) curves in CO_2 saturated 0.1 M NaHCO_3 , and (g) Faradaic efficiency toward formate at various potentials. Adapted with permission.^[66] Copyright 2016, Nature Publishing Group.

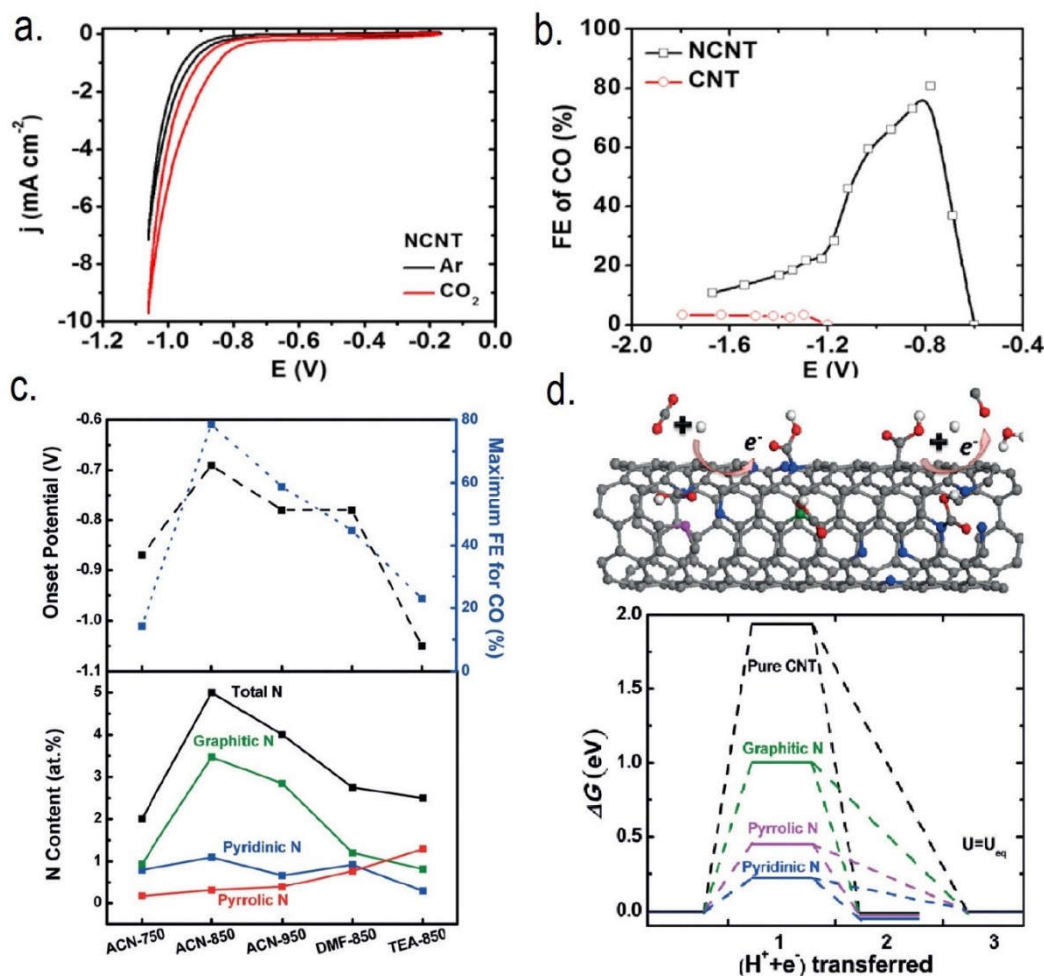


Figure A.4 (a) Cyclic voltammetry plots for NCNTs in Ar (black) and CO₂ (red) saturated 0.1 M KHCO₃ electrolyte at a scan rate of 50 mV s⁻¹. (b) Comparison of Faradaic efficiency towards CO against cell potential for NCNTs (black) and CNTs (red). Adapted with permission.^[31] Copyright 2015, American Chemical Society. (c) Resultant onset potential (black dash) and maximum Faradaic efficiency toward CO (blue dots) for various NCNTs against their respective total N content and N composition. (d) Free energy diagram of CO formation at equilibrium potentials for pyridinic N (blue), pyrrolic N (purple), graphitic N (green), and the carbon network of pure CNTs (black) with schematic representation of the process on different N defects in the CNT. Adapted with permission.^[68] Copyright 2015, Wiley-VCH Verlag GmbH & Co.

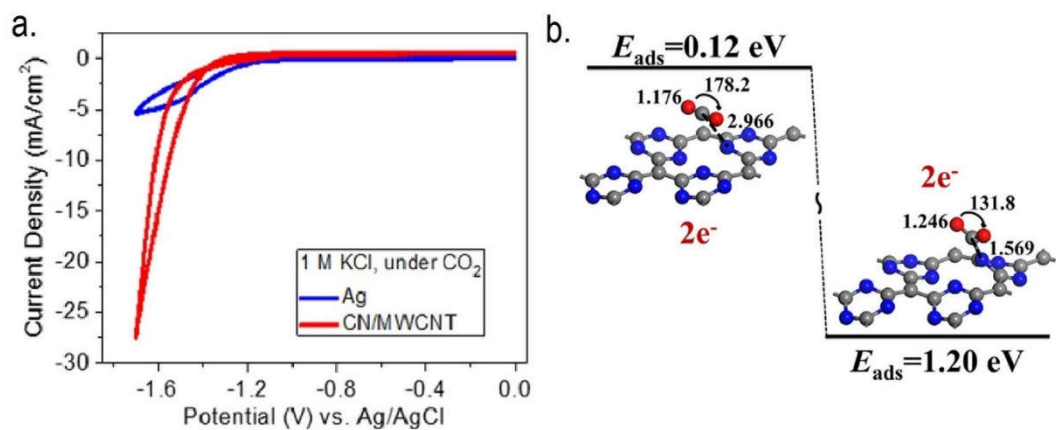


Figure A.5 (a) Cyclic Voltammetry plots of carbon nitride/MWCNT composites and Ag nanoparticles in CO₂ saturated 1 M KCl electrolyte. Adapted with permission.^[52] Copyright 2016, Wiley-VCH Verlag GmbH & Co. (b) The energy change of the adsorption and stabilisation process of a CO₂ molecule on the surface of negatively polarised graphitic carbon nitride. Adapted with permission.^[70] Copyright 2015, Nature Publishing Group.

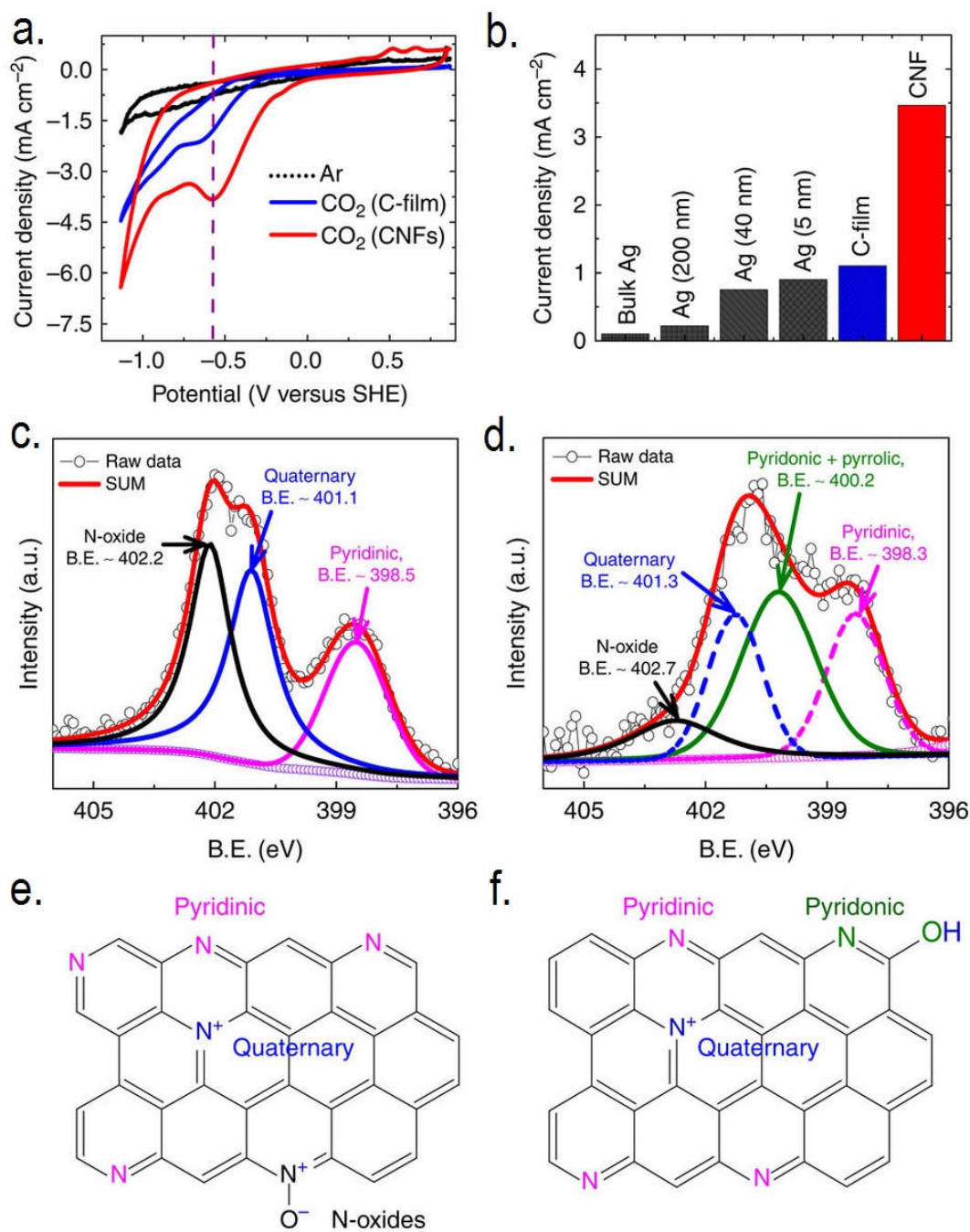


Figure A.6 (a) Cyclic Voltammograms plots for CO₂ reduction on carbon nanofibres (CNFs) in Ar saturated (black curve) and CO₂ saturated (red curve) EMIM-BF₄ electrolyte, and on carbon films in CO₂ saturated (blue curve) EMIM-BF₄ electrolyte. The dashed line represents the CO₂ reduction peak for the CNFs. (b) Comparison of peak CO₂RR catalytic current densities for CNFs and other electrocatalysts in EMIM-BF₄ electrolyte. (c) Deconvoluted N 1s spectrum of CNFs before and (d) after electrochemical testing. (e) Corresponding atomic N configurations before and (f) after electrochemical testing, on the basis of XPS analysis. Adapted with permission.^[30] Copyright 2016, Nature Publishing Group.

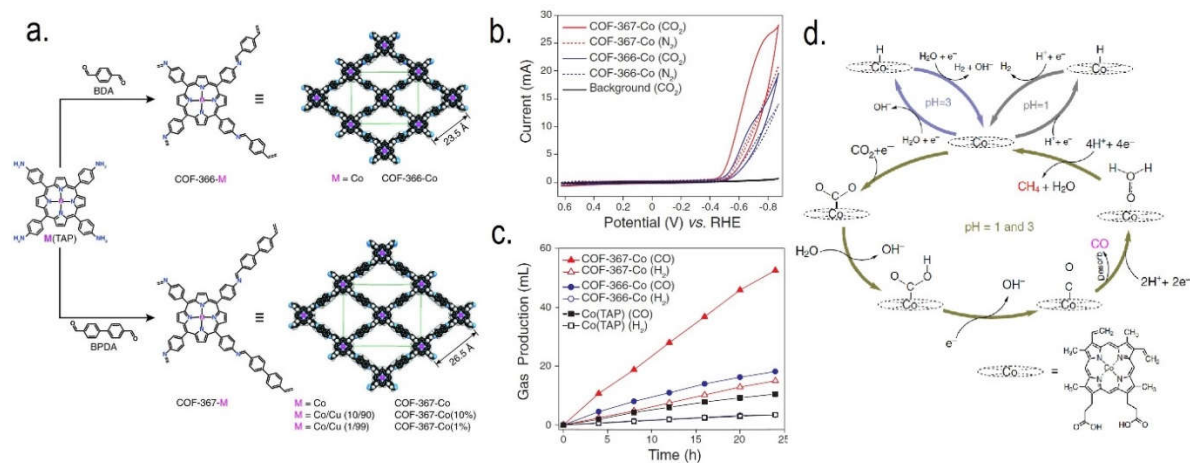


Figure A.7 (a) Schematic representation of the covalent organic framework (COF) constructed of cobalt porphyrins linked with BDA (COF-366-Co) and BDPA (COF-367-Co). Included in the model is the pore size for each structure. (b) Cyclic Voltammetry plots for COF-366-Co and COF-367-Co in N_2 and CO_2 saturated 0.2 M potassium phosphate electrolyte (pH 7.2). (c) Long term electrolysis at -0.67 V *vs.* RHE as a function of the accumulated CO and hydrogen produced on COF-366-Co, COF-367-Co, and their molecular analogue Co(TAP). Adapted with permission. Copyright 2015,^[80] The American Association for the Advancement of Science. (d) Proposed mechanism of the electroreduction of CO_2 on a cobalt protoporphyrin at pH 1 and 3. The chemical structure of the cobalt protoporphyrin is shown in the bottom right. Adapted with permission.^[81] Copyright 2015, Nature Publishing Group.

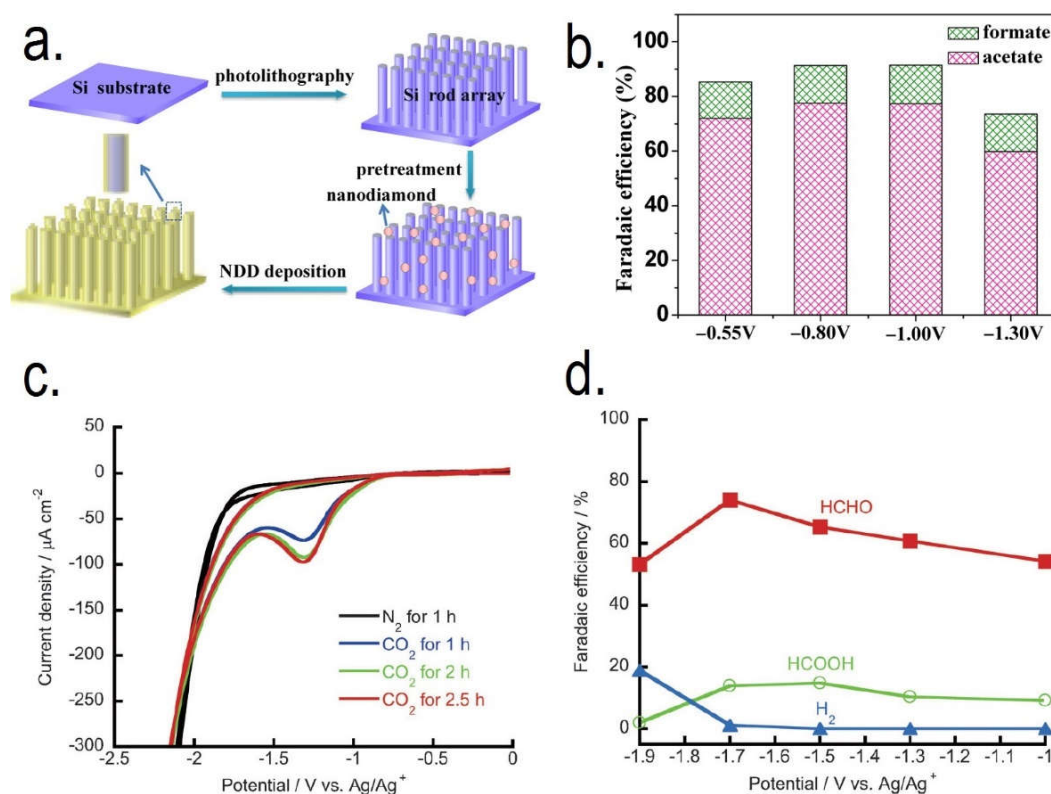


Figure A.8 (a) Schematic representation of the synthesis route for producing N-doped nanodiamond (NDD) on a Si rod array. (b) Faradaic efficiencies toward CO_2 reduction to acetate and formate on optimised NDD between -0.55 and -1.30 V in CO_2 saturated NaHCO_3 electrolyte. Adapted with permission.^[92] Copyright 2015, The American Chemical Society. (c) Cyclic Voltammetry plots for B-doped nanodiamond (BDD) in 0.1 M methanol solution after saturation with N_2 for 1 hour (black line) and saturation with CO_2 after 1 (blue line), 2 (green line), and 2.5 (red line) hours. (d) Faradaic efficiencies toward CO_2 reduction to formaldehyde (red), formic acid (green), and hydrogen (blue) on BDD between -1.0 and -1.9 V in CO_2 saturated methanol solution. Adapted with permission.^[93] Copyright 2014, Wiley-VCH Verlag GmbH & Co.

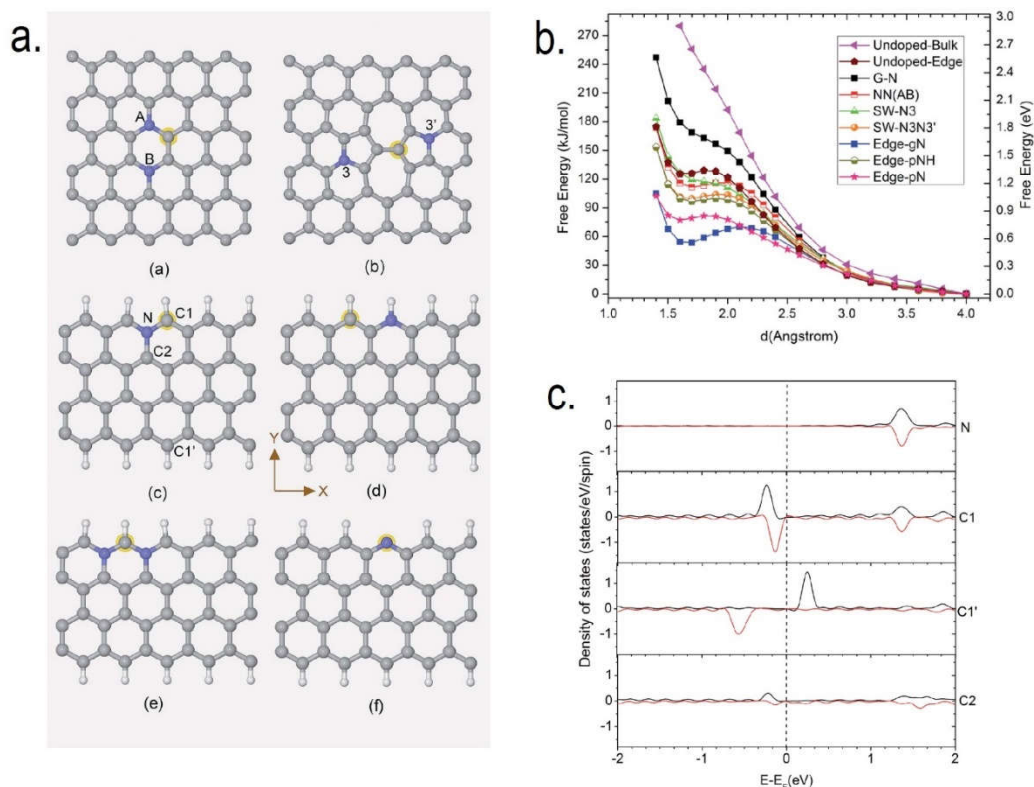


Figure A.9 (a) Unit cells constructed of carbon (grey spheres), nitrogen (blue spheres), and hydrogen (white spheres) atoms used for DFT calculations of CO₂ activation barriers on a) graphitic N doped pristine graphene (NN(AB)), b) gN doped Stone Wales defective graphene (SW-N3N3'), c) graphitic N doped zigzag edge graphene (Edge-gN), d) pyridinium doped zigzag edge graphene (Edge-pNH), e) two graphitic N doped zigzag edge graphene (Edge-2gN, and f) pyridinic doped zigzag edge graphene (Edge-pN). The yellow halos signify the atoms with highest DOS just below the Fermi level and thus CO₂ approach site. (b) Free energy profiles of the approach of the carbon in the CO₂ molecule with the active sites in the outlined unit cells. (c) The DOS of the Edge-gN structure for selected atoms shown in (a), with up-spin and down-spin states shown. Adapted with permission.^[11] Copyright 2016, The Royal Society of Chemistry.

Table A.1-1 Performance summary of recently reported carbon-based electrocatalysts for CO₂ reduction.

Catalyst	Electrolyte	Onset Potential [V] ^a	Applied Potential [V] ^{a,b}	Current Density [mA cm ⁻²] ^b	Products (Faradaic Efficiency [%])	Ref. (Year)
N-Graphene	0.5 M KHCO ₃	-0.30	-0.84	7.5	HCOO ⁻ (73%)	[51] (2016)
N-Graphene Foam	0.1 M KHCO ₃	-0.3	-0.58	1.8	CO (85%), HCOO ⁻ (3%)	[29] (2016)
B-Graphene	0.1 M KHCO ₃	-1.15 (vs. SCE)	-1.4 (vs. SCE)	2.1 ^c	CHOO ⁻ (66%)	[50] (2015)
NGM/CP	[Bmim]BH ₄	-1.0 ^c	-1.4	1.42	CH ₄ (93.5%), CO (4.2%), H ₂ (2.1%)	[54] (2016)
NGQD	1 M KOH	-0.26	-0.75	89 ^c	C ₂ H ₄ (31%), CO, C ₂ H ₅ OH, HCOO ⁻ , CH ₄ , CH ₃ COO ⁻ , n-C ₃ H ₇ OH	[55] (2016)
Cu/CNS	0.1 M KHCO ₃	-0.5 ^c	-1.2	1.4 ^c	C ₂ H ₅ OH (63%), CH ₄ (6.8%), CO (5.2%)	[64] (2016)
p-NG-Cu	0.5 M KHCO ₃	-0.7	-0.9	8.5 ^c	C ₂ H ₄ (19%), HCOO ⁻ (3.8%), CH ₄ (0.9%), C ₂ H ₆ (0.6%)	[63] (2016)
Graphene-Sn Quantum Sheets	0.1 M NaHCO ₃	-0.85 (vs. SCE)	-1.8 (vs. SCE)	21.1	HCOO ⁻ (89%)	[66] (2016)
PEI-NCNT	0.1 M KHCO ₃	-1.2 (vs. SCE)	-1.8 (vs. SCE)	7.2	HCOO ⁻ (85%)	[53] (2014)
NCNT	0.1 M KHCO ₃	-0.70	-0.78	1.0	CO (80%)	[31] (2015)
g-C ₃ N ₄ /MWCNT	0.1 M KHCO ₃	-0.45	-0.75	6 ^c	CO (60%)	[71] (2015)
CN/MWCNT	1 M KCl	-1.46 (vs. Ag/AgCl)	-1.62 (vs. Ag/AgCl)	90	CO (98%), H ₂ (2%)	[52] (2016)
CNF	EMIM-BF ₄	-0.23	-0.573	4	CO (98%)	[30] (2013)
BDD	0.1 M MeOH (TBAP)	-1 (vs. Ag/AgCl) ^c	-1.7 (vs. Ag/AgCl)	<1	HCHO (74%), HCOOH (15%)	[93] (2014)
NDD	0.5 M NaHCO ₃	-0.36	-1.0	0.75 ^c	CH ₃ COO ⁻ (77.6%), CHOO ⁻ (14.6%)	[92] (2015)

Table A.1-2 Performance summary of recently reported carbon-based electrocatalysts for CO₂ reduction (cont').

Catalyst	Electrolyte	Onset Potential [V] ^a	Applied Potential [V] ^{a,b}	Current Density [mA cm ⁻²] ^b	Products (Faradaic Efficiency [%])	Ref. (Year)
FeMn-N-C	0.1 M KHCO ₃	-0.36	-0.5	2.5 ^c	CO (80%)	[94] (2015)
Co-porphyrin MOF	0.5 K ₂ CO ₃	-0.5 ^c	-0.7	1	CO (76%)	[79] (2015)
Co-porphyrin COF	0.5 M KHCO ₃	-0.40	-0.67		CO (90%)	[80] (2015)
Co-protoporphyrin	0.1 HClO ₄ (pH 1-3)	-0.5	-0.6 (pH 3)	0.08	CO (60%)	[81] (2015)
Fe-porphyrin	DMF/10% H ₂ O (0.1M TBAPF ₆)	-1.22	-1.35	1.15	CO (95%)	[82] (2015)
Cu-porphyrin	0.5 M KHCO ₃	-0.676	-0.976	11	CO (11%), CH ₄ (26%), C ₂ H ₄ (6%)	[83] (2016)

^{a)} Reported values are presented *vs.* RHE unless otherwise noted.

^{b)} This value corresponds to the potential at which the Faradaic efficiencies are reported.

^{c)} Values have been interpolated from presented data and are not directly reported by the authors.

Appendix B

Publications and Presentations

Publications Included in this Thesis:

1. **A. Vasileff**, Y.P. Zhu, Y.Q. Zhao, X. Zhi, L. Ge, H.M. Chen, Y. Zheng, S.-Z. Qiao, Electrochemical Reduction of CO₂ to Ethane through Stabilization of an Ethoxy Intermediate, *Angew. Chem. Int. Ed.* 2020, *10.1002/anie.20204846*.
2. **A. Vasileff**, Y. Zheng, S.-Z. Qiao, Improving Ethylene Selectivity of Copper-Based Electrocatalysts for CO₂ Reduction by Gold Deposition. 2020, In Preparation.
3. **A. Vasileff**, X. Zhi, C. Xu, L. Ge, Y. Jiao, Y. Zheng, S.-Z. Qiao, Selectivity control for electrochemical CO₂ reduction by charge redistribution on the surface of copper alloys, *ACS Catal.* 2019, *9*, 9411.
4. **A. Vasileff**, C. Xu, Y. Jiao, Y. Zheng, S.-Z. Qiao, Surface and interface engineering in copper-based bimetallic materials for selective CO₂ electroreduction, *Chem* 2018, *4*, 1809.
5. **A. Vasileff**, C. Xu, L. Ge, Y. Zheng, S.-Z. Qiao, Bronze alloys with tin surface sites for selective electrochemical reduction of CO₂, *Chem. Comm.* 2018, *54*, 13965.
6. **A. Vasileff**, Y. Zheng, S. Z. Qiao, Carbon Solving Carbon's Problems: Recent Progress of Nanostructured Carbon-Based Catalysts for the Electrochemical Reduction of CO₂, *Adv. Energy Mater.* 2017, *7*, 1700759.

Other Publications during Candidature:

7. Y. Zheng, **A. Vasileff**, X. Zhou, Y. Jiao, M. Jaroniec, S.-Z. Qiao, Understanding the roadmap for electrochemical reduction of CO₂ to multi-carbon oxygenates and hydrocarbons on copper-based catalysts, *J. Amer. Chem. Soc.* 2019, *141*, 7646.
8. C. Xu, **A. Vasileff**, D. Wang, B. Jin, Y. Zheng, S.-Z. Qiao, Synergistic catalysis between atomically dispersed Fe and a pyrrolic-NC framework for CO₂ electroreduction, *Nanoscale Horiz.* 2019, *4*, 1411.
9. X. Zhi, Y. Jiao, Y. Zheng, **A. Vasileff**, S.-Z. Qiao, Selectivity roadmap for electrochemical CO₂ reduction on copper-based alloy catalysts, *Nano Energy* 2020, *71*, 104601.
10. Y. Zheng, Y. Jiao, Y. Zhu, Q. Cai, **A. Vasileff**, L. H. Li, Y. Han, Y. Chen, S.-Z. Qiao, Molecule-level g-C₃N₄ coordinated transition metals as a new class of electrocatalysts for oxygen electrode reactions, *J. Amer. Chem. Soc.* 2017, *139*, 3336.
11. Y. Zheng, Y. Jiao, **A. Vasileff**, S. Z. Qiao, The hydrogen evolution reaction in alkaline solution: from theory, single crystal models, to practical electrocatalysts, *Angew. Chem. Int. Ed.* 2018, *57*, 7568.
12. Y. Zhao, B. Jin, **A. Vasileff**, B. Shi, Y. Jiao, S. Z. Qiao, The Ampoule Method: A Pathway towards Controllable Synthesis of Electrocatalysts for Water Electrolysis, *Chem. Eur.* 2020, *26*, 3898.
13. Y. Zhao, T. Ling, S. Chen, B. Jin, **A. Vasileff**, Y. Jiao, L. Song, J. Luo, S. Z. Qiao, Non-metal Single-Iodine-Atom Electrocatalysts for the Hydrogen Evolution Reaction, *Angew. Chem. Int. Ed.* 2019, *58*, 12252.
14. Y. Zhao, B. Jin, **A. Vasileff**, Y. Jiao, S.-Z. Qiao, Contemporaneous oxidation state manipulation to accelerate intermediate desorption for overall water electrolysis, *Chem. Comm.* 2019, *55*, 8313.

15. Y. Zhao, B. Jin, **A. Vasileff**, Y. Jiao, S.-Z. Qiao, Interfacial nickel nitride/sulfide as a bifunctional electrode for highly efficient overall water/seawater electrolysis, *J. Mater. Chem. A* 2019, *7*, 8117.
16. H. Jin, C. Guo, X. Liu, J. Liu, **A. Vasileff**, Y. Jiao, Y. Zheng, S.-Z. Qiao, Emerging two-dimensional nanomaterials for electrocatalysis, *Chem. Rev.* 2018, *118*, 6337.
17. H. Jin, X. Liu, S. Chen, **A. Vasileff**, L. Li, Y. Jiao, L. Song, Y. Zheng, S.-Z. Qiao, Heteroatom-doped transition metal electrocatalysts for hydrogen evolution reaction, *ACS Energy Lett.* 2019, *4*, 805.
18. H. Jin, X. Liu, Y. Jiao, **A. Vasileff**, Y. Zheng, S.-Z. Qiao, Constructing tunable dual active sites on two-dimensional C₃N₄@MoN hybrid for electrocatalytic hydrogen evolution, *Nano Energy* 2018, *53*, 690.
19. H. Jin, X. Liu, **A. Vasileff**, Y. Jiao, Y. Zhao, Y. Zheng, S.-Z. Qiao, Single-crystal nitrogen-rich two-dimensional Mo₅N₆ nanosheets for efficient and stable seawater splitting, *ACS nano* 2018, *12*, 12761.
20. J. Liu, Z. Wang, Z. Lu, L. Zhang, F. Xie, **A. Vasileff**, S.-Z. Qiao, Efficient Surface Modulation of Single-Crystalline Na₂Ti₃O₇ Nanotube Arrays with Ti³⁺ Self-Doping toward Superior Sodium Storage, *ACS Mater. Lett.* 2019, *1*, 389.
21. J. Liu, Y. Zhang, L. Zhang, F. Xie, **A. Vasileff**, S. Z. Qiao, Graphitic Carbon Nitride (g-C₃N₄)-Derived N-Rich Graphene with Tuneable Interlayer Distance as a High-Rate Anode for Sodium-Ion Batteries, *Adv. Mater.* 2019, *31*, 1901261.
22. J. Liu, Y. Zheng, Y. Jiao, Z. Wang, Z. Lu, **A. Vasileff**, S. Z. Qiao, NiO as a bifunctional promoter for RuO₂ toward superior overall water splitting, *Small* 2018, *14*, 1704073.
23. J. Liu, Y. Zheng, Z. Wang, Z. Lu, **A. Vasileff**, S.-Z. Qiao, Free-standing single-crystalline NiFe-hydroxide nanoflake arrays: a self-activated and robust electrocatalyst for oxygen evolution, *Chem. Comm.* 2018, *54*, 463.
24. J. Liu, C. Guo, **A. Vasileff**, S. Qiao, Nanostructured 2D materials: prospective catalysts for electrochemical CO₂ reduction, *Small Methods* 2017, *1*, 1600006.

25. J. Liu, D. Zhu, C. Guo, **A. Vasileff**, S. Z. Qiao, Design strategies toward advanced MOF-derived electrocatalysts for energy-conversion reactions, *Adv. Energy Mater.* 2017, *7*, 1700518.
26. J. Liu, D. Zhu, T. Ling, **A. Vasileff**, S.-Z. Qiao, S-NiFe₂O₄ ultra-small nanoparticle built nanosheets for efficient water splitting in alkaline and neutral pH, *Nano Energy* 2017, *40*, 264.
27. J. Liu, Y. Zheng, D. Zhu, **A. Vasileff**, T. Ling, S.-Z. Qiao, Identification of pH-dependent synergy on Ru/MoS₂ interface: a comparison of alkaline and acidic hydrogen evolution, *Nanoscale* 2017, *9*, 16616.
28. J. Liu, D. Zhu, Y. Zheng, **A. Vasileff**, S.-Z. Qiao, Self-supported earth-abundant nanoarrays as efficient and robust electrocatalysts for energy-related reactions, *ACS Catal.* 2018, *8*, 6707.
29. X. Wang, **A. Vasileff**, Y. Jiao, Y. Zheng, S. Z. Qiao, Electronic and Structural Engineering of Carbon-Based Metal-Free Electrocatalysts for Water Splitting, *Adv. Mater.* 2019, *31*, 1803625.
30. X. Wang, Y. Zhu, **A. Vasileff**, Y. Jiao, S. Chen, L. Song, B. Zheng, Y. Zheng, S.-Z. Qiao, Strain effect in bimetallic electrocatalysts in the hydrogen evolution reaction, *ACS Energy Lett.* 2018, *3*, 1198.
31. F. Xie, L. Zhang, Y. Jiao, **A. Vasileff**, D. Chao, S. Qiao, Hydrogenated Dual-Shell Sodium Titanate Cubes for Sodium-Ion Batteries with Optimized Ion Transportation, *J. Mater. Chem. A* 2020.
32. C. Ye, L. Zhang, C. Guo, D. Li, **A. Vasileff**, H. Wang, S. Z. Qiao, A 3D hybrid of chemically coupled nickel sulfide and hollow carbon spheres for high performance lithium–sulfur batteries, *Advanced Functional Materials* 2017, *27*, 1702524.
33. B. Bayatsarmadi, Y. Zheng, **A. Vasileff**, S. Z. Qiao, Recent Advances in Atomic Metal Doping of Carbon-based Nanomaterials for Energy Conversion, *Small* 2017, *13*, 1700191.

34. C. Guo, J. Ran, **A. Vasileff**, S.-Z. Qiao, Rational design of electrocatalysts and photo (electro) catalysts for nitrogen reduction to ammonia (NH₃) under ambient conditions, *Energy Environ. Sci.* 2018, *11*, 45.
35. S. H. Hsu, J. Miao, L. Zhang, J. Gao, H. Wang, H. Tao, S. F. Hung, **A. Vasileff**, S. Z. Qiao, B. Liu, An earth-abundant catalyst-based seawater photoelectrolysis system with 17.9% solar-to-hydrogen efficiency, *Adv. Mater.* 2018, *30*, 1707261.
36. K. Qu, Y. Wang, **A. Vasileff**, Y. Jiao, H. Chen, Y. Zheng, Polydopamine-inspired nanomaterials for energy conversion and storage, *J. Mater. Chem. A* 2018, *6*, 21827.
37. Y. P. Zhu, Y. Jing, **A. Vasileff**, T. Heine, S. Z. Qiao, 3D synergistically active carbon nanofibers for improved oxygen evolution, *Adv. Energy Mater.* 2017, *7*, 1602928.
38. S. Yang, K. Zhang, C. Wang, Y. Zhang, S. Chen, C. Wu, **A. Vasileff**, S.-Z. Qiao, L. Song, Hierarchical 1T-MoS₂ nanotubular structures for enhanced supercapacitive performance, *J. Mater. Chem. A* 2017, *5*, 23704.

Presentations:

1. **A. Vasileff**, Selectivity control for electrochemical CO₂ reduction using copper-based alloys, ChinaNANO, Beijing, China, August 2019. (Oral Presentation)
2. **A. Vasileff**, Copper and Copper Alloy electrocatalysts for the selective reduction of CO₂ to fuels and chemicals, Research Seminar, School of Chemical Engineering, The University of Adelaide, November 2019. (Oral Presentation)